Politecnico di Milano
Department of Energy

doctoral program in energy and nuclear science and tecnology

Modeling, optimization and experimental evaluation of Solar Direct Steam Generation for integration into industrial heating processes

Doctoral Dissertation of:
Antoine FREIN

Supervisor:
Prof. Mario MOTTA

Tutor:
Prof. Livio MAZZARELLA

The Chair of the Doctoral Program:
Prof. Carlo Enrico BOTTANI

2017 - XIX PhD Cycle

Abstract

The aim of this PhD is to demonstrate the potential and the feasibility of solar Direct Steam Generation (DSG) for the specific application of industrial heating processes. In order to study the physical phenomena which take place in a solar DSG plant and affect its generation and performance: modeling activities (three models developed), experimental lab tests and real case studies applications have been carried out. One of the major difficulties in modeling of two phase flow is to determine the geometry of the flow, i.e., the liquid and gas distribution over the cross section. In this field none of the existing semi-empirical correlations for flow pattern prediction is suitable for solar DSG: ie. diabatic two-phase flow defined for water at high pressure (3-30 bar) in large tube diameter (ca. 70 mm). Therefore we aimed to further develop the semi-empirical correlations of Kattan Thome and Favrat (KTF) and its updated version (Zurcher, Thome and Favrat), developed for similar conditions: diabatic two-phase flow with refrigerants at low pressure (< 9 bar) and for small pipe diameters (< 14 mm). Thus, the first part of this PhD consists in the validation of extension of the flow pattern map outside of its original boundary conditions.

Further a DSG test bench was developed at the Department of Energy of Politecnico di Milano (POLIMI - DENG) and the *modified KTF* correlations have been performed for water fluid under laboratory scale. More than 100 steady-state tests have been performed and a good agreement is observed between experimental results and *modified KTF* correlations.

In literature, published performance results from existing "real" operating solar DSG installations are yet scarce. Good practice examples are required to demonstrate the feasibility of solar DSG for the integration into industrial heating processes. Thus, the model (validated with the experimental data above mentioned) has been applied to a solar DSG plant installed in Amman-Sahab / Jordan at RAM Pharmaceuticals Company with the objective to quantify and evaluate the performance for two different periods of 14 days each, in winter and in summer. Pressure distribution, pressure drops and liquid level variation are the variables compared between measurement and expected results, for two characteristic days, one in each period.

An innovative flow pattern analysis is presented and three levels of optimization are proposed to improve energy performance and plant behavior (stability, safety). The first one focuses on the methodology to design the solar field layout (parallel vs series, ideal mass flow rate) for a MW plant. The second one analyzes the effect of fast moving evaporation start point and it defines the conditions to avoid harmful conditions at absorber outlet. And finally, night heat loss has been reduced by approximatively 20% on a summer day thanks to the optimized control strategy implemented in April 2016 at RAM plant.

Keywords: *Direct Steam Generation; flow pattern; modeling; experimental activity; monitoring analysis*

Contents

Chapter 1

Introduction

In this introductory chapter the motivation, the technological background and the research program and goals are presented.

1.1 Motivation

Currently there is a worldwide pressure to reduce fossil fuel consumption, due to the environmental awareness of anthropogenic impact by carbon dioxide emissions on global warming. The Paris Agreement, COP 21, recognized that the climate change represents an urgent and potentially irreversible threat to human societies and the planet. An objective has been defined and fixed to hold the increase of the global average temperature well below 2 °C above pre-industrial levels [1]. This limitation constitutes an important driving force behind a progressive introduction of clean and viable alternatives in all energy consuming sectors. At European level, the decarbonisation of the energy system has been a goal for the last decades [2]. Nevertheless, most of the EU's initiative has been focused mainly on the integration of sustainable energy in the power system such as photovoltaic and wind energy. However, fuels consumed for heat production (industry sector, residential sector and commerce and trade sector) represents approximatively 35% of the OECD's total final energy consumption in 2014 [3], from which the industry sector represents approximatively 43%.

In 2015, Naegler highlighted this paradox, ie. high share of heat in the Energy system and low attention, by comparing the European legislation regarding renew-

able energy. He noticed a strong discrepancy between the heating sectors compared to power and transportation sectors. In fact, there was neither a legislation with direct aim of promoting renewable heating on the EU level, nor any official target for heat renewable share of the heating sector while there was one for power and transportation [4].

In this context, the industrial sector has been identified as a high-potential and still largely unexplored application for heating renewable technologies. Chapter 3.2.1 highlights the huge potential of industrial process heat in the range of medium temperature level which represents between 3.6% and 5% of the overall final energy consumption of EU27 in 2012 [5]. The only two commercially mature renewable heating technologies able to reach that range of temperatures are the biomass and the concentrating solar technologies, the latter having clear advantages in terms of environmental impact (no particulate production, smaller land use) and energy supplying (no need for purchasing the fuel). Thus, the market potential for this technology is very large.

However, Solar Heat for Industrial Processes (SHIP) is still a niche market and its market penetration has been slow and difficult in the last decades. Philibert, in the IEA's report, highlighted the barriers to solar thermal technologies diffusion and ranked them in three main categories: technical, economic and institutional, legal and behavior barriers [6].

- Despite the main technical barriers have been solved, the long history of disappointing projects (lower energy performance than expected) generated a disapproval of solar energy. Moreover, to reach high temperature only concentrated solar collectors are viable solution. However, these technologies are applicable only on the region with high DNI.

- Economic barrier is due to the relatively low solar efficiency (depending to the location) and relatively high cost per MWh compared to energy price competitor. This lack of competitiveness is due to two main reasons:

  - the lack of quantification of the air pollution in fossil fuel price
  - the direct or indirect subsidies to other energy sources (natural gas) in some developing countries where solar irradiation is very high.

And finally, the industrial sector requires a very short return on investment due to the investment strategy based on three or five year term which is not compatible with the expected lifetime of the solar projects (ca. 20 years)

- Permits are from times to times refused due to the non-compatibility with existing standards. For instance, it is an issue for solar DSG as it is considered as a distributed steam generation and has to fulfill restrictive standards. Finally the lack of awareness of the current status of solar technology discourages the implementation of system that requires little more attention than conventional system to be effective.

1.2 Technological Background

The project scope is to investigate the application of medium temperature [100°C-250°C] Direct Steam Generation (DSG) from a solar Linear Fresnel Reflectors (LFR) into industrial heating processes.

1.2.1 Single axis concentrated solar technology

To generate steam between 100 °C and 250 °C single axis tracking solar concentrated technology is mostly applied. Linear Fresnel Reflector (LFR, used in this study) and Parabolic Trough Collector (PTC) have a line-focus and consequently only needs to track the sun about one axis, see figure 1.1.

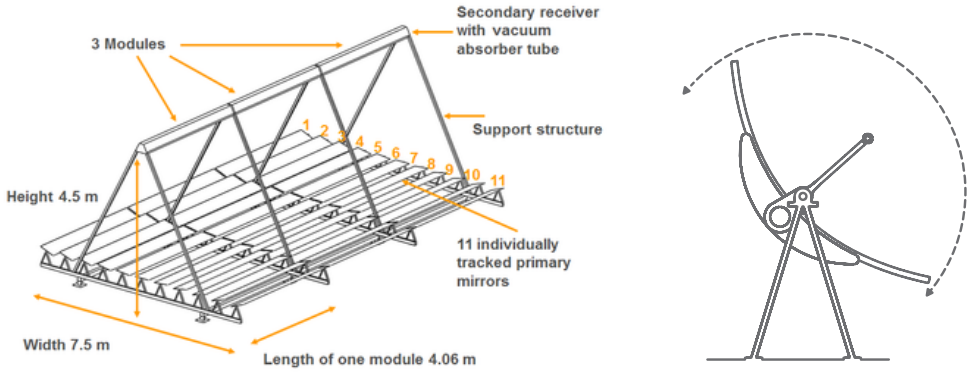

(a) (b)

Figure 1.1: (a) schematic LFR from Industrial Solar (LF-11's datasheet). (b) schematic PTC from Soltigua (PTMX's datasheet).

A parabolic trough collector is composed by a reflector, curved as a parabola and an absorber tube installed on the focal line of the reflectors. The parabolic reflectors rotate to track the sun movement during the day and focus the direct solar irradiation to the receiver where heat is transferred to the fluid.

A linear Fresnel collector typically includes array of tracked reflectors that are installed on a horizontal plane. The tracking of each row is performed to focus the solar irradiation to the stationary linear receiver. A secondary mirror, installed above the receiver, improves the optical accuracy of system. Zhu performed a description of the state of the art of Linear Fresnel technology [7].

The comparison of these two technologies shows on the one hand that the LFR: is more economic, has a higher ground coverage, and has lower wind load. On the other hand, PTC has a higher optical efficiency due to the combination of fixed receiver and the one axis tracking reflectors in a horizontal plane for LFR (greater cosine losses).

1.2.2 Solar Direct Steam Generation

Beyond the solar collector, the working fluid is another important component in a concentrating solar thermal energy system. For the working fluid, also called heat transfer medium, a wide range of materials such as pressurized water, steam, synthetic oil, air, pentane and molten salts could be used. For indirect steam generation, the working fluid is liquid and the steam is generated through a liquid/steam heat exchanger. The so-called solar DSG (Direct Steam Generation) is the concept where steam is generated directly inside the absorber through the concentrating solar collectors. The absorber is a long horizontal stainless pipe where the evaporation takes place. Sub-cooled water flows at the absorber inlet where solar heat is transferred to the fluid. The water temperature increases while water flows in the absorber until it reaches the saturated temperature where flow boiling starts, see example of figure 1.2. Further details are described in Chapter 2.

DSG configuration has a great potential, as it heavily simplifies system integration of solar heat at supply level, which makes the technology attractive from the economic and environmental point of views. However, the use of two-phase flow in the solar loop requires a more advanced control system. The control of water mass

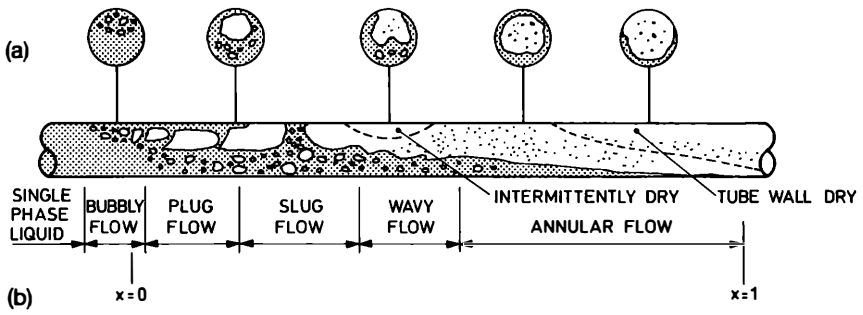

Figure 1.2: Two-phase flow patterns in horizontal tubes [8]

flow rate has to be done carefully to avoid harmful flow pattern, ie. liquid steam distribution that could damage the components such as absorber. An advanced control system is required in order to avoid flow and pressure instability due to fast variation of absorber mass content during transient condition.

1.3 Goals and research program

The aim of this PhD is to demonstrate the feasibility of solar Direct Steam Generation for the specific application of industrial heating processes. The type of study is both numeric and experimental since detailed numerical models are developed and validated on the Direct Steam Generation Laboratory and then applied to a real case study.

The description of the technology of solar Direct Steam Generation (DSG) is presented in the chapter 2 and the potential of the specific application is highlighted in chapter 3. In order to study the physical phenomena which take place in solar DSG plant and affect its generation and performance, three numerical models have been developed and described in chapter 4. A DSG test bench was built at the department of Energy of Politecnico di Milano (POLIMI), with the objective to validate Model 1 and some of its assumptions, presented in chapter 5. In particular, the validation of the updated version of Kattan Thome and Favrat flow pattern map (Zurcher, Thome and Favrat [[88], [89]]) outside of its validity range.

In literature, published performance results from existing installations are yet scarce. Good practice examples are required to demonstrate the feasibility of solar DSG for integration into industrial heating processes. Thus, the validated model has been applied to a installed solar DSG in Amman-Sahab / Jordan at RAM Phar-

maceutcials Company with the objective to quantify and evaluate the performance in winter and in summer, see chapter 6. Finally, novel control strategies and innovative designs are proposed and tested to improve the overall performance and plant stability, see chapter 7.

Chapter 2

Solar Direct Steam Generation

2.1 Objectives

This chapter has the objective to describe the technology of solar Direct Steam Generation (DSG) for readers unfamiliar with the basics of this system or readers seeking general descriptions such as state of the art, advantages and drawbacks of the Direct Steam Generation (DSG), simplify design and control scheme or the expected plant behaviors.

2.2 State of the art of Solar DSG

Historically, the solar DSG technology has been developed and optimized for CSP applications (power production). Thus, the development of medium temperature DSG has to be based on the knowledge acquired in this field. In fact, John Ericsson at the end of the 19^{th} century developed the first solar system of 3.25 m^2 to drive a small engine of 373 W. Some years later, the first large-scale solar thermal energy system was developed by Schuman in 1912-1913. It consisted in five PTC of 62 m length used to drive a steam engine of 40 kW. The generated power was used to pump water for irrigation in Egypt [9], see figure 2.1.

Then, the DSG development slowed down for several years until it came back in the 80's as a response of the oil crisis in 70's. In fact, 5 solar thermal plants using steam as working fluid were installed all over the world (Italy, Japan, U.S.A., Spain and Russia) between 1981-1986 [10]. The largest was the Solar One project

Figure 2.1: Schuman's Parabolic trough collector

which consisted in a vertical central receiver system with a peak power generation of 10 MW_e, installed in Dagett (California). It ran and was connected to the grid for three years [11]. However, receiver tube had some problems of leakage due to cracking of pipes in the receiver, attributed to thermal cycling and unsatisfactory welding techniques. From the 80's to nowadays, numerous CSP plants have been developed mainly using the indirect steam generation technology, with working fluid such as pressurized water, pentane, oil or nitrate salt. In particular, the SEGS projects (Solar Energy Generating Systems) leads to the installation of 9 CSP plants in California from 1984 to 1990. The total installed peak power is 324 MWe and indirect configuration was chosen with oil as working fluid.

Meanwhile, numerous research projects have demonstrated the feasibility of the DSG process in horizontal parabolic trough collectors. The well-known DISS project, led by the two research centers CIEMAT and DLR, had the objective to study solar Direct Steam Generation under real solar condition and it led to several publications [[12], [13], [14], [15], [16], [17], [18], [19], [20]]. After more than 3000 running hours from 1999 to 2001, the DISS project gave the opportunity to develop the experience and know-how in the following fields: modeling, control and operational experience.

The research project called INDITEP has the goal of bringing the DISS concept up to pre-commmercial scale, ie. to produce an engineering design for a 5 MWe large scale prototype [21]. Theses two research projects (DISS, INDITEP) mainly deal with PTC and not LFR.

The development of LFR technology appears a bit latter with project such as Solarmundo [22] in 2002 or CLFR [10] projects in 2008. This late interest comes due the simpler and cost effective design of LFR which compensates its lower optical efficiency compared to PTC. Lately, a large CSP plant based on LFR and DSG, called PE-2, has been installed in the south of Spain by Novatec solar. It is in operation since August 2012 and generates saturated steam at 55 bar for a peak capacity of 150 MW_t and 30 MW_e (total mirror surface of 302,000 m^2), see figure 2.2 [23]. The generated steam pressure in CSP application is usually lot higher than the one of industrial application, since it can go up to 110 bar such as the 50 MW_e plant installed by Areva Solar at Kimberlina, which runs until 106 bar.

Figure 2.2: Linear Fresnel Reflector installed at PE-2 plant [23]

Nevertheless, solar DSG is not yet a common technology for industrial applications: in the last decade, in the knowledge of the author only three projects of solar DSG for industrial heating processes have been developed:

- 108 m^2 parabolic trough solar plant is in operation since July 2010 in an aluminum anodizing plant [[24], [25]]. The saturated steam pressure is generated to feed a steam line at 4 bar-a;
- 1200 m^2 of Linear Fresnel Reflectors, ie. 0.6 MW_t, were commissioned at the end of 2014 with the DSG configuration for a brick manufacturing [26]. The saturated pressure is 12 bar.
- 394 m^2 of Linear Fresnel Reflectors, ie. 222 kW_t have been commissioned in May 2015 for a pharmaceutical company in Jordan [[27], [28]]. The Generated

saturated steam had been directly connected to the steam supply of the factory at 6 bar-g. Industrial Solar GmbH (ISG), a Linear Fresnel Reflector manufacturing company, installed the plant and performed the monitoring of the plant until now. During this PhD work, I had the opportunity to do an exchange period in Industrial Solar offices of 4 months to evaluate the plant performance, see chapter 6. Further research program has been performed on this plant such as the Solstream project [29]. Its project goal is the development of a hybrid solar-fossil standard system for solar process steam generation.

2.3 Solar Direct Steam Generation

Steam generation with solar concentrated technology is usually performed with indirect configuration, ie. by generating steam trough a liquid/steam heat exchanger. In the primary solar loop, the heat transfer medium is always liquid. Pressurized water or synthetic oil are usually used. For this configuration, solar heat is transfered to the working fluid trough sensible heat. The so-called solar DSG (Direct Steam Generation) is the concept where steam is generated directly inside the absorber through concentrating solar collectors. For power applications, this absorber is composed by three regions: the subcooled, the boiling (two-phase mixture) and the superheated region(only steam). Whereas for industrial application, saturated steam is the final product thus superheating region is not required anymore. Such plants (DSG) present numerous advantages as economic and thermal performance improvement and environmental constraint reduction, described in details in section 2.3.2. However, due to a two-phase mixture along the DSG loop, new challenges exist in control and plant sizing compared to the conventional indirect configuration.

2.3.1 Principle and component description

Figure 2.3 shows a simplified scheme of solar DSG for industrial application. The solar steam is delivered in parallel with the steam boiler on the supply level, as described in the integration guideline of IEA SHC task 49 [30]. The drum liquid level setpoint is maintained thanks to feed pump, called P1, that feeds make-up water

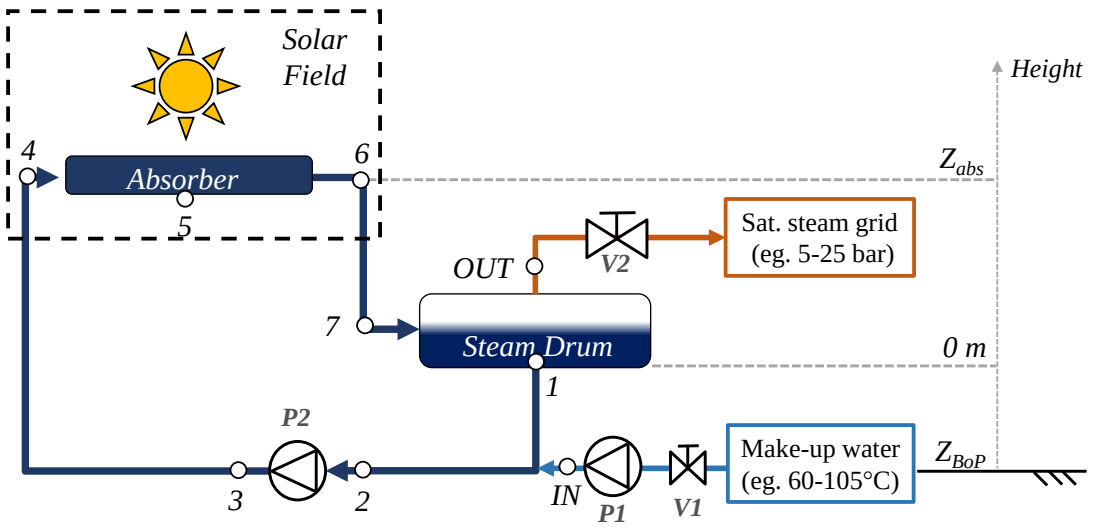

Figure 2.3: Simplified Solar DSG scheme for industrial application *(circles represent the sensor position/nomenclature)*

(point IN) to the solar heating system. For the integration concept of solar DSG, a steam drum has to be used. The two-phase flow of steam and liquid water from concentrating collectors (point 6) flows to the steam drum where the two phases are separated. The steam is delivered to the steam network and the condense flows to the pump P2. In order to avoid cavitation at the pump, vertical liquid water column separates the steam drum to the pump. This water column has to be sufficiently high to compensate the NPSH of the pump. At the inlet of the recirculation pump P2, the condense water and in comparison the colder feed water are mixed. The subcooled liquid flows at absorber inlet (point 4) and water is heated and then evaporates along the absorber. Point 5 indicates the middle of the solar collector loop and point 6 the absorber outlet where the highest steam quality is obtained. The steam generation increases the pressure in the fixed volume of the solar system. In case of sufficient pressure in the steam drum, the steam is fed into the conventional steam circuit (point OUT). A controlled valve is used to maintain the required pressure in the factory's steam grid. While solar steam is fed into the existing circuit, the conventional steam boiler reduces its steam production.

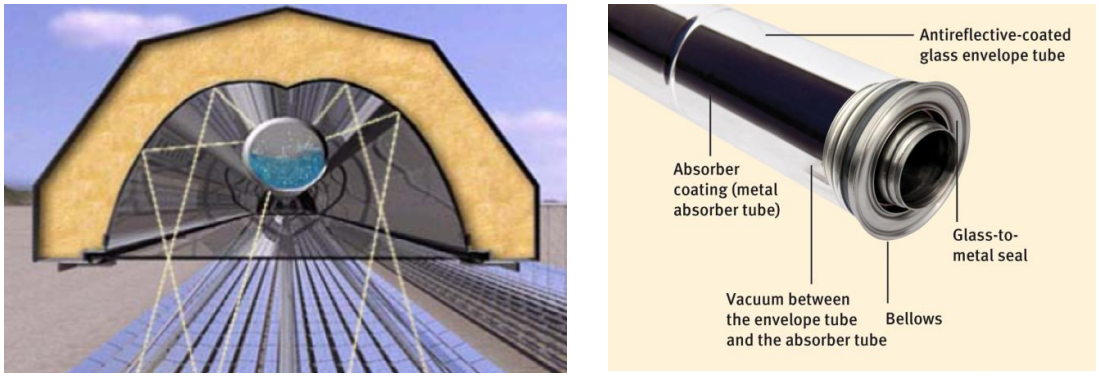

(a) (b)

Figure 2.4: (a) secondary mirror with the receiver (Source: Novatec Solar). (b) receiver description (Source: Schott).

2.3.1.1 Solar Field

The solar field is composed by several concentrated solar collector, LFR in our case study, which focus the solar beam into the receiver. For industrial application, the expected plant size for the next few years (in the author opinion) is in the range of 0.2 $MW_{peak,t}$ and 2.0 $MW_{peak,t}$, ie. a total absorber length in the range 65 m - 650 m. Due to the size limitation, the solar field layout could variate between the series configuration (all LFR connect in a unique loop) and the two parallel rows. The different solar field layouts are investigated in the section 7.2. A secondary mirror is installed above the receiver in order to increase the optical accuracy, ie. the number of solar beam reaching the receiver, see figure 2.4(a). In numerous applications, an advanced receiver, called evacuated tube, is used in order to minimize the heat loss. Figure 2.4(b) shows an example of the Schott's solar receiver. The external glass envelope tube lets entering the solar beams which are absorbed by the metal pipe, called absorber. Vacuum between the glass tube and the absorber tube reduces the convective and conductive heat loss and thus improves the thermal efficiency. To maintain a high level of vacuum, the sealing has to be of high quality and a below is installed at the end of the receiver to compensate the difference of thermal dilation of the glass and of the tube during running condition.

2.3.1.2 Steam drum

The steam drum is a key component of DSG plants, see figure 2.5. Indeed, Steam Drum is installed to separate the biphasic fluid, stabilize the operation of

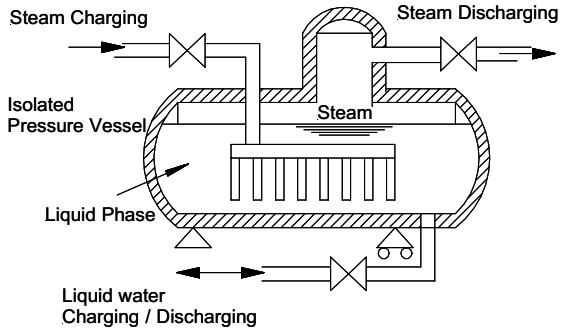

(a)

(b)

Figure 2.5: (a) steam drum scheme [31]. (b) Horizontal steam drum installed at RAM plant (©: S. Anders)).

solar steam generation, and work as a buffer storage to decouple the load from the generation.

It is composed by one or two inlet(s) and two outlets. The first inlet is the two-phase flow from concentrating collectors. Steam drum separates the two phases (liquid and steam) and the condense is recirculated to the steam drum (first outlet) whereas saturated steam feeds the process steam line (second outlet). To balance the mass decrease of the solar system, boiler feed water is fed to the solar heating system in order to maintain the drum liquid level setpoint. The water inlet could be at the pump inlet, as shown in figure 2.3 or at the second drum inlet.

Horizontal configuration of the steam drum is usually chosen due to the following advantages :

- it maximizes the energy stored in the water, ie. the water at the bottom of the drum equals to the saturation condition during charging process of the steam drum (no stratification).

- It minimizes the specific mechanical load distribution, since the steam drum is often installed in a roof.

- It minimizes the reaction times and maximizes the high discharging rates [31], which is due to larger boundary area between liquid and steam.

2.3.2 Pros and cons of the technology

Direct steam generation plants present new boundary condition respect to the conventional steam generation (indirect). Thus, it is important to list their advantages and drawbacks:

- **Thermal Performance:** the expected plant efficiency is higher for DSG plant since no liquid/steam heat exchanger is used, thus the whole solar field piping operates at the live steam pressure range. This means a lower operation temperature that reduces slightly the system heat loss. This thermal improvement is limited due to the small heat loss reduction. In fact, section 4.4.1 shows that the heat gain is two orders of magnitude higher than heat losses.

- **Economic:** the potential economical benefit of using the direct steam generation for power application has already been acknowledge in numerous publications. In 1996, the DISS project estimated a 15% investment cost reduction over state-of-the-art of PTC solar power plant technology using synthetic oil [13]. In 2012, Feldhoff et al. showed the economic potential of DSG power plant without storage [32]. In fact, LEC (levelized electricity cost) could be reduced by about 5-8% compared to an oil plant. The economical potential is due to a simplification of the system integration, ie. the liquid/steam heat-exchanger and auxiliary synthetic oil systems are eliminated. Moreover, removing the synthetic oil also reduces the operation and maintenance costs, since each year 5% of oil has to be replaced. The energy consumption for antifreeze control is also reduced, since the minimum oil temperature is 14 °C [9]. However, DSG plant requires a higher operating pressure which increases the cost of piping and hydraulic components. This latter reduces the economic saving mention above.

- **Environment constraint :** by using steam instead of oil, the risk of fire and leakage are eliminated thus the environment constraint is reduced.

- **Existence of two-phase flow:** the control of water mass flow rate has to be done carefully to avoid harmful flow pattern, ie. liquid steam distribution that could damage components such as absorber. An advanced control system

is required in order to avoid flow and pressure instability due to fast variation of absorber mass content during transient condition.

2.3.3 Expected behavior

In the following paragraph, four characteristic expected plant behaviors are described. The pressure and level variations are described for a simplified day profile, see figure 2.6.

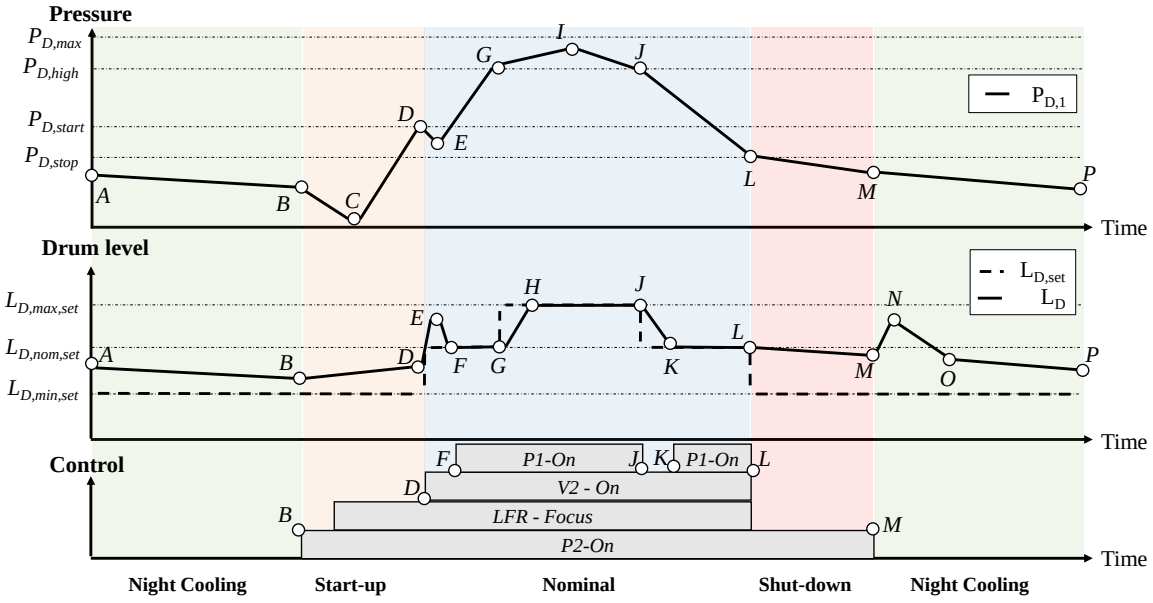

Figure 2.6: Pressure and steam drum level variations for a characteristic day

2.3.3.1 Night cooling:

During the night, the system is closed and the heat losses of the solar system reduce the overall pressure of the system. The recirculation pump (called P2 in figure 2.3) is in stand-by mode thus the recirculation mass flow rate is null. The different parts of the circuit are cooled down according to the local heat losses. In the liquid section, sensible heat loss leads to temperature decrease whereas in the two phases section, latent heat loss slowly reduces the steam pressure and thus its temperature of saturation. After an ideal shut-down, the recirculation loop is liquid and all the steam of the solar system is gathered in the steam drum. Thus, it is expected that recirculation loop temperature decreases faster than the steam drum temperature.

The local heat loss coefficient of the piping is higher than the rest of the circuit thus the temperature decrease in the piping is faster until reaching the ambient temperature. In the absorber, the expected cooling is slower due to the vacuum between the envelope tube of glass and the absorber tube. Thus in the morning, the temperature distribution in the recirculation loop is strongly dis-uniform, with the piping temperature lower than the absorber temperature which is lower than the steam drum temperature.

This temperature decrease of the recirculation loop leads to a water density increase thus the mass of the recirculation loop increases in proportion. As the system is closed during stand-by, the extra mass of the recirculation loop is fed by liquid saturated from the steam drum. For this reason, the liquid level of the steam drum is expected to decrease during the night (from A to B and O to P). A detailed analysis of night cooling effect is done with Model 3 in the section 7.4.

2.3.3.2 Start-up:

The DISS project shows that start-up phase could be long (approx. 1h for an operation pressure of 30 bar) and has to be optimized [33]. The duration is proportional to the state of the collector loop in the morning, thus night heat loss has to be minimized.

In the morning, just before start-up, the average temperature of the recirculation loop is lower than the steam drum temperature, see previous section. When the irradiation is sufficient the *first step* of the start-up procedure is to activate the recirculation pump to reach the required mass flow rate before the mirrors focus the solar beam on the absorber. Thus, during the first minutes of the start-up phase, the saturated liquid from the steam drum fill the recirculation loop whereas the cold liquid is mixed with the two-phase mixture of the steam drum and leads to system pressure drop (point C). As the steam drum is designed to emphasize the mixing, the new equilibrium is expected to be reached very quickly.

To quantify the pressure drops due to the mixing of cold water from the recirculation in the steam drum, the following calculation has been performed. The initial temperature of the recirculation loop is fixed to 40 °C (which is an expected value after one or two days of stand-by) and the volume of liquid in the steam drum at

initial condition is set to 50% of the total volume (V_{drum}). The ratio between the volume of the steam drum and the volume of the recirculation loop, $\frac{V_{drum}}{V_{abs}}$, and the initial pressure of the steam drum are the two parameters of the simulation. A perfect mixing assumption is used to calculate the final pressure, ie. the system is fully mixed in the solar system volume (drum + recirculation loop).

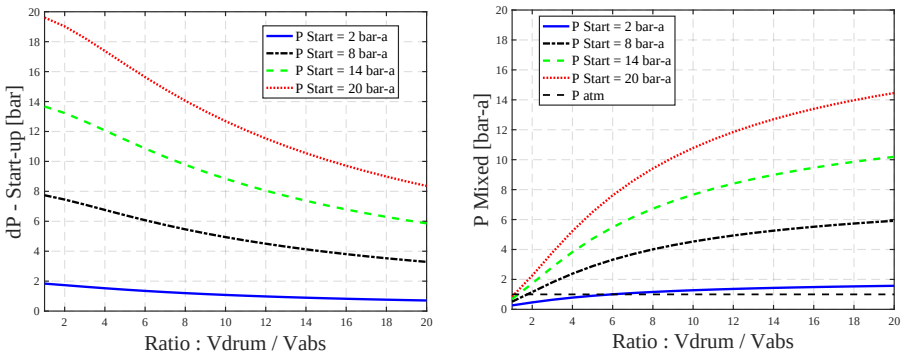

Figure 2.7: Expected pressure drop (left) and system pressure after mixing (right)

Figure 2.7 shows the effect of initial pressure and volume ratio on the final pressure. As expected, while the ratio increases the pressure drops decreases as the quantity of cold water becomes negligible compared to the content of the steam drum. For volume ratio lower than 2 the final pressure is almost independent to the initial pressure and the system goes to under-pressure. For high initial pressure and low volume ratio, a large pressure drop is expected, and could generate mechanical stress. This pressure drop reduction is observed in section 6.4.6 with the case study of RAM and the assumption of fully mixed system is validated.

The *second step* of the control consists in focusing the mirrors on the absorber in order to heat the solar system and increase the pressure. As a consequence, the liquid level in the steam drum increases for two physical reasons:

- the smooth level increase is due to the lower mass density of the liquid in the recirculation loop which reduces the mass content in the recirculation loop;
- the fast level increase is due to the start of boiling in the absorber.

The boiling within the absorber starts once the heat flux is sufficient to reach the saturated temperature at pressure of the absorber. Liquid saturated at drum pressure flows to the absorber inlet, since the feed-in water is null, thus a small quantity of solar heat gain generates the first boiling. A fast movement of evaporation start

point is expected toward the absorber inlet. This strong mass reduction of the absorber content generates a mass flow rate peak at the absorber outlet, which could generate vibrations at the absorber outlet. This phenomena has been observed in the Pye's transient model [34]. This mass reduction in the absorber would increase the liquid level in the steam drum. The start-up phase ends once the drum pressure reaches the pressure set-point (point D) to open the steam valve (called V2 in figure 2.3). Opening this valve, the pressure decreases suddenly in the solar system (point E) and the specific enthalpy of the subcooled water becomes suddenly higher than the liquid saturated specific enthalpy at the new pressure. Thus, most of the absorber content evaporates, phenomena called flashing, and large quantity of water is transfered to the steam drum which generates an outlet mass flow rate peak and a fast level increase (point E), phenomena observed in the section 6.4.4.

In order to avoid any on/off cycling of the steam valve a threshold has to be added to the opening pressure setpoint.

2.3.3.3 Nominal condition:

In nominal condition, the steam is fed to the process line and the mass content of the solar system decreases. The boiler feed water is fed in the solar system to control the level of the steam drum. This control is very sensitive as a non accurate mass flow rate control could generate a system instability. In fact, if a large feed-in water is fed to the system to increase a too low steam drum level then its first effect is to reduce even-more the steam drum level. Indeed, large feed-in water decreases strongly the inlet absorber temperature which leads to fast movement of the evaporation start point to absorber outlet. This phenomena, describes in section 7.3, leads to possible harmful condition at the last part of the absorber. Moreover, this fast movement decreases the steam drum level since the absorber is filled with the inlet feed-in water plus the water from the recirculate condense. This further decrease could generate an even higher feed-in mass flow rate as the difference between the steam drum level and its setpoint increases. This issue could be solved with a low reaction control and it is the reason why advanced control strategy has to be implemented. Valenzuela et.al described advanced control strategy to stabilize the steam generation [[19], [20]].

During the day, the variation of the solar irradiation and of the process load lead to pressure variation of the steam drum. The steam drum energy storage should be maximized to decouple as much as possible the heat generation to the load. It is feasible by installing a large steam drum and by having a large pressure range in the steam drum (ie. difference between the minimum and maximum running pressure). An advanced control strategy for increasing the energy storage capacity would be to increase the level setpoint (point G) of the steam drum when the measured pressure of the steam drum becomes too close to the maximum pressure. In fact, adding some cold water would decrease the average specific enthalpy (thus decrease the pressure) and increase the mass content of the system (thus the capacity storage of the steam drum).

2.3.3.4 Shut down:

When the solar heat gain is too low to generate steam the mirrors are unfocused (point L). An ideal shut down is done when the recirculation is filled with liquid and all the steam is stored in the steam drum. It is done by increasing the mass flow rate some minutes before shut down, in order to push the steam to the steam drum and to cool down the absorber in order to avoid flashing when the pump would stop. During this phase the inlet and outlet mass flow rates are usually stopped, thus the recirculation loop is filled with saturated liquid at the drum pressure. When the pump is active the recirculation loop pressure is higher than the one in the steam drum, thus the inlet saturated liquid at steam drum remains liquid. However, when the pump stops, the absorber, installed usually higher than the steam drum, has suddenly a lower pressure than the steam drum. Thus, the hot liquid in the absorber evaporates leading to a liquid level increase in the steam drum (point N), see phenomena in section 6.4.4. A optimized control strategy has been proposed to avoid the flashing of the absorber during shut down. It consists in filling the absorber with a mixing of condense water with some feed-in water before the shutdown. The specific enthalpy in the absorber is reduced and does not flash when the recirculation pump is stopped. Furthermore, this new control strategy reduces also the heat losses during the night by pushing the hot water in the well insulated steam drum. The effect of the optimized control strategy has been quantified in section 7.4.

2.4 Operation experience

2.4.1 Thermal stress of absorber

Liquid and steam distribution in the tube could generate a strong thermal stress on the absorber. In particular, stratified or dry-out flow patterns (described in section 4.2.1) are the two harmful flow conditions to be avoided. In fact, the low heat transfer rate in the dry region and the non-uniform solar heat flux can lead to a non-uniform circumferential temperature distribution in the pipe cross section. A large circumferential temperature difference causes a thermal stress on the absorber tube, as a consequence the metal tube bends and could break the vacuum space glass envelope, as reported by Odeh [35]. The bending of the receiver during stratified flow pattern could cause a deflection up to 6.5 cm for a 2.9 m long receiver tube [15] [17].

This thermal stress has been analyzed from the numerical point view with a typical flux distribution at the outer circumference of an absorber tube for parabolic trough collectors and stratified flow pattern [36]. This study showed that the highest temperature difference occurs in the superheating section where the low heat transfer rate emphasizes the non uniform heat flux. A temperature difference of 21 °C is expected. With LFR, the typical flux distribution is less dis-uniform than PTC and the peak heat flux is in the bottom part of the tube thus it is expected a lower temperature difference over the cross section.

From experimental activity, Ajona reported that stratified flow in the absorber causes a temperature difference up to 50 °C around the absorber tube wall while annular flow produces a temperature difference of up to 3 °C [12]. At dry-out condition, the absorber and the fluid reach very high temperatures due to the low heat transfer rate of the steam. At high temperature, the different thermal dilatation between absorber tube and glass cover could damage the sealing and compromise the vacuum.

Advanced absorbers have been developed to solve this thermal stress issue. For example, the Cu-Fe bimetallic absorber consists in using a pipe with disuniform thermal conductivity (lot higher for the Cu) to balance the non-uniform internal convective heat transfer rate [37], [38]. A large improvement has been obtained with a maximum temperature difference that has been reduced from above 40 °C to

10 °C. However, the high material cost of the bimetallic tube is still a barrier for its development.

2.4.2 Instability of Parallel rows

The study of parallel pipes behavior is crucial for large scale solar system. In fact, the mass flow distribution is not always well balanced and lead to different fluid thermal-hydraulic behavior between the different strings. Numerous authors studied the phenomena experimentally and theoretically [[39], [40], [41], [42]] for different boundary conditions such as number parallel rows(2-4), symmetric versus asymmetric heating or horizontal versus tilted pipe. Steady state analysis shows multiple solutions for the flow rate distributions in certain intervals and transient simulations allow to check the system response to finite disturbance. Lately, a detailed analysis has been performed with the simulator RELAP for the study of DSG in two parallel pipes [43]. Asymmetric heat flow is studied under different mass flow rate. At high flow rate the splitting ratio is nearly symmetric whereas at low mass flow rate it shows an unfavorable behavior of DSG plant. In fact, most of the liquid tends to flow in the pipe which absorbs less energy and it leads to hot liquid outlet in the first row and high steam quality in the other one.

In the context of industrial application (MW solar plant), there are two alternatives for the solar field layout: the series configuration (all absorber connect in a unique loop), or the two parallel rows. Theses alternatives are discussed in the section 7.2.4.

Chapter 3

Industrial heating processes

3.1 Objectives

This chapter has the objective to describe the specific application of industrial heating processes for users unfamiliar with this application. A general description of industrial processes is presented. It includes: the evaluation of its large potential evaluation, the description of heat generation alternatives and a detailed analysis of the most diffused configuration (centralized steam network). Then, industrial heating process is analyzed from the point of view of solar integration.

3.2 Industrial process description

3.2.1 Industrial process potential

The total energy consumption of industrial process is composed by two main vectors: electricity and direct-fired fuels (gas, oil, biomass, ...). Electricity is used in various ways from mechanical drive, thermal machines (chiller, heat pump) or electrochemical reactions. Direct-fired fuels are used to generate heat at the supply level or at the process level. The use of heat has a wide variety of applications, including washing, dyeing, drying, pasteurizing, sterilizing, cooking and much more. The importance of industrial sector is very large as for example the United States industrial sector represents roughly one-third of the nation's delivered energy supply [44]. In Europe, similar ratio is observed where industry sector represents 25% of the total final energy consumption from which 69% is fuel, see figure 3.1. Nevertheless,

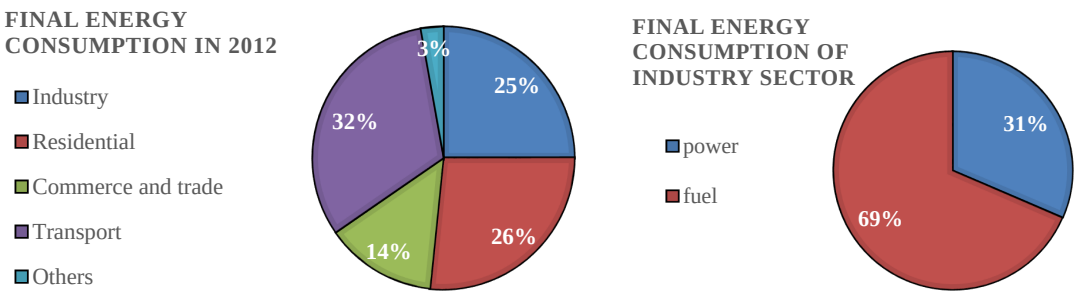

Figure 3.1: Final energy consumption, EU-28, 2012 [4] and [5]

the final heat consumption of industry sector is not sufficient to quantify the decarbonization potential. In fact, the renewable energies for heat generation such as the solar technology are temperature dependent. Naegler shows that the energy share of each level of temperature slightly fluctuates according to the approach used (different database) [4]. Three levels of temperature are defined: low (<100 °C), medium (>100 °C and < 400 °C for the first approach and < 500 °C for the second approach) and high temperature. These two approaches show that low temperature level represents between 25% and 26%, medium temperature between 21% and 27% and finally high temperature represents the largest share of the heat in the industrial sector with approximatively the half of the heat consumption in this sector.

3.2.2 Heat generation

Heat generation could be performed with centralized or distributed systems. For centralized heat generation, a boiler burns fossil fuel to warm-up a heat transfer medium such as pressurized water, oil or steam. Then, the medium would deliver the heat at the point of use. For distributed heat generation is possible to generate heat where it is required, using electricity or burning fuel. The latter configuration is more rare than the centralized heat generation in the industrial sector.

Centralized Steam generation is one of the most used systems. For example, in 2006, 40% of the total energy consumed in U.S. industry was for steam generation [45]. This large use of steam as heat transfer medium is due to its numerous advantages presented below [46]:

- low environmental impact due to a low toxicity and no fire risk;
- high thermal performance due to high heat capacity (latent heat) and high

heat transfer rate during condensation;

- high easiness of use due to: the ease to transport, the ease to control (pressure and temperature relation, condensation at constant temperature) and flexibility of the system (sterile thus suitable for food, pharmaceutical and health sectors);

- economical solution due to a low cost of water and cost effectiveness of distribution of the points of use (no need of expensive circulating pump and of advanced pipework).

3.2.3 Description of a centralized steam network

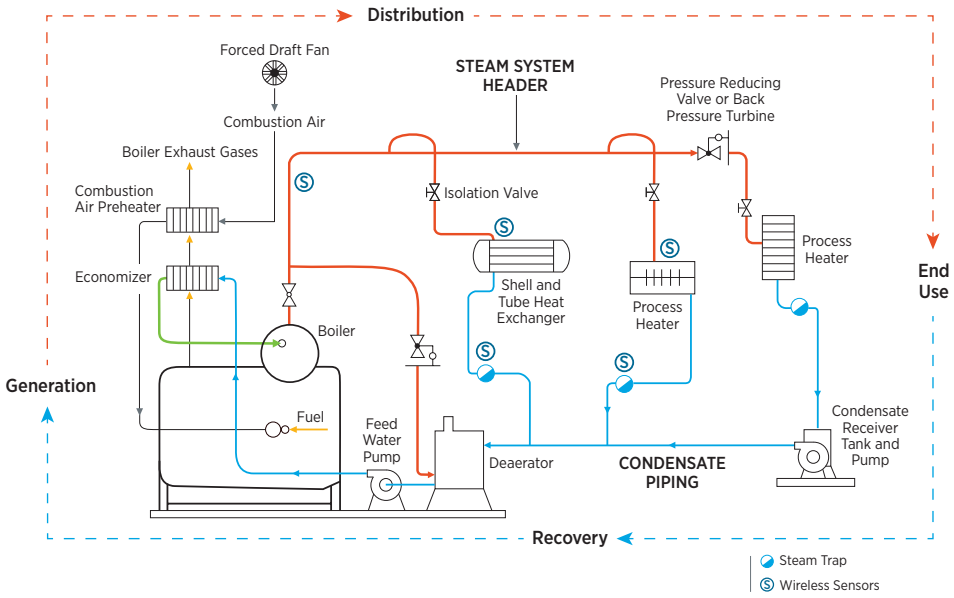

Figure 3.2: Steam System Schematic [45]

To evaluate the different integration concepts of solar thermal technology, it is necessary to understand the life cycle of steam. The centralized heat generation using steam as a heat transfer medium is described in details in this section as it is the most diffused configuration in the industrial sector. Four sections are defined to describe the life-cycle of the steam, illustrated in figure 3.2:

- **Generation:** the steam generation area is composed by a water tank, at atmospheric pressure which gathers the so-called feed water. This liquid water flows to the deaerator and then is warmed-up until saturation condition with

steam. The objective is to strip incondensable gas which has a lower solubility at saturation condition. Then, the hot water is pumped to the steam boiler. For efficient plant, an economizer is installed to cool down the flue gas at the outlet of the boiler and to heat the incoming water. Liquid water is heated and evaporated in a fixed volume. A pressure raise is expected as steam has a lower density than liquid water. Once the required pressure is reached, the saturated steam flows to the end-user trough the distribution network.

- **Distribution:** a pipe network delivers the generated steam at the different end-users. This distribution is done at different levels of pressure. The main line, called steam system header, is at the boiler outlet pressure. Various branches are connected to the header to serve the final user. These branches could be at lower pressure in order to feed heat at different saturated temperatures. This pressure reduction is done thanks to a device called throttles. The other device used in pipe network is the steam trap. It consists in removing the liquid drops due to steam condensation which are gathered in the condensate piping. This liquid drops could cause water hammering due to fast velocity of the steam flow.

- **End use:** End use could be split in two types: open and closed processes. The first one uses directly the saturated steam in the process whereas for the second one the steam condenses in a heat exchanger. The steam used in an open process is lost and fresh water has to be reintegrated, called make-up water. For closed process, condensate at the outlet of heat exchanger flows to the condensate piping.

- **Recovery:** Efficient industrial process has to reuse the condensed steam after the load to save water, energy and chemicals used to treat the fresh water. The condensate flows to the feed water tank which will be used for the steam generation. Nevertheless, condensate piping is pressurized and its pressure has to be reduced to the ambient pressure before entering into the tank. This flashing operation generates liquid saturated and steam at ambient pressure. This flash steam is usually used to warm-up the feed water inside the deaerator or to feed heat to low temperature loads.

The condense from open processes is usually contaminated and can not be used in the recirculation piping. Therefore, the water mass is lost and it has to be balanced with some cold make-up water. However, the energy content in the contaminated condensed steam can be recovered to warm-up this fresh water.

3.3 SHIP: Solar Heating for Industrial Processes

3.3.1 Potential

A large range of solar thermal technologies exists on the market. For low temperature level: flat plate solar collector and evacuated tubes are the two available technologies. For medium temperature level, concentrated technology has to be used. Single axis concentrated solar technology can be used up to 400 °C. Linear Fresnel Reflector (LFR) is more suitable for the lower part of medium temperature range and Parabolic Trough Collector (PTC) for the upper part. Advanced heat recovery systems would reduce the available heat consumption at low temperature. For medium temperature level (above 100 °C) the potential benefit of using solar heat in industrial processes has already been acknowledged [47]. The only two commercially mature renewable heating technologies able to reach that range of temperatures are the biomass and the concentrating solar technologies, the latter having clear advantages in terms of environmental impact (no particulate production, smaller land use) and energy supplying (no need for purchasing the fuel). Chapter 3.2.1 highlights the huge potential of industrial process heat in the range of medium temperature level which represents between 3.6% and 5% of the overall final energy consumption of EU27 in 2012. Thus, the market potential for this technology is very large. Nevertheless, it is currently at the very early stages of developement. In the past decades several solar industrial process heat plants have been constructed. In January 2017, of the 195 ship plants listed in the IEA SHIP plants database [48], 25 plants are larger than 1000 m^2 and 119 have been installed in the last 10 years. However, only 25 involve linear concentrating technology, which shows that the market penetration of medium temperature plant is slow and difficult. Moreover, only two of them are larger than 1000 m^2: one in Arizona of 3.5 MW of PTC with pressurized water for

Frito Lay company in operation since 2008 and one in China (Tianjin) of 1.05 MW of PTC using thermal oil for Procter&Gamble company in operation since 2016. Existing solar DSG plants are not numerous and are listed in section 2.2. This difficult development is due to: unstable oil prices does not enable forecast investment for ship plants; the applicability of solar heat sources depends on the geographical location (concentrated technology needs high Direct Normal Irradiation(DNI)) and the other market barrier penetration are listed in chapter 1.

3.3.2 Integration Concept

Within IEA SHC Task 49, an integration guideline has been developed where the different possible solar integration points are listed and discussed [30]. The first distinction is the difference between the integration at supply and at process level. The first one has the strong advantage to be a simple integration: standardized approach could be used and the process specificity becomes less crucial. Moreover, at supply level the heat potential is large as the generated steam would deserve each process of the plant. On the other hand, the largest heat potential at supply level, which is the integration at the steam boiler outlet (point D in figure 3.3), would require concentrated solar technology such as LFR or PTC. They are more expensive technologies and require Direct Normal Irradiation (DNI). At process level, discussed at point E, the integration is more complex and a full understanding of the process is required but heat could be generated close to the needed process temperature. Figure 3.3 summarizes 5 integration points:

A : **Pre heating of make-up water.** This integration point has a large heat potential for the case of open processes, where contaminated steam has to be replaced. The low temperature range of the make-up water is a strong advantage for solar thermal technology such as flat plat collector or evacuated tube. Nevertheless, the heat potential could be strongly reduced with efficient heat recovery measures. Thus, this integration point is very promising for open processes for which no heat recovery is possible.

B : **Heating of feed-water.** Increasing the water inlet temperature of the deaerator would reduce the steam consumption to reach saturation condition.

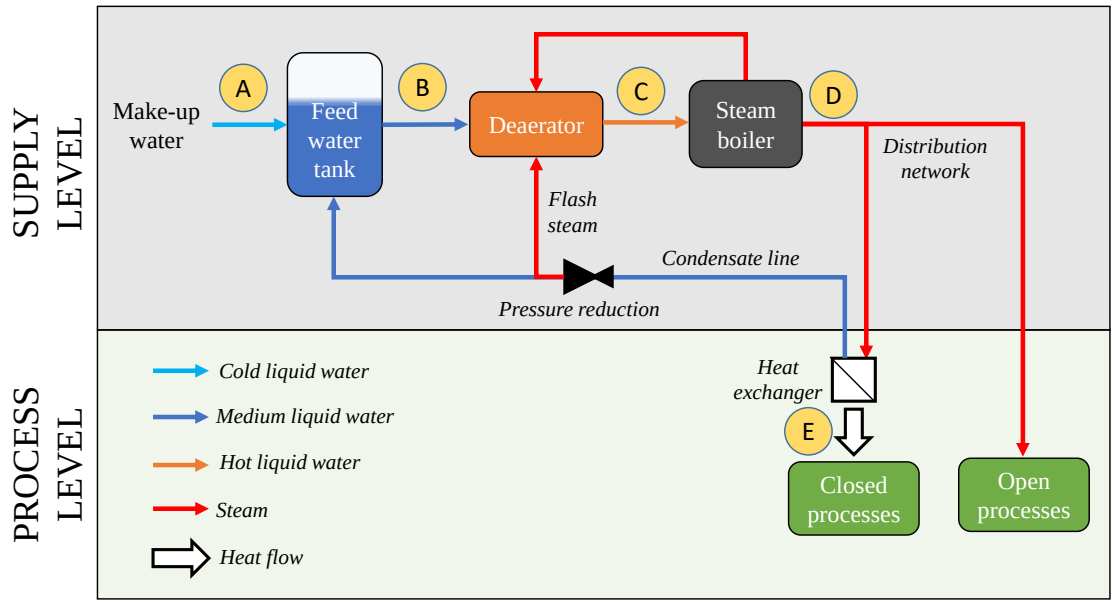

Figure 3.3: Solar heat integration points with a simplified heat generation scheme

The temperature range, 80 °C-100 °C, leads to low efficiency for low temperature solar technology. Despite a relatively low temperature difference, the heat potential could be large as a very large mass flow rate flows to the deaerator. Moreover, this integration would be efficient only if the free available flash steam from the condense line is fully used in the process.

C : **Pre-heating of boiler feed water.** The entire mass flow has to be heated to generate steam into the boiler. This integration point consists in preheating of the water inlet, for instance from 100 °C to 150 °C, to reduce the fuel consumption. Nevertheless, this integration is not possible with advanced steam boilers which use an economizer to cool down the outlet hot flue and concentrating collectors are required.

D : **Steam generation in parallel with the boiler.** A large heat potential is available and it is not affected by the installation of advanced heat recovery systems. Nevertheless, it requires concentrating collectors thus DNI is required. This integration concept is the one discussed in this PhD and the one with the largest potential.

E : **Process level integration.** The solar integration at the process level would allow to reduced the working temperature in the solar loop. In fact, steam

is used to transfer the heat in numerous processes which have low required temperature. For example, dyeing processes have large water and energy consumption due to multiple sub-cycles. Nowadays, heat is usually delivered to the inlet dyeing water (eg. 40 °C) with internal steam heat exchanger to the required temperature. Nevertheless, the inlet water temperature of this sub cycle could be pre-heated to 60 °C to ensure the necessary dyeing quality and to reduce the steam consumption [49]. This solar heat integration is possible at low temperature thus by using flat plate solar collectors. The main drawbacks of this integration point is the need for a deep knowledge of the process and the lower heat demand than the heat demand at supply level which includes all the plant processes.

3.3.3 Specificity of industrial heating process for solar DSG

Solar DSG for integration into industrial heating processes is usually applied at the integration point D, called $SL_{S,PD}$ according to the classification of the IEA SHC Task 49 [30]. Practically, the saturated steam generated by the solar plant would be integrated into the process steam line, so the solar field operates in parallel to the existing steam boiler. An increase of the solar steam generation reduces the required steam from the conventional boiler and vice versa when the solar steam is reduced. Due to non continuous solar irradiation availability, the solar system should be designed (size of drum volume) according to the modulation capacity of the steam boiler.

Historically, the solar DSG technology has been developed and optimized for CSP applications (power production), see chapter 2.2. Thus, the development of medium temperature DSG should be based on the knowledge acquired in this field. Nevertheless, it is crucial to highlight the specificity of industrial applications and the main technical differences of using solar concentrated technology in industrial processes instead of power production. A non exhaustive list is presented below:

- Saturated steam is required instead of superheated steam. The superheated part is the most stressed region for the absorber. For instance, the highest temperature differences occur in the superheating section [36]. Thus, removing this section simplifies the safety control of the plant.

- In the present analysis we had a lower steam quality target than the value suggested by Eck et al. (0.7-0.8), which is recommended for CSP applications since it allows the use of different type of separators (cyclone and baffle) and enables superheated collectors to be run in their ideal operation ranges [50]. For industrial heating processes, there is not any superheated region thus steam quality at the absorber outlet could be reduced.

- Lower pressure range is required, from 3 to 30 bar-g, ie. 140 °C-240 °C, instead of 55-110 bar-g in case of power generation, see section 2.2. Thus, lower pressure rating and a lower insulation efficiency can be used.

- For industrial process, the solar plant should be installed close to the end user. It could be an issue if the target area is not suitable for concentrating solar technology (low DNI, no space available ...)

- Smaller installations are installed due to smaller heat load and due to smaller available area (ie. rooftop installation), industrial processes are frequently located on places where buildings are densely packed.

- Lower steam stability is required. In fact, for power generation the steam generation has to be very stable at the steam turbine inlet. For industrial process, the steam variation should only match the boiler modulation capacity and its characteristic time.

- At the contrary of power generation, for which the solar loop is closed, the industrial application is an open loop. Feed-in water is continuously evaporated and the concentration of ions in the steam boiler increases. Thus, a frequent blow-down of the steam drum should be scheduled in order to maintain the water aggressiveness in the design range.

- For CSP plant the return liquid is similar to saturation condition whereas for the industrial processes it is a mix of feed-water and recirculate condensate. Advanced control strategy to reduce night heat losses could be performed by using the "colder" water available, see section 7.4.

Thus, on the one hand industrial application looks to be simpler and more flexible than power application but on the other hand the installation of smaller system

would limit the economy of scale. Moreover, in the power application dedicated maintenance technicians are available on site while industrial application the maintenance technicians are not specialized on solar technology.

Chapter 4

Numerical Models

4.1 Objectives

In order to study the physical phenomena which take place in solar DSG plant and affect its generation and performance, a specific class of mathematical models has been developed and implemented in this PhD.

Numerous two-phase flow models have been developed in the last decades. A state of the art of existing models that could be used for solar DSG plants is presented, in section 4.3. The advantages and drawbacks of the system simplifications, such as one or three dimensional, the number of conservation equations or dynamic versus steady state are done in order to select the suitable approach. Once some of theses simplifications are applied, some physical phenomena such as heat transfer rate, pressure drops or flow pattern can not be computed anymore and have to be modeled trough empirical or semi-empirical correlations. The most suitable correlations (heat transfer rate, pressure drops and flow pattern) to model a solar DSG plant are presented in the section 4.4.

Based on the literature review presented in the section 4.3 and 4.4, three numerical models have been developed:

- A first model (steady state Model 1), see section 4.5, is developed to study performance and behavior (pressure drops, steam drum level, flow pattern) of existing solar DSG plants. It is applied to the test laboratory (chapter 5) and to a specific case study (chapter 6).

- A second model (dynamic Model 2) is developed to analyze the potential harmful conditions at the absorber outlet due to fast moving evaporation start point within the absorber, see section 4.6.1.

- A third model (dynamic Model 3) is developed to characterize and quantify the night heat loss of the solar DSG plant and the potential energy saving due to optimized control strategy, see section 4.6.2.

4.2 Physical description of DSG application

The so-called solar DSG (Direct Steam Generation) is the concept, where steam is generated directly inside the absorber through concentrating solar collectors. The absorber is a long horizontal stainless pipe where the evaporation takes place. Sub-cooled water flows at the absorber inlet where solar heat is transferred to the fluid. The water temperature increases while water flows in the absorber until the water reaches the saturated temperature where flow boiling starts. The two-phase mixture at the outlet of the absorber flows to the steam drum where the two phases (liquid and steam) are separated. A more detailed description of the solar direct steam generation has been done in section 2.3.

The research project is aimed at the development of a solar DSG system concept optimized for the specific industrial heating processes. Indeed, a system operation with two-phase flow requires a specific optimization to limit the pressure losses, maximize the heat transfer rates and avoid the harmful flow patterns. One of the major difficulties in the modeling of two phase flows is to determine the geometry of the flow, i.e., the liquid and gas distribution over the cross section, called *two-phase flow pattern*. Flow pattern can not be predicted a priori and it affects the other design parameters such as heat transfer rate and pressure drops. In the following two sections, the observed flow patterns in two-phase flow in horizontal tube are presented and then discuss in the context of solar DSG.

4.2.1 Flow pattern description

Two-phase flow pattern has been firstly defined for vertical flow. In horizontal tubes, they are similar but the liquid is influenced by gravity force and this grav-

ity force tends to stratify the liquid phase in the bottom part of the tube. The characterization of flow patterns, based on the Alves description [51], are described below and are represented in the extracted figure 4.1 from Collier and Thome's book "Convective boiling and condensation" [8]:

- **Stratified flow:** the boundary between stratified vs non-stratified flow patterns are defined using the transition mechanism developed by Taitel and Dukler [52]. Kelvin-Helmholtz instability tends to transit out from stratified flow pattern whereas the gravity force tends to maintain the flow in this equilibrium condition. In fact, two phenomena are competing: on the one hand the gas is accelerating above the crest and leads to pressure reduction (due to Bernoulli effect) and thus the wave tends to grow; on the other hand the gravity force is pushing the liquid phase on the bottom part of the tube. Thus, the criterion to understand which of the two forces is dominating determines if the flow pattern is stratified or not.

  - *Stratified:* complete separation of the liquid and gas flow appears at low mass flow rate. The interface between the liquid and gas is smooth and perfectly horizontal.

  - *Wavy Stratified:* the liquid phase is mainly on the bottom part of the tube but the interface is disturbed by liquid waves that climb up the side of the tube. The crest do not reach the top the tube and the gas core is not blocked. At high steam quality, the top of the tube appears dry at very high mass flow rate, which characterize the dry-out region.

- **Intermittent flows:** Once non-stratified flow pattern condition is reached the flow could be intermittent or annular. The transition criterion evaluates the possibility to have the gas core blocked at any location by the liquid (Barnea's unified model [53]). It could happen in two different conditions: due to the instability of the liquid film at the wall perimeter; due to the result of large supply of liquid in the film.

  - *Bubbly:* the vapor bubbles are dispersed in the liquid. In horizontal flow, bubbly flow patterns appear mainly at high mass flow rate. In fact, at

low mass flow rate the bubbles are in the upper half of the pipe whereas they are dispersed in the tube when the inertia force are dominating.

  - *Plug:* this flow pattern, also called elongated bubble, is characterized by elongated bubble along the top of the pipe separated with liquid phase whereas the bottom part of the tube is continuously liquid.
  - *Slug:* the elongated bubble becomes similar in size with pipe diameter then the bottom part is also affected by this discontinuous phase change.

- **Annular:** this stable condition is reached when the flow pattern is non-stratified and transition criteria see above are not reached.
  - *Annular flow:* a continuous liquid film is formed around the whole pipe and the gas phase is flowing in the middle of the tube. For horizontal pipe the liquid film is thicker at the bottom part.

Mist flow pattern occurs at very high steam velocities and leads to strip all the liquid from the wall and the drops are mixed into the uniform gas phase. This condition is not reached in the specific application of solar DSG.

4.2.2 Flow pattern characteristics

As mention before, the prediction of liquid and steam distribution in the flow channels is crucial in DSG plant where possible harmful conditions could appear such as stratified or dry-out flow patterns.

Stratified flow must be avoided since this unfavorably affects the absorber tube temperatures due to high differences in heat transfer between wetted and dry sections of the tube [54]. It is well known that the desire flow pattern for solar DSG is the annular flow pattern. In fact, this flow pattern leads to stable flow condition and the heat transfer rate is high and uniform along the absorber perimeter which avoids any thermal and mechanical stress of the system.

Dry-out conditions must be avoided due to the risk to have very high absorber and fluid temperatures which can become harmful to hydraulic components, if the design temperature is lower. At high temperature, the different thermal dilatation between absorber tube and glass cover could damage the sealing and compromise the vacuum.

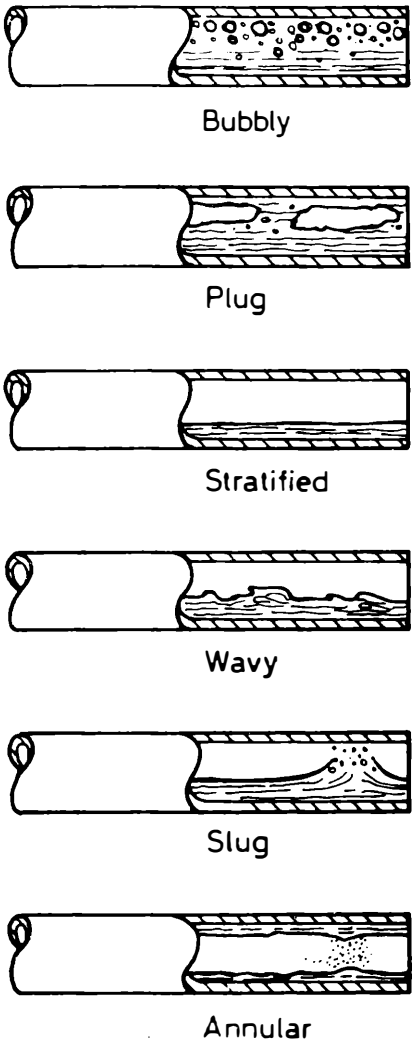

Figure 4.1: Flow pattern description in horizontal flow [8]

Pye in PhD thesis [10] declares that "slug" and "plug" regimes are undesirable because the large variations in fluid momentum between the gas and the liquid "slugs" results in large forces when the flow encounters resistance in the form of pumps, heat exchangers, pipe bends and other equipment. Based on the literature review of mechanical instability of two-phase flow, Miwa shows that "slug" and "churn" (*typical for vertical pipe*) flow regimes have the strongest fluctuation compared to other flow regimes [55]. Nevertheless, the absorber is a long horizontal pipe and fluid momentum has a limited impact if the intermittent flow regime does not reach the outlet piping bend.

In the case of stratified wavy flow pattern, the top part of the pipe could stay dry for a limited period and generate (in some extends) a small dis-uniform temperature profile along the pipe perimeter.

To conclude to ensure the safe operation of solar DSG, we desire the largest share of annular flow, avoiding stratified and dry-out conditions in the whole solar field and avoiding the intermittent flow pattern at the level of special piece of the solar field (pipe bends, sensor, thermal below, ...). In case intermittent regime could reach the outlet of the solar field a flow mixer should be installed.

4.3 Two-phase flow models

Two-phase flow in tube is a subject largely studied. In fact, the prediction of two-phase flow behavior is crucial in numerous fields as thermal machine design (e.g. steam boilers or refrigerant system), offshore oil production or more recently nuclear power stations. As a result, numerous studies have been conducted into computational modeling of two-phase flow.

To model two-phase flow (solar field) with a good accuracy and an appropriate degree of complexity is a real issue. Thus, according to the specific objective, different assumptions have to be done in order to simplify the modeling For instance, the detail required for nuclear applications is lot greater than the specific application of solar concentration. In fact, the driving force behind fast transitory is reduced since heat flux are many times lower. The characteristic time in nuclear sector could reach few milliseconds whereas time characteristics of solar application is of few sec-

onds/minute. Thus, it is safe to say that the complexity used in nuclear sectors is not needed.

4.3.1 System of equations

The three conservation equations written as differential equation are defined on the general form as eq. 4.1, eq. 4.2 and eq. 4.3

$$\frac{\partial \rho}{\partial t} + \vec{\bigtriangledown} \cdot (\rho \vec{w}) = 0 \tag{4.1}$$

$$\rho \left(\frac{\partial \vec{w}}{\partial t} + \vec{w} \cdot \vec{\bigtriangledown} \vec{w} \right) = \vec{B} + \vec{\bigtriangledown} \cdot \vec{\sigma} \tag{4.2}$$

$$\rho \left(\frac{\partial e}{\partial t} + \vec{w} \cdot \vec{\bigtriangledown} e \right) = -\vec{\bigtriangledown} \cdot \vec{q} + q''' + \vec{\bigtriangledown} \cdot (\vec{\sigma} \cdot \vec{w}) \tag{4.3}$$

where $\vec{w}$ is the fluid velocity [m/s], ρ is the density [kg/m3], $\vec{B}$ is the body force [N], $\vec{\bigtriangledown} \cdot \vec{\sigma}$ is the surface force [N], e is the total energy per unit of mass [J/kg], $\vec{q}$ is the heat flux vector over the surfaces [J/m^2], q''' is the heat rate generation per unit of volume [J/m^3], $\vec{\bigtriangledown} \cdot (\vec{\sigma} \cdot \vec{v})$ is the energy dissipation per unit of volume [J/m^3]

The two-phase flow numerical models used for this work are based on a control volume approach. The system of equations on the integral form is composed of 6 conservation equations, ie. three conservation equations for each phase. The equation of continuity, the equation of change of momentum and the equation of conservation of energy are written in Appendix A in the form used in this application.

Different degrees of model complexity can be used and the main system simplifications usually applied to solar DSG are listed below (non exhaustive list) :

- **The number of conservation equations used.** Model using the 6 conservation equations allows the full description of the two-phase flow for each cell: velocity, acceleration and temperature of each phase. In particular, subcooling, superheating and a velocity ratio (the ratio between the steam and liquid velocities) different from one are allowed in the control volume. The simplification of the system of equations down to 3 conservation equations for the liquid/steam mixture is generally applied for solar DSG application.

- **The choice of the dimensional description.** The most advanced approach is the 3 dimensional approach, called Computational Fluid Dynamics (CFD),

which consists in the discretization of the flow domain in fine meshes. This methodology is very expensive in terms of computation costs but reaches the most accurate results. Two-phase flow model is often simplified in 1D model, however it represents a strong simplification on the resolution of the flow field. In fact, phenomena such as pressure drops or heat transfer rate are the results of fluid velocity vector at the level of external boundary (internal wall). This information is not available for 1D model as real vector variables are projected to the main flow direction. Thus, 1D models are completed by empirical or semi-empirical correlations, presented in the section 4.4.

- **Steady state or dynamic approaches.** With steady state approach the system of equation is assumed time independent, which means that the system inertia is low compared to the analyzed time characteristic. Transient phenomena can be observed only with the dynamic approach.

4.3.2 State of the art of solar DSG modeling

In the specific case of solar DSG, lots of works have been done for power generation, ie. with a superheated section. We can distinguish two kind of models: those focusing on control system optimization, where transient phenomena have to be modeled, and those focusing on system design optimization. Very few numerical models have been developed for longterm analysis such as the performance evaluation tool used in the chapter 6.

To model two-phase flow is complex thus the model has to be built according to the objective. In the following sections, the models for two different objectives, ie. Control system and design optimization, are presented.

4.3.2.1 Control system optimization

In the context of control system analysis, an appropriate degree of complexity should be found for the developed model. Very detailed and accurate models, such as the one used in nuclear sector, are too expensive in terms of computation costs to be of practical use; on the other hand a correct description of transient phenomena should be characterized.

Example of models using an appropriate degree of complexity are presented below. They have been classified in two categories: those focusing on the flow boiling in a horizontal pipe and those focusing on the steam drum.

Absorber. In this section the central part of the model is the flow boiling in the absorber. In the 60's, for the application of once-through boiler in large central station power plants, Adams describes the modeling techniques and compares models and field test transients, indicating the model's validity for control studies [56]. For a control purpose he used the finite volume method using mean value for each section, called lumped parameter models. It is the simplest approach to model two phase flow, which replaces complex spatially-continuous processes with simplified processes involving a small number of concentrated entities.

Ray in 1980 presented a lumped model [57] for a once-through sub-critical steam generator. A typical tube has been modeled in three sections: sub-cooled water, biphasic mixture and superheated steam. The three control volumes are time varying and used to developed the model equations. Steady state approach is applied and it defined several equilibrium points for different irradiation intensities. Around these points a linearisation is done and transient responses of step disturbances are presented.

In this context, Lippke developed a transient model to analyze the frequently changing irradiation conditions and clouds passing the solar field of a once-through DSG system [54]. The model have been validated with lab-scale results and scaled to larger system. The model is assuming an homogeneous mixture, one dimensional approach and the momentum equation assumed as quasi-stationary.

In the framework of the DISS project [16], Hirsh presented a two-phase flow model [58] to study the transient behavior of parabolic trough power plants in recirculation mode. It has been developed on the Modelica environment, equations are based on homogeneous equilibrium for one dimensional approach. The thermodynamics variables are transformed into explicit equations. After model validation, the control system is optimized under solar irradiation disturbance and keeping the boundary conditions constant: mass flow rate and specific enthalpy at the inlet and pressure at the outlet. Optimizations focused on the liquid loads on field separator and drainage system in the case of irradiation disturbances. Follow-up articles using

the developed dynamical model are presented to optimize the feed water control, the minimum recirculate rate and the temperature control at the end of the superheated section [[59], [60]].

Casella developed a dynamic model of two-phase flow in a diabatic pipe in the object-oriented modeling environment [61]. It has been implemented in the Modelica library ThermoPower, which is available as an open-source code [62]. The tube is discretized in finite volume and a strong focus on the computation methodology is done in order to avoid non-physical artefacts due to phase boundary crossing the discretization nodes. It is done thanks to the exact computation of the mean density in volumes where phase transition appears. This model, called object in Modelica environment, has been used in the dynamic Model 2 described in the section 4.6.1.

To conclude the numerical models used for control optimization purpose are usually one dimensional approach (fluid properties are uniform at any given cross section), using the dynamic approach and 3 conservation equations applied to the fluid mixture. It leads to only one mixture velocity, i.e. the velocity ratio is not characterized, and both phases are always in thermal equilibrium. Other system simplifications are done such as axial heat flow along the pipe wall is neglected, the dynamic effects of gas-pressure changes are negligible and the momentum equation is simplified (quasi-stationary or stationary).

Transient phenomena of few minutes to several hours are analyzed with good accuracy. Nevertheless, flow pattern is not part of the analysis of this kind of model.

Drum. In this section the central part of the model is the steam drum. Astrom's model describes the complex dynamics of Drum-boiler including drum, down-comer and riser components [63]. The liquid-steam is assumed at thermal equilibrium and the metal temperature variation is correlated with the change of saturated temperature. The energy and mass balances capture the gross behavior of boiler such as the pressure variation. Nevertheless, the distribution of steam and water in the system is required to obtain a model which can describe the behavior of the drum level. The steam distribution in the riser is solved under the steady state assumption for a homogeneous mixture with a dimensional approach. Boiling is assumed to start at the inlet of the riser. The article has been thought for a steam boiler system but could be extend to solar DSG. The main differences are a longer riser (higher ratio

between $\frac{V_{riser}}{V_{drum}}$) and variable specific enthalpy at riser inlet which leads to variable start point of boiling. These latter points generate strong instability of the system, i.e. large pressure and level variation during start-up.

For the dynamic simulation of charging and discharging, the thermal equilibrium model is not suitable to get an accurate pressure description. In fact, during discharging the evaporation process leads to a lower pressure in the accumulator than predicted with the equilibrium model and vice versa during the charging. Thus, non-equilibrium model is developed based on mass and energy balances of each phase by Stevanovic to quantify this phenomena [64].

4.3.2.2 Design optimization

Literature review shows that design optimization has been performed using different levels of details for component analysis (such as absorber) and for system design. The following two paragraphs describe these two types of models

Absorber characteristics. Optimization of detailed engineering for a precommercial DSG solar thermal power plant have been performed by Eck [36]. Thermohydraulic analysis defines the maximum temperature difference and maximum stress (pressure and irradiation) under dissymmetric heat flux in order to select the right wall thickness and material of the absorber. Some studies, as ones of Lobon [65], [66], modeled the absorber pipe with CFD approach under steady state condition. Results are validated and show a very good agreement with experimental data. It quantifies temperature gradient of absorber under non uniform insolation. Nevertheless, Lobon indicates that fully converged solutions are achieved in roughly 4 h per collector which could be a strong barrier for numerous application.

System sizing. Numerical models, mainly in steady state condition, have been developed in the framework of DSG for CSP applications, to evaluate the pressure drop and two-phase flow patterns in absorber tubes [[67], [35], [68], [69], [10], [70]]. These models investigate the critical operating conditions and have been used to optimize the running operation, eg. flow conditions under different radiation level, Ledinegg instability, tube diameter, optimal flow rate, pump sizing and solar field layout.

Odeh introduced a general model of heat loss of Parabolic trough collector (PTC) which is based on wall temperature and in principle applicable for any working fluid. Its model is applied: to quantify and optimize absorber heat loss [67], to study pressure drops based on Martinelli correlation and flow pattern based Taitel and Dukler correlations [35], to investigate the critical operating conditions and to optimize steady-state operation [68], to evaluate the potential of different configuration of solar field (orientation, inclined collectors, appropriate spacing between collector) [69].

Pye developed a transient numerical models to design a new *Compact Linear Fresnel Reflector* [10]. For instance the transient two-phase flow model was used to size the orifices to avoid the Ledinegg instability, and then to size the control valve and recirculation pump [34]

Lately, Sun presented his steady state model based on thermal equilibrium, Taitel and Dukler flow pattern correlation and internal heat transfer rate calculated according to the flow pattern [70]. The model is validated with INDITEP's data and DISS' data. The originality of his analysis is the optimization process based on two parameters the DNI and the steam quality at the separator level. Moreover, it shows that water and absorber temperature difference is very low in the boiling section compared to other section superheated and liquid.

To conclude, system sizing optimizations for power generation are usually done under steady state condition, with the one dimensional approach and by using a set of three equations of conservation. Moreover, flow pattern correlations are always based on the formula of Taitel and Dukler [41], which was developed in case of adiabatic two-phase flows rather than for diabatic processes of evaporation or condensation. In the context of the industrial heating processes, new boundary conditions have to be used: saturated steam, smaller solar field, lower operation pressure than CSP. Chapter 7.2 presents the optimization process of a MW solar DSG plant for industrial sector based on flow pattern analysis. A methodology to define the optimal mass flow rate and solar field layout is described [71].

4.4 Existing two-phase flow correlations applicable to DSG

Different correlations for heat transfer rate, pressure drop and flow pattern of two-phase flow are available in literature. In the following sections, the most suitable correlations for modeling solar Direct Steam Generation are presented.

4.4.1 Heat transfer rate

The heat transfer rate prediction of force convection boiling in a horizontal tube is used to quantify the temperature difference between the fluid and the internal wall of the absorber, see eq. 4.4. In fact, solar heat is transfered from the hot absorber surface according the internal convection coefficient inside the pipes. Inaccuracy of heat transfer rate overestimates or underestimates the wall temperature and thus slightly affects the evacuated tube heat loss. Nevertheless, the overall performance and the plant behavior is only slightly affected due to the fact that heat gain is two orders of magnitude higher than heat losses at nominal condition. For instance, for a fluid at 200 °C for conventional evacuated tube, the expected linear heat loss of the absorber is approximatively 0.04 kW/m whereas the peak linear heat gain for a DNI of 1000 W/m^2 and an optical efficiency of 60% is approximatively 3.3 kW/m.

$$\dot{Q}_{trans} = h_{conv,w} \cdot A \cdot (T_{abs} - T_w) \tag{4.4}$$

where $\dot{Q}_{trans}$ is the heat transfered to the fluid [kW], $h_{conv,w}$ is the water convective heat transfer [kW/m^2.K] and A is the superficial area [m^2].

Collier and Thome [8] provide a description of the different heat transfer regions in the case of vertical tube. From subcooled liquid to Dry-out condition the heat transfer rate is increasing passing trough different heat transfer regions: liquid convective heat transfer, subcooled nucleate boiling, saturated nucleate boiling and two-phase force convective. The heat transfer rate increases with higher steam quality in the liquid and boiling regions. But, once it reaches the dry-out region is suddenly drops to expected value for dry saturated vapor. The simplified figure 4.2 extracted and modified from the book *Convective boiling and condensation* [8] for the specific case

of solar linear concentrated technology shows the variation of the heat transfer coefficient with steam quality and with two different heat fluxes ($\dot{Q}_i < \dot{Q}_{ii}$).

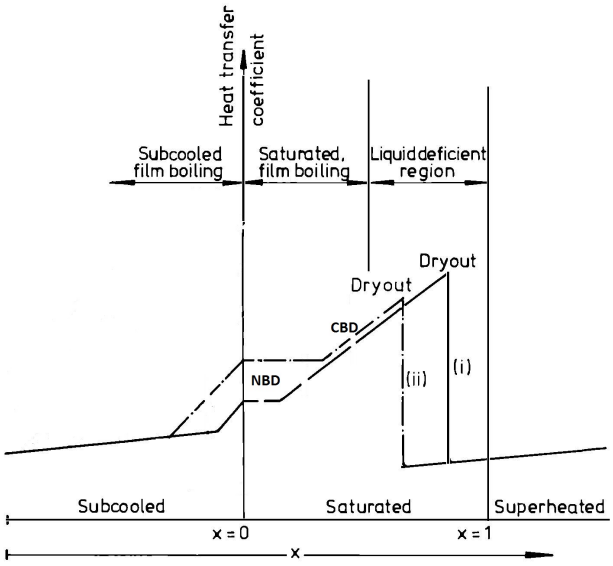

Figure 4.2: Variation of heat transfer coefficient with quality with increasing heat flux as parameter [8]

4.4.1.1 Subcooled

Historically single-phase liquid heat transfer for smooth pipes typically is predicted using dimensionless correlation, see eq. 4.5: the Nusselt number (Nu) defined as eq. 4.6 and 4.7, Reynolds number (Re) defined as eq. 4.8 and Prandtl number (Pr) defined as eq. 4.9.

$$h_{conv} = \frac{k \cdot Nu}{D} \tag{4.5}$$

$$Nu = 4.36 \text{ in laminar flow} \tag{4.6}$$

$$Nu = 0.023 \cdot Re^{4/5} \cdot Pr^{n} \text{ with n =0.3 (heating) in turbulent flow} \tag{4.7}$$

$$Re = \frac{G \cdot D}{\mu} \tag{4.8}$$

$$Pr = \frac{\mu \cdot c_p}{k} \tag{4.9}$$

where h_{conv} is the convective heat transfer [kW/m^2.K], k is the thermal conductivity [kW/m.K], D is the pipe diameter [m], G is specific mass flow rate [kg/s.m^2] , μ is dynamic viscosity [kg/m.s], c_p is the specific heat capacity [kJ/kg.K].

However, in 50's forced convection heat transfer correlations in pipes are strongly

improved by Petukhov correlations [72] as accuracy in the range $0.5 < \mathrm{Pr} < 200$ is 6%. These correlations are valid for high Re number ($\mathrm{Re} > 10^4$) and in 1976 Gnielsinki [73] extended the range of validity down to 2300 by making small adjustment, see eq. 4.10 and eq. 4.11.

$$f = \frac{1}{\left(1.82 \log_{10} Re - 1.64\right)^2} \tag{4.10}$$

$$Nu = \frac{(f/8)\,(Re - 1000)\,Pr}{1 + 12.7\sqrt{f/8}\,(Pr^{2/3} - 1)} \tag{4.11}$$

where f is the friction factor [-].

4.4.1.2 Two phase boiling

The heat transfer coefficients could be calculated in the boiling region with two different approaches.The first one takes into account the type of boiling: nuclear and convective; whereas the second one takes into account the flow pattern of the fluid.

The first model is an extension of vertical tube methods with some adaptations to characterize stratified flow patterns. To calculate the heat transfer rate a strong effort have been made to differentiate between nucleate boiling and convective boiling. For heat transfer rate calculation, the first one is mainly affected by heat flux whereas for the second one mass flow rate and flow quality are the main parameters. In both cases, the heat transfer rate is defined based on a dimensional analysis and proportional to the liquid only heat transfer rate, see eq. 4.12. For vertical pipes, two dimensional numbers are used: Convection number, Co, that combines all arguments related to the pressure gradient as quality and density ratio see eq. 4.13; Boiling number, Bo that characterizes the effect of heat flux on nucleate boiling *(ratio between actual heat flux and the overall heat flux to get fully vapor).* When nucleate boiling is dominating (low steam quality) the convection number (Co) is large and the ratio $\frac{h_{conv,bi}}{h_{conv,lo}}$ is proportional only to boiling number (Bo) and almost independent to Co. In the opposite, when convective boiling is dominating (higher steam quality) the ratio is proportional to the inverse of Co.

The most important additional parameter for horizontal tube is the Froude number, Fr_{lo}, which characterizes the strength of the flow's inertia respect to the gravitational forces that drives the separation of the liquid and vapor phases. The Froude number is required to adapt the heat transfer rate when the top of the tube becomes relatively dry which is characterized by a low Froude number. In this specific case correlation for vertical tubes overestimate the heat transfer rate.

$$\frac{h_{conv,bi}}{h_{conv,lo}} = f\left(Co, Bo, Fr_{lo}\right) \tag{4.12}$$

$$Co \equiv \left(\frac{1-x}{x}\right)^{0.8} \cdot \left(\frac{\rho_g}{\rho_l}\right) \tag{4.13}$$

$$Bo \equiv \left(\frac{\dot{Q}_w}{G \cdot h_{lat}}\right) \tag{4.14}$$

$$Fr_{lo} \equiv \left(\frac{G^2}{\rho_{lo}^2 \cdot g \cdot D}\right) \tag{4.15}$$

where $h_{conv,bi}$ is the convective heat transfer rate of the two-phase flows [kW/K.m^2], $h_{conv,lo}$ is the convective heat transfer rate of liquid only [kW/K.m^2], x is the steam quality [-], ρ_g is density of the steam phase [kg/m^3], ρ_l is density of the liquid phase [kg/m^3], $\dot{Q}_w$ is the water heat flux [kW/m^2], G is the specific mass flow rate [kg/s.m^2] and g is the gravitational acceleration [m/s^2].

Numerous correlations have been defined in the last century based on this model, hereafter a non exhaustive list is presented. Chen developed the first correlation in the 60's [74] to represent boiling heat transfer based on two mechanisms of micro and macroconvective heat transfer. The interaction between the two mechanisms was defined based on dimensionless functions (Re, Martinelli parameter and a bubble-growth suppression function). In 1982 Shah updated this methodology, in order to use it for boiling in both vertical and horizontal channels. His method is in the form of a graphical chart [75]. Four years later Gungor and Winterton [76] found a new form of Chen form validated on a large database (3693 points) covering both the nucleate and convection dominated boiling regimes for fluid such as water and refrigerants.

And finally in 1990 Kandlikar [77] refined this approach to get more accurate

results. His method consists in calculating both heat transfer rate for nucleate, see eq. 4.16, and convective boiling, eq. 4.17, and the largest value is chosen. The Kandlikar correlations lead to mean deviation of ±16% for water and are valid for uniform heat flux, steady state condition and steam quality lower than 0.8 (no dry-out conditions). It does not include the effect of partial dryout on the top perimeter of the tube.

$$\left.\frac{h_{conv,bi}}{h_{conv,lo}}\right|_{nbd} = (1-x)^{0.8} \cdot \left(0.6683 \cdot Co^{-0.2} f_0 + 1058 \cdot Bo^{0.7} F\right) \tag{4.16}$$

$$\left.\frac{h_{conv,bi}}{h_{conv,lo}}\right|_{cbd} = (1-x)^{0.8} \cdot \left(1.136 \cdot Co^{-0.9} f_0 + 667.2 \cdot Bo^{0.7} F\right) \tag{4.17}$$

with:

$$F = 1 \quad \text{for stainless steel tubing} \tag{4.18}$$

$$f_0 = \begin{cases} 1 & for \quad Fr_{lo} \geq 0.04 \\ ((25 Fr_{lo}^{0.3})) & for \quad Fr_{lo} < 0.04 \end{cases} \tag{4.19}$$

The second model takes into account the flow pattern of the fluid, defined by Kattan-Thome-Favrat [[78], [79]]. It has been developed as the foregoing flow boiling correlations are not very accurate for stratified types of flows nor for local conditions with partial dryout on the top perimeter of the tube. Their method is based on their own two-phase flow pattern map for horizontal evaporating flows (described in section 4.4.3).

4.4.2 Pressure drops

Pressure drops prediction for single and two phase flow is a topic well documented as used in the design phase in numerous field (hydraulic components, piping, ...). Nevertheless, expected accuracy in flow boiling is in the range of ±30% [80] it is the reason why a suitable correlation has to be used for the specific application of solar DSG.

4.4.2.1 Single liquid phase

For single phase the pressure drops is calculated based on the following eq. 4.20, and the different existing correlations are used to define the friction factor, f in the different conditions.

$$dp = \frac{1}{2} f \frac{L}{D} \frac{G^2}{\rho} \tag{4.20}$$

where f is the friction factor [-], L is the length [m], D is the diameter [m], G is the specific mass flow rate [kg/s.m2], ρ is the density [kg/m^3].

In laminar flow condition, i.e. Re $<$ 3000, the friction factor is defined as f = 64/Re in case of laminar flow. For turbulent flow, Re $>$ 3000 and when pipe roughness is negligible the Petukhov correlation 4.10 could be used. For rough pipes, the friction factor is calculated solving iteratively the non linear Colebrook equation. For higher Re number ($> 10^4$), algebraic equation defined by Haaland [81] can be computed, see eq. 4.21.

$$f = \frac{1}{\left(1.8 \log_{10}\left(\frac{6.9}{Re} + \left(\frac{\varepsilon/D}{3.7}\right)^{1.11}\right)\right)^2} \tag{4.21}$$

where ε is the wall roughness [m].

4.4.2.2 Two-phase flow

Two-phase pressure drops, $\left(\frac{dp}{dx}\right)_{Bi}$, are calculated through the calculation of the head loss of liquid phase, $\left(\frac{dp}{dx}\right)_l$, and multiplied by a parameter, see equation 4.22. This coefficient depends on the model used: Friedel, Lockhart and Martinelli, Gronnerud, Chisholm, Bankoff, Chawla or Muller-Steinhagen and Heck.

$$\left(\frac{dp}{dx}\right)_{Bi} = \Phi^2 \left(\frac{dp}{dx}\right)_l \tag{4.22}$$

Whalley [82] made an extensive comparison between various published correlations, and large database to provide a methodology to support the choice of correlation (from Collier and Thome's book [8]). The recommendations he made are as follows:

- When $(\mu_l/\mu_g) < 1000$ and $G < 2000kg/(sm^2)$ then the Friedel (1979) [83] correlation should be used.

- When $(\mu_l/\mu_g) > 1000$ and $G > 100kg/(sm^2)$ then the Chisholm (1973) [84] correlation should be used.

- When $(\mu_l/\mu_g) > 1000$ and $G < 100kg/(sm^2)$ then the Lockhart and Martinelli (1949) [85] correlation should be used.

For the specific application of water in the pressure range from 1 to 30 bar the ratio $(\mu_l/\mu_g) = [5; 20]$ is lower than 1000 and specific mass flow rate is always lower than $2000\,\mathrm{kg/(sm^2)}$, therefore the Friedel correlation looks to be the most suitable correlation.

In the case of Friedel correlation, the parameter Φ is calculated according to dimensional numbers as Froude number, eq. 4.15, that represents the ratio between flow inertia and gravity and as Weber number, eq. 4.25, that represents the ratio between the fluid's inertia compared to its surface tension. The parameter Φ is calculated based on eq. 4.23.

$$\Phi^2 = A + 3.43x^{0.695}\,(1-x)^{0.24}\left(\frac{\rho_l}{\rho_g}\right)\left(\frac{\mu_g}{\mu_l}\right)^{0.22}\left(1-\frac{\mu_g}{\mu_l}\right)^{0.89} Fr_l^{-0.447} We_l^{-0.0334} \tag{4.23}$$

$$A = (1-x)^2 + x^2\left(\frac{\rho_l \cdot f_{GO}}{\rho_g \cdot f_{LO}}\right) \tag{4.24}$$

$$We_l = \frac{G^2 \cdot D}{\rho_l \cdot \sigma} \tag{4.25}$$

where μ_g is the dynamic viscosity of the steam phase [Pa/s], μ_l is the dynamic viscosity of the liquid phase [Pa/s], ρ_g is the density of the steam phase [kg/m^3], μ_l is the density y of the liquid phase [kg/m^3], x the steam quality [-], f_{GO} is the friction factor of the steam only [-], f_{LO} is the friction factor of the liquid only [-] and σ is the surface tension for water[N/m].

4.4.3 Two-phase flow pattern

Flow pattern maps are used to predict local flow pattern in a tube. Semi-empirical correlations defined different regions of these maps where each of them

indicates a specific flow pattern. Historically, flow pattern maps were built for adiabatic two-phase flows. In the specific case of horizontal tubes, the correlations of Backer (1954) [86] and Taitel and Dukler (1976) [52] are the most widely used. The baker map is based on empirical analysis done for air/water mixture at 25 °C and atmospheric pressure and pipe diameters of 25 and 51 mm. The Taitel and Dukler correlations introduced flow transition mechanism and empirical parameters in order to generalize and extend the correlations. Then later on in 1986, Barnea combined existing transition mechanism with empirical correlation to create a unified model that incorporates the effect of fluid properties, pipe size and angle of inclination. Lately in the 90's, Steiner adapted existing adiabatic correlation to specific case of diabatic condition by predicting the onset of dry-out for the top part of tube in the case of annular regime [87]. Most of the recent two-phase flow regime maps found in the literature are Steiner's type flow maps, i.e. with quality on the horizontal axis and mass flux on the vertical axis. Finally, the Kattan, Thome and Favrat (KTF) correlations [[88] [78]] and its updated version [89] have been developed and tuned for large number of points: five type of refrigerants have been used (R-134, R-123, R-402A, R-404A R-502) and various heat flux, pipe diameter, specific mass flow rate and pressure have been tested, see summarized table 4.1. This updated version developed by Zurcher, Thome and Favrat, called *modified KTF* map in this work and in the Wolverine textbook [78] are described in Appendix B.

Table 4.1: Test condition range for *modified KTF* map [88], [89]

Variables	***Unit***	***Min***	***Max***
Heat flux	kW/m^2	0.44	58
Pressure	bar	1.12	8.88
Diameter	mm	8	14
Specific mass flow rate	$kg/(s.m^2)$	20	500
Steam quality	-	1%	99%

4.5 Model 1: Detailed steady state model

A detailed steady state mathematical model developed for MW solar DSG plant sizing purposes [71] has been further worked out to define the expected plant behavior. The model outputs are: energy performance evaluation over the studied period and a detailed analysis of the plant behavior such as pressure drops analysis, steam drum level variation, flow pattern analysis and steam quality at the absorber outlet. Algebraic equations of the plant components have been developed and implemented in MATLAB environment. In the following section the full model is described.

4.5.1 General Description

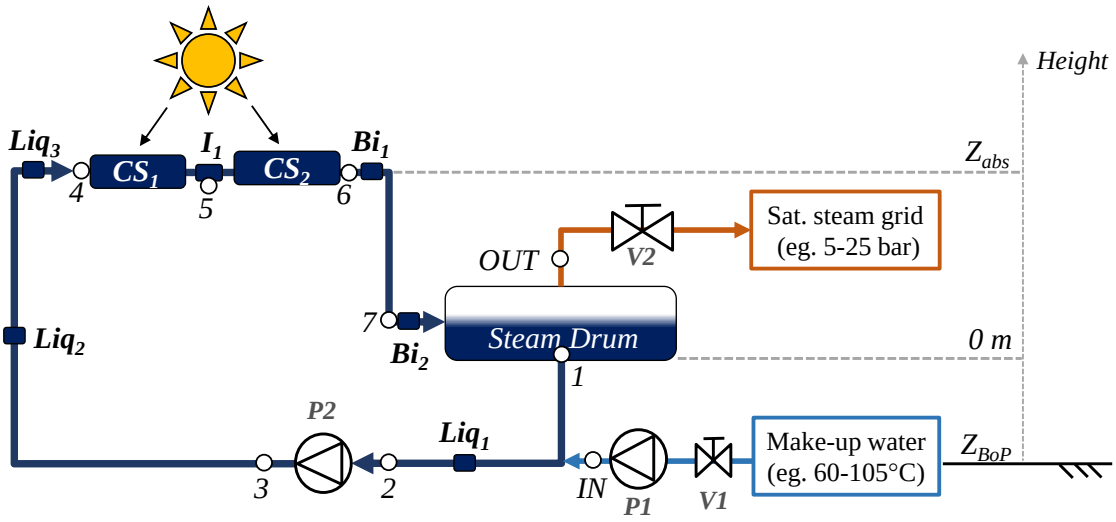

Figure 4.3: Simplified Solar DSG scheme of Model 1

A new steady-state model is implemented, suitable to simulate the operating conditions of a solar heating plant for Industrial process. The recirculation loop is divided 8 different sections : Liq1, Liq2, Liq3, CS1, I1, CS2, Bi1, Bi2, as shown in figure 4.3 where for each section the parameters such as diameter, length, insulation thickness and conductivity property, height and local pressure drops coefficient are defined. Figure 4.3 shows the serie configuration where each LFR module are installed in an unique row. It is possible to simulate parallel rows by using a lower mass flow rate in the sections Liq3, CS1, I1, CS2, and Bi1. For instance, the scenario with 2 parallel rows leads to a mass flow rate split in half in the section from

Liq3 to Bi1 in the condition of a perfect balanced solar field. Only one row of the solar field is simulated assuming that the other rows have similar behavior. Thus, only symmetric solar field can be simulated. The steam drum is the last node of Model 1 which is assumed at thermal equilibrium and defined as the reference height level. The steam drum parameters such as diameter, height, insulation thickness and thermal conductivity have to be defined. The recirculation pump, called P2 in the figure 4.3, is assumed to be an ideal pump which increases the pressure drops to balance the loop pressure drops without any thermal heat gain.

The recirculation pump (P2) of the solar DSG is switched on and off by the control system. When the system is inactive (eg. due to low irradiation) the mass flow rate is null and is called in this study **stand-by mode**. When the pump is active, the mass flow rate is positive and this condition is called **active mode**. Therefore, there is a case distinction for the calculation methodology to obtain the pressure and specific enthalpy along the recirculation loop. In fact, the methodology to describe the plant behavior is very different if the mass flow rate is null or not. Figure 4.4 shows the Model 1 framework.

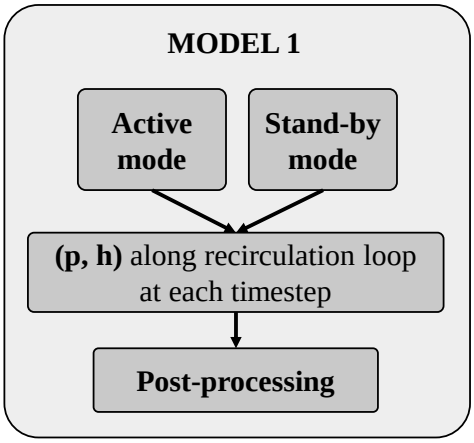

Figure 4.4: Model 1 framework

In the active mode, a spatial discretization of the ordinary differential equations has been implemented. It allows to analyze the physical phenomena within the absorber tube, which result in pressure losses and heat transfer.

In the standby mode, the pressure and enthalpy calculation is done using the temperature and pressure inputs at the characteristic points from 1 to 6 along the recirculation loop and shown by white circle in figure 4.3.

The post-processing model uses two state variables (pressure and specific enthalpy) defined along the recirculation loop for both modes. The two state variable selection allows the calculation of all fluid properties in terms of these variables thanks to IAPWS IF97 standards formulation [90].

Assumptions: The following assumptions have been used to build the mathematical model in both modes:

- **Steady-state:** the model output is assumed time independent, i.e. it should not be affected by previous time step.
- **Finite volume:** the recirculation loop is discretized in fixed finite volumes for the whole simulation.
- **One-dimensional** approach is used, i.e. uniform condition over the pipe cross section and thus only uniform heat flux can be modeled.
- **Homogeneous distribution** in each two-phase finite volume, i.e. velocity ratio between the two phases is equal to one.
- **Thermal equilibrium** of the phases within the reference volume.
- **Pressure drops are lumped** downstream of the reference volume. Momentum pressure drops are neglected and a simplified static pressure drop is used.

4.5.1.1 Active mode model

As the fluid is flowing, the thermodynamic states are calculated iteratively based on the previous node and starting from input data (P1 and T2)

Input. Figure 4.5 shows the 5 inputs of the active mode model:

- P_1: drum pressure at the bottom [bar];
- T_2: inlet temperature of the recirculation pump [°C];
- $\dot{m}_3 = \dot{m}_{rec}$: recirculation mass flow rate [kg/s];
- T_a: ambient temperature [°C];
- $\dot{Q}_{in}$: Gross heat at the absorber [kW].

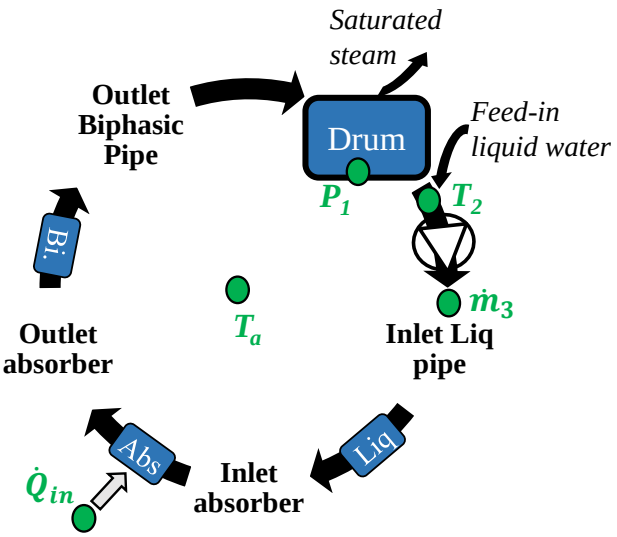

Figure 4.5: Recirculation loop - Input active model 1 (green dots)

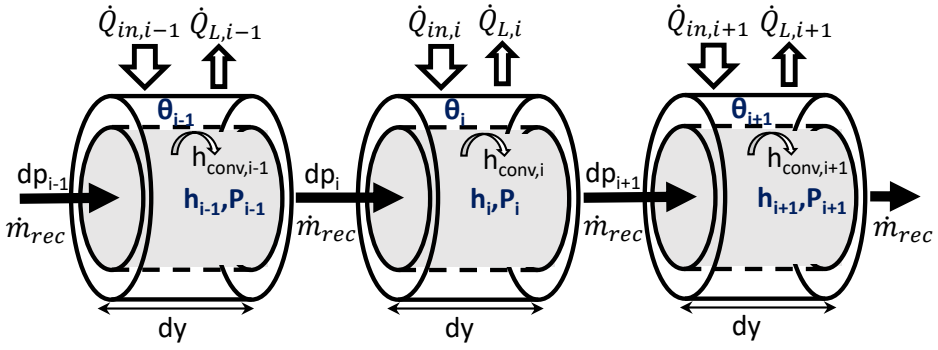

Figure 4.6: Spatial discretization of pipes/absorber;

Methodology. The coefficients dp_i (overall pressure drop) and $h_{conv,i}$ (heat transfer rate) are calculated for each finite volume i, based on the fluid dynamics in the previous volume i-1, see figure 4.6.

The overall pressure drop is composed of four variables: pressure drops in components (local pressure drops), linear, static and momentum pressure drops. The linear pressure drop is calculated by the Petukhov correlation [72] for liquid phase, whereas the Friedel correlation [83] is applied in case of biphasic flows. The momentum pressure drop is neglected whereas the geostatic pressure distribution is simplified in three levels: Steam drum, Balance of Plant container (BoP) and Absorber. The steam drum level has been chosen arbitrary as the reference level. And finally, the pressure drops in components are calculated in each section based on valve characteristics (local pressure drops from data sheet) and piping installation (curves, Tee, ...). The correlations are defined in the section 4.4.2.

In the single (liquid) phase, the heat transfer rate is calculated by the Gnielinski correlation [73], as long as the Reynolds number is in the range $[2.3 \cdot 10^3; 5 \cdot 10^6]$. In the biphasic flow, the Kandlikar correlation [77] is applied. The correlations are defined in the section 4.4.1.

The linear heat gain ($\dot{Q}_{in}$) is an input of the model. Whereas the heat losses ($\dot{Q}_L$) are a result of the model, calculated based on pipe insulation in case of piping (thickness and conductivity at specific temperature) or absorber heat loss coefficients in case of absorber tubes [91].

4.5.1.2 Stand-by mode model

For the stand-by mode, when the forced recirculation by the pump is stopped, the previous approach (active mode) is not suitable to calculate the specific enthalpy along the recirculation loop. In fact, neighboring nodes only slightly impact the reference volume (only small natural circulation and heat conduction). On the contrary, the local heat losses strongly affect this specific enthalpy, but are difficult to estimate with a good accuracy.

The Model 1 is built as a steady state model thus the chosen methodology has to be independent of the previous time step, ie. inputs defined at time t have to be sufficient to calculate the two state variables (p, h) along the recirculation loop.

Due to this constraint, stand-by mode has to use numerous inputs defined along the recirculation loop. Then, temperature distribution of each section is defined by using the most similar temperature input point. For instance, it has been used the temperature input 2, see figure 4.3, to define the temperature of the liquid section *Liq1*.

The pressure distribution is calculated using the same approach and by using the three plant levels (BoP, Steam drum and absorber). Finally, the specific enthalpy along the recirculation loop can be calculated by using the temperature and pressure distribution. In the specific case where the temperature in a specific section is higher or equal to the saturated temperature (calculated with the pressure distribution), then it is assumed that the considered section is liquid at saturation condition.

This methodology defines a rough approximation of the pressure and specific enthalpy of each finite volume of the recirculation loop based on inputs defined at the specific time step. The validation of this approximate model is done thanks to the Temperature profile analysis at start-up and shut down in the case of RAM plant, see section 6.3.1. This model is also compared and validated to the semi-empirical dynamic model 3 of night cooling in the section 7.4.1.

4.5.1.3 Post processing model

The previous two modes define the pressure and specific enthalpy for the whole recirculation loop at each time step of the analyzed period. Based on the two state variables, further analysis is applied with the post-processing model. The input nomenclature and positions are defined in figure 4.3. The post processing model is usually applied with monitoring data and leads to the comparison between expected and measured results.

Mass and Enthalpy of solar system. Once the pressure and enthalpy in the recirculation loop are known, the density is calculated for each volume, based on IAPWS IF97 standards formulation [90]. Thus, the water mass and enthalpy in the piping and absorber pipes are calculated. The mass and enthalpy of the steam drum content are calculated based on liquid level, temperature and pressure measurement. Metal enthalpy is calculated based on the plant configuration (wall thick-

ness, diameter and length of piping, absorber and steam drum) assuming a density of 8000 kg/m^3 and specific heat capacity of 0.5 kJ/(kg K). The metal temperature is calculated in active mode, see eq. 4.40, while in stand-by mode it is assumed equal to the water temperature. The overall water mass of the solar system is the sum of fluid inside the recirculation loop and in the steam drum. And the overall enthalpy includes the water enthalpy plus the one of the metal.

Mass balance and Level variation. A mass balance over the studied period is applied on the overall solar system, see eq. 4.26. The inlet feed-in water ($(M_{in})_{meas}$) and the outlet steam ($(M_{out})_{meas}$) are input data and integrated from t_{ini} to t_{end}. The integration time is selected when the whole recirculation loop is liquid. Initial time, t_{ini}, is set just before start-up. For instance for the case study in chapter 6, it has been chosen 10 min before the activation of the recirculation pump. Final time, t_{end}, could be set just before shut down when the pump still pressurized the recirculation loop (approach used for temperature profile analysis, see section 6.3.1) or after shutdown once the flashing disappears, used for Model 1. For instance for the case study, t_{end} equals 1 h after shut down. The solar system mass is composed by the recirculation loop ($(M_{rec})_{sim}$) and by the steam drum ($(M_D)_{sim}$) calculated with eq. 4.29.

A mass balance of the solar system is applied over the studied period and a mass deviation coefficient ε_M is defined, see eq. 4.30. Theoretically this deviation should always be zero. However, when the Model 1 uses measured data as input, it is not always true. In fact, the inaccuracy in the measurement data or leakage of the solar system could generate a positive or negative coefficient.

The drum level is calculated for each time step under perfect mass balance assumption, i.e. ε_M equals zero and the drum water content mass at time t is the unknown. The initial simulated drum level is set equal to the measured one at the beginning of the day. Two artificial simulated drum levels are introduced. The first one, called $L_{SF=Steam}$, represents the drum level if the whole solar field (SF), i.e. the section from CS1 to Bi2 are full of saturated steam at the pressure measured in the drum. The second one, called $L_{SF=Liq}$, represents the drum level in the case the fluid in the piping and solar field is liquid saturated at drum pressure.

$$\Delta M = [M_{in} - M_{out}]_{meas} - \left[(M_{rec} - M_D)_{t_{end}} - (M_{rec} - M_D)_{t_{ini}}\right]_{sim} \quad (4.26)$$

$$(M_{in})_{meas} = \int_{t_{ini}}^{t_{end}} \dot{m}_{in} dt \quad (4.27)$$

$$(M_{out})_{meas} = \int_{t_{ini}}^{t_{end}} \dot{m}_{out} dt \quad (4.28)$$

$$(M_D)_{sim} = \rho_l(T_1, P_1, L_{D,1}) L_{D,1} + \rho_{g,sat}(P_1)\left[V_D - L_{D,1}\right] \quad (4.29)$$

$$\varepsilon_M = \frac{\Delta M}{(M_{in})_{meas}} \quad (4.30)$$

where the variables not defined above are : $\dot{m}_{in}$ *the inlet mass flow rate [kg/s],* $\dot{m}_{out}$ *the outlet mass flow rate [kg/s],* $L_{D,1}$ *the drum level in volume [m*^{3}*],* V_D *is the volume drum defined as a parameter [m*^{3}*],* ρ_l *the liquid density [kg/m*^{3}*],* $\rho_{g,sat}$ *the saturated steam density [kg/m*^{3}*].*

Energy performance analysis. The energy performance analysis quantifies the deviations between the expected and the measured delivered energy, see eq. 4.31. The expected energy gain $(Q_{gain})_{sim}$ is the solar gross heat $\dot{Q}_{in}$, including optical loss and partial load behavior minus the heat loss of the overall system $Q_{L,tot}$, including steam drum heat loss and absorber heat loss for the whole active mode. The start-up loss $(Q_{start-up})_{sim}$ is defined as the enthalpy difference of the solar system between t_{ini} and t_{end} defined in the previous section. And finally, the real energy gain $(Q_{net,gain})_{meas}$ is the energy difference between the delivered saturated steam at the pressure P1 (monitored data) and the inlet energy from feed-in liquid water at the temperature T3 (monitored data) at atmospheric pressure, see eq 4.32. To quantify the energy deviation between expected and measured, the coefficient ε_Q is defined, see eq. 4.35.

$$\Delta Q = (Q_{net,gain})_{meas} - [Q_{gain} - Q_{start-up}]_{sim} \tag{4.31}$$

$$(Q_{net,gain})_{meas} = \int_{t_{ini}}^{t_{end}} [\dot{m}_{out} h_{g,sat}(P_1) - \dot{m}_{in} h_f(T_3, P_a)]\, dt \tag{4.32}$$

$$(Q_{gain})_{sim} = \left[\dot{Q}_{in} - Q_{L,tot}\right]_{sim} \tag{4.33}$$

$$(Q_{start-up})_{sim} = [H_{rec} + H_D]_{t_{end}} - [H_{rec} + H_D]_{t_{ini}} \tag{4.34}$$

$$\varepsilon_Q = \frac{\Delta Q}{[Q_{gain} - Q_{start-up}]_{sim}} \tag{4.35}$$

where the variables not defined above are : $\dot{m}_{in}$ *the inlet mass flow rate [kg/s],* $\dot{m}_{out}$ *the outlet mass flow rate [kg/s],* $h_{g,sat}$ *the specific enthalpy of saturated steam [kJ/kg],* h_f *the specific enthalpy of the feed-in water [kJ/kg],* H_{rec} *the enthalpy of the recirculation loop (metal and content) [kJ],* H_D *the enthalpy of the steam drum (metal and content) [kJ].*

Flow pattern analysis. Once pressure, temperature and steam quality distribution have been calculated for the whole recirculation loop, the flow pattern distribution in each finite volume of the solar field is analyzed.

Historically, flow pattern maps were built for adiabatic two-phase flows, see section 4.4.3. In more recent years, new flow patterns specific to evaporation (diabatic) in horizontal tubes and tuned for refrigerants in small-diameter pipes have been developed by Kattan, Thome and Favrat (KTF) [88] and then modified by Zurcher, Thome and Favrat [89]. In the present study, the *modified KTF* correlations have been adapted to water flow in larger diameter pipes (70 mm compared to 8-14 mm). These semi-empirical correlations are based on the diameter, pressure and heat flux and they define different regions for each flow pattern (e.g. stratified, wavy stratified, intermittent, annual and mist flow). Based on the specific mass flow rate and the steam quality of the reference volume, the *modified KTF* correlation can effectively define the associated flow pattern. These correlations are not defined for very low steam quality, lower than 0.01 see table 4.1, thus this condition is added extra to the previous flow pattern list. The flow pattern distribution consists in defining the flow pattern expected for each node of the absorber. This analysis is iterated

for each time step and shows the evolution of the flow pattern during the studied period into the solar field.

Pressure drops of the whole system. The pressure head of the recirculation pump is measured as the difference of P2 and P3, pump inlet and outlet pressure. The expected pressure drops are compared for each time steps to the real measurement.

4.5.2 Numerical description

4.5.2.1 Active mode model

The pressure of each node is calculated based on the conditions in the previous node (eq. 4.36, eq. 4.37). Starting from the bottom of the steam drum, the pressure distribution in the recirculation loop could be defined from node to node along the loop iteratively to the pressure at the outlet of the biphasic pipe, i.e at the entrance of the steam drum. The start and end pressures in the recirculation loop should match, because it is a closed loop. Thus, a second iteration is applied to the pressure distribution, by changing the hydraulic head of the pump.

$$\begin{aligned} &\text{if } i = pump \\ &\qquad P_i = P_{i-1} + dp_{pump} \end{aligned} \tag{4.36}$$

$$\begin{aligned} &\text{if } i \neq pump \\ &\qquad P_i = P_{i-1} - dp_{fri,i}(h_{i-1}, P_{i-1}) \cdot dy \\ &\qquad\quad - dp_{comp,i}(h_{i-1}, P_{i-1}) - dp_{stat,i}(h_{i-1}, P_{i-1})) \end{aligned} \tag{4.37}$$

where $dp_{fri,i}$ is linear friction pressure drop [bar/m], $dp_{comp,i}$ is the singular pressure drop [bar] and $dp_{stat,i}$ is the geostatic pressure drop [bar], dp_{pump} is the hydraulic head of the pump [bar]

The Linear friction $dp_{fri,i}$ is calculated based on existing correlations defined in the section 4.5.1.1 according to the fluid conditions (liquid or two-phase), and the geostatic $dp_{stat,i}$ and singular pressure drops $dp_{comp,i}$ are calculated with eq 4.38 and eq 4.39:

$$dp_{comp,i}(h_{i-1}, P_{i-1}) = \frac{\zeta \cdot \dot{m}_{rec}^2 \cdot 10^{-5}}{2A^2 \cdot \rho(h_{i-1}, P_{i-1})} \tag{4.38}$$

$$dp_{stat,i}(h_{i-1}, P_{i-1}) = \Delta z \cdot \rho(h_{i-1}, P_{i-1}) \cdot g \cdot 10^{-5} \tag{4.39}$$

where ζ is the component pressure loss coefficient [-], $\dot{m}_{rec}$ is the recirculation mass flow [kg/s], A is the inner cross section in the component [m^2], Δz is the height difference in [m], g is the gravitational acceleration [m/s^2], and is the ρ density of the fluid [kg/m^3].

In each finite volume i, energy balance is applied to two different systems: the pipe or absorber metal (eq. 4.40) and the fluid inside the absorber (eq. 4.41).

$$M_{m,i} C_{p,m} \frac{\partial \theta_i}{\partial t} = \dot{Q}_{in,i} - \dot{Q}_{L,i} - \dot{Q}_{trans,i} \tag{4.40}$$

$$\frac{\partial M_i h_i}{\partial t} = \dot{Q}_{trans,i} + \dot{m}_{in} h_{in} - \dot{m}_{out} h_{out} \tag{4.41}$$

where $M_{m,i}$ is the metal mass in node i [kg], $C_{p,m}$ is the specific heat capacity of the metal [kJ/kg.K], and θ_i is the temperature in the metal [°C], M_i water mass of volume i, h_i is the average specific enthalpy of volume i, $\dot{Q}_{in,i}$ is the heat gain (Model input) [kW], $\dot{Q}_{L,i}$ is the heat losses of node i see eq. 4.43 [kW] and $\dot{Q}_{trans,i}$ is the water heat gain see eq. 4.42 [kW].

For the case study in chapter 6, the input $\dot{Q}_{in,i}$ is the linear optical gain of the LFR and for the experimental activity in chapter 5 is the electrical consumption of the heaters.

$$\dot{Q}_{trans,i} = \pi D \cdot h_{conv,i} \cdot [\theta_i - T_i] \cdot dy \tag{4.42}$$

$$\dot{Q}_{L,i} = \left[U_1 \cdot (\theta_i - T_a) + U_4 \cdot (\theta_i - T_a)^4\right] \cdot dy \tag{4.43}$$

where D is the internal diameter [m], U_1 is convective and conductive heat loss coefficient [kW/m.K], U_4 is the radiative heat loss coefficient [$kW/m.K^4$], dy is the finite volume length [m], T_i is the water temperature of finite volume i [°C] and θ_i is the metal temperature of finite volume i [°C]

The convective heat transfer rate $h_{conv,i}$ is calculated based on existing corre-

lations defined in the section 4.5.1.1 according to the fluid conditions (liquid or two-phase). For the piping section, the coefficient U_1 is calculated based on thickness and conductivity of the insulation, see eq. 4.44, whereas U_4 is set to zero. For the absorber section the coefficients defined in the absorber tube datasheet have been used [91].

$$U_1 = \left[\frac{1}{2\pi \cdot k_{ins}} \cdot ln\left(\frac{D + 2 \cdot sp_{ins}}{D}\right) + \frac{1}{h_{conv,a} \cdot \pi \cdot ((D + 2 \cdot sp_{ins})}\right]^{-1} \tag{4.44}$$

where k_{ins} is the insulation conductivity [kW/m.K], D is the internal diameter [m], sp_{ins} is the insulation thickness [m], $h_{conv,a}$ is the convective heat transfer rate of the air [kW/K.m^2]

Thanks to the steady state approach, the mass flow rate is assumed constant throughout the loop and the time derivatives of the absorber metal temperature and of the average enthalpy of the finite volume are neglected. Inside each finite volume, the thermodynamic parameters are assumed uniform thus the outlet specific enthalpy equals the average specific enthalpy of this specific volume whereas the inlet specific enthalpy equals to the one of the previous volume. Thus, eq. 4.40 and eq. 4.41 can be expressed as eq. 4.45 and eq. 4.46.

$$\frac{\dot{Q}_{in,i}}{dy} = \pi D \cdot h_{conv,i}(h_{i-1}, P_{i-1}) \left[\theta_i - T_i(h_{i-1}, P_{i-1})\right] + \left[U_1 \left(\theta_i - T_a\right) + U_4 \left(\theta_i - T_a\right)^4\right] \tag{4.45}$$

$$h_i = h_{i-1} + \frac{\pi D \cdot h_{conv,i}(h_{i-1}, P_{i-1}) \cdot [\theta_i - T_i(h_{i-1}, P_{i-1})] \cdot dy}{\dot{m}_{rec}} \tag{4.46}$$

For each time step two iterations are applied, the first one to solve this non-linear system of equations for each finite volume and the second one to maintain the constraint of the initial and final pressure being equal for a closed loop. The same system of equations is applied for all the sections (liquid, biphasic and solar field). In the specific case of liquid and biphasic pipes: the heat gain ($\dot{Q}_{in,i}$) is zero, U1 is calculated on the base of insulation thickness, U4 is neglected. Moreover, a finer discretization is applied to the absorber compared to the liquid and biphasic pipes.

4.5.2.2 Standby mode model

To estimate the specific enthalpy distribution over the whole recirculation loop, defined in figure 4.3, the temperature and pressure inputs from position 1 to position 6 are used. Specific enthalpy for the liquid pipe from the steam drum outlet to the pump inlet (Liq_1) is calculated thanks to the pressure and temperature at position 2. For the pipe from the pump outlet to the absorber inlet (Liq_2 and Liq_3), the pressure P3 and the average temperature of T3 and T4 are used. From the absorber outlet to drum inlet (Bi_1 and Bi_2) the temperature and pressure at the position 6 is used.

And finally, for the absorber sections a more complex approach is developed. In fact, the linear heat loss are smaller for the absorber than the pipes. Thus, when there is no flow, the temperature inputs at position 4 (absorber inlet), at position 5 (between the two collector strings) and at position 6 (absorber outlet) underestimate the temperature within the absorber. In fact, the temperature inputs on the edge of the absorber have higher heat losses since heat losses is higher in the pipe than in the evacuated tube. To model this higher temperature inside the absorber than on the edge, a theoretical temperature is defined called $T_{teo,abs}$. $T_{teo,abs}$ is assumed equal to the minimum between the saturated temperature at the pressure at position 5 (P5) and the temperature at position 5 plus a empirical temperature difference. Start-up temperature profile analysis, defined in section 6.3.1.1, quantifies this temperature difference. For instance, in the specific case of RAM plant it has been tuned equal to 8 °C, see section 6.3.1.3. Then, a linear distribution is assumed to connect the monitored inlet temperature, the assumed inside temperature of the absorber and the monitored outlet temperature. Hence, for the first half of the solar field T4 (inlet), T5(outlet) and $T_{teo,abs}$(inside) are used whereas for the second half T5(inlet), T6(outlet) and $T_{teo,abs}$(inside) are used.

In the specific case where the temperature in a specific section is higher or equal to the saturated temperature (calculated with the pressure distribution), then it is assumed that the considered section is liquid at saturation condition. Thus, the water is assumed liquid for the whole recirculation loop and the specific enthalpy could be calculated thanks to IAPWS IF97 standards formulation [90].

4.6 Dynamic model

Two dynamic models have been developed to study two transient phenomena of solar DSG plant. The first one, called dynamic Model 2, is developed to analyze the potential harmful conditions at the absorber outlet due to fast moving evaporation start point within the absorber, see section 4.6.1. The second model, called dynamic Model 3, is developed to characterize and quantify the night heat loss of the solar DSG plant and the potential energy saving due to optimized control strategy, see section 4.6.2. Figure 4.7 shows the two different model boundary.

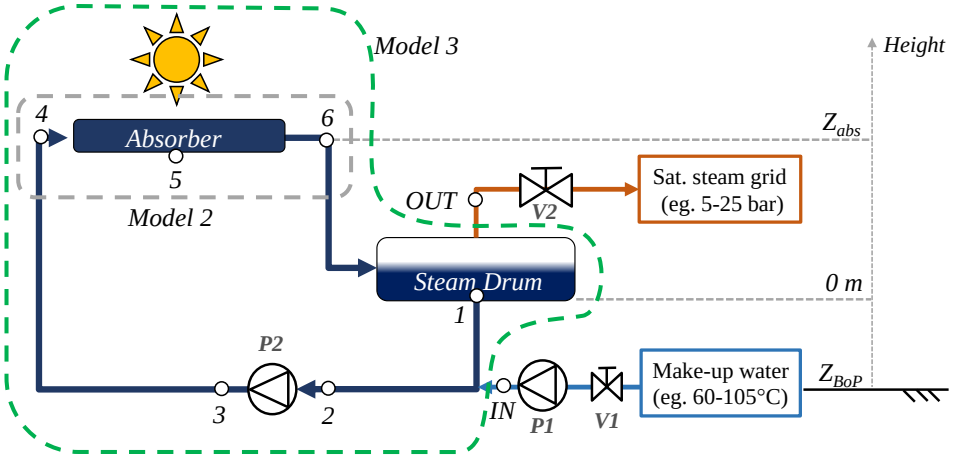

Figure 4.7: Boundary of Dynamic models

4.6.1 Model 2: Absorber

The Model 2 focuses on the physical phenomena that happen inside the absorber during transient condition. In fact, the objective is to observe the steam quality and mass flow rate at the outlet of the absorber when the model inputs are varying. In particular, when the inlet temperature at the absorber or the linear heat flux decreases or increases suddenly.

4.6.1.1 General description

One of the difficulties of Solar DSG system is the interaction of the different components that leads to hardly understand unexpected phenomena, as for example the one described in the section 2.3.3. Within the objective to study only the impact

of fast moving evaporation start point within the absorber, the model focuses only on the diabatic two-phase flow in a pipe where the boundary conditions are controlled externally. The boundary conditions are listed below:

- Specific enthalpy at absorber inlet (position 4).
- Mass flow rate at absorber inlet (position 4).
- Pressure at the absorber outlet (position 6).
- Optical heat flux.
- Ambient temperature.

The model parameters are pipe diameter, pipe length, absorber heat loss coefficients. The two main model outputs are the mass flow rate and specific enthalpy at the absorber outlet (position 6).

4.6.1.2 Assumption

Based on the state of the art of existing model for transient phenomena, see section 4.3, Model 2 has been built as a one dimensional approach, based on homogeneous mixture and thermal equilibrium in each finite volume. The heat transfer rate between the tube and the mixture is assumed constant in this study since it has only a minor impact in the overall results. In fact, the numerical model simplification presented in section 7.2.5.1 shows a relatively low impact of this parameter. For instance, for the case study in section 7.3 it has been chosen a convective heat transfer rate equals to 10 $kW/(m^2K)$, value in the expected heat transfer range from the absorber inlet and absorber outlet. The pressure drops calculation is lumped downstream and defined based on a the simplified correlation based on operation point. The heat loss of the evacuated tube is calculated based on the correlations defined by the DLR's test [91], also used in Model 1, see eq.4.43.

4.6.1.3 Numerical model description

The models of fluid flow in pipes using finite volume and one dimensional approach, described in section 4.3.2, result accurate if the fluid properties do not change drastically across each finite volumes. In the specific case of two phases flow this

hypothesis does not hold anymore. In fact, strong discontinuity appears in volumes containing a phase change boundary thus non-physical artefacts will be generated. This discontinuity is emphasized during fast moving of evaporation starting point within the absorber that strongly stress the model. In order to tackle this issue, Casella presented a two-phase fluid flow model [61], developed in an object-oriented environment publicly available [62]. This model is based on the exact computation of the mean density in volumes where phase transition occurs. This approach avoids the non physical artefacts and strongly smooths the resolution of system of equations.

The mathematical description of the model is presented in the Casella's work [62] and the main concept is summarized here below. The mass balance of the reference finite volume is defined in eq. 4.47:

$$\pi \frac{D^2}{4} \frac{\partial \rho}{\partial x} + \frac{\partial \dot{m}}{\partial t} = 0 \tag{4.47}$$

The density function is very stiff according to the time variable at the evaporation starting point. The idea consists in using the pressure and specific enthalpy as two state variables, which have smooth variation according to the time. And then in calculating the partial derivative of the density according to the two state variables, see eq. 4.48.

$$\pi \frac{D^2}{4} \left[\frac{\partial \rho}{\partial h} \frac{\partial h}{\partial t} + \frac{\partial \rho}{\partial p} \frac{\partial p}{\partial t} \right] = - \frac{\partial \dot{m}}{\partial x} \tag{4.48}$$

Integrating the eq. 4.48 over the small finite volume i and assuming small variation of h and p along the reference volume, eq. 4.49 and eq. 4.50 are obtained. The peculiarity of this model is the exact computation of the mean density, $\bar{\rho}_i$, in each reference volume, in particular where phase transition occurs. Thus, the average density is continuous with their partial derivatives with respect to the two selected state variables (p, h). This property improve the stability of the system and avoid any numerical artefact during the moving of start evaporation point.

$$\pi \frac{D^2}{4} dy \left[\frac{\partial \bar{\rho}_i}{\partial h} \frac{\partial \tilde{h}_i}{\partial t} + \frac{\partial \bar{\rho}_i}{\partial p} \frac{\partial \tilde{p}_i}{\partial t} \right] = \dot{m}_j - \dot{m}_{j-1} \tag{4.49}$$

$$\bar{\rho}_i = \frac{1}{dy} \int_{(i-1)dy}^{idy} \rho dx \tag{4.50}$$

This two-phase fluid flow model uses as thermal connector ("input") the heat transmitted to the fluid. Thus, the metal inertia and the heat loss function of the evacuated tube are not included. The model has been completed by adding an energy balance on the absorber pipe (metal), see eq. 4.51. The effect of the thermal conductivity in the absorber is simulated with eq.4.52 and eq.4.53. Then, the heat loss of the evacuated tube has been simulated by using eq.4.54. And finally, the heat transmitted to the fluid needed by the two-phase fluid flow model is calcualted with eq. 4.55.

$$\frac{\partial \theta_{vol,i}}{\partial t} = \frac{\dot{Q}_{int,i} + \dot{Q}_{ext,i}}{\rho_m \pi dy \left(\frac{D_{m,ext}^2 - D_{m,int}^2}{4} \right)} \tag{4.51}$$

$$\dot{Q}_{int,i} = \frac{k_m \cdot (2\pi dy) \cdot (\theta_{int,i} - \theta_{vol,i})}{log \left(\frac{D_{m,int} + D_{m,ext}}{D_{m,int}} \right)} \tag{4.52}$$

$$\dot{Q}_{ext,i} = \frac{k_m \cdot (2\pi dy) \cdot (\theta_{ext,i} - \theta_{vol,i})}{log \left(\frac{D_{m,ext}}{D_{m,int} + D_{m,ext}} \right)} \tag{4.53}$$

$$0 = \dot{Q}_{ext,i} + \dot{Q}_{L,i} - \dot{Q}_{in,i} \tag{4.54}$$

$$0 = \dot{Q}_{int,i} + \pi D_{m,int} \cdot h_{conv} \cdot (T_{w,i} - \theta_{int,i}) \cdot dy \tag{4.55}$$

$\dot{Q}_{L,i}$ is defined as eq. 4.43, h_{conv} is the constant internal heat transfer rate (=10 kW/(m^{2}K)), k_m is the metal conductivity (15 W/(mK)), ρ_m is the metal density (8000 kg/m^3).

The numerical model has been implemented in Dymola environment using the already existing models (object *flow1DFV2ph* and object *MetalTubeFV*) from the *Thermopower* library [62]. Figure 4.8 shows the result of the implemented Model 2.

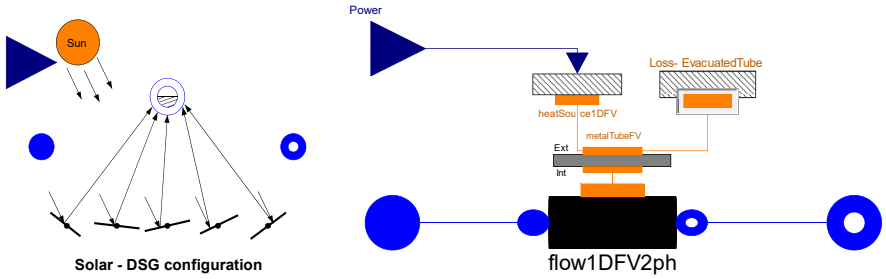

Figure 4.8: Model 2 in Dymola environment

4.6.2 Semi-empirical Model 3: Night cooling

The Model 3 has the objective to quantify the night heat loss and the improvement of the new control strategy.

4.6.2.1 General description

To optimize the night heat loss, a dynamic semi-empirical lumped model of the overall system, called Model 3, is built based on plant configuration (volume and pipe length), theoretical heat loss coefficient values (U_1, U_4), and correction factors for each node. These coefficients, called c1, are tuned experimentally thanks to the temperature profile analysis during start-up.

For instance, for the RAM plant the heat loss tunning has been done in section 7.4.1. Table 4.2 summarizes the parameters used in the case study presented in section 7.4.

Table 4.2: Volume and heat loss coefficient of RAM plant

Node nb.	***Name***	***V*** *[L]*	***c1·L·U1*** *[kW/K]*	***L·U4****[kW/K^4]*
1	Liq1	21	6.2E-03	0
2	Liq2	35	7.5E-03	0
3	Liq3	31	4.6E-03	0
4	CS1	123	6.5E-03	2.94E-10
5	Int1	24	1.5E-03	0
6	CS2	123	6.5E-03	2.94E-10
7	Bi1	10	7.8E-04	0
8	Bi2	2	1.9E-04	0
9	Drum	2000	8.9E-03	0

The model is applied when the feed-in water and steam outlet flow rates are zero for the whole night, i.e. the solar DSG plant is a closed system during the night. A lumped model is used, where each node of the model represents a section of the recirculation loop, see figure 4.3.

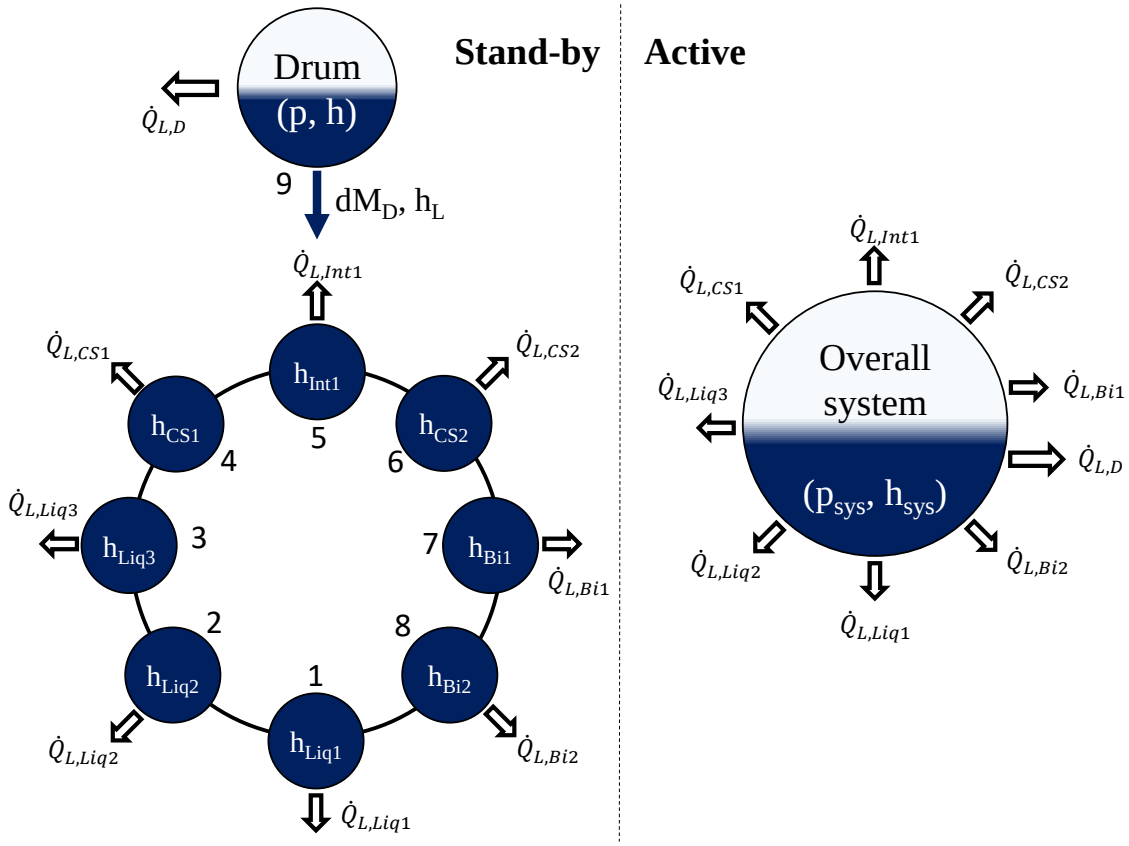

Figure 4.9: Scheme Model 3

As Model 1, two modes, called active and stand-by mode, are developed to distinguish when the recirculation pump is active or not.

For the **active mode**, the lumped model is composed of one node with the two phases assumed at thermal equilibrium for the whole system. The recirculation loop contains liquid saturated water. And the overall heat loss is the sum of heat losses in each section at saturated temperature.

When the system is in **stand-by mode**, the lumped model is composed of 8 liquid nodes along the recirculation loop and one two-phase node at thermal equilibrium for the steam drum. The energy balance is applied for the 8 liquid nodes based on heat loss of the specific section (proportional of node temperature). Then, pressure and specific enthalpy of the steam drum is calculated with the energy and

mass balance on the steam drum. The liquid nodes are only slightly influenced by the pressure variable, thus it is assumed an uniform pressure for the whole system equals to drum pressure. Density and hence the mass are calculated for the 8 liquid nodes. Then, based on mass balance on the closed system, the mass inside the steam drum is calculated. The steam drum pressure is the last degree of freedom to match the two-phase thermal equilibrium density function with expected density, calculated as steam drum mass divided by steam drum volume. During night cooling, the mass content of the recirculation loop increases slowly and the steam drum mass decreases proportionally . This mass flow rate is low and could be neglected for simplify numerical model, a quantification of this effect is shown in the section 7.4. Nevertheless, in the framework of Model 3, a simplified approach is used to model the mass flow rate from the Drum to the recirculation loop. In fact, it is assumed that the liquid saturated water from the steam is integrated in each node according to its mass increase. A more realistic approach would be to respect the piping connection of the recirculation loop, but it looks to be an excessive effort in comparison to the result improvement. The natural circulation between the different nodes due to non uniform density is neglected. In fact, in the solar DSG plant a correct stratification is observed (warmer water in the absorber and colder in the BoP) thus the water tends to stay in its position. The only non stratified node is the steam drum, as it is the warmest node situated below the top absorber. Nevertheless, no circulation is expected as a motorized valve or a siphon isolate these two nodes.

4.6.2.2 Numerical model description

The Model 3 is composed of two modes, described below.

Active mode The mass and energy balances are applied to the unique node of the closed system, see eq. 4.56 and eq. 4.57.

$$\frac{\partial \rho_{sys}(P_{sys}, h_{sys})}{\partial t} = 0 \tag{4.56}$$

$$V_{sys}\rho_{sys}\frac{\partial h_{sys}}{\partial t} = -\dot{Q}_{L,sys} \tag{4.57}$$

where ρ_{sys} is the average density of the whole system [kg/m^3], P_{sys} is the pressure at the drum level [bar], h_{sys} is the average specific enthalpy of the system [kJ/kg] and V_{sys} is the fixed volume of the system (the sum of each section) [m^3]

The heat loss of the overall system, $\dot{Q}_{L,sys}$, is the sum of the heat loss of each section at saturated temperature, see eq. 4.58. Integrating eq. 4.56, the DAE used in the Active Mode is set as follow where the two state variables are P_{sys} and h_{sys} :

$$\dot{Q}_{L,sys} = \sum_{i=1}^{9} \left[c_{1,i} \cdot L \cdot U_{1,i} \left(T_{sat} - T_a \right) + L \cdot U_{4,i} \left(T_{sat} - T_a \right)^4 \right] \tag{4.58}$$

$$\rho_{sys}(P_{sys}, h_{sys}) = M_{0,sys} \tag{4.59}$$

$$\frac{\partial h_{sys}}{\partial t} = \frac{-\dot{Q}_{L,sys}}{M_{0,sys}} \tag{4.60}$$

where $M_{0,sys}$ is the initial water mass of the solar system [kg].

Stand-by mode The mass increase of each liquid nodes during cooling phase is balanced with the mass decrease in the steam drum. Thus, the outlet mass flow of the steam drum is the sum of the inlet mass flow rate of each liquid node (closed system), see eq. 4.61. The mass and energy balances are applied for each node, see eq. 4.63, 4.64, 4.65 and 4.66 where heat loss is calculated with eq. 4.62. The water and metal temperatures are assumed to be equal.

$$\dot{m}_{out,D} = \sum_{i=1}^{8} \dot{m}_{in,i} \tag{4.61}$$

$$\dot{Q}_{L,i} = \left[c_{1,i} \cdot L \cdot U_{1,i} \left(T_{sat} - T_a \right) + L \cdot U_{4,i} \left(T_{sat} - T_a \right)^4 \right] \text{ for i=1...9} \tag{4.62}$$

where $\dot{m}_{out,D}$ is the mass flow rate at the drum outlet [kg/s], $\dot{m}_{in,i}$ is the mass flow rate at the inlet of the section i [kg/s], $c_{1,i} \cdot L \cdot U_{1,i}$ is the semi-empirical convective and conductive heat loss coefficients of node i [kW/K], $L \cdot U_{4,i}$ is the radiative heat loss coefficient of node i [kW/K^4].

$$V_i \frac{\partial \rho_i}{\partial t} = \dot{m}_{in,i} \text{ for i=1...8} \tag{4.63}$$

$$V_i \rho_i \frac{\partial h_i}{\partial t} + h_i V_i \frac{\partial \rho_i}{\partial t} = -\dot{Q}_{L,i} + \dot{m}_{in,i} h_{L,D} \text{ for i=1...8} \tag{4.64}$$

$$V_D \frac{\partial \rho_D}{\partial t} = -\dot{m}_{out,D} \tag{4.65}$$

$$V_D \rho_D \frac{\partial h_D}{\partial t} + h_D V_D \frac{\partial \rho_D}{\partial t} = -\dot{Q}_{L,D} - \dot{m}_{out,D} h_{L,D} \tag{4.66}$$

where V_i is volume of section i [m^3], ρ_i is the average density of section i [kg/m^3], h_i is the specific enthalpy of the section i [kJ/kg], $\dot{Q}_{L,i}$ is the heat loss of section i [kW], $h_{L,D}$ is the liquid saturated specific enthalpy of the steam drum [kJ/kg], $\dot{Q}_{L,D}$ is the heat loss of the steam drum [kW].

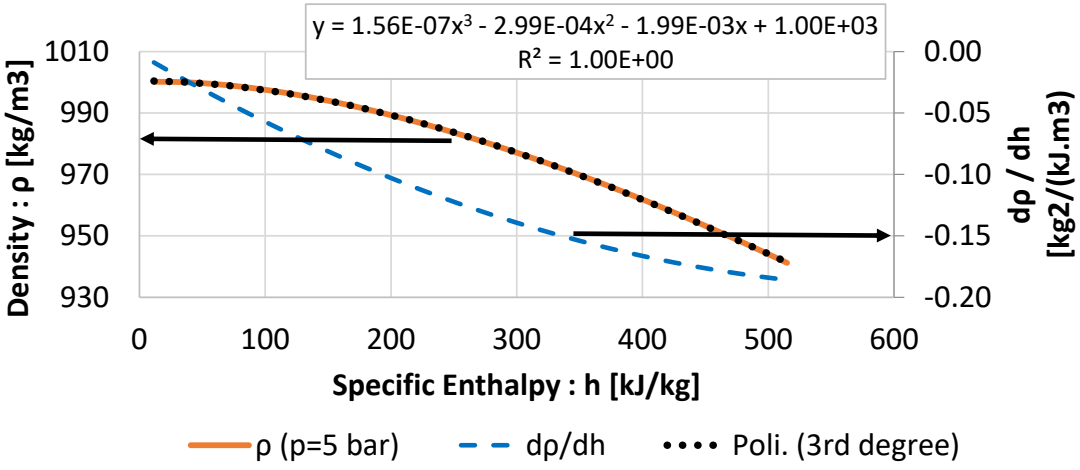

Figure 4.10: Interpolation of water density variation in liquid phase

The density of liquid nodes, ρ_i, is assumed independent of the pressure and it can be interpolated with a polynomial equation according to the specific enthalpy. A good accuracy is obtained with a third degree equation with $a_3 = 1.56e-7$, $a_2 = -2.99e-4$, $a_1 = -1.99e-3$ and $a_0 = 1.00e3$ see eq. 4.67 and figure 4.10, calculated for a pressure of 5 bar-a. Thus, the mass flow rate inlet into each liquid node is an equation of only its specific enthalpy, see eq. 4.69.

$$\rho_i = a_3 \cdot h^3 + a_2 \cdot h^2 + a_1 \cdot h + a_0 \tag{4.67}$$

$$\frac{\partial \rho_i(h_i)}{\partial h} = 3a_3 \cdot h_i^2 + 2a_2 \cdot h_i + a_1 \tag{4.68}$$

$$\dot{m}_{in,i} = V_i \cdot \frac{\partial \rho_i(h_i)}{\partial h} \cdot \frac{\partial h_i}{\partial t} \tag{4.69}$$

To conclude for the stand-by mode, the 10 unknown variables are the specific enthalpy of 8 liquid nodes and the pressure and specific enthalpy of the steam drum. The specific enthalpy of each liquid node is obtained solving eq. 4.70. The pressure and specific enthalpy of steam drum are obtained solving the last two differential equations, eq. 4.71 and 4.72.

$$\frac{\partial h_i}{\partial t} = \frac{-\dot{Q}_{L,i}(h_i)}{V_i \left[\rho_i(h_i) - \frac{\partial \rho_i(h_i)}{\partial h} \cdot (h_L(p_D) - h_i)\right]} \text{ for i=1...8} \tag{4.70}$$

$$\frac{\partial h_D}{\partial t} = \frac{-\dot{Q}_{L,D}(h_D, p_D)}{V_D \left[\rho_D(h_D, p_D) - \dot{m}_D(h_1, ..., h_8) \cdot (h_D - h_L(p_D))\right]} \tag{4.71}$$

$$\frac{\partial \rho_D(p_D, h_D)}{\partial t} = -\frac{\dot{m}_D(h_1, ..., h_8)}{V_D} \tag{4.72}$$

Chapter 5

Experimental Activity

5.1 Objectives

A DSG bench was developed at the department of Energy of Politecnico di Milano (POLIMI), with the objective to validate Model 1 and some of its assumptions:

- pressure distribution over the recirculation loop;
- head loss correlations implemented in the numerical model;
- validation of flow pattern map outside of its boundary conditions.

The latter is the most original point as the flow pattern map used in Model 1 is an extension of the *modified KTF* correlations [[88], [89]] which have been developed and tuned for refrigerant in small diameter pipe at low pressure. The map is compatible for refrigerants and it is not demonstrated that they are suitable for steam-water systems as its surface tension and density ratio are high with respect to the refrigerant database. In the present study, the *modified KTF* correlations have been used outside their boundary conditions for water flow in larger diameter pipes (70 mm compared to 8-20 mm) and higher pressure (3-25 bar compared to 1.1-8.9 bar). Moreover, for the specific application of solar DSG for industrial heating processes, the flow patterns involved are: intermittent, stratified wavy and annular. An experimental campaign with the objective to validate the use of water instead of refrigerant for these specific transition curves is performed. The validity of pressure and diameter extrapolations to real case study are discussed in section 5.2.3.

5.2 Facility

The DSG laboratory is described in this section with installed components and sensors presentation and test methodology and boundaries discussion.

5.2.1 DSG Test Bench Description

5.2.1.1 General description

A laboratory test bench developed at the department of Energy of Politecnico di Milano has been built to study solar DSG applications into process heat. It has the role to complete and validate the numerical model developed in the previous section 4.5. As already highlighted, two-phase flow is a subject largely studied. Nevertheless, the existing flow pattern correlations have not been validated under the conditions of solar DSG. Thus, existing semi-empirical correlations are extended in the numerical Model 1 and have to be validated experimentally. On the one hand it would be ideal to apply this validation on real scale system but on the other hand numerous barriers would not allow a full validation. In fact, due to size limitation, to uncertainty on solar heat flux, to damage risk or to interference with real industrial process, it is real issue to validate the flow pattern maps on the solar DSG condition. For this specific reason, a test bench has been developed in a laboratory context in order to validate flow pattern boundaries for a diabatic two phase flow under new conditions. It has been focused only on the conditions typical of solar application, i.e. intermittent, stratified wavy and annular flow pattern, see figure 5.5.

The laboratory should characterize the water evaporation in a horizontal pipe and it should maximize different boundary conditions:

- Pipe diameter and design pressure as close as possible of the standard absorber diameter (66 mm) and average industrial process pressure [5 - 30 bar-g].
- Flexibility to reach various points of *modified KTF* maps (specific mass flow rate and steam quality) to characterize flow pattern.
- Generate steady state condition
- Measured steam quality and mass flow rate and identified flow pattern with the highest accuracy possible.

- Limited investment cost, eg. chiller is out of the available budget.

Moreover, the requirements of maximum pressure and temperature of each component have to be respected.

In order to generate various two phase flow conditions, a variable and controllable pump/inverter and electrical heater are chosen. Electrical heaters are chosen due to the following advantages: high heat flux density, easily controllable and measurable, economic and easy installation.

In order to simulate the linear heat flux of solar irradiation, the electrical heaters are installed along the tested horizontal pipe. In the specific case of Linear Fresnel Reflector (LFR), the heat flux over the cross section is not uniform. The circumferential distribution of irradiation on the absorber tube has been calculated via Raytracing for the Mirroxx's LFR for different projected transversal angle of the sun [92]. It shows larger heat flux on the bottom of the tube respect to the top for each sun position. This non uniform heat distribution leads to non uniform temperature distribution over the cross section. However, it is expected a lower temperature dis-uniformity for LFR than PTC since the highest heat flux is always on the bottom part of the tube which is in contact with liquid phase for each flow patterns (excepted dry-out condition) thus in the area where the internal heat transfer rate is high.

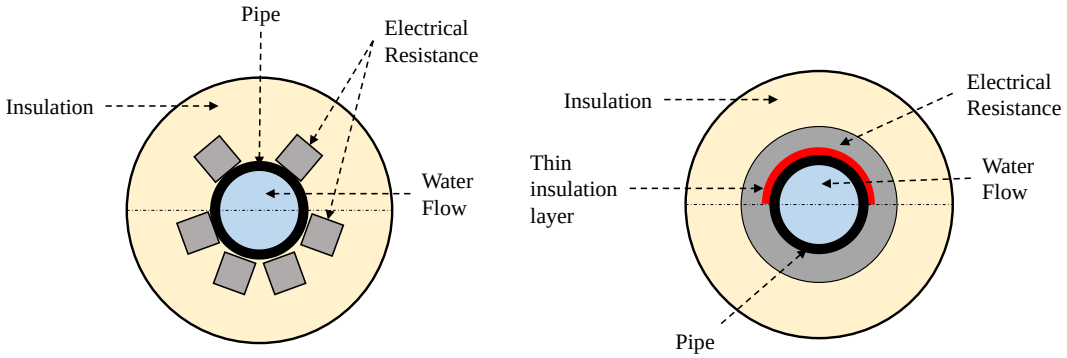

Figure 5.1: Cross Section evaporated pipe: configurations to generate non uniform heat flux *(left: Straight elec. heater - installed along the pipe, right: Spiral elec. heater installed around the pipe)*

For large pipe diameter, it could be thinkable to install more straight electrical resistance on the bottom part of the pipe or add a small resistive layer between the spiral electrical heater and the top of the pipe, in order to increase the contact

resistance heat transfer in the upper part of the pipe, see figure 5.1.

Nevertheless, uniform heat flux (figure 5.2) has been chosen for three main reasons:

- First, the density heat flux has to be maximized due to space restriction which is not the case in the two proposed configurations in figure 5.1.
- Then, the *modified KTF* correlations have been defined for uniform heat flux thus the extension process of the validity range has to be done by changing only one parameter at the time. For this test bench, it is tested the use of water.
- And finally, for small pipe diameter (eg. 15 mm) this dis-uniformity is negligible since the distance between the hottest and the coldest in small.

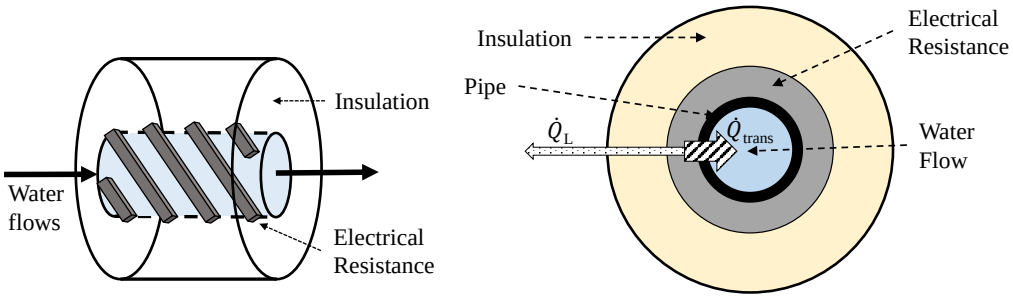

Figure 5.2: Cross section of evaporation pipe

The DSG test bench could be divided in three sections, see figure 5.3:

- the recirculation loop composed by the pump, the connecting pipes and the horizontal evaporation pipe with electrical heater, called by analogy *absorber*
- a larger pipe to store the generated steam, called *steam drum*
- the pre-vessel and vessel tank to absorb the liquid dilatation.

Generate steady state condition is an issue as the heat gain is not dissipated trough a chiller. Steady state condition is reached if the inlet temperature of evaporation pipe, mass flow rate and electrical heat flux stays almost constant during the whole test period. The innovative approach is to maintain saturated temperature at the absorber inlet and to control the pressure increase. Steam generated into the

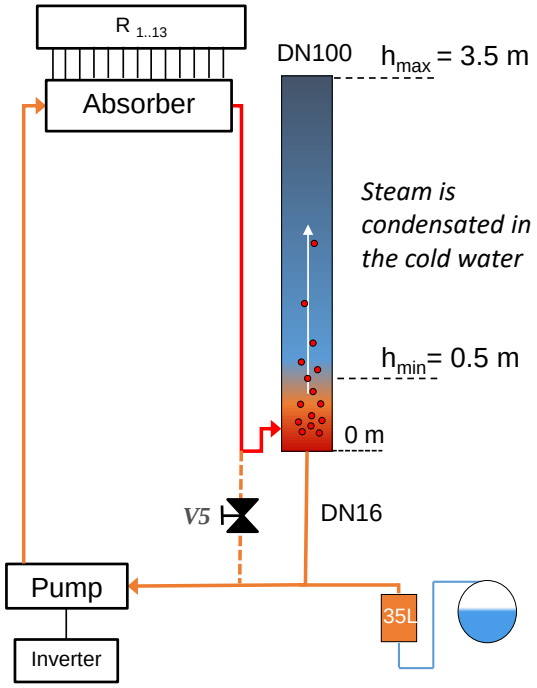

Figure 5.3: Simplify laboratory scheme

absorber would condense in the cold water store in the tank and the liquid saturated water should recirculate to the absorber. Thus the two-phase flow inlet is installed at the bottom part of the steam drum. A strong stratification is generated: the bottom part at saturated condition and the top at cold temperature. In fact, initially the whole tank is cold (eg. 25 °C - ambient temperature) and the steam first condense in the bottom part and slowly the boundary between hot and cold water goes up during the test. The liquid water of the system is warmed-up during the whole test and the thermal dilatation is absorbed through an over-sized vessel tank. A manual valve, called V5, is used to by-pass the steam drum during the warm-up of the recirculation loop in order to emphasize the stratification.

To select the proper design condition (pressure, heat gain, diameter and mass flow rate) a sensitivity analysis is done over the *modified KTF* correlations. The two flow pattern boundaries, Stratified/Wavy Stratified (called $\dot{m}_{S-SW}$) and Intermittent/Annular ($x_{Int/An}$), are defined only according to the pressure variable. The flow pattern boundary, Annular/Mist ($\dot{m}_{An/Mist}$), is proportional to the pressure and pipe diameter. This specific boundary is not used in the solar DSG context. And finally the last flow pattern boundary between the Wavy stratified and Intermittent-Annular ($\dot{m}_{SW/Int-An}$) is proportional to the three variable inputs (pressure, tem-

perature and linear heat flux) and is the only one including the effect of diabatic condition. Figure 5.4 shows the influence of these three inputs over the *modified KTF* correlations. Two conditions are compared: the first one based on an example of a real case study at 20 bar-a, 66 mm and 3.3 kW/m and the second one based on an example of laboratory condition, i.e 2 bar-a, 15.7 mm and 2.5 kW/m. At lower pressure the four boundary correlations are pushed to lower steam quality. In fact, at low pressure conditions the two phase mixture has a lower density. Thus an equivalent specific mass flow rate generates higher volume flow rate, ie. a more turbulent flow. Hence, stratified or wavy stratified flow pattern, appear at lower specific mass flow rate. The linear heat flux influences only the wavy stratified boundary at high steam quality, which defines the dry-out area. At high linear heat flux, the dry-out area increases. And finally the diameter reduction has two effects. The first one is to increase the specific heat flux and thus Dry-out area. The second one is to increase the ability to maintain the water on the wall (Weber coefficient). Thus, a lower specific mass flow rate is required to generate annular flow pattern.

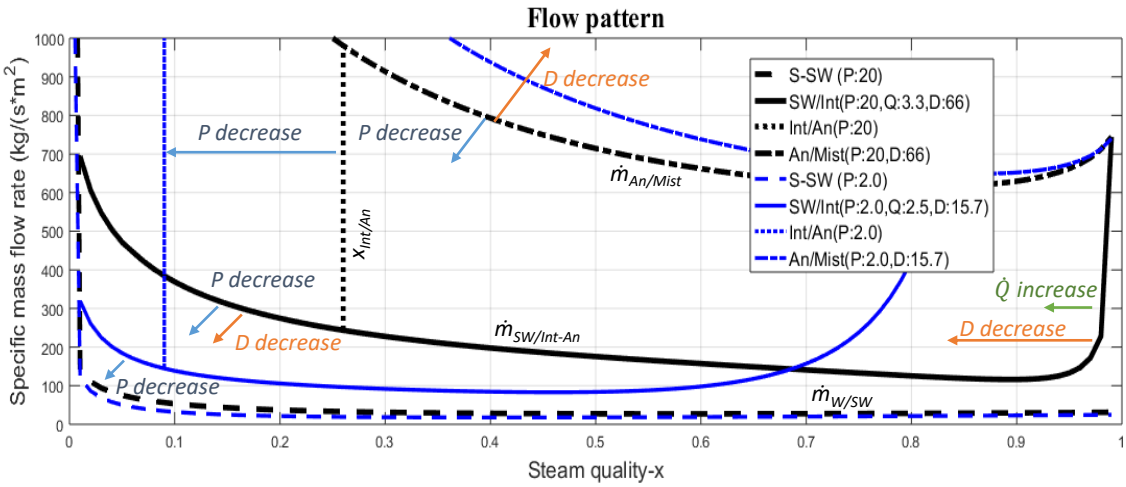

Figure 5.4: *Modified KTF* correlations variation according to Temperature, Pressure and heat flux

The choice of the design pressure defines the design temperature of the system (saturated condition). For temperature higher than 120-150 °C, the components are composed by more resistant and expensive materials. Thus, it has been chosen a design pressure relatively low to minimize the investment cost. Based on investment cost available and space available (7 m), the overall heat gain is chosen equal to 15.6

kW (13 electrical heaters). To keep temperature lower than 125 °C the maximum pressure is fixed at 2.3 bar − a. An inner absorber diameter of 15.7 mm is chosen to maximize the diameter size but still reach steam quality in order to validate the flow pattern boundaries: Stratified / Wavy Stratified, Wavy Stratified / Intermittent-Annular and Intermittent / Annular. The flow pattern is observed trough a sight tube of 15.0 mm. And lastly, the mass flow rate is calculated to reach a value between 25 to 1000 kg/s.m^2. Figure 5.5 (with log axis) defines the test area for a pressure around 1.9 bar-a, a sight tube of 15.0 mm and a linear heat flux of 2.5 kW/m (15.6 kW / 6.25 m).

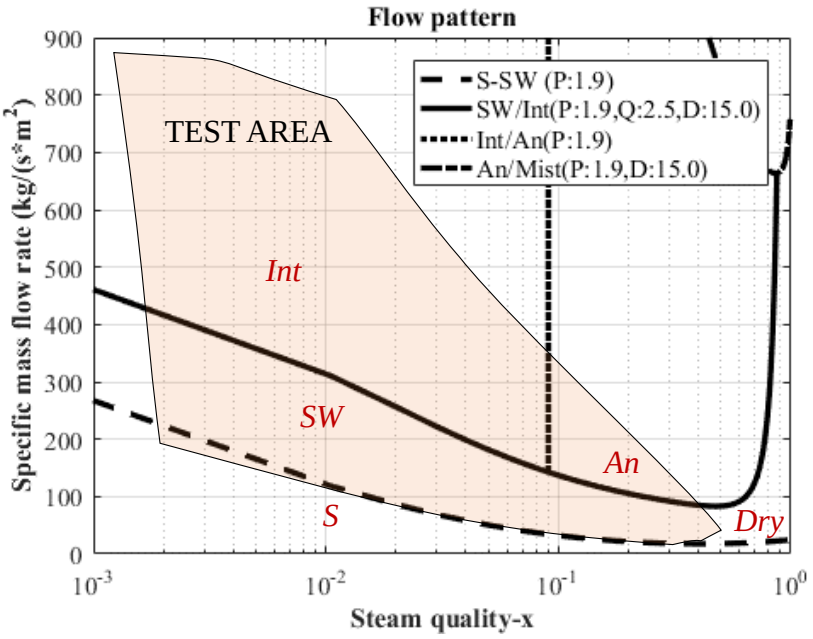

Figure 5.5: Test area of *modified KTF* flow pattern

5.2.1.2 Components

The DSG laboratory consists of 13 electrical heaters of 1.2 kW each, installed in series in spiral over a stainless pipe of DN15, see figure 5.6. The electrical heater has an external gain in stainless steel and can be used until 750 °C. This product is particularly interesting for this application, since the power generated is only slightly influenced by working temperature and the initial straight resistance could be curved with a low curvature radius (min 3.5 mm).

The whole plant is insulated with 32 mm of mineral wool which has a maximum running temperature of 400 °C and a thermal conductivity proportional to the

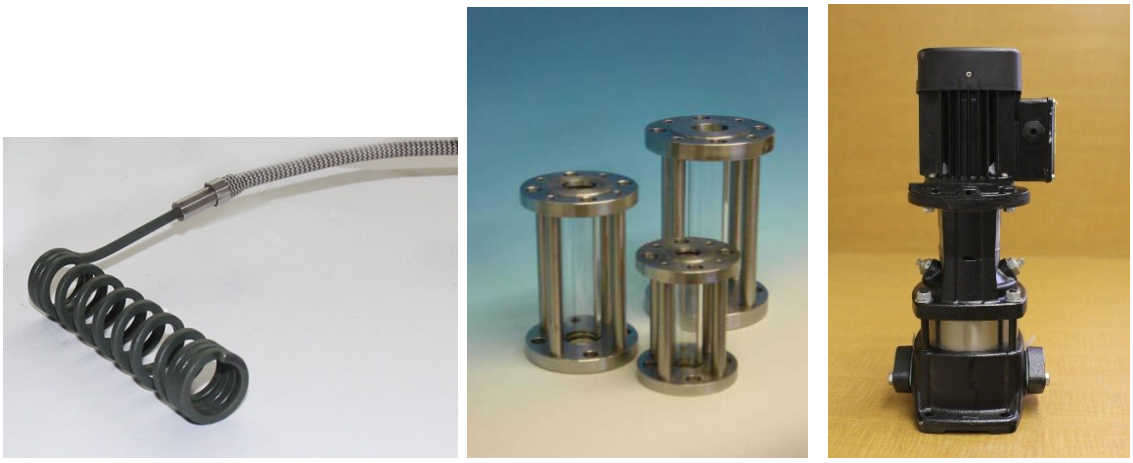

Figure 5.6: *Left:* Electrical Resistance (Lorenzoni - LR 3.3x3.3 L.1800), *Middle:* Sight tube T (Visilum STB-015-A), *Right:* pump (Grundfoss CR 1S-2)

temperature, as shown in table 5.1 A thicker insulation layer is installed over the

Table 5.1: Temperature dependency of mineral wool thermal conductivity

Temperature	***Thermal conductivity (λ)***
° C	W/mK
10	0.039
25	0.043
120	0.052
220	0.075
320	0.111
420	0.149

resistance to ensure that a large share of the electrical heat is transferred to the fluid (between 90-96%), see figure 5.2. Two layers of insulation have been installed: the first one is 40 mm of mineral wool and the second one is 12 mm of ceramic fiber blanket.

The mass flow rate is controlled trough a centrifugal pump combined with an inverter. Figure 5.7 shows the characteristic curve of the pump model CR1S-2. It matches with the extreme working conditions of the recirculation loop: (0.01 m^3/h; 1.0 m), (0.55 m^3/h; 7.5 m) and (0.70 m^3/h; 2.2 m). The pump and inverter (CUE 0.55) are selected from Grundfoss' manufacturer.

The system regulation and data monitoring are developed in Labview and im-

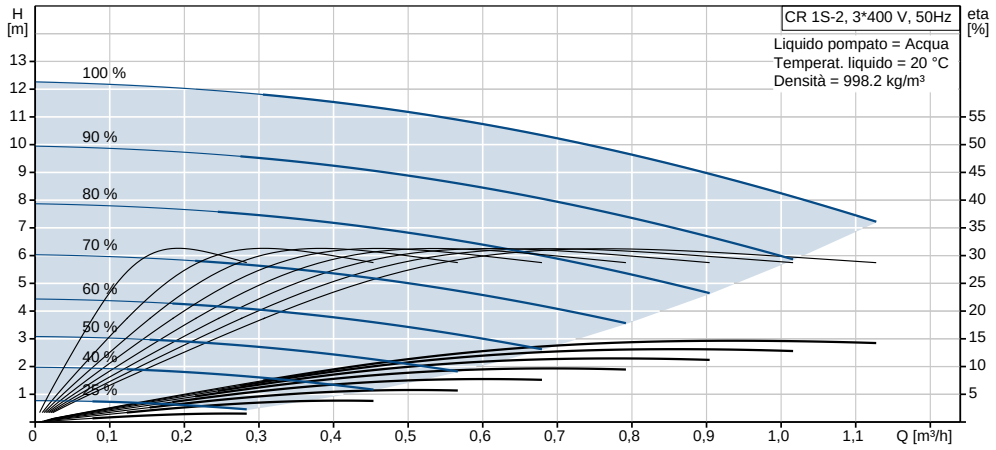

Figure 5.7: Characterisctic curve of the Grundfoss pump, model CR1S-2

plemented in National Instrument device, Compact RIO 9073. A discrete regulation of the generated power is controlled trough the activation of each resistance. An over-sized vessel tank of 80 L is installed to absorb the thermal dilatation of the liquid water and the water evaporation. Stainless steel pipes are installed in order to maintain the water transparency (clean) and allow the flow pattern identification trough visual techniques. And finally, the flow pattern is observed trough 4 transparent sight tubes of 15.0 mm diameter and 120 mm length, see figure 5.6. The position of the sight tubes is shown in figure 5.8. They are mounted inline with the pipe of 15.7 mm. The sight tubes are not heated but the flow pattern observed is the one leaving directly the absorber, thus diabatic flow pattern conditions are analyzed.

5.2.1.3 List sensors

The DSG bench is equipped with 6 temperature sensors, 3 pressure sensors and one flow rate sensor distributed over the recirculation, see figure 5.8. Three electrical meters are installed to measure the power given to the three section of electrical heaters (R1 to R6, R7 to R10 and R11 to R13). The table 5.2 summarizes the uncertainty of each installed sensor.

5.2.1.4 Installation & practical experiences on the test bench

This section has the objective to highlight good practices during the installation of the DSG test bench.

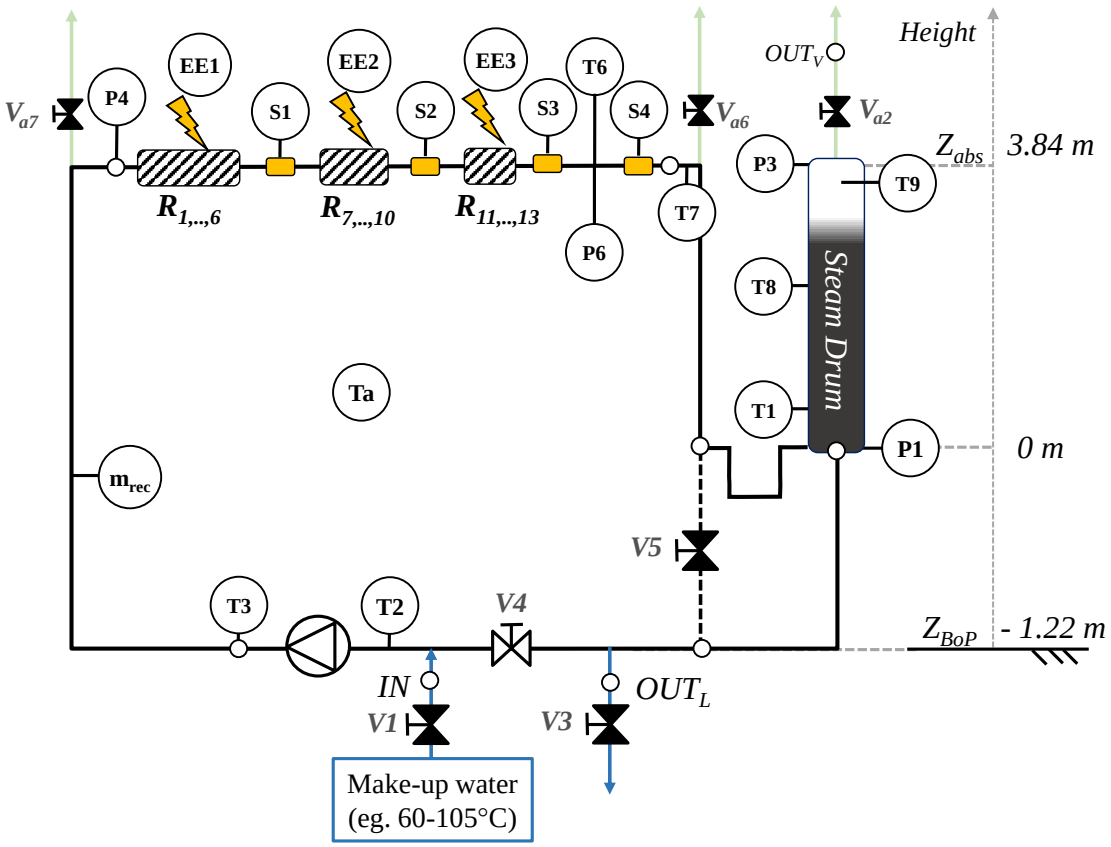

Figure 5.8: Sensor positions in the DSG test bench

Dirty sight tube To identify the flow pattern the sight tube has to be clean. Unfortunately, the sight tubes get dirty with dust and oil (used to cut and thread the pipes). After several cleaning processes and numerous steam generations, the sight tubes are transparent (clean) but this effort could have been avoided with a more careful installation of the piping. Use of flanges has been useful to remove easily the sight tubes and clean them manually.

Table 5.2: DSG Bench list sensors

Measure	***Sensor type***	***Accuracy***
Water flow rate	Electro-magnetic flow meter	0.5% reading if >0.06 m^3/h; 2.5% reading if <0.06 m^3/h
Water temperature	Pt100	Class A EN 60751
Pressure sensors	Endress-Hausser, Cerabar M	0.15 % of span
Electrical meters	IME. Cod TM8P	0.5 % reading EN 50470-3

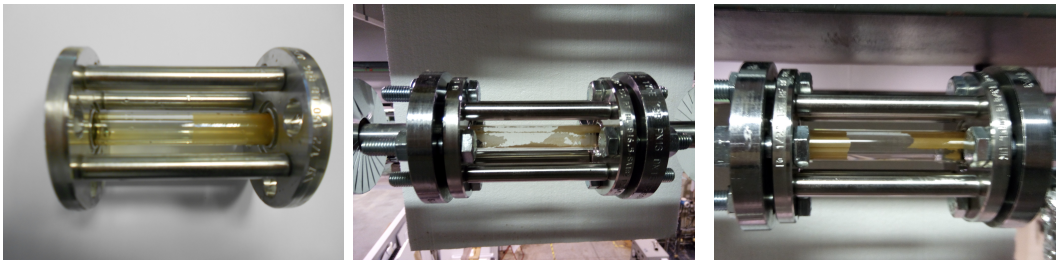

Figure 5.9: Sight Tube - Dirty

Avoid pump cavitation The saturated liquid from the steam drum flows at the pump inlet. In order to avoid cavitation at the recirculation pump, the pump has to be installed some meters below the bottom part of the steam drum, in order to compensate the NPSH of the specific pump in each flow conditions, see figure 5.8.

Empty easily the plant Manual valves (V_a in figure 5.8) in the top part of DSG bench have been installed to help the air entrance. Horizontal biphasic pipes have been installed slightly tilted to let the water fall to outlet valve.

High temperature condition Some components, as pump, pressure sensors and vessel tank have a maximum working conditions very close or lower than the maximum design temperature. For the circulation pump a safety control strategy has been implemented in order to stop the electrical heater and the recirculation pump itself when we reach the maximum temperature of the pump, 120 °C. On request, the maximum temperature of the pump could be designed to 180 °C. The pressure sensors are designed for a maximum temperature of 125 °C, thus a siphon is always installed between the connection point and the pressure sensor to avoid any contact between the steam and the sensors. The vessel tank has a maximum working temperature of 80 °C, thus a pre-vessel tank has been installed to protect the internal membrane. Its size is equal to the water evaporation of absorber, biphasic pipe and 2/3 of the steam drum, 36 L, see figure 5.10.

Improvement contact resistance The ratio between heat gain and heat loss of the electrical heater should be as high as possible in order to reach higher steam quality and higher accuracy. It is done trough an accurate installation of the electrical heater minimizing the contact heat transfer resistance and maximizing the insulation to the atmosphere.

Figure 5.10: Vessel tank protection

The 5 figures 5.11, 5.12, 5.13, 5.14, 5.15 show the different steps of the installation. First, pre-design spiral with the correct radius of curvature, is installed over the evaporation pipe. To minimize thermal bridge, a small layer of insulation is installed between the piping support and the pipe. The second step consists in maximizing the area of contact of the hot source with the pipe. I did it in three steps: by stretching the electrical heater, adding the aluminum foil in the spiral gap and holding the whole system with metal hose clamp, see figure 5.12. The third step consists in covering the resistance with an aluminum foil to avoid dust contact due to mineral wool, see figure 5.13. The fourth and fifth steps consist in installing the two layers of insulation with an external aluminum foil, see figure 5.14 and 5.15.

Figure 5.11: Heater installation: step 1

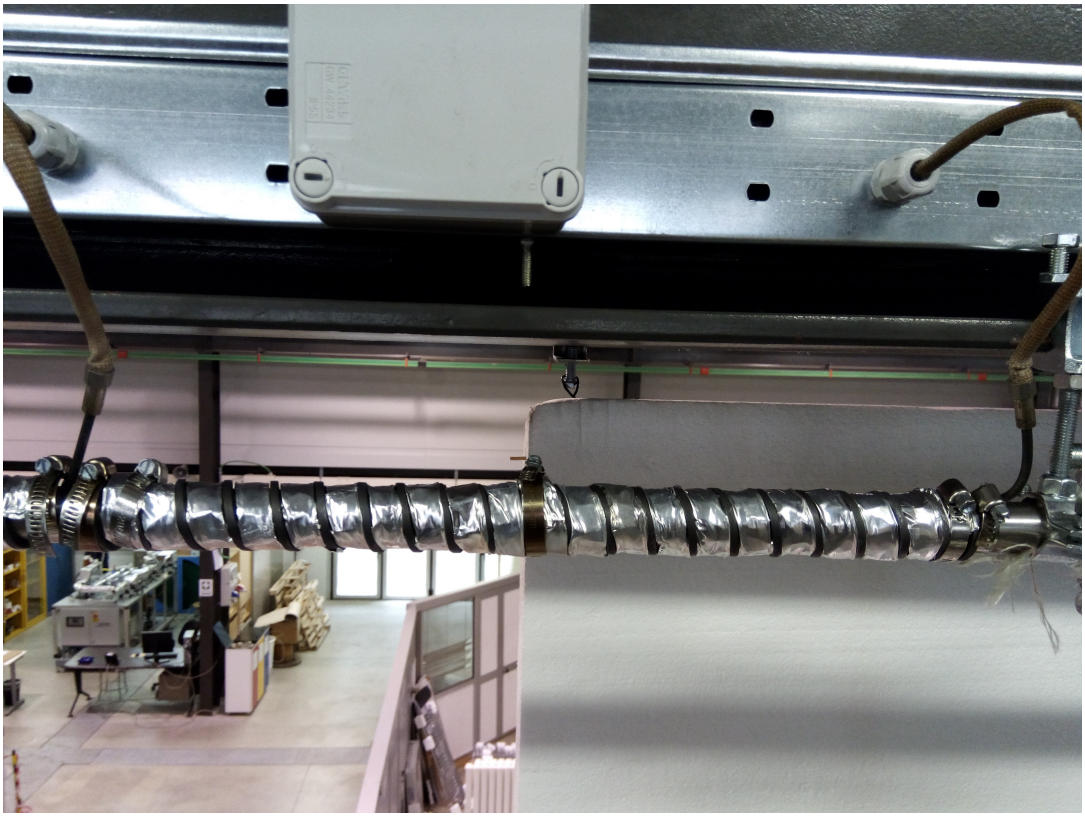

Figure 5.12: Heater installation: step 2

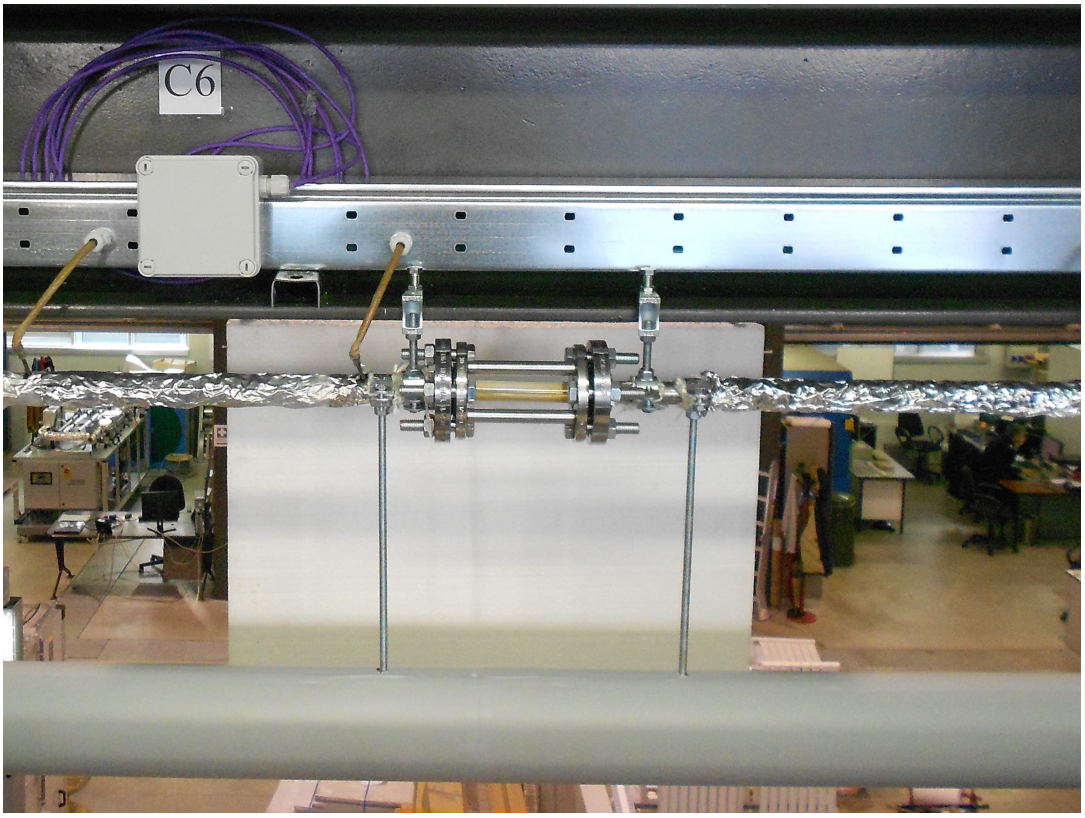

Figure 5.13: Heater installation: step 3

Figure 5.14: Heater installation: step 4

Figure 5.15: Heater installation: step 5

Figure 5.16: Overall installation

5.2.2 Flow pattern detection

The flow pattern detection is a real issue due to arbitrary description of each flow pattern and due to the fact that flow pattern transition is a gradual process.

5.2.2.1 State of the art

Several methodologies are used to identify the two-phase flow pattern. We can distinguish between the non invasive methods, as visual and the ones based on photon attenuation, and invasive methods as the ones based on pressure measurement, electrical conductivity and refractive index. A good description of existing methodology is presented in the chapter 1 of Hewitt's book: *Multiphase Science and Technology* [52].

Visual methods: the simplest method is the visualization trough transparent sight tube and it is the most used in the works to build flow pattern maps. For example of Kattan Thome and Favrat works used high quality video to define the so called KTF correlations [88]. At low flow rate, eye visualization can be sufficient whereas specific photographic methods are useful at high flow rates. Jassim et al. developed an automatic methodology based on image recognition which classifies a large number of images into either liquid, intermittent, stratified or annular flow [93]. Based on this approach, a probabilistic flow pattern maps have been developed for refrigerant condensation in horizontal tube [94]. A good agreement with existing correlation have been achieved.

Methods based on photon Attenuation: the use of X-ray or gamma-ray attenuation methods lead to more direct measurement of void distribution. The two most diffuse techniques are the "one shot" method and the neutron scattering method. These methods lead to high accuracy but the main limitation is their high cost and the need for careful installation and operation to ensure safety.

Method based on pressure measurement: the wall pressure fluctuation characterizes the manner in which the liquid and gas are distributed in the pipe and their velocities. Hubbard and Dukler [95] applies a power spectral density of the wall pressure fluctuation to characterize flow pattern. Three basic spectra have been

characterized. The first one includes stable flow pattern, as stratified and annular pattern, where liquid and steam area are always separated. The second one considers intermittent flow (eg. plug, slug) where the wall pressure is strongly influenced by the slug passage frequency. And finally, flow pattern as bubbly or mist flow does not show strong wall pressure dependency according to spectral frequency. Thus this methodology could be used to define the intermittent flow pattern region. But it is not suitable for the annular/wavy stratified transition curve.

Methods based on Electrical conductivity: to measure flow pattern, the use of wire mesh is one of the most diffuse technology as the one proposed by the research center Helmhotz Zentrum Dresden Rossendorf [96]. It allows a fast visualization and quantification of two-phase and multiphase flows thanks to two parallel electrode grids [97]. It is based on strong difference of water electrical conductivities in liquid and steam phases.

Methods based on refractive index: the local void fraction can be measured by a miniature resistive prove, a U-shaped fiber-optical sensor or a hot-wire anemometer. An optical probe is sensitive to the change in the refractive index of the surrounding medium. If the refractive index of the measured point is higher than 1.15, which is the case of the liquid water, than the light is refracted and the phototransistor is not exited. In the contrary when fluid refractive index is lower than 1.15, which is the case of steam water, than the incident ray is reflected to the phototransistor sensor.

5.2.2.2 Selected approach

Facility: The methodology developed and applied during his PhD is based on Jassim's methodology [93], where the facility is composed by a standard camera (with 640x480 pixel resolution and 30 frame per second shutter speed), a sight tube, a light and a diffuser. The diffuser is a white paper with black vertical lines of 2 mm width and distant of 3 mm. The striped background serves to enhance the image. Figures 5.17 and 5.18 show the flow visualization facility.

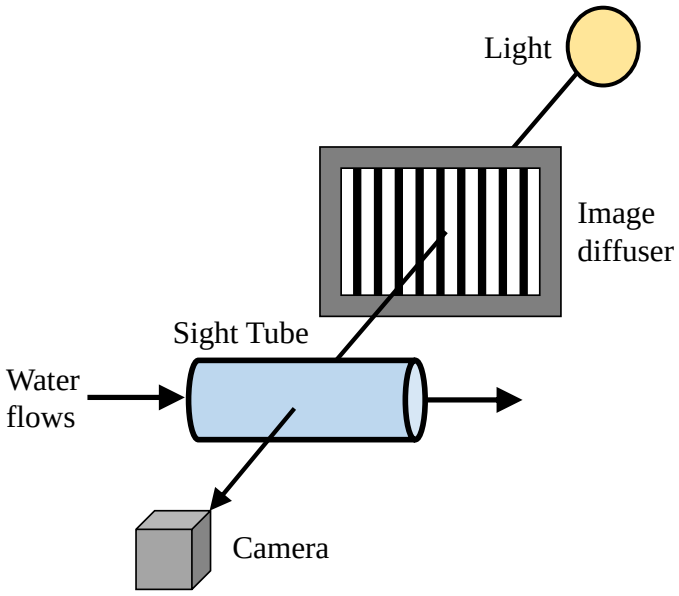

Figure 5.17: Scheme - Flow pattern detection facility

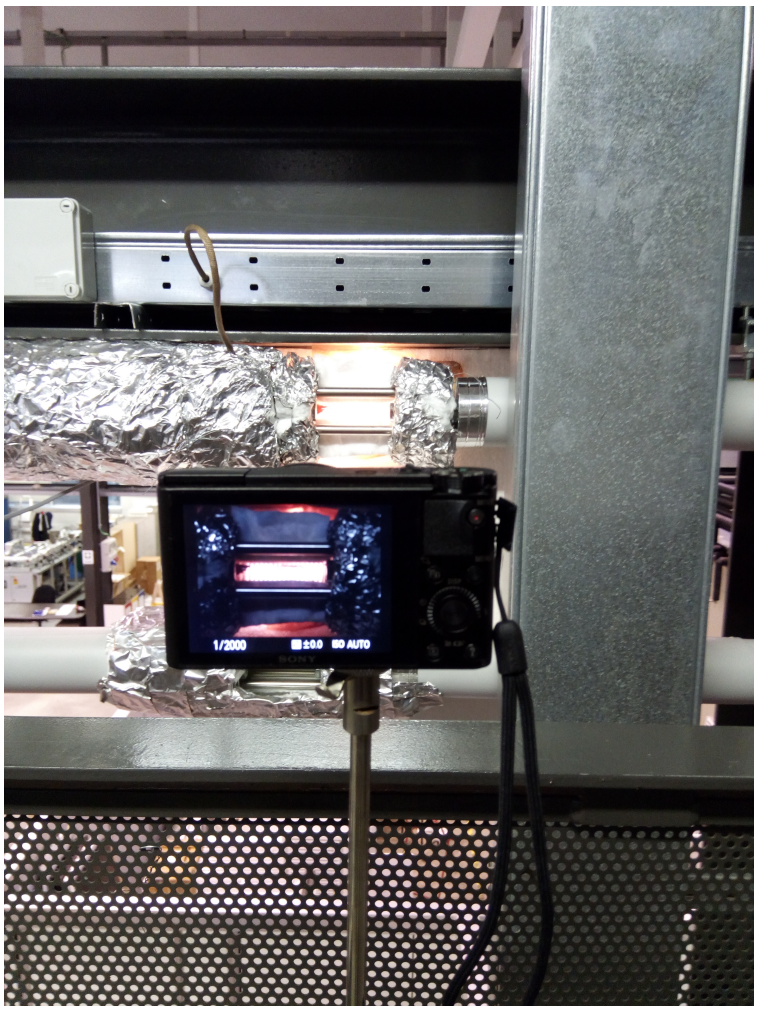

Figure 5.18: Photo - Flow pattern detection facility

Figure 5.19: Liquid - test 0201

Figure 5.20: Stratified - test 0301

Figure 5.21: Wavy Stratified - test 0304

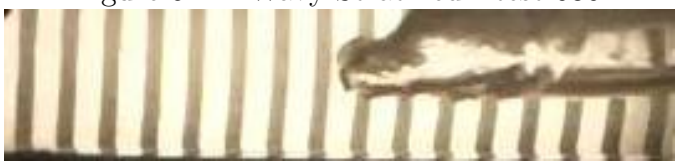

Figure 5.22: Elongated bubble (Plug) - test 0204

Figure 5.23: Intermittent 1 - test 0408

Figure 5.24: Intermittent 2 - test 1006

Figure 5.25: Annular - test 1013

Figure 5.26: Dry-out - test 1310

Qualitative Flow pattern identification: To classify each flow pattern some qualitative criteria have been used and defined below.

- Liquid: all the vertical lines are observed at the different height of the sight tube.

- Stratified (limit S-WS): in the bottom and upper part of the tube, vertical lines are observed and the interface between the liquid and steam phases is smooth. This condition has small waves thus we are expecting to see this condition in the boundary of stratified and wavy stratified flow pattern.

- Wavy Stratified (limit WS-Slug): liquid is observed on the bottom part of the tube and some vertical lines are observed in the top part. The interface is disturbed by liquid waves that climb up the side of the tube. Wavy stratified is defined if the crest does not reach the top the tube. In this scenario, it happens from time to time but not as often as the Intermittent 1 description where the vertical lines are never observed in the top part.

- Elongated bubble (Plug): elongated bubbles are observed in the top part of the tube. In the remaining part of the tube, vertical lines are observed trough liquid phase.

- Intermittent 1 - Plug at high frequency: vertical lines are observed only in the bottom part (only liquid). Indeed, the liquid steam mixture flows very fast, thus the camera does not manage to focus and it is not possible to observe vertical lines in the upper part.

- Intermittent 2 - Slug: this flow pattern is an extension of intermittent 1. Elongated bubble becomes similar in size with pipe diameter and so the bottom part is also affected by this discontinuous phase change. The flow is unstable and "black" slug is observed.

- Annular: as intermittent 2, no vertical lines are observed but in this scenario the flow is very stable (no "black slug"). On the top and bottom part of the tube a black interface is observed.

- Dry-out: vertical lines are observed in the middle of the tube (steam). A small liquid layer is observed in the bottom and top of the tube and it characterized the differences with superheated steam.

In order to avoid to be influenced by the expected results, videos are watched in random order and successively. This process is repeated twice to reduce subjective judgment and when the identification is not clear the video is defined NaN.

5.2.3 Extrapolation of *modified KTF* correlations

The experimental activity done in the laboratory has the objective to validate the use of *modified KTF* correlations for the specific application of solar DSG into industrial process. Nevertheless, due to size limitation only a partial validation is applied. The use of water instead of refrigerant is tested only for small pipe diameter (15.0 mm) and low pressure (around 1.9 bar-a). This section has the objective to "justify" the extrapolation to higher pressure and to larger diameter. Three considerations have been described below. They are not sufficient to demonstrate the full extrapolation of the correlation to solar DSG applications but justify why we could expect similar results.

The *modified KTF* correlations are semi-empirical and based on fluid properties (density of liquid and steam, viscosity and surface tension of liquid phase), based on flow conditions (diameter, pressure and heat flux) and based on dimensionless numbers as Froude and Weber ratio of liquid phase. In particular, the ratio Froude-Weber takes into account the high surface tension of water respect to gravity force. The *modified KTF* correlations are defined for this ratio in the range of [0.8; 6338]. In laboratory condition, this ratio is 38 and around 1000 for the real case study. In both conditions the ratio Froude-Weber for the liquid phase is inside the *modified KTF* correlation boundary, thus the use *modified KTF* correlations for water in the solar DSG conditions seems reasonable.

Modified KTF correlations are defined for small diameter however historically these correlation are developed based on Backer's correlations [86], which have been developed for large diameter, between 25 and 51 mm. Thus we could expect that the physics behind these new flow pattern maps are acceptable for water/steam with a diameter of 66 mm.

Figure 5.4 shows the influence of pressure, diameter and heat flux on the *modified KTF* correlations. In the case of laboratory sizing (blue line) the correlations are "pushed" to lower steam quality and specific mass flow rate. These conditions are strongly different from the conditions of refrigerant data [88]. For instance the transition curve from intermittent to annular is varying between 0.25 and 0.4 for the different refrigerant data and equals to 0.09 in the laboratory condition. Whereas the real solar DSG conditions (black line) have the *modified KTF* correlations defined close to the condition where the equations have been tuned, eg. 0.26 in figure 5.4. Thus, if the flow pattern map defined in laboratory condition is validated, we could expect a good agreement of *modified KTF* correlations in less restrictive conditions.

5.3 Methodology

The methodology consists to generate various steady state conditions of mass flow rate - steam quality at the absorber outlet and then identify the flow pattern according to the criteria defined in the section 5.2.2.2. These points should cover a large share of the test area defined in Figure 5.5. It is quite straight forward to measure the mass flow rate, since the electromagnetic sensor installed at the pump outlet is used to measure the volume flow rate. For the steam quality is more complex as no direct sensor could measure it. To measure indirectly the steam quality three approaches would have been possible:

- measure the liquid mass flow rate at the inlet and outlet of the absorber. The outlet liquid phase should be separated before to measure it.
- cool the two-phase flow mixture to sub-cool condition and quantify this energy.
- calculate the steam quality thanks to the monitored electrical heater.

All of them would lead to same order of magnitude of uncertainties thus it has been chosen the third one which is more economic. A specific model to calculate the net heat gain to the fluid is developed and calibrated trough 10 calibration tests. Once the calibration is done, the steam quality could be calculated for each steady state test thanks to numerical Model 1, described in section 4.5. The steam quality

uncertainty of this approach is estimated for the different conditions of the test area, see section 5.3.4.

5.3.1 Test condition

A steady state test is defined at stable conditions of mass flow rate and temperature inlet for a duration of at least 30 s with a constant heat flux. More than 100 steady state tests have been carried out, with different mass flow rate and electrical heat rate. A strong instability is observed for the conditions with "low" mass flow rate ($< 100\,\mathrm{kg/s\,m^2}$) and "high" steam quality (> 0.3).

To generate stable test conditions, the following methodology is applied for each test. First, the whole system is filled with cold water at ambient temperature (eg. 25 °C). The valve V5, defined in figure 5.8, is opened to by-pass the steam drum and the pump recirculates the water at high mass flow rate. All the electrical heaters are activated and the pressure is maintained around $1.4\,\mathrm{bar} - \mathrm{a}$. First the air vents ($V_a$ in figure 5.8) then the manual valve V3 are opened to control the pressure increases due to water thermal dilatation. Once outlet temperature of the absorber, T7, equals to 90 °C, then manual air vents and valve V5 are closed and the hot water flows to the steam drum. At this point the system is closed, which corresponds to point A in the figure 5.27, where only the electrical heaters used for the test are activated. Once T1 equals to 110 °C, then the pump inverter is set to the required test condition. The video starts once the mass flow rate is stabilized and it lasts at least two minutes.

Thus, at initial condition (point A), the tank water is cold (e.g 25 °C), the recirculation loop is hot at 90 °C and the pressure equals to 1.4 bar-a at steam drum bottom. To highlight the role of the vessel tank, the thermal phenomena are split in different steps, which could happen at the same time in reality:

- A - B: thermal dilation of the recirculation loop from 90 °C to 120 °C
- B - C: water evaporation of the absorber (eg. 0.9 L for the test DSG bench) and biphasic pipe (eg. 15.9 L for the test DSG bench)
- C - D: thermal dilation of the steam drum from 25 °C to 120 °C. In reality the bottom part of steam drum is at saturated condition thus the volume of cold

water is smaller.

- D - E: water evaporation in the steam drum to reach the maximum pressure (eg. 2.2 bar-a for the test DSG bench). The expected water evaporation in the steam drum is 11 L.

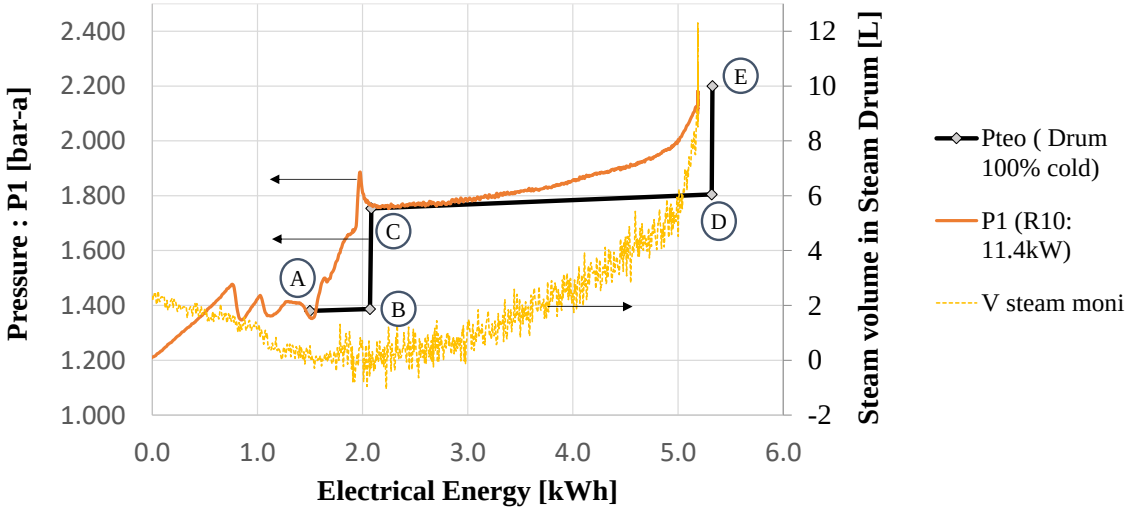

Figure 5.27: Pressure variation expected (simplified approach) and monitored during steady state test

The analysis of the monitored pressure variation (sensor P1) of a real steady state test highlights the real plant behavior. The example of the test bench is used to highlight the phenomena that happens at the same time. Figure 5.27 shows that the phenomena A-B and B-C happen at the same time and most of the inlet steam condenses at the beginning of condition C-D. Then, the steam drum warms-up and the steam condensation is reduced and the remaining steam is accumulated in the top. In the range 2.0 - 4.5 kWh, the pressure increases slowly and reaches a maximum increase of 0.12 bar-a/kWh. In the following section 5.3.2, the condition of steady state is discussed based on this maximum increase rate. Moreover, the final monitored steam level, equals to 12 L, is in agreement with the calculated water evaporation of the steam drum, 11 L.

5.3.2 Modeling approach

The steam quality is calculated for each steady state test thanks to numerical Model 1 and a heat flux model.

5.3.2.1 Heat flux model

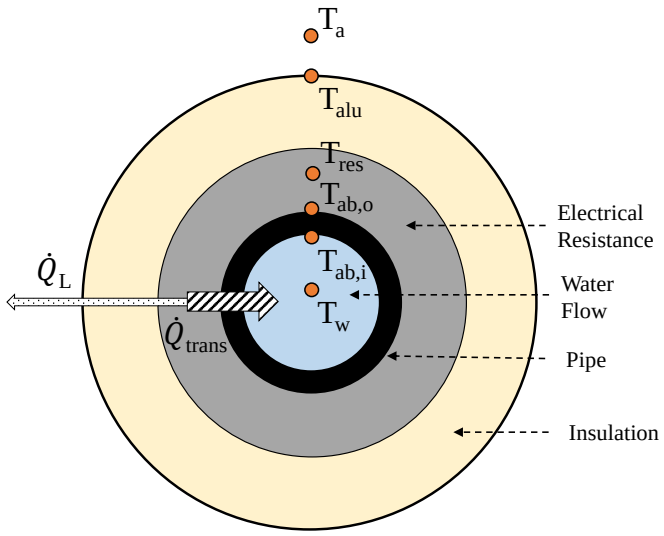

Figure 5.28: Cross Section of evaporation piping with insulation and electrical resistance

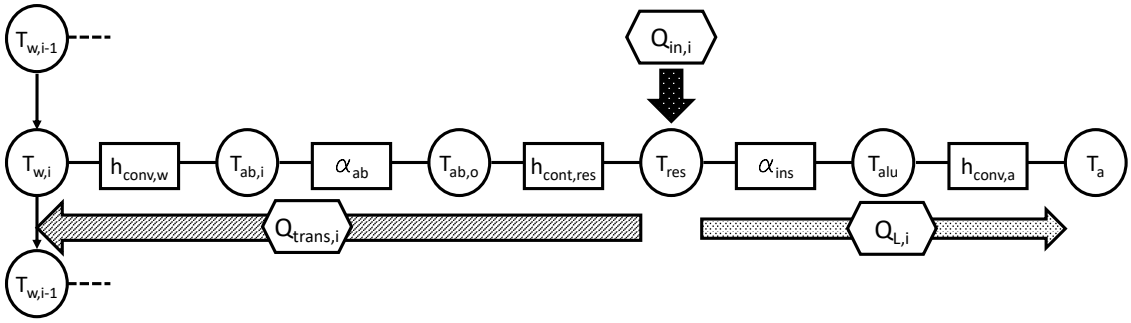

Figure 5.29: Heat flux model for evaporation piping

The heat flux model is a lumped steady state model where the boundary conditions are ambient temperature T_a, water temperature T_w and electrical heater consumption $\dot{Q}_{in}$. The objective is to quantify the ratio $\frac{\dot{Q}_{trans}}{\dot{Q}_{in}}$, i.e. to quantify the ratio of the monitored electrical consumption transferred to the fluid in the different flow conditions. This ratio is used as an input of the Model 1 to calculate water flow boiling. The model has 6 nodes presented in figures 5.28 and 5.29. Based on the size and material properties, five resistive components have been included in the model:

- **Convective air resistance (R_{air}):** calculated based on convective heat transfer rate, see eq. 5.1. Initially the convective heat transfer rate $h_{conv,a}$ is cal-

culated thanks to Morgan correlation [99] in quiescent room condition. The value is varying between 4 W/m^2.K to 6 W/m^2.K for each electrical heater in the different flow conditions. This parameter is not sensitive (see figure 5.32 and figure 5.33) and is kept and constant equal to 5 W/m^2.K for the first two resistances and to 4 W/m^2.K for the rest.

- **Conductive resistance of insulated layer (R_{ins}):** calculated based on thermal insulation properties, see eq. 5.2. The thermal conductivity k_{ins} of the insulation has a strong temperature dependency, as defined in table 5.1. Thus, it is calculated iteratively based on T_{res}. For the test bench, it has been used the values from the component data sheet, which have been calculated in accordance with EN 14303:2009.

- **Contact Resistance from electrical heater (also called *electrical resistance*) to stainless pipe (R_{res}):** calculated based on the thermal contact conductance $h_{cont,res}$, see eq. 5.3. From literature for stainless steel / stainless steel contact, a high heat transfer rate is found in the range of 2000-3700 W/m^2.K. This very large uncertainty range is due to numerous empirical parameters which affect this value. In fact, the contact pressure is the most influence factor, but material roughness, surface deformation and surface cleanliness can also affect this value. As presented in section 5.2.1.4 the steps 1 to 3 are done to improve the heat transfer contact. Nevertheless, the resistance contact area represents 1/4 of the overall pipe external area, thus a first guess of the thermal contact conductance would be between 500 W/m^2.K and 1000 W/m^2.K referred to the external area of the pipe. This value has a strong uncertainty and the calibration process focuses on the setting of thermal contact conductance of each resistance.

- **Conductive resistance of stainless pipe, called absorber (R_{ab}):** is calculated based on a constant thermal conductivity for stainless steel k_{ab}, equal to 17 W/m.K, see eq. 5.4.

- **Convective resistance between the internal pipe and the water flow (R_w):** is calculated based on the heat transfer rate $h_{conv,w}$, see eq. 5.5. Model 1 defines the convective heat transfer rate according to the flow conditions (mass

flow rate, specific enthalpy and pressure). For further information see the description of Model 1 in section 4.5.

$$R_{air} = \frac{1}{\pi \cdot D_{ins,o} \cdot h_{conv,a}} \tag{5.1}$$

$$R_{ins,i} = \frac{1}{2\pi \cdot k_{ins}(T_{res}) \cdot ln\left(\frac{D_{ins,o}}{D_{ins,i}}\right)} \tag{5.2}$$

$$R_{res,i} = \frac{1}{\pi \cdot D_{pipe,o} \cdot h_{cont,res}} \tag{5.3}$$

$$R_{ab} = \frac{1}{2\pi \cdot k_{ab} \cdot ln\left(\frac{D_{ab,o}}{D_{ab,i}}\right)} \tag{5.4}$$

$$R_{w} = \frac{1}{\pi \cdot D_{ab,i} \cdot h_{conv,w}} \tag{5.5}$$

$$T_{res} = \frac{\dot{Q}_{in,i} + \frac{T_{w,i}}{R_{res,i} + R_{pipe} + R_{conv,i}} + \frac{T_{a,i}}{R_{ins,i} + R_{air}}}{\frac{1}{R_{res,i} + R_{pipe} + R_{conv,i}} + \frac{1}{R_{ins,i} + R_{air}}} \tag{5.6}$$

$$\dot{Q}_{trans} = \frac{T_{res} - T_a}{R_{res,i} + R_{pipe} + R_{conv,i}} \tag{5.7}$$

$$\dot{Q}_{L} = \frac{T_{res} - T_{w,i}}{R_{ins,i} + R_{air}} \tag{5.8}$$

5.3.2.2 Model 1 application

This section describes how Model 1 is applied to the laboratory context and discuss its assumptions. Only the active mode is used for the test condition thus the model inputs are: Drum pressure at the bottom (P1); inlet temperature at the recirculation pump (T2); recirculation mass flow rate ($\dot{m}_{rec}$); ambient temperature (T_a) and linear heat gain defined trough heat flux model, see section 5.3.2.1. The sensors position and the different sections of the DSG test bench are represented in figure 5.30 and the parameters are summarized in table 5.3

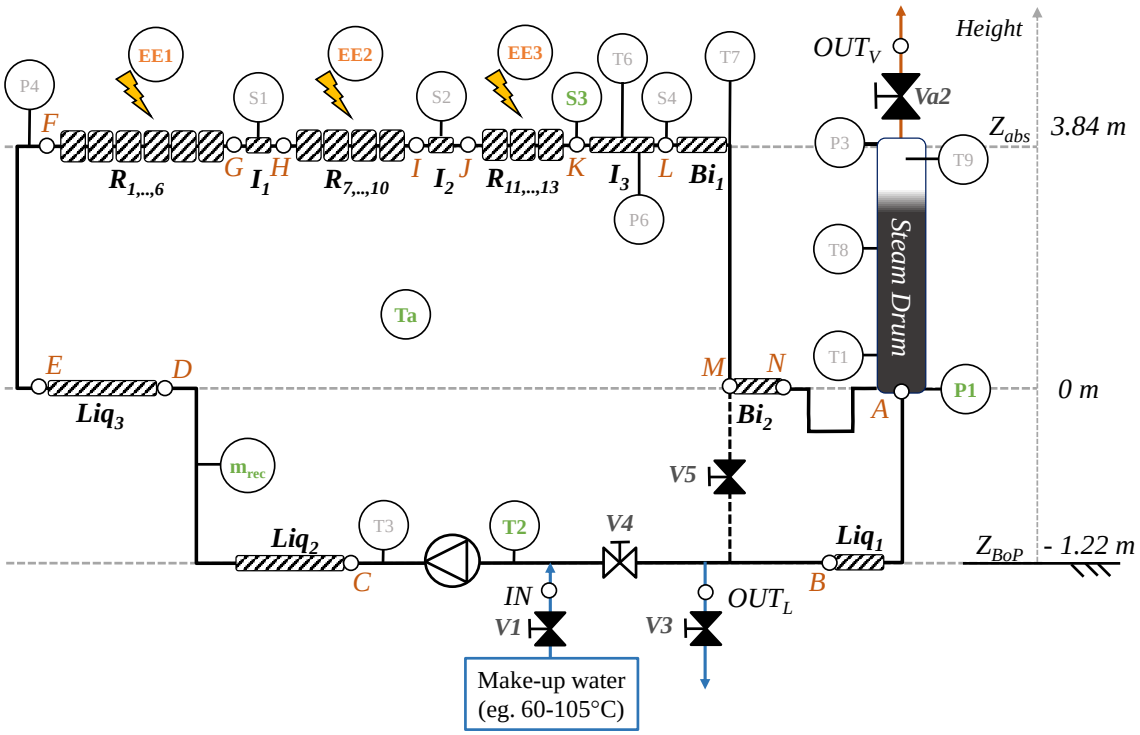

Figure 5.30: Scheme of DSG test bench implemented in Model 1

Table 5.3: DSG bench parameters for Model 1.

Name	***Z*** *[m]*	***L*** *[m]*	***D*** *[mm]*	ζ *[-]*	U_1 *[kW/K.m]*
Liq1	-1.2	2.5	30.1	5.5	2.1E-04
Liq2	-1.2	2.2	30.1	58.5	2.1E-04
Liq3	0.0	3.6	18.0	4.5	2.8E-04
R1 ..6	3.8	2.9	15.7	0.0	*
Int1	3.8	0.2	15.0	0.1	1.6E-03
R7..10	3.8	2.0	15.7	0.0	*
Int2	3.8	0.3	15.0	0.1	1.6E-03
R11..13	3.8	1.5	15.7	0.0	*
Int3	3.8	0.6	15.0	3.6	1.6E-03
Bi1	3.8	5.8	38.9	0.6	3.5E-04
Bi2	0.0	4.1	38.9	6.7	3.5E-04
Steam Drum	0.0	2.6	101.3	-	1.4E-03

**heat flux model*

Assumption: Numerical Model 1 is described in section 4.5. This paragraph discusses the two main model assumptions:

- **One dimensional model.** Since the linear heat flux is uniform over the cross section, we expect an uniform distribution of thermodynamic state variables over the cross section. Moreover, the pipe diameter (15 mm) is two orders of magnitude lower than the evaporation length (6.9 m) thus the state variable variation in the cross section (eg. variation of specific enthalpy) is negligible in comparison to the state variable variation from the inlet to the outlet of the absorber. The assumption is reasonable due to the two reasons described above.

- **Steady state approach.** The steady state approach is used when the system inertia is negligible, i.e. the intern energy variations of the metal (pipe and resistance) and of water are negligible compared to net heat gain to the fluid. The metal inertia variation is proportional to saturation temperature variation when internal heat transfer rate is constant (it is acceptable assumption except for dry-out transition), see eq. 5.9. In section 5.3.1, the test condition analysis shows that measured pressure increase per unit of electrical heat is approximatively 0.12 bar-a/kWh, i.e. an increase of the saturated temperature of approximatively 2.0 °C/kWh. Assuming the stainless steel pipe and stainless heaters as unique component, the intern energy increase, calculated based on eq. 5.9, represents less than 0.1% of electrical heat gain.

  The water internal energy is strongly dependent to the density value in each finite volume. Let's assume two extreme scenarios: the water in the absorber is fully liquid saturated in the first case and fully saturated steam in the second scenario. Due to the pressure increase, internal energy variation, calculated based on eq. 5.10, is respectively 0.35% of electrical heat gain for the first scenario and 0.0001% for the second one.

  Thus, the two time derivatives can be neglected for the test conditions and the steady state approach is reasonable.

$$\frac{\partial U_m}{\partial t} = \frac{\partial \left[C_{p,m} M_m \theta_m\right]}{\partial t} \approx C_{p,m} M_m \frac{\partial T_{w,sat}}{\partial t} \ll \dot{Q}_{in} \tag{5.9}$$

$$\frac{\partial U_w}{\partial t} = \frac{\partial \left[\rho_w h_w - p_w V_w\right]}{\partial t} \approx \frac{\partial \rho_{w,sat} h_{w,sat}}{\partial t} \ll \dot{Q}_{in} \tag{5.10}$$

5.3.3 Calibration

The accuracy of the heat flux ratio is crucial in order to maximize the accuracy of Model 1 in particular the steam quality calculation. Thus, the five parameters of the heat flux model should be tuned under the steady state test condition before being used for the steam quality extrapolation. Unfortunately, it is not possible to measure with a good accuracy the real heat gain with a two-phase flow. Thus, the calibration of the model parameters is done when the water is liquid all along the absorber and the sensitive heat could be measured. The calibration approach is the following.

- First, it is highlighted that the contact heat transfer rate $h_{cont,res}$ is the parameter with the highest uncertainty compared to the other four parameters. Thus, the calibration process has to tune this parameter for each electrical heaters.

- Then, it has been performed a sensitivity analysis to show the relevance of the test calibrations, since the test calibrations are performed under different conditions than the real test conditions. The sensitivity analysis shows that the ratio $\frac{\dot{Q}_{trans}}{\dot{Q}_{in}}$ is independent from the fluid state and from laboratory external condition thus the calibration of $h_{cont,res}$ could be done when the water is liquid all along the absorber.

- And finally, test methodology and calibration results are described.

5.3.3.1 Parameter uncertainty

Heat flux model uses the following 5 parameters to characterize the heat flux ratio: k_{ab}, k_{ins}, $h_{conv,a}$, $h_{conv,w}$ and $h_{cont,res}$. Three levels of uncertainty are defined.

- The highest level of accuracy is for the first two parameters, which are defined based on literature review and component data sheet (EN 14303).

- Then, the next two parameters are depending to existing empirical correlations and they should lead to relatively good approximation. In the case of $h_{conv,w}$ for the active heater, we could expect values between 0.5 and 6 kW/K.m^2

during the 10 calibration tests and between 1 and 22 kW/K.m^2 during the steady state tests, see figure 5.31.

- The worst level is for the last parameter ($h_{cont,res}$), which is strongly dependent to installation quality thus it could lead to strong uncertainty. It is the parameter that has to be tuned with the calibration tests.

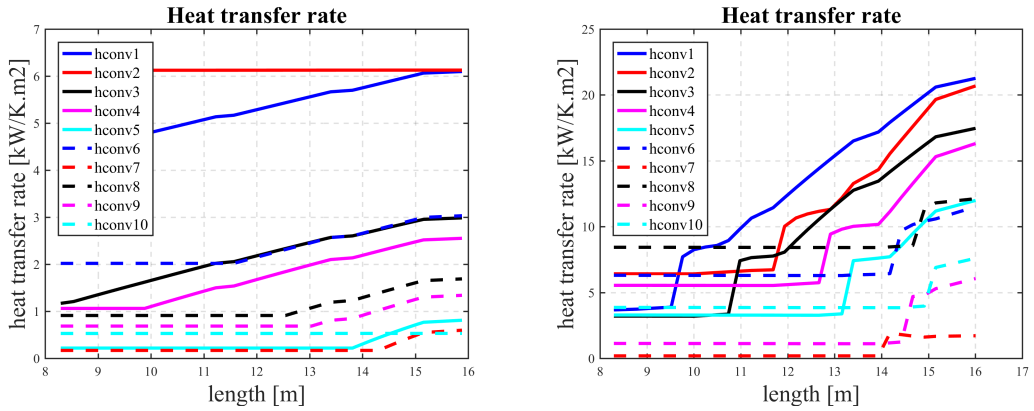

Figure 5.31: heat transfer rate variation $h_{conv,w}$ along recirculation loop for the 10 calibration tests (left) and for 10 representative steady state test (right)

Table 5.4 defines one representative condition for the calibration and one for the steady state test. The variation range of each parameter is defined in order to apply the sensitivity analysis in the next section.

Table 5.4: Initial Value of heat flux model parameters for sensitivity analysis under calibration and test conditions

Parameter	***Condition***	***Unit***	***Value***	***Range***
T_w	Calibration	°C	80	
T_w	Test	°C	120	
$h_{conv,w}$	Calibration	W/m^2.K	2.5e3	500-6.25e3
$h_{conv,w}$	Test	W/m^2.K	10e3	2e3-25e3
k_{ab}	Cal. and Test	W/Km	17	12-22
$h_{cont,res}$	Cal. and Test	W/m^2.K	500	100-1250
k_{ins}	Cal. and Test	W/Km	0.11	0.039-0.183
$h_{conv,a}$	Cal. and Test	W/m^2.K	5	3-9

5.3.3.2 Sensitivity analysis

A sensitivity analysis is applied to the heat flux model parameters to figure out if the calibration under sensible heat gain could be extrapolated to the test condition. The sensitivity analysis consists into the variation of the 5 parameters of the heat flux model around the calibration and test conditions, see table 5.4. Then the variation of the ratio $\frac{\dot{Q}_{trans}}{\dot{Q}_{in}}$ is analyzed.

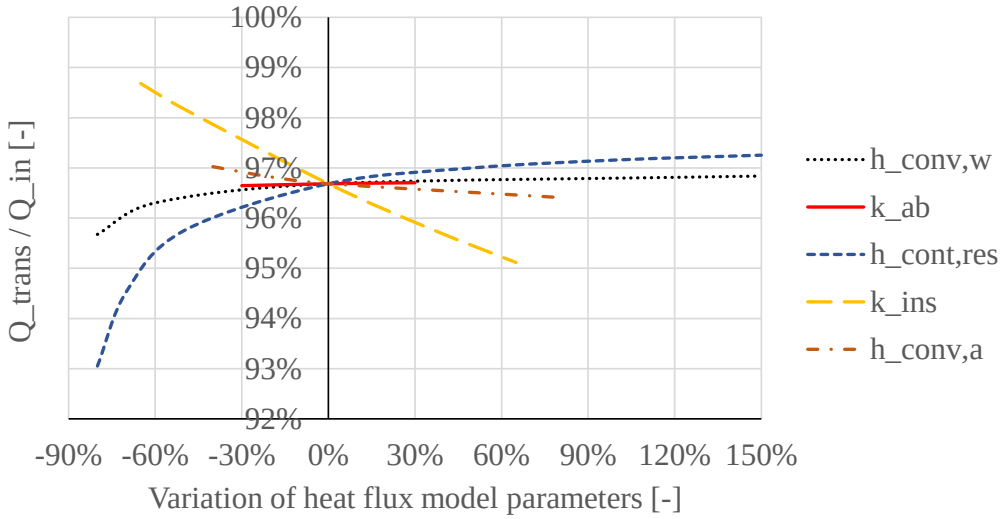

Figure 5.32: Sensitivity analysis of heat flux model in calibration condition

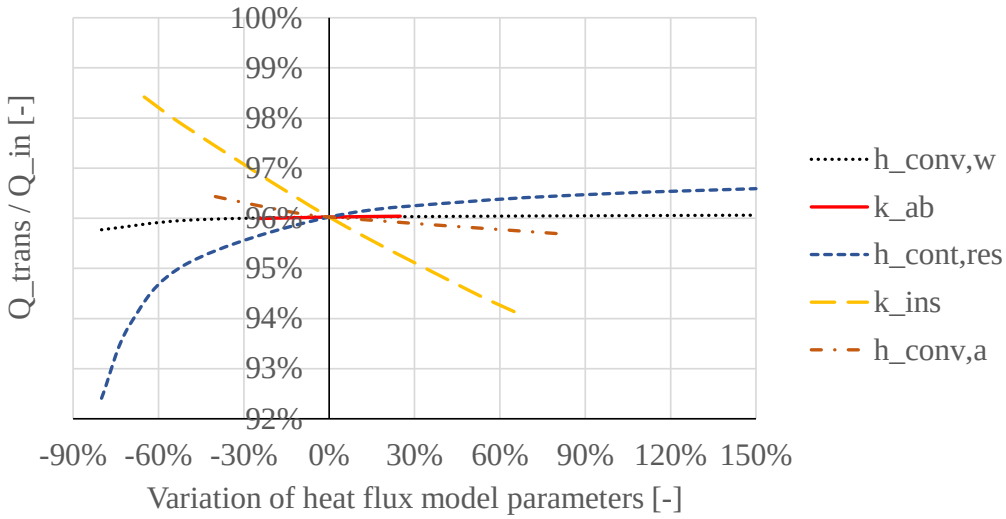

Figure 5.33: Sensitivity analysis of heat flux model in test condition

Figure 5.32 and figure 5.33 show that thermal contact conductance and the insulation thermal conductivity are the two most sensible parameters. Low water convective heat transfer rate slightly impacts this ratio, this condition happens only

for few calibration tests. Nevertheless, $h_{conv,a}$ and $h_{conv,w}$ have a low variation over the heat flux ratio. Thus, we could consider the ratio $\frac{\dot{Q}_{trans}}{\dot{Q}_{in}}$ independent from the fluid state and from laboratory external condition. Hence, the calibration of $h_{cont,res}$ can be applied with a good accuracy under sensible heat gain.

5.3.3.3 Calibration test methodology

Water at constant temperature is fed to the system thanks to the tap water. Valve V1 and V3 are opened and valve V4 is closed, see figure 5.30. Once the whole system is at the tap water temperature (between 15-25 °C) and the pressure is stable then the calibration test can start. Electrical heaters are activated and the sensible heat gain monitored for at least 50 min. Then, the electrical heaters are switched off and the sensible heat gain is monitored until it reaches a new steady state condition very close to initial state.

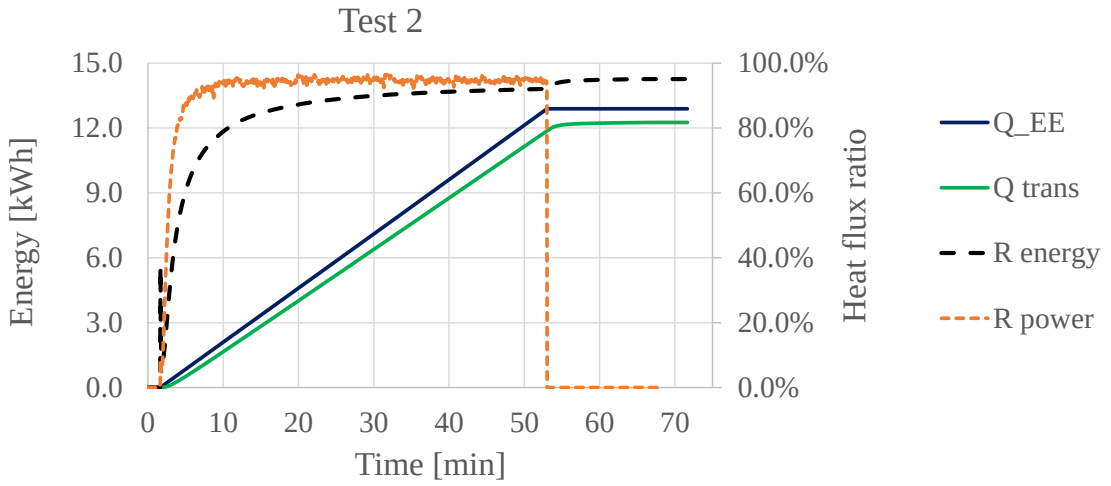

Figure 5.34: Example of Test 2 with the heat flux ratio calculated instantaneously with power and cumulated with the energy

Figure 5.34 shows the example of test calibration with all the 13 resistances activated. The number of active electrical heater is modified to generate all the configurations. The mass flow rate is set to get a large temperature difference between the inlet and outlet of the absorber and to maintain the water into liquid phase. Ten calibration tests are performed and table 5.5 summarizes the test conditions.

Table 5.5: Calibration test conditions

TEST	T_a	***Res Active***	v_{rec}	T_{in}	ΔT
	°C	-	m^3/h	°C	°C
1	23.1	R1 - R13	0.58	18.2	21.1
2	23.3	R1 - R13	0.84	16.8	14.5
3	23.6	R1 - R13	0.16	17.4	76.1
4	24.2	R1 - R13	0.17	18.5	70.5
5	23.7	R1 - R10	0.15	20.0	63.1
6	23.6	R1 - R3	0.07	23.6	39.8
7	23.3	R1 - R7	0.14	23.5	44.0
8	23.0	R1 - R2	0.05	23.6	35.7
9	23.5	R1 - R5	0.12	24.0	38.3
10	24.1	R1 - R4	0.10	24.9	39.2

5.3.3.4 Calibration results

Once ten calibration tests are performed, the transmitted heat flux and electrical heat are calculated over the whole period. The first one integrates the sensible gain plus the variation of intern energy of the water and metal between the beginning and the end. Intern energy variation is lot smaller than sensible gain. The second one integrates the meter electrical consumption during the whole period. The objective is to calibrate the contact thermal conductance of each resistance in order to minimize the difference between the expected and measured ratio. An objective function is applied in Matlab, called *lsqnonlin*, to tune the 13 $h_{cont,res}$. A minimum and maximum boundaries are defined, equal to: 15 $W/m^2.K$ and 1500 $W/m^2.K$ and seven extra constraints are defined below (see eq. 5.11 to eq. 5.15):

$$R_{res,1} = R_{res,2} = R_{res,3} \tag{5.11}$$

$$R_{res,4} = R_{res,5} = R_{res,6} \tag{5.12}$$

$$R_{res,7} = R_{res,8} \tag{5.13}$$

$$R_{res,9} = R_{res,10} \tag{5.14}$$

$$R_{res,12} = R_{res,13} \tag{5.15}$$

Table 5.6: Thermal contact conductance after calibration process

Num. Res.	$h_{cont,res}$
-	$kW/m^2.K$
1	0.175
2	0.175
3	0.175
4	0.260
5	0.260
6	0.260
7	1.318
8	1.318
9	1.483
10	1.483
11	1.488
12	1.479
13	1.479

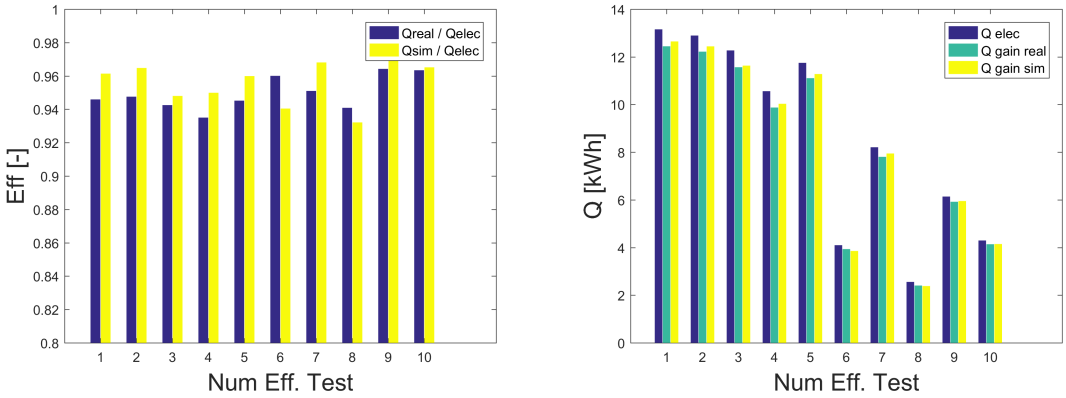

Figure 5.35: Test calibration results

Table 5.6 shows the result of the optimization. The first block of electrical heaters (from 1 to 6) has low contact thermal conductance. This result was expected since during the installation before the steps 2 and 3 the electrical heaters were activated and only the first block of heaters turned to black red (500 -600 ° C). It indicates a bad contact between the electrical heater and the pipes. After the steps 2 and 3, presented in section 5.2.1.4, it was not the case anymore but this block did not reach

the efficiency of the other two blocks. Figure 5.35 shows the comparison between the expected and measured results. The left figure shows the ratio comparison with a maximum error of ±2% for the 10 calibration tests. The right figure shows the energy gain comparison where a good agreement is observed between expected and measured.

5.3.4 Uncertainty range

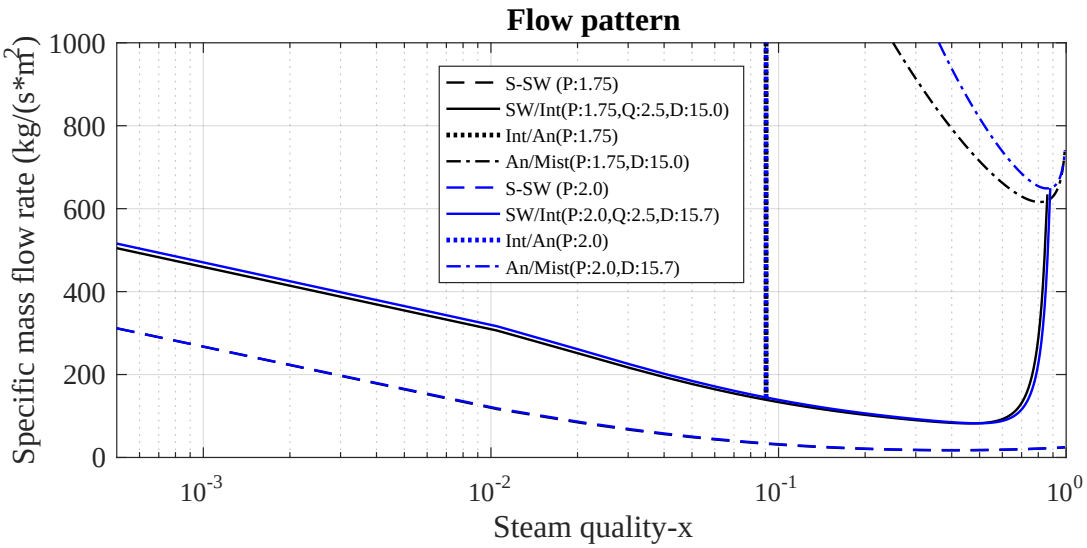

Figure 5.36: Sensitivity of *modified KTF* map in the laboratory test range

The steady state tests generate three dimensional points, composed by steam quality, specific mass flow rate and flow pattern. They are compared to the *modified KTF* flow pattern maps defined for a diameter of 15.0 mm, pressure of 1.9 bar-a and a linear heat flux of 2.5 kW/m, see results in figure 5.40. Nevertheless, these points are generated for various pressure in the range 1.75 to 2.0 bar-a and the stainless steel pipe has an intern diameter of 15.7 mm. Figure 5.36 shows the effect of pressure and diameter variations from (1.75 bar-a, 15.0 mm) to (2.0 bar-a, 15.7 mm). The variation of the transition curves are negligible except for the annular/mist boundary which is not analyzed in this work.

The effect of diameter variation between the sight tube and the steel absorber has no effect in the transition curve calculation but affects the calculation of the specific mass flow rate. In fact, the specific mass flow rate calculated in the sight tube is 9.6% higher than the one calculated in the absorber. For instance, a specific

mass flow rate of 300 kg/s m^2 in the sight tube corresponds to a specific mass flow rate of 274 kg/s m^2 in the absorber. Thus, this diameter variation introduces a small uncertainty on the specific mass flow rate calculation, nevertheless it has been chosen to use the specific mass flow rate at the point of observation of the flow pattern (ie. sight tube).

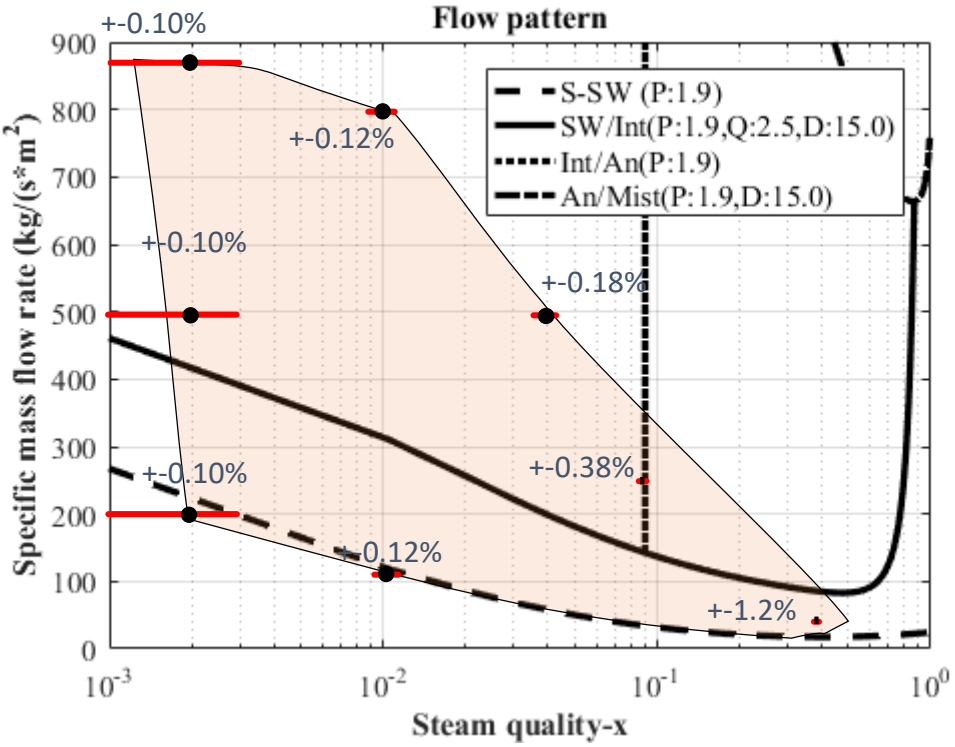

Figure 5.37: Uncertainty map

Steam quality uncertainty is calculated based on the sensor uncertainty and on the heat flux model uncertainty. The calibration process shows an absolute uncertainty of heat flux ratio lower than ±2%. To be conservative it has been used ±3%. Then, the sensor uncertainties, defined in table 5.2, are propagated using standard deviation in order to quantify the steam quality uncertainty. Figure 5.37 shows the steam quality uncertainty on the overall test area which turns to be very competitive respect to other methodologies to calculate the steam quality.

5.4 Results

5.4.1 Pressure distribution over the recirculation loop

Figure 5.38 shows the pressure distribution validation. The expected pressure variation along the recirculation loop (full blue line) is compared with the three pressure sensors installed at the bottom of the drum (P1), at the absorber inlet (P4) and outlet (P6). A good agreement is observed for the two selected steady state tests, see figure 5.38. No static pressure difference is observed trough pressure sensors P1 and P6. It means that the vertical downward pipe from the absorber outlet to the drum inlet is fully liquid-steam mixture. This phenomena increases the pressure head of the pump as the pressure decrease due to upward pipe is not compensate by the pressure increase in downward pipe. Nervetheless, the pressure distribution over the recirculation loop is only partially validated as no pressure sensor is installed at the pump inlet and outlet. The pressure drops due to friction (dashed black line) are shown in figure 5.38. The latter shows the pressure distribution in the theoretical condition where the static pressure is not considered, i.e the whole plant is at the same level.

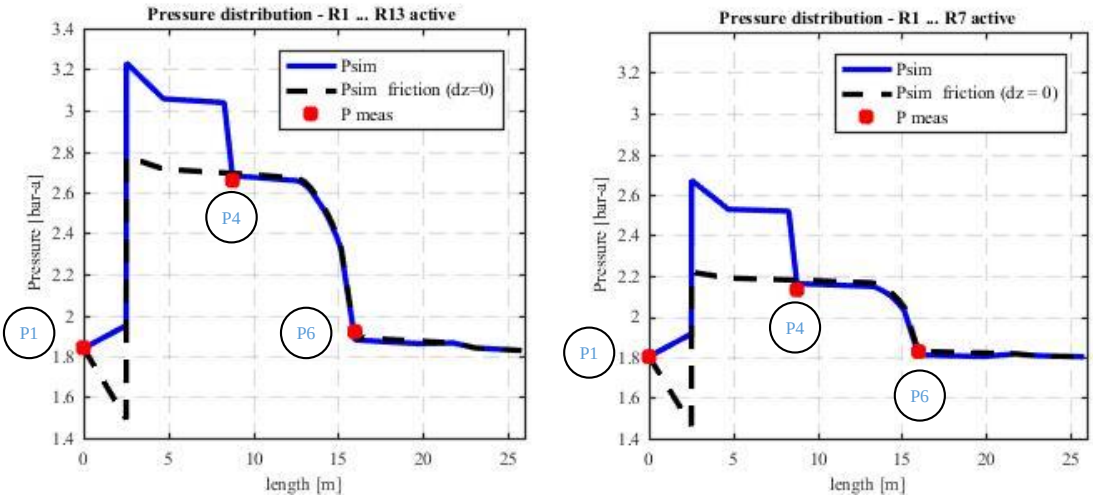

Figure 5.38: Pressure distribution along recirculation loop with 13 active electrical heaters (left) and 7 active electrical heaters (right)

5.4.2 Pressure drops

To extend the pressure drops analysis, the expected pressure drop of the absorber for each steady state is compared to the measured one. Figure 5.39 shows that most of the points are within the interval ± 25%.

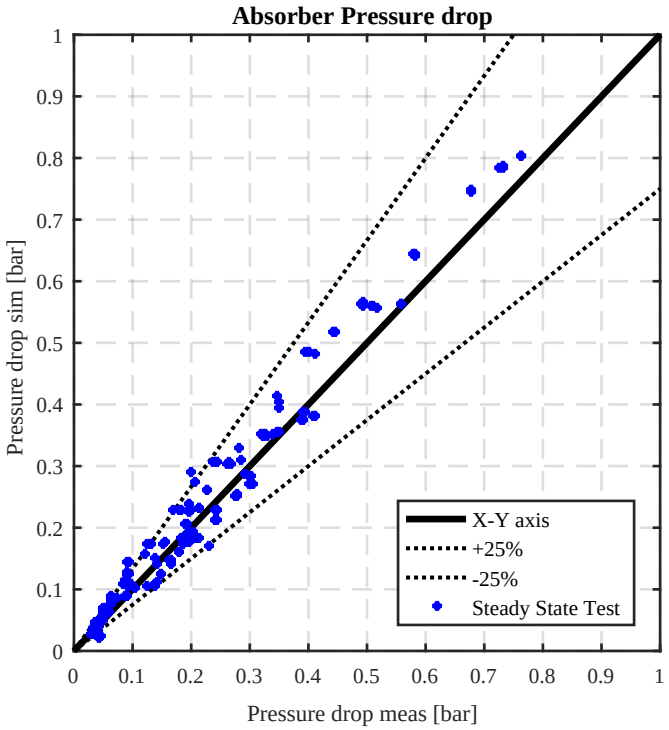

Figure 5.39: Comparison between expected and measured pressure drops for the Steady state tests

5.4.3 *Modified KTF* flow pattern map

5.4.3.1 *Modified KTF* flow pattern map validation

The DSG test bench, presented in section 5.2.1 to extend the flow pattern map outside of its usual operating conditions. In fact, KTF correlations [88] then latter its modified version [89] have been developed and tuned for refrigerant in small diameter pipe at low pressure. However, in the present study, the *modified KTF* correlations have been used outside their validity range for water flow in larger diameter pipes (70 mm compared to 8-20 mm) and higher pressure (3-30 bar compared to 1.1-8.9 bar). The experimental activity has the objective to validate the use of water instead of refrigerant for the flow pattern transition curves in typical conditions for solar DSG

between intermittent, stratified wavy and annular. Figure 5.40 shows the results of the steady state tests and a good agreement is observed with the *modified KTF* theory. Indeed, most of the points are within the expected area. This result validates the use of the *modified KTF* correlations in the case of water for the studied test area.

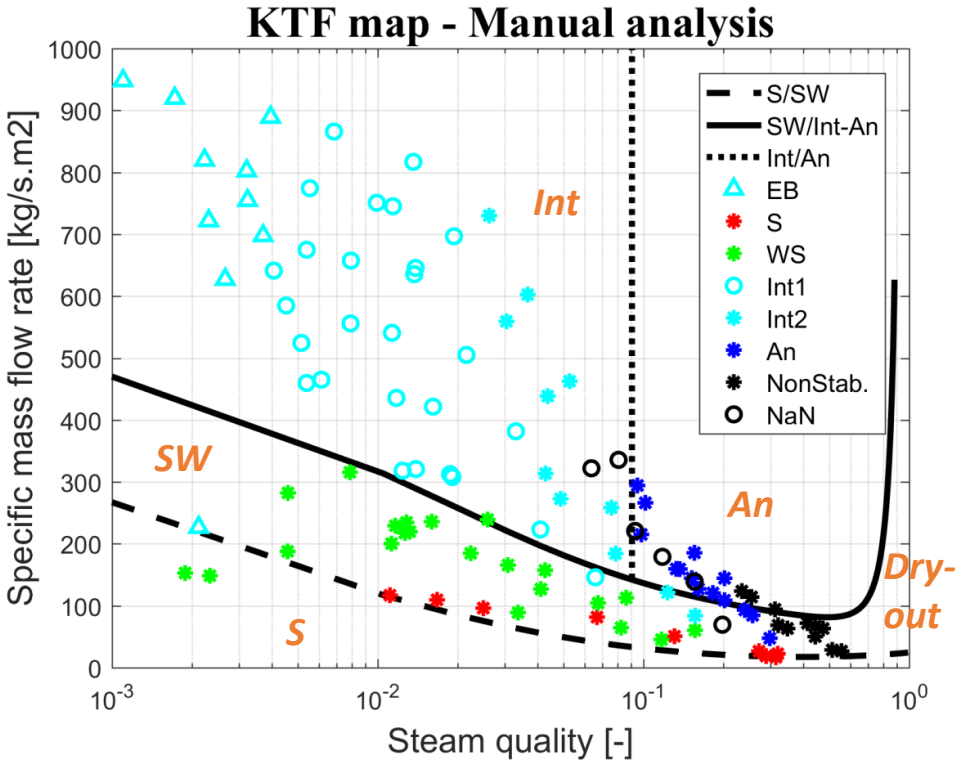

Figure 5.40: Flow pattern maps validation for water as medium

It would be interesting to extend further the test area in order to increase the number of points at the transition curve intermittent/annular and stratified wavy/annular. Nevertheless, the latter area is difficult to test under diabatic condition as unstable mass flow rate would not allow to generate steady state condition. In fact, the black dots represent non stable conditions where the flow transits from Annular to Dry-out flow patterns and vice versa. Figure 5.41 shows the example of three unstable tests (not constant volume flow rate during the test) that correspond to previous cited black dots.

5.4.3.2 Instability region

Numerous two-phase flow instabilities have been characterized in literature. Ruspini [100] did an updated review in 2014 of two-phase flow instabilities including

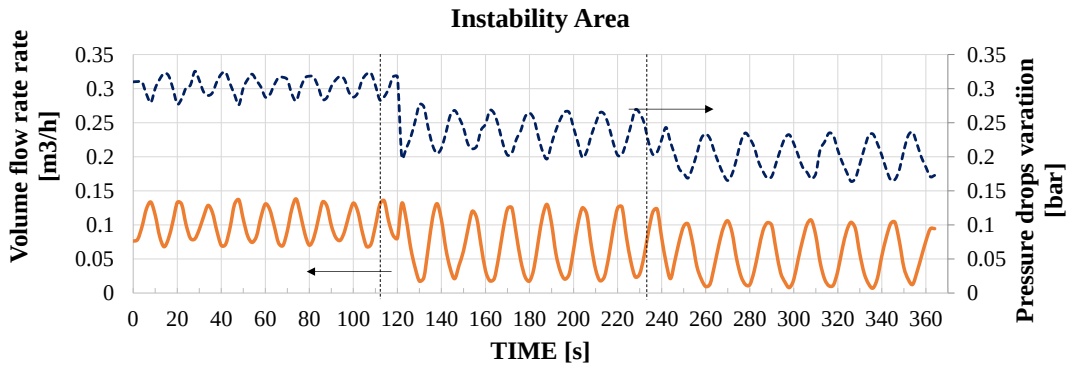

Figure 5.41: Volume flow rate and pressure drops variation of three unstable tests

experimental and analytical results regarding density-wave and pressure-drop oscillations, as well as Ledinegg instability. For flow boiling, the Ledinegg instability [101] is one of the most analyzed instabilities in literature. It is the basic phenomena associated with a flat or even decreasing characteristic curve (pressure drop versus mass flow rate).

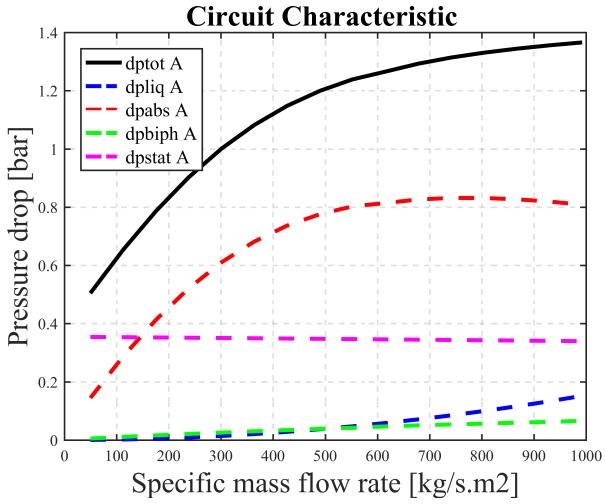

Figure 5.42: Charactateristic curve of DSG bench at maximum power

Figure 5.42 shows the characteristic curve of the test bench (full line) with all the linear electrical heaters activated (conditions of high steam quality). At low mass flow rate (ie. $G < 150\,kg/s\,m^2$), the characteristic curve is very steep, thus the phenomena observed could not be classified as the Ledinegg instability.

This phenomena is classified as a flow pattern transition instability. The instability region appears for low mass flow rate (ie. $G < 150\,kg/s\,m^2$) which corresponds to relatively low heat transfer rate since the heat transfer rate is proportional to mass flow rate. The sensitivity analysis, see figure 5.33, shows that the heat flux

ratio (result of the heat flux model) is sensitive to low heat transfer rate between fluid/liquid. Moreover, the heat transfer rate decreases significantly from annular to dry-out flow patterns. Thus, the water steam quality is expected to decrease from annular to dry-out condition since the quantity of transfered energy to the flow is sensitive to low heat transfer rate.

Figure 5.43 shows the cycling phenomena taking place in the transition from annular to dry-out. Once the flow reaches annular flow pattern the heat transfer rate increases: an increase of steam quality is expected. Thome's pressure drops model according to flow pattern [102] shows that in case of refrigerant the linear pressure drops always increases as a function of steam quality (except for mist flow pattern). Thus, a mass flow rate would decrease to match pump characteristic curve. The new equilibrium is found once the pressure drops increase due to the increase of the steam quality which is balanced with the pressure drop decrease due to mass flow rate decrease. Nevertheless this new equilibrium would be at lower mass flow rate and higher steam quality and could enter in the dry-out flow pattern area and thus the heat transfer rate would be reduced suddenly.

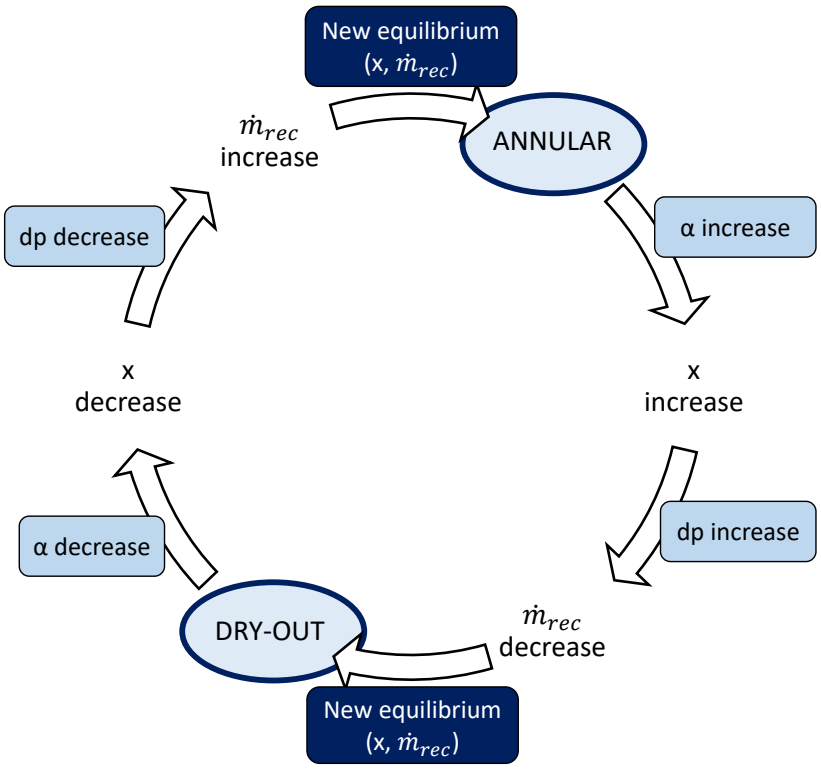

Figure 5.43: Flow pattern maps validation for water as medium

Chapter 6

Case Study

6.1 Objectives

A system operation with biphasic flow requires a specific optimization to limit the pressure losses, maximize the heat transfer rates and avoid the harmful flow patterns. Requirement as pump cavitation protection, avoiding the flashing of the solar field and pressure stability should be satisfied for each plant condition. This analysis is applied to a real case study for two distinct periods one in winter (two weeks) and one in summer (two weeks). It is based on the comparison between a validate numerical model and monitored data. The first step consists on a daily analysis of the mass and energy balance for the two specific periods, called global analysis. Then a detailed analysis is applied to one sunny day in winter (2015/12/25) and one in summer (2016/07/03), where the mass and energy balance are within the uncertainty range.

6.2 Description

This section describes the installed system (components ans sensors) and evaluates the uncertainty range of the indicators used in the following section.

6.2.1 Plant description

Industrial solar installed a solar system of 18 linear Fresnel modules in serial for a total aperture area of 394 m^2 in 2015 at RAM Pharmaceutical Industries

Co. Ltd (RAM Pharma), a pharmaceutical manufacturing company in Amman (Jordan) [28], [27], see figure 6.1. The solar steam is delivered in parallel with the steam boiler on the supply level, as described in the integration guideline of IEA SHC task 49 [30], with a maximum peak capacity of 222 kW_{th}. For the integration concept of direct solar steam generation, a steam drum is used that is fed by a two-phase flow of steam and liquid water from concentrating collectors. A 2 m^3 Steam Drum has been installed to separate the biphasic fluid, stabilize the operation of solar steam generation, and work as a buffer storage to decouple the load from the generation. Boiler feed water is fed to the solar heating system through a feed pump in order to maintain the drum liquid level setpoint. A mixture of the accumulated water and of feed water, in comparison the coldest, is fed to the collector loop where it is partially evaporated. In case of sufficient pressure in the steam drum, the steam is fed into the conventional steam circuit. A controlled valve is used to maintain the required pressure in the factory's steam grid. While solar steam is fed into the existing circuit, the conventional steam boiler reduces its steam production. In this specific case study, the solar steam is sufficient, so that the conventional steam boiler switches off for the whole daylight during sunny days. The plant parameters as pipe length, diameter, height, insulation thickness and characteristics, and component pressure drops, which all have been implemented based on the as-build plant, summarized in table 6.1

Figure 6.1: RAM plant photos (©: S. Anders)

The recirculation loop is divided in sections as shown in figure 6.2. The piping section connecting the steam drum with the inlet of the absorber pipes of the solar collector field is called Liq, since it is always filled with liquid water below saturation conditions. The recirculation pump is in that section as well as the tee piece, where

Table 6.1: Solar DSG parameters - RAM case study

Name	***Z*** *[m]*	***L*** *[m]*	***D*** *[mm]*	ζ *[-]*	$\boldsymbol{U}_1$ *[kW/K.m]*	$\boldsymbol{U}_4$ *[kW/K⁴.m]*
Liq1	-6.3	17.8	38.4	53.3	7.6E-05	0
Liq2	-6.3	21.6	38.4	15.7	7.6E-05	0
Liq3	0.0	26.7	38.4	2.7	7.6E-05	0
CS1	4.5	36.0	66.0	0.0	1.8E-04	8.2E-12
Int1	4.5	7.5	56.3	6.8	8.6E-05	0
CS2	4.5	36.0	66.0	0.0	1.8E-04	8.2E-12
Bi1	4.5	4.0	56.3	0.9	8.6E-05	0
Bi2	0.0	1.0	56.3	20.0	8.6E-05	0
Steam Drum	0.0	2.6	1000	-	7.8E-04	0

feed water is mixed into the recirculation flow on the suction side of the recirculation pump. The sections called CS1 and CS2 represent the two Collector Strings of the solar field, where heat is gained by absorption of solar irradiation during collector operation, while it is just a piping section with heat loss during standby. The interconnection piping between the collector strings is called Int. The piping section connecting the outlet of the solar collector field with the inlet of the steam drum is called Bi, because during collector operation it is leading the two-phase mixture of steam and liquid water from the solar collector to the steam drum. In spite of the name, this piping section usually is filled up with liquid water in standby mode.

6.2.2 Study Framework

The analysis of the case study has the objective to quantify performance deviation, to characterize unexpected behaviors and to optimize existing system. Thus, an expected behavior has to be defined and it is done based on the numerical Model 1 defined in section 4.5. The Model 1 is run every 2.5 min using average monitoring data. Then the results from numerical model and from data processing are compared. Two indicators on mass, ε_M, and on energy balance, ε_Q, lead to a global analysis on several days. Then a detailed analysis is applied on some specific days where expected and measured system pressure drops, liquid level variation of the

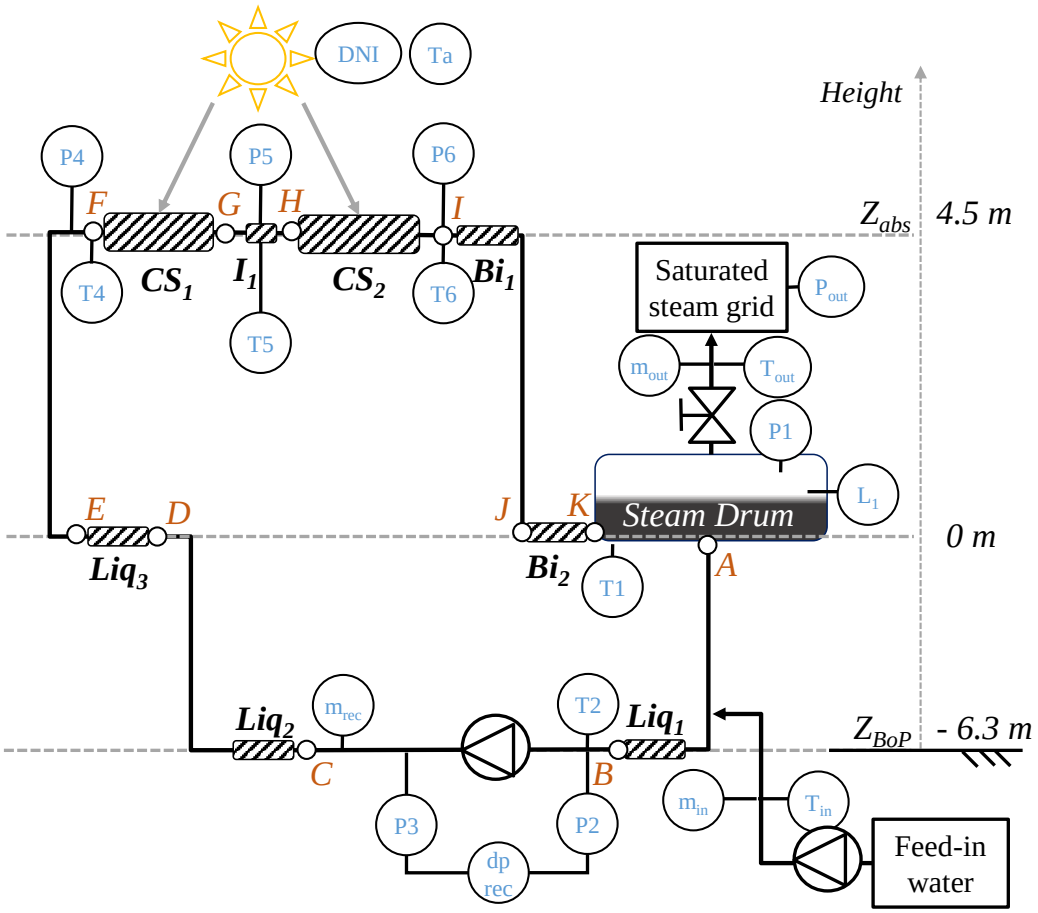

Figure 6.2: RAM scheme.

steam drum are compared. And finally, flow pattern analysis, not available from monitoring data, is done based on existing correlations, see summary figure 6.3. The full orange lines from the monitoring data to Model 1 represent the active model inputs whereas the dashed ones are extra variables used for the stand-by model. The green full lines from monitoring data to data processing are the inputs used to elaborate the measured indicators.

Each of the model assumptions are evaluated in this specific case study boundary:

- **One dimensional finite volume model.** This simplification is possible as the recirculation loop length (> 120 m) is three orders of magnitude higher than the pipe diameter (38.4 mm - 66 mm, depending on pipe section) but it limits the study to only uniform heat flux.

- **Steady state approach.** In this specific case study the inertia of the recirculation loop is small compared to the simulation time step [2.5 - 5 min].

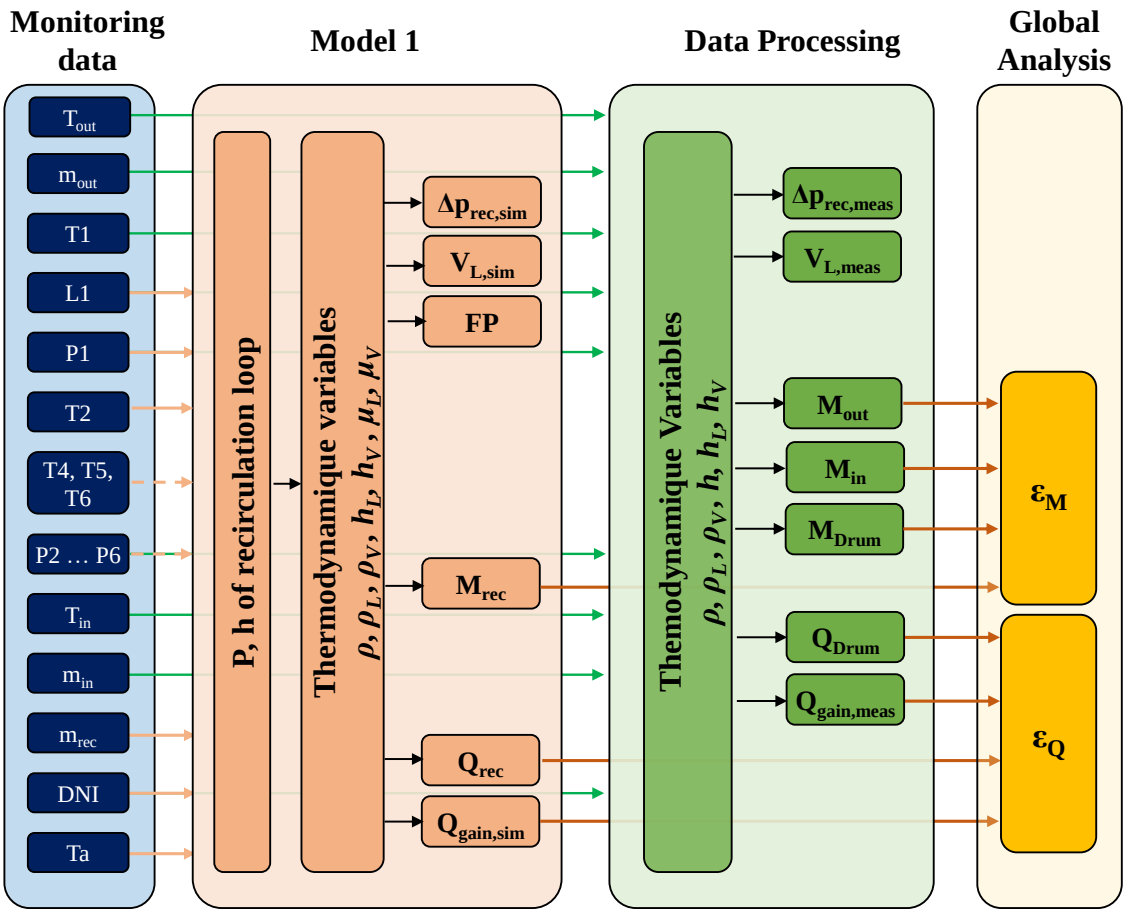

Figure 6.3: Case study analysis framework

In fact, with a flow rate of 1.0 - 1.5 kg/s, the fluid in the recirculation loop is exchanged after less than 4 min, when the system if completely filled with liquid water, and after only 2 min during direct steam generation conditions. Moreover, the ratio between the overall metal inertia and the heat gain during operation is small thus could be neglected. For instance at peak power, the linear heat gain is 3.1 kW/m and for a metal heat capacity of 1.7 kJ/(m.K) the ratio is lower than 0.6 s/K.

- **Homogeneous distribution** and **thermal equilibrium** of the two phases in the flow. Homogeneous distribution implies a slip ratio of 1 between the liquid and the steam phases. Under these assumptions, a common set of conservation equations can be used for single-phase and two-phase flow. In reality, this slip ratio should increase with the steam quality, as presented for instance by Chisholm correlation [103]. Nevertheless, the error by homogeneous assumption is low for low steam quality and steady state model. In fact, a higher slip ratio would lead to a decrease of the void fraction, and thus homogeneous assumption leads to an underestimation of the density. In this numerical model the density of a biphasic volume element is used to calculate the recirculation mass that will be underestimated. It leads to a small overestimation of the expected steam drum level variation. In specific boundary of RAM plant, the expected level under homogeneous assumption and the one with a slip ratio calculated with Chisholm correlations [84] are compared. In the worst condition, we could expect a maximum difference equal to 22 L which could be neglected in this specific case study but it has to be verified for larger system.

- **Momentum equation** is treated in a stationary manner. In fact, the propagation of pressure disturbances is much faster than the process of mass and energy transport.

The numerical Model 1 inputs of the active model are listed in figure 4.5. Based on the sensors installed in this specific case study, see figure 6.2, the following inputs have been used:

- Bottom drum pressure: Top pressure (P1) and liquid level (L1) of the drum.

- Inlet pump temperature: T2.

- Recirculation mass flow rate: $\dot{m}_{rec}$.
- Linear heat flux: proportional to DNI (see following paragraph)
- Ambient temperature: Ta.

For the stand-by model the recirculation loop state is described thanks to all the sensors installed on the field, i.e. temperature sensors T2, T4, T5 and T6 and pressure sensors from P2 to P6 and assuming a system fully liquid, see sensor position in figure 6.2.

The linear heat transfer gain is calculated based on DNI, sun position [104], and the overall IAM of the collector, which is calculated as the product of two different IAMs related to transversal and incident angles [105], [106] and [107], see equation 6.1. The IAM values have been provided by the manufacturer (Industrial Solar), who obtained them from raytracing analysis. The IAM values are defined by assuming an overall error of 3 mrad in the raytracing model, accounting for the statistically independent errors such as shape error, tracking error, alignment error, position error and torsion. Nevertheless, the mirror are assumed fully clean thus a deviation between measured and simulation solar gain is expected if the system is not cleaned with a sufficient frequency. Industrial Solar introduced a partial load function into the control strategy to deal with the condition where the solar gain is higher than the load and the pressure system reached the maximum pressure. In this specific case a small share of the reflectors are unfocused to match the solar gain with the load. The number of reflectors unfocused is a know variable and it is used to modify the expected solar gain as a linear proportion between the number of reflectors focused and unfocused. This approach is assuming an uniform contribution of the reflector which is a simplification. It would lead to an higher uncertainty of the expected gross solar gain (no thermal loss), $\dot{Q}_{in,i}$.

$$\dot{Q}_{in,i} = \eta_0 \cdot IAM_L(\theta_i) \cdot IAM_T(\theta_T) \cdot \dot{Q}_{DNI} \cdot W \cdot L \cdot \frac{M_{on}}{M_{all}} \tag{6.1}$$

The coefficients width (W), length (L), the number of mirrors (M_{all}), optical efficiency (η_0) and the longitudinal and transversal Incidence Angle Modifiers (IAM_L and IAM_T) are parameters defined based on component characteristics. Whereas DNI heat flux ($\dot{Q}_{DNI}$) and number of active mirrors (M_{on}) are monitored data

6.2.3 Measurement apparatus

The solar system is equipped with 8 temperature sensors, 7 pressure sensors, 1 water level sensor and 3 flow rate sensors distributed in the hydraulic circuit, see figure 6.2. A weather station is installed, where ambient temperature, direct, diffuse and global irradiation are monitored. The monitoring data are registered every second from May 2015 to nowadays. The sensor accuracy and typology are listed in table 6.2.

Table 6.2: Sensor List of RAM plant

Measure	***Sensor type***	***Accuracy***
Water flow rate ($\dot{v}_{in}$)	Electro-magnetic flow meter	±0.2% of reading if > 0.064 m^3/h; ±0.5% of reading if <0.064 m^3/h
Water flow rate ($\dot{v}_{rec}$)	Electro-magnetic flow meter	±0.3% of reading
Saturated Steam flow rate ($\dot{v}_{out}$)	Target principle flow meter	±2% of reading, if >20% fs; ±2 % of fs, if < 20% fs
Water temperature (T1 ... T7)	Pt100	Class A EN 60751
Ambient temperature (Ta)		±0.15 % of reading
Pressure sensor (P1)		±0.25 % of span
Pressure sensor (P2 ... P7)		±0.5 % of span
Water level sensor (L1)	Guided Radar (TDR) Level Transmitter	± 10 mm
Direct Normal Irradiation (DNI)	Photodiodes Solarmeter	Global: ±5 $W.m^{-2}$, ±12% of reading; Diffuse: ±20 $W.m^{-2}$, ±15% of reading; Cos. corr.: ±10% of incoming radiation over 0 - 90° Zenith angle

The sensor uncertainties are propagated, using standard deviation, in order to quantify the uncertainty of global and detailed analysis indicators. The uncertainty calculation has been applied for four characteristics days: the two days selected for the detailed analysis and the days with the lowest and the highest steam generation in the studied period.

The fluid properties (density, saturated enthalpy) which are used in the mass and energy calculation are influenced by the sensor uncertainties. To quantify this deviation the relative uncertainty is calculated at nominal condition, table 6.3. This relative uncertainty is assumed constant for the rest of the uncertainty propagation.

Table 6.3: Measurement uncertainties of thermodynamic variables due to sensor measurement uncertainties at nominal condition.

Variable	***Nominal condition***	***Absolute value***	***Relative uncertainty***	***Absolute uncertainty***	***Units***
h_V	P = 10 barg	2781	0.01%	0.15	kJ/kg
h_L	P = 10 barg	782	0.11%	0.9	kJ/kg
h_{feed}	T = 60 °C, P = 1 barg	252	0.50%	1.1	kJ/kg
ρ_L	P = 10 barg	883	0.02%	0.2	kg/m^3

The mass indicator, ε_M, is defined in equation 4.30. Its uncertainty is calculated combining the following three uncertainties:

- $[M_{in} - M_{out}]_{meas}$: Inlet and outlet mass into the solar system , which is calculated using the flow rate sensors uncertainty at each time step and each absolute uncertainty is sum up for the whole day.

- $[M_{D,t_{end}} - M_{D,t_{ini}}]_{sim}$: Mass difference into the steam drum between start-up and shut down, which is the combination of the level uncertainty (refer to the level setpoint) and the density uncertainty calculated at nominal condition.

- $[M_{rec,t_{end}} - M_{rec,t_{ini}}]_{sim}$: Mass difference into the recirculation loop between start-up and shut down. Its uncertainty is assumed equal to the one estimated with the temperature profile approach, see section 6.3.1.

Table 6.4 summarized ε_M and $[M_{in} - M_{out}]_{meas}$ for the 4 selected days as they are daily dependent. The uncertainties of mass difference between start-up and shut down are assumed constant for this specific period and equals to 12 kg for the steam drum and to 15 kg for the recirculation loop.

Thus, for days with low mass inlet or outlet, the uncertainty of mass difference has a strong impact on the mass balance indicator. This uncertainty decreases for

Table 6.4: Measurement uncertainties of Mass balance indicator

Day	***Variable***	***Absolute value***	***Absolute uncertainty***	***Units***
16/12/2015	$[M_{in} - M_{out}]_{meas}$	102.1	±2.3	kg
	ε_M	17.0%	±14.2%	-
25/12/2015	$[M_{in} - M_{out}]_{meas}$	53.8	±11.3	kg
	ε_M	4.0%	±5.3%	-
30/06/2016	$[M_{in} - M_{out}]_{meas}$	-24.5	±30.5	kg
	ε_M	3.0%	±2.9%	-
03/07/2016	$[M_{in} - M_{out}]_{meas}$	-5.1	±19.3	kg
	ε_M	0.5%	±3.8%	-

sunny days and tends to the asymptote of 2% which is the average relative uncertainty of steam flow rate sensor, i.e. the uncertainty of mass difference between start-up and shut down becomes negligible.

The energy indicator, ε_Q is defined in equation 4.35. Thus, four elements contribute to the calculation of the energy indicator uncertainty:

- $[Q_{gain}]_{sim}$: Simulated heat gain, its relative uncertainty is assumed equal to the relative uncertainty of the gross heat, DNI value by LFR efficiency. The monitoring DNI is obtained as the difference between global and diffuse horizontal irradiations divided by the cosinus of the zenith angle, θ_z. The uncertainty of the gross heat has to be calculated all along the days as it changes with the sun position and with the ratio global/diffuse irradiations. It is higher during the morning and the evening when the cosinus values is low, see figure 6.4. Nevertheless, this higher relative uncertainty has a low impact on the daily uncertainty since the gross heat gain is low when zenith angle is high (lower efficiency of solar collector at higher zenith angles).

- $[Q_{netgain}]_{meas}$: Measured net heat gain, its uncertainty is calculated with the uncertainties of inlet and outlet daily mass, see table 6.4, plus the relative uncertainty of the specific enthalpies (liquid and saturated steam) at nominal condition.

- $[H_{D,t_{end}} - H_{D,t_{ini}}]_{sim}$: Energy difference of the Steam Drum between start-up and shut down. Its uncertainty is calculated combining the uncertainties of its mass and of its specific enthalpy. The uncertainty of average specific enthalpy of the drum is assumed equal to the relative uncertainty of the liquid saturated specific enthalpy at nominal condition.

- $[H_{rec,t_{end}} - H_{rec,t_{ini}}]_{sim}$: Energy content of the recirculation loop. Its uncertainty is calculated by using the mass content uncertainty defined above and assuming an error of ±5°C for the average temperature calculation of the recirculation loop.

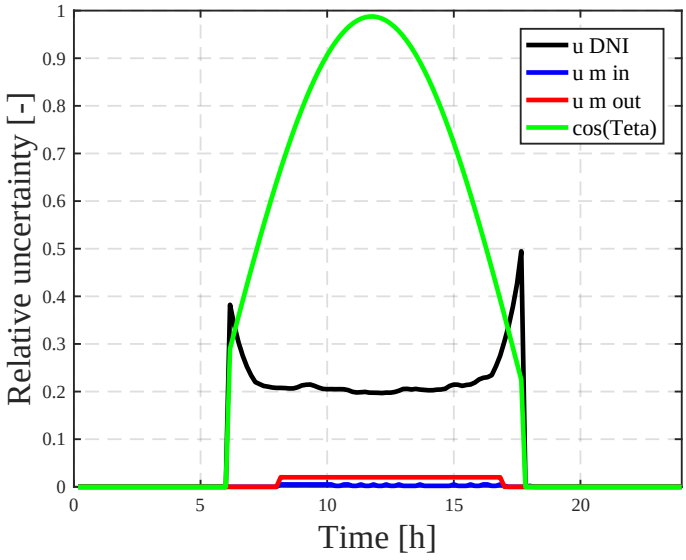

Figure 6.4: Relative uncertainty of 3 sensors on the 2016/07/03

The absolute uncertainties of the energy difference between start-up and shut down is assumed constant and equal to ±3.7 kWh/day for the steam drum and 4.1 kWh/day for the recirculation loop. The other two contributions, list above, are affected by the days profile. Thus, they are calculated for each of the four characteristic days. The strongest contribution comes from the simulated heat gain since it strongly depends to the DNI sensors which has a very low accuracy. Table 6.5 shows the results of $[Q_{gain}]_{sim}$, $[Q_{netgain}]_{meas}$ and the energy indicator for the four selected days.

Finally, the measured indicators as overall pressure drops and the level variation (in volume) are calculated. The pressure drops calculation is the pressure difference of sensors P3 and P2. It fluctuates between 1.2 bar and 1.8 bar whereas the absolute

Table 6.5: Measurement uncertainties of Energy balance indicator

Day	***Variable***	***Absolute value***	***Absolute uncertainty***	***Units***
16/12/2015	$[Q_{gain}]_{sim}$	181	±53.6	kWh/day
	$[Q_{netgain}]_{meas}$	72.0	±1.6	kWh/day
	ε_Q	43.3%	±46.3%	-
25/12/2015	$[Q_{gain}]_{sim}$	585	±128	kWh/day
	$[Q_{netgain}]_{meas}$	384	±8.5	kWh/day
	ε_Q	24.7%	±25.9%	-
03/07/2016	$[Q_{gain}]_{sim}$	765	±165	kWh/day
	$[Q_{netgain}]_{meas}$	685	±15.1	kWh/day
	ε_Q	5.5%	±22.8%	-
30/06/2016	$[Q_{gain}]_{sim}$	1023	±215	kWh/day
	$[Q_{netgain}]_{meas}$	1037	±23	kWh/day
	ε_Q	6.4%	±22.3%	-

uncertainty is 0.04 bar, i.e. relative uncertainty between 2% and 3%. The absolute uncertainty of level sensor L1 is 0.01 m and the liquid level in the steam drum varies between 0.3 m and 0.8 m thus we could expect a relative uncertainty between 1.3% and 3.3%. The liquid volume in the steam drum is calculated as a function proportional to the square of the level measurement, thus its uncertainty is evaluated between 1.8% and 4.7%.

6.3 Performance analysis

The performance analysis has been applied to two distinct periods, one in winter and in summer. The first one consists of 13 days in December 2015, from the 16^{th} to the 28^{th}, and the second one of 14 sunny days from the 24^{th} June 2016 to the 7^{th} July 2016. The first analysis consists in an original evaluation of start-up and shut down thermodynamic conditions (enthalpy and mass) of the recirculation loop and steam drum. The second and third analyses consist in comparing the measured and expected mass and energy performance. The numerical Model 1 is applied with a time step of 5 min. In figure 6.8 and figure 6.9, cleaning days have been indicated

in red, raining days in orange, and the days where a detailed analysis have been applied in green color.

6.3.1 Start-up heat loss

The objective is to evaluate the start-up losses used in the mass and energy balance analysis. It is done by comparing the enthalpy and mass of the recirculation loop and of the steam drum at the beginning of the day and at the end of the previous day. For the steam drum the enthalpy calculation is based on level, temperature and pressure sensors. In the specific case of the recirculation loop, the enthalpy evaluation is more complex as specific enthalpy is not uniform in the different pipe sections and absorber. The approach developed in this section is based on the temperature analysis during one recirculation of the water at start-up and shut down, approximatively 300 s for a flow rate of 1.45 kg/s. Temperature sensors installed in the recirculation loop are used to evaluate the enthalpy and mass content in the different sections.

6.3.1.1 Temperature profile methodology:

The first step consists in identifying the integration period during the start-up and shut down periods. Start time, called t_1, is defined when the recirculation pump is activated and stop time, called t_4, is defined when the recirculation pump is stopped in the evening. The integration stop times ($t_{2,L}$, $t_{2,SF}$) during start-up should be defined. The volume of water that flowed trough the sensor T4 (absorber inlet), called V_{liq}, and at the sensor T6 (absorber outlet), called V_{abs}, are counted. Time $t_{2,L}$ is set when V_{liq} equals the design volume of the liquid sections (Liq 1, 2 and 3) and time $t_{2,SF}$ is set when V_{abs} equals the design volume of the solar field sections (CS1, I1, CS2), see the example of the morning of the 26^{th} December with figure 6.5. The same approach is used to define the integration start times ($t_{3,L}$, $t_{3,SF}$) during shut down. The volume of water that flowed trough the sensor T2 (pump inlet), called V_{liq}, and at the sensor T4 (absorber inlet), called V_{abs}, are counted. Time $t_{3,L}$ is set when V_{liq} equals the design volume of the liquid sections (Liq 1, 2 and 3). Time $t_{3,SF}$ is set when V_{abs}, equals the design volume of the solar field sections (CS1, I1, CS2), see the example of the evening of 25^{th} December with figure 6.6. Then the

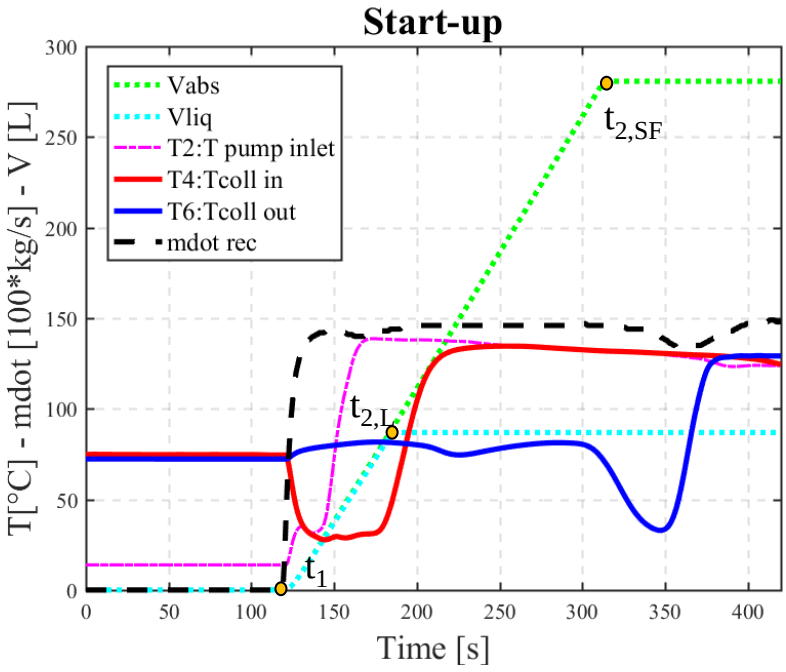

Figure 6.5: Temperature profile - Start-up of 2015/12/26

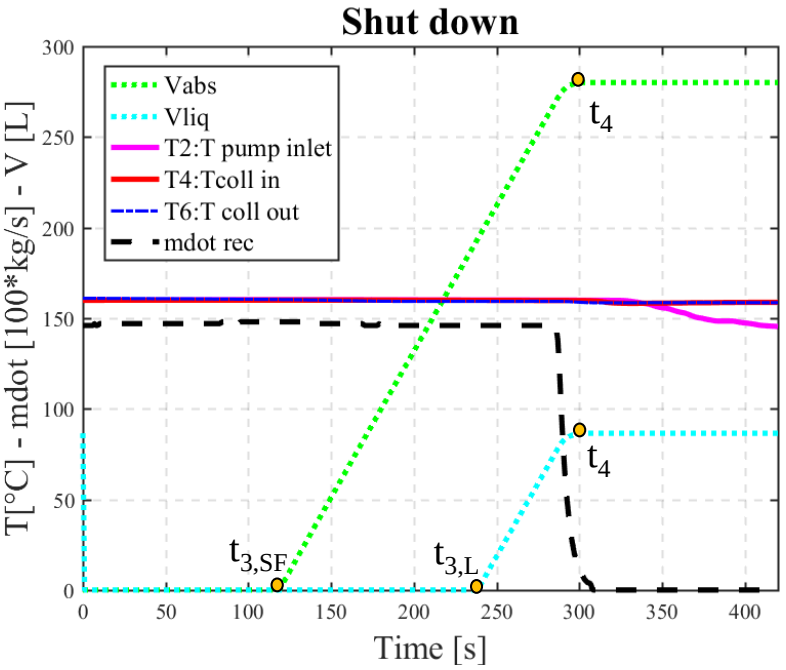

Figure 6.6: Temperature profile - Shut down of 2015/12/25

mass content of the liquid and solar field sections are obtained integrating the mass flow rate ($\dot{m}_{rec}$) during these two intervals. Enthalpy of the respective two sections for start-up and shut down are obtained integrating the product mass flow rate, specific enthalpy during these two intervals. Specific enthalpy is calculated by using

the corresponding temperature sensors: T2 for liquid section during shut down, T4 for liquid section during start-up and solar field section during shut down and T6 for solar field section during start-up. For the steam drum, mass and enthalpy are calculated at the times t_1 and t_4 based on level, temperature and pressure sensors. Start-up loss is the cumulated heat loss over night which is calculated as enthalpy difference between shutdown and start-up.

6.3.1.2 Temperature profile assumptions:

This approach is feasible as the monitoring time step is very short 1 s and temperature sensors have a fast response. The section volume inaccuracy over or under estimates the start-up heat loss. Nevertheless, these assumptions have a good accuracy as the temperature difference in the different section is high ($> 10°C$) during start-up and it is easy to visualize the end of a section. In fact, integration stop time $t_{2,L}$ should be set before drum saturated liquid reaches the inlet absorber (T4), characterized with a fast temperature increase. The integration stop time $t_{2,SF}$ is characterized by a temperature decrease when cold water from liquid section reaches sensor T6.

The recirculation loop is assumed fully liquid. It is safe assumption in the morning after the whole night cooling and in the evening when the recirculation pump is still active and the reflectors are unfocused. In fact, saturated liquid from the drum is pressurized and remains liquid in the solar field.

And finally, the biphasic pipes are neglected in this approach as the outlet solar field temperature is used. It is not an issue as the pipes called Bi represent approximatively 2 % of the recirculation loop mass.

6.3.1.3 Temperature profile results:

The analysis of the start-up temperature profile (in particular sensor T6) shows an average temperature difference of 8 °C between the value T6 before start-up and the temperature peak which happens 60 s after the start-up (water that remains inside the absorber the whole night), for instance see figure 6.5.

The start-up analysis is applied to the winter and summer periods for the nights associated to the two detailed days. The start-up heat loss of the recirculation

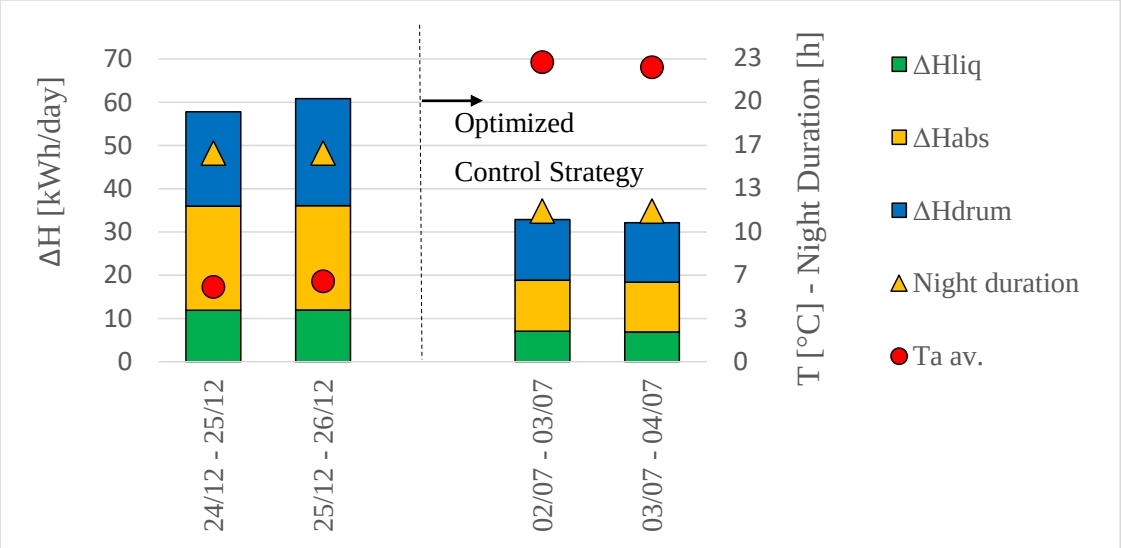

Figure 6.7: Temperature profile analysis

loop is divided in three sections: liquid pipes, solar field and drum. As expected the start-up heat loss is higher in winter than in summer due to several reasons, see figure 6.7. A warmer ambient temperature in summer and a shorter stand-by duration reduce the night heat loss. However, this heat loss reduction is also due to an optimized control strategy, described in section 7.4, which has been implemented the 15^{th} April 2016. It reduced the heat loss of the recirculation loop (liquid and solar field sections). The quantification of the effect of the optimization is done thanks to the validate dynamic Model 3 in the section 7.4.

6.3.1.4 Temperature profile uncertainty:

The main uncertainty of the temperature profile approach is the liquid and absorber volumes which impact the integration periods. This uncertainty is reduced by the tuning of the integration interval based on temperature profile analysis. An uncertainty of ± 5 sec is assumed for the calculation of mass content in the liquid section and solar field section. A mass flow rate of 1.5 kg/s leads to a recirculation mass uncertainty (liquid plus absorber sections) of ± 15 kg. Thus, mass variation of the recirculation loop has an absolute uncertainty of ± 21 kg by using standard deviation. The calculation of the start-up heat loss uncertainty is done combining the mass content uncertainty defined above and the temperature sensor uncertainty. For a standard night heat loss of 35 kWh, the absolute uncertainty is ± 2.9 kWh.

6.3.1.5 Stand-by model validation:

The stand-by model is using the same volume defined in the temperature profile approach. Thus, it is assumed that the mass calculation and mass variation of the recirculation loop have an absolute uncertainty of ± 15 kg and ± 21 kg. For the calculation of the start-up heat loss uncertainty, the average temperature is not measured with the temperature profile approach but interpolated with the sensors installed all over the recirculation loop. It is assumed an error of ±5°C in the average temperature calculation of the recirculation loop. For a standard night heat loss of 35 kWh, the absolute uncertainty is ± 4.1 kWh.

We expected that the night start-up heat loss calculated with the stand-by model approach be lower than the one calculated with temperature profile approach. In fact, in the stand-by model t_{end} is set 1 hour after t_4, see section 4.5.1.3 for more details. Thus, the night duration is shorter for the stand-by approach and the missed heat loss of the recirculation loop is approximatively 3 kWh. This lower start-up heat loss has a low impact on the performance evaluation as it represents less than 1% of measured solar gain for the two detailed days. Including this missed energy, the two approaches have a very good agreement with a deviation lower than ±4 kWh/day. In the uncertainty section, it has been used ±5 kWh/day.

6.3.2 Mass balance

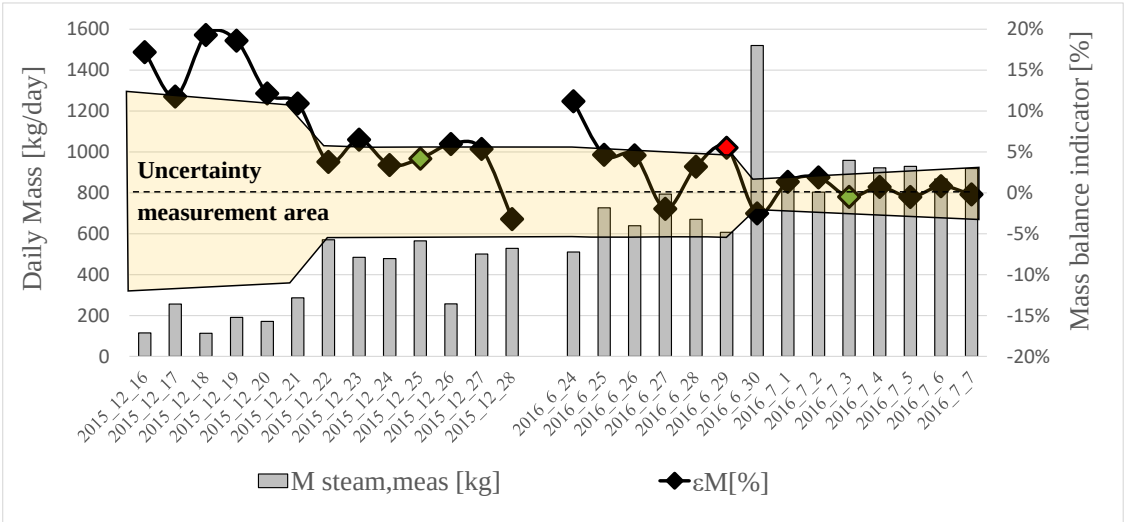

Figure 6.8: Mass balance for winter and summer periods.

To apply further analysis, it is crucial to verify the mass balance of the system. Figure 6.8 shows the measured steam delivered, the mass balance indicator and the uncertainty measurement area of the mass balance indicator. This area is referring to table 6.4 and is proportional to the daily steam delivered. Thus, a mass balance indicator out of the uncertainty measurement area means that the deviation between expected and real measurement could not be explained by uncertainty propagation. For the first 6 days of December, the mass balance accuracy is low as ε_M is higher than 10% and slightly out of the uncertainty measurement area thus they would be excluded of further analysis, e.g. energy balance. For the rest of the days, except the 24^{th} of June the mass balance is on the edge of measurement uncertainty and are very accurate for the last 8 summer days. Nevertheless, figure 6.8 reports that the mass balance is mainly positive which means that the water inlet is higher than the outlet. There are several possible reasons for a positive mass balance, which all have been observed, but could not be quantified. One such reason can be a measurement inaccuracy caused by a small steam mass flow rate below 0.01 kg/s, where the sensor is insensitive, which sometimes occurs, when the steam valve is not fully shut at "shut position". Also the amount of manual blow down from the drum is not measured and increases the mass balance indicator. In fact, the technicians of the RAM factory have been observed by Industrial Solar to draw hot water from the recirculation circuit out of a manual drain valve to fill up a bucket in order to have hot water for cleaning purpose. In all cases this "missing" water mass has been taken from either hot condensate or even steam, and hence some of the energy generated by the solar system does not show in the measurements, so the measured real energy gain is underestimated.

6.3.3 Energy balance

The mass balance inaccuracy affects strongly the accuracy of the energy balance during the first 6 days of December and for the first one of summer, thus they are excluded for the rest of the energy analysis. Figure 6.9 shows the measured energy gain, the energy balance indicator and the uncertainty measurement area for the energy indicator, ε_Q. This area is defined in table 6.5 and is very large due to an inaccurate DNI sensor. As expected the steam generated in summer is higher,

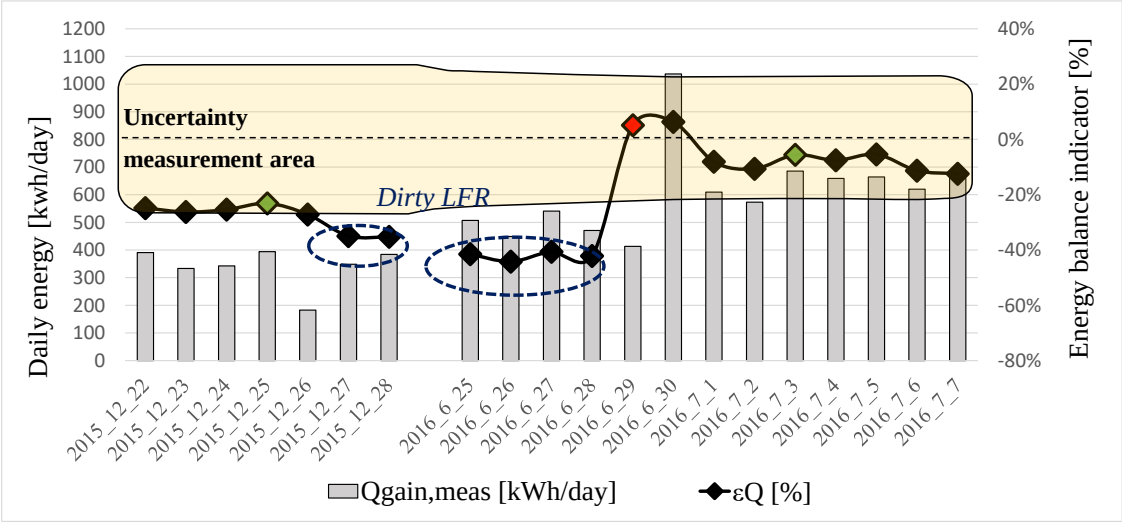

Figure 6.9: Energy balance for winter and summer periods.

nevertheless the solar steam delivered in winter is significant. The energy balance shows that for 14 days out of 21 days, the measured energy balance is within the uncertainty range of the model, and for the other 6 days, measured energy balance is outside of uncertainty range, which is likely due to bad cleaning conditions. In fact, figure 6.9 shows an increase of 45% in the measured daily energy balance in summer after cleaning. A strong effect like this was expected, as the previous cleaning day was 33 days before, and air can be dusty in summer in Jordan. In this specific case, the potential steam generation is often higher than the required steam, so there is no need for RAM Pharma to clean the solar field more frequently. The cleaning frequency is planned in function of their order situation and hence production load. In figure 6.9, a slow decrease in efficiency in the days following the cleaning can be seen, which could be explained by dust deposit. In fact, the winter period is on the edge of the uncertainty range as the last cleaning day was on the 17^{th} of December and after 10 days the energy indicator is outside of the range.

6.4 Detailed analysis

One sunny day in winter (2015/12/25) and one in summer (2016/07/03), where the mass and energy balance are within the uncertainty range, have been selected for a detailed analysis.

6.4.1 Power analysis

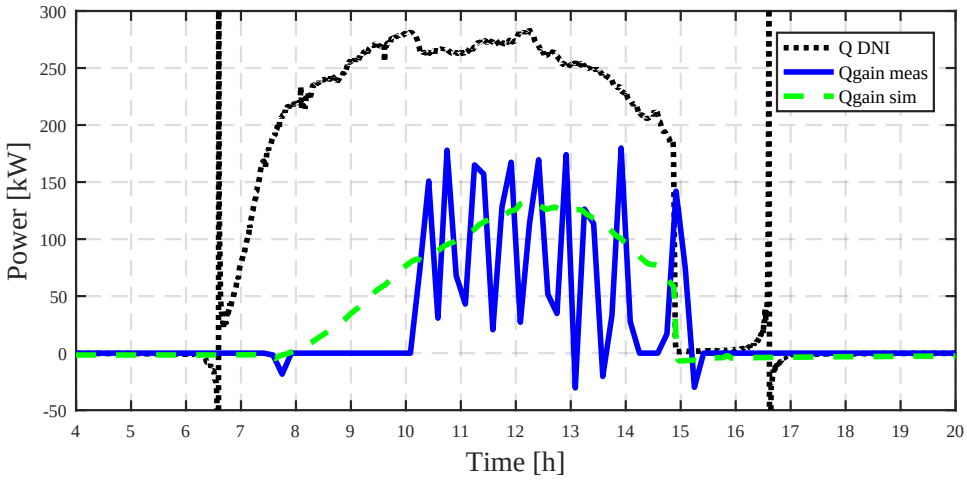

Figure 6.10: Daily power comparison of the 2015/12/25

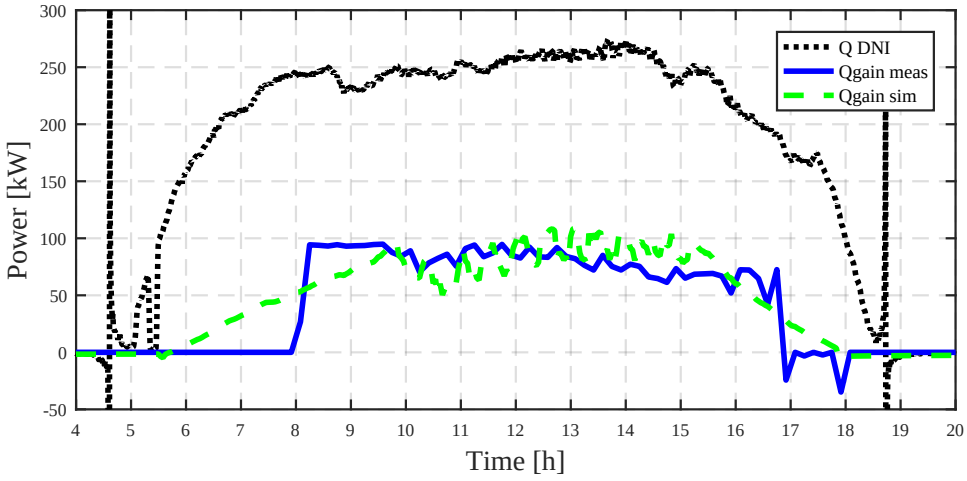

Figure 6.11: Daily power comparison of the 2016/07/03

As expected, the daily power analysis shows, that the measured net gain $Q_{gain,Meas}$, is slightly shifted in time compared to the simulated net gain $Q_{gain,Sim}$. In fact, the solar heat in the morning first compensates the night heat losses, before the system

reaches the required pressure to provide steam to the user. The first delivered steam appears approximately two hours after the start of the active mode, a value expected as IAM efficiency is very low due to a low sun position and due to a short collector string length (36m) causing comparatively high end losses at early morning. The start-up time would decrease for longer collector strings such as used for larger solar fields. The real gain is very stable in summer and very unstable in winter. This instability is due to the daily specific load on one side, and due to solar system pressure variations on the other. The reason for the second issue is discussed later on, where also some solutions are proposed on how to smooth this pressure variation.

6.4.2 Specific enthalpy and pressure distribution

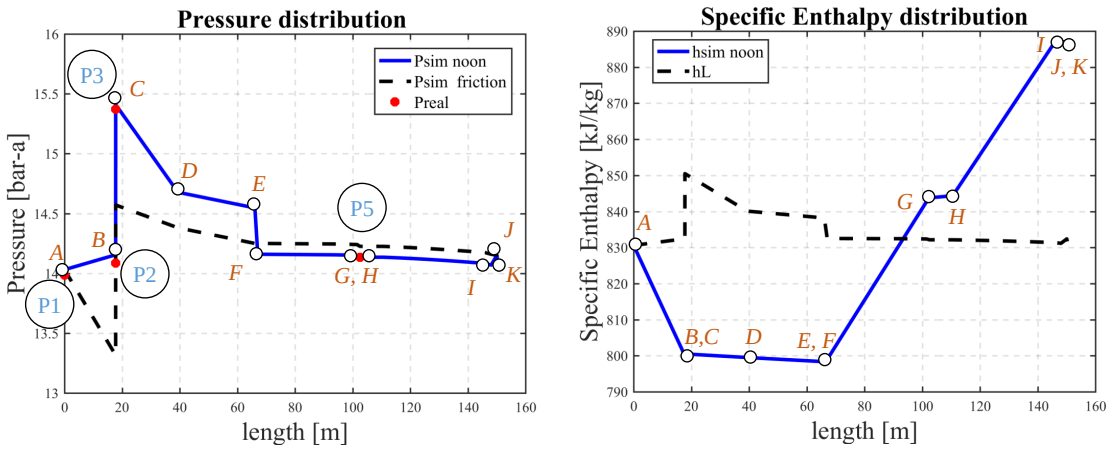

Figure 6.12: Pressure (a:left) and specific enthalpy (b:right) distribution at 12:30 pm for the 2016/07/03)

Figure 6.12 shows an example of the pressure and specific enthalpy distribution along the recirculation loop, for 2016/07/03 at 12:30 pm. The variables $P_{sim,frict}$ and h_L are introduced and represent respectively the pressure distribution neglecting the geostatic pressure and the liquid saturated specific enthalpy at the corresponding simulated pressure. The figure 6.12 reports a good match between the simulated pressure (blue line) and the measured pressure (red dots). The sensors P4 and P6, see figure 6.2, get damaged at the end of April, thus data are not available for the summer period. The effect of geostatic pressure is significant as the pump basement is 6.3 m below the drum and the absorber tube is 4.5 m above the drum. In fact,

a pressure difference of 1.0 bar can be reached whereas the overall head loss due to friction is around 1.2 bar. To quantify geostatic pressure variation is complex, as the fluid density in those vertical pipes which could carry a biphasic flow is unknown. For the upward vertical pipes from C to D and from D to E the fluid is liquid as they are on the pressure side of the pump without any heat gain. But the downward pipes from A to B and from I to J could be biphasic thus reducing geostatic pressure gain. Figure 6.12 shows, that the specific enthalpy at the pump inlet (point B) is far away from the point of cavitation. In this specific case, due to geostatic gain and to mixing with "cold" feed water, the specific enthalpy at point B is 30 kJ/kg below the value for liquid saturated water. Moreover figure 6.12 shows that the energy gain due to the waste heat of the recirculation pump is negligible, and finally that the first steam appears at the end of the first solar collector string, after a distance of 90 m piping length from the steam drum.

6.4.3 Analysis of head loss

Figure 6.13 shows the overall pressure drop over the recirculation loop. The head losses, monitored every second and simulated in time steps of 2.5 min, are averaged over 10 minutes to filter the noise. A good agreement between simulation and measurement during active steam production can be observed, and the measured values stay within the measurement uncertainty range (0.09 bar) of the simulated values. During the start-up and shut-down period the simulated overall pressure drop is underestimated compared to the measurement. Five specific points on 2015/12/25 are analyzed in detail.

The first, third and fourth points (indicated by black lines in figure 6.13, left side) show a good agreement between simulation and monitored data, see figure 6.14. The first case, which was still during standby in the early morning, shows a system fully liquid, where the solar field is at a lower pressure than the steam drum due to geostatic height difference. The other two cases at the end of start-up and at noon during active steam production have a solar field pressure equal or higher than the drum pressure.

Then for the second and fifth point (indicated by orange lines), the model does not match with the monitoring data, see figure 6.15. For each of those two the

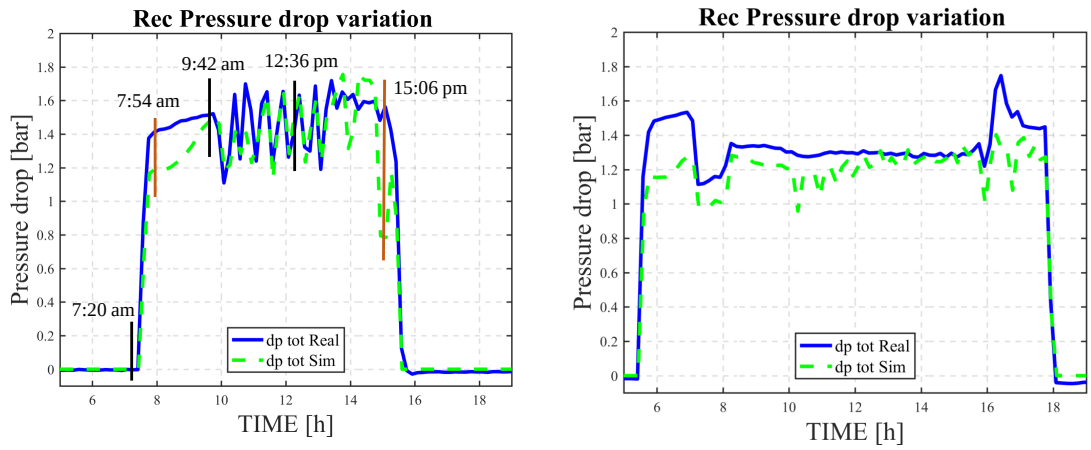

Figure 6.13: Overall pressure drop on 2015/12/25(left) and on 2016/07/03 (right).

difference is due to a wrong density calculation for the downward pipes. In the first one on the left of figure 6.15, the simulation calculates the fluid from I to J as liquid, whereas in reality during the start-up this vertical pipe is immediately biphasic. Which is caused by steam back flow from the drum to the collector outlet when the motor valve between the collector and the drum is opened. In fact, the measured value of sensor P6 (absorber outlet) is slightly higher than P1 (drum pressure) whereas the position of P6 is 4.5 m above P1, and the pressure drop from I to K could not compensate this geodetic height difference. The figure on the right has two differences: the first one, already seen with the point at 7:45 am, where the downwards pipe from I to J is assumed liquid instead of biphasic; the second one is with the downward pipe from A to B, where the model assumed liquid phase instead of biphasic. In fact, data showed that the measured value of P2 (pump inlet pressure) is similar to the value of $P_{sim,friction}$.

In order to study the risk of cavitation, the comparison of the temperature sensors at the bottom of the drum (T1) and at the inlet of the pump (T2) with the equivalent saturated temperature have been done. It shows the boiling of the vertical pipe from A to B during shut-down and a short period of cavitation, see figure 6.16. The steam drum operates as a small steam accumulator. During the charging period, some temperature stratification is building up in the steam drum. This stratification disappears during the discharging period where the liquid temperature reaches thermal equilibrium temperature even seems to be slightly above

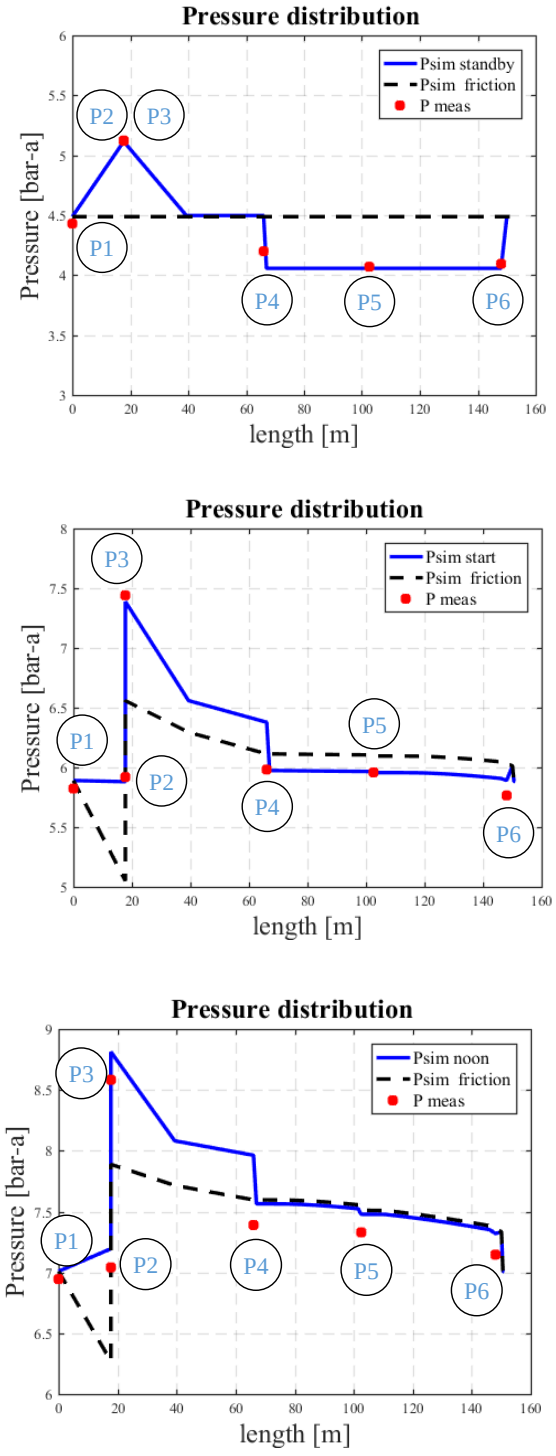

Figure 6.14: Pressure distribution at 7:20am (top), at 9:42am (middle), at 12:36pm (bottom) on 2015/12/25.

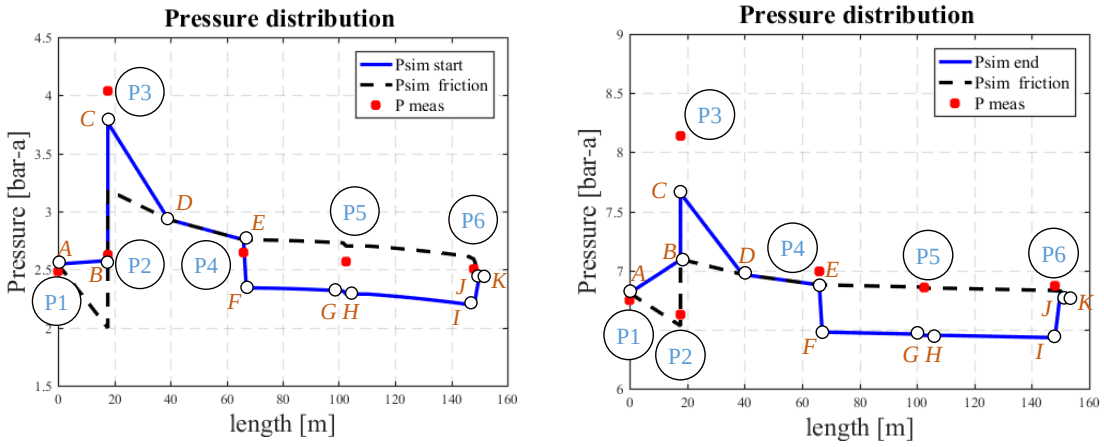

Figure 6.15: Pressure distribution at 7:45 am (left), at 15:06 pm (right) of the 25/12/2015.

in the last hour of the day. During these small intervals, e.g at 15h06, the water at the pump inlet is at saturated condition, hence cavitation appears as the pump could not maintain the setpoint of 1.5 kg/s and dropped down to 1.0 kg/s in spite of the controller turning up the pump drive to maximum speed.

To avoid excessive biphasic fluid in the downward pipes from drum outlet (A) to the pump inlet (B) and to protect the recirculation pump from cavitation, three design recommendations are proposed:

1. to use larger pipe diameter from A to B;

2. to do the mixing of recirculated condensate with feed water directly beneath the outlet of the steam drum;

3. to either use a continuous feed water flow instead of switching the feed water pump on and off or to use a small mixing vessel to mix the feed water with the recirculation water and thereby achieve more constant temperature at the pump inlet, which is below saturation.

The first alternative layout would reduce the fluid velocity, thus the dynamic pressure reduction. In case of low pressure (eg. $3\,\text{bar}-\text{a}$), an increase of the pipe diameter from DN32 to DN50 reduces the pressure reduction from $0.024\,\text{bar}-\text{a}$ to $0.003\,\text{bar}-\text{a}$, see table 6.6. Thus, the saturated temperature decrease is reduced from $0.27\,°\text{C}$ to $0.03\,°\text{C}$ and the risk of flashing inside the pipe from A to B is reduced.

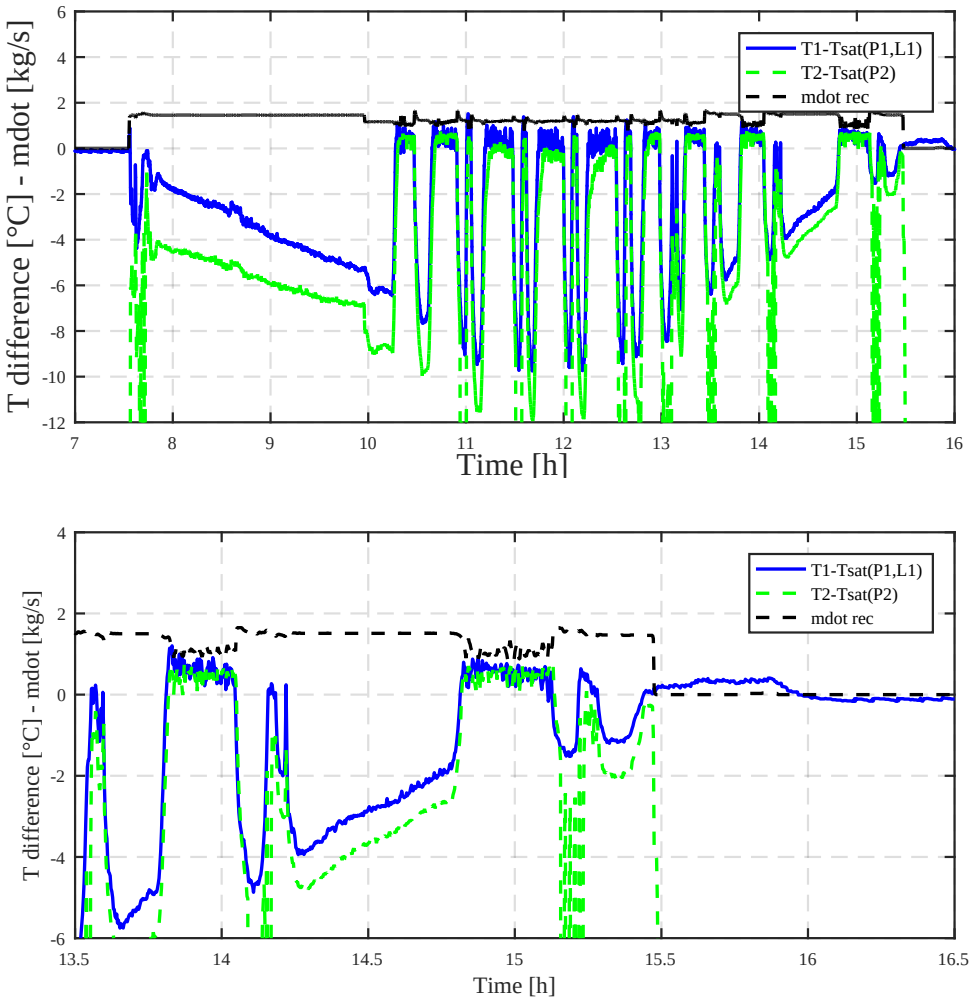

Figure 6.16: Identification of saturation condition at steam drum and at pump inlet on 25/12/2015

At higher pressure, the saturated temperature decrease is lower thus the need to use a larger pipe is lower. The second alternative would cool down this downward pipe below saturation condition and hence avoid boiling during fast pressure decrease. For the downward pipe from the absorber outlet (I) to the steam drum inlet (J), it is recommended to install a siphon that would avoid initial steam back flow from the drum to the collector outlet and thereby reduce the extra pressure drop during start-up.

6.4.4 Level variation analysis

The heart of the solar DSG control strategy is the Drum level control. In fact, the drum level can vary strongly due to phase change in the solar field, due to mass

Table 6.6: Saturated temperature in section "liq1" for Drum pressure and pipe diameter

$P_{drum,bot}$	bar-a	3		10		20	
$T_{L,drum} : T_L(P_{1,bot})$	° C	133.5		179.9		212.4	
ρ_L	kg/m^3	932		887		850	
m_{dot}	kg/s	1.5		1.5		1.5	
D_{liq1}	mm	30.1	52.5	30.1	52.5	30.1	52.5
v_{liq1}	m/s	2.26	0.74	2.38	0.78	2.48	0.82
Δp_v	bar	0.024	0.003	0.025	0.003	0.026	0.001
$T_{L,liq1} : T_L(P_{1,bot} - \Delta p_v)$	° C	133.3	133.5	179.8	179.9	212.3	212.4
$T_{L,drum} - T_{L,liq1}$	° C	**0.27**	**0.03**	**0.11**	**0.01**	**0.07**	**0.01**

balance variation or due to the night cooling of the solar system. Homogeneous assumption used for the mass calculation of the recirculation loop underestimates the expected steam drum level. Nevertheless, its impact is negligible in the specific case of RAM plant since the main flow pattern is wavy stratified flow pattern which has a low slip ratio (close to 1). Figure 6.17 and figure 6.18 show very good agreement on the level variations during active steam production, from 11 a.m. to 3 p.m. on December 25^{th} and from 8 a.m. to 5 p.m. on July 3^{rd}. Thus, it validates the numerical model during active steam production. The expected rate of level decrease due to night cooling is similar to the measured one, varying from 3.5 l/h at the beginning of the night to 1.5 l/h at the end. This level decrease is caused by an increase in the liquid water density throughout the recirculation loop due to cooling. The final level difference on December 25^{th} is due to a small error in the overall mass balance. In fact, when liquid is drawn by technician like for blow-down, it would not be monitored and would affect the overall mass balance (e.g. at 14.5 h of the 25^{th}: unexpected Drum level decrease). During start-up and shut-down periods the simulated level is higher than the monitored one, i.e. the simulated solar field seems to contain more steam. This gap is higher than the measurement uncertainty of the measured level. Thus this error comes from model uncertainty, which is high when the steam quality is low. In fact, a small error in the pressure or specific enthalpy calculation would lead to have steam instead of liquid or vice versa. Moreover, the heat flux uncertainty is higher when the sun is low, see figure 6.4, i.e during start-

up and shut down. The black and grey lines show the level variation due to mass balance and pressure variations. The black line shows the simulation result under the assumption that all absorber pipes are filled with steam only, while the grey line shows the simulation result under the assumption that all absorber pipes are filled with liquid water only. When there is a biphasic flow in the absorber pipes, the measured values should always be between the black and the grey lines. Their slow increase (black and grey lines) during start-up is due to pressure increase, the fast increase is due to feed water and lastly level decreases when steam is delivered.

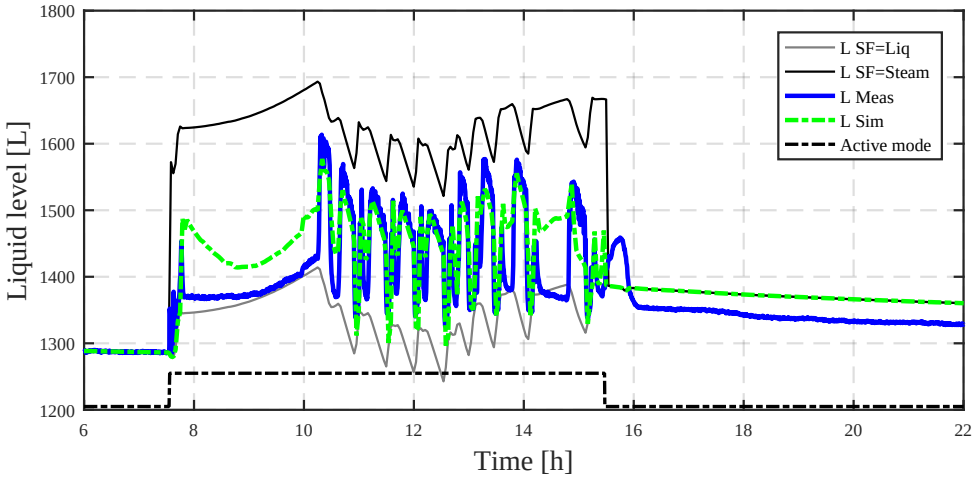

Figure 6.17: Level drum variation of the 2015/12/25

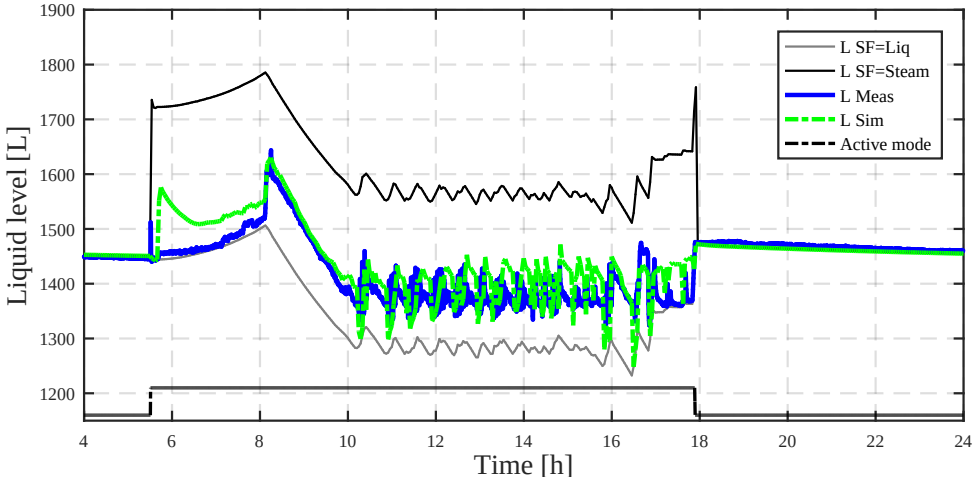

Figure 6.18: Level drum variation of the 2016/07/03

Within the given accuracy of the measurement data, four interesting aspects could be observed thanks to the analysis of the steam drum level.

During the start-up, the analysis of the simulation results with regard to head losses shows that the downward pipe from absorber (I) to the drum (J) is mainly biphasic, nevertheless the monitored drum level data analysis shows that the recirculation loop is almost liquid, so the measured level (blue line in figure 6.17 and figure 6.18) stays close to the gray line. From simulation point of view, it is an opposite analysis, the downward pipe is expected to be liquid thus the pressure in the solar field is lower compared to the drum and some steam could be generated. For an advanced level control, knowing the exact water mass in your system is crucial.

As second aspect, during mode transition, from active to stand-by mode, the recirculation pump stops and an unexpected flashing inside the absorber pipes of the solar field is observed, as shown for the 25^{th} of December. After this behaviour had been observed, the control strategy has been changed in April 2016 to prevent this phenomena. With the new control strategy, just before this transition of operation modes, some feed water, which is much colder compared to the recirculated condensate, is fed into the system and mixed with the recirculated condensate water to replace the hot water from the recirculation loop. After this replacement, the water in the absorber pipes, resembling the geodetically highest point in the system, is cold enough, that the pressure reduction in the absorber pipes after stopping the recirculation pump does not cause any re-evaporation As an advantage, the hot water and steam is now stored in the well-insulated steam drum overnight, and heat losses over night are reduced. Especially removing any steam from the absorber pipes is reducing heat losses, because now the absorber pipe content can cool down by sensible heat only instead of latent heat, so the temperature will drop more swiftly and the heat losses will drop accordingly. But in the same time, this should be done carefully to avoid large level increase or condensation of steam in the drum. Figure 6.18 shows that the flashing effect disappeared with this new control, which had been implemented in April 2016, and hence the saturated steam inside the drum does not condense quickly, as the measured pressure stayed almost constant overnight, see figure 6.26.

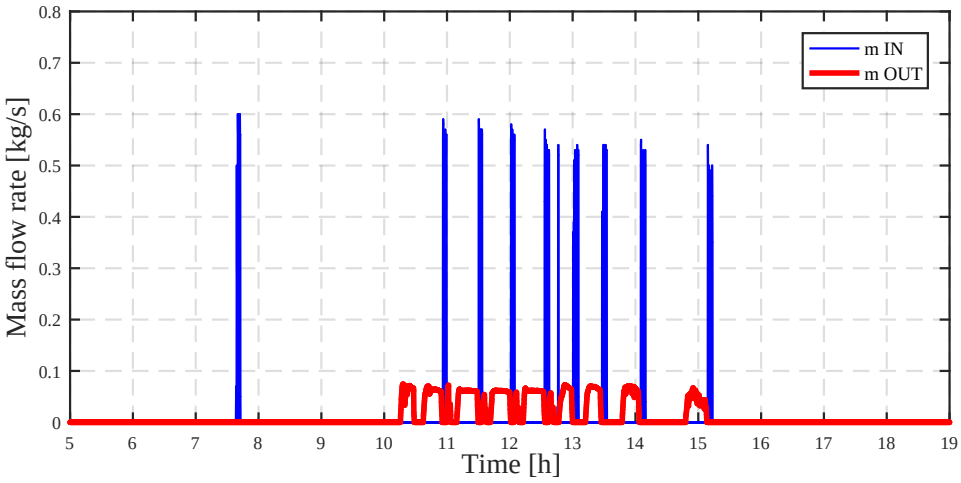

Figure 6.19: Level drum variation of the 2015/12/25

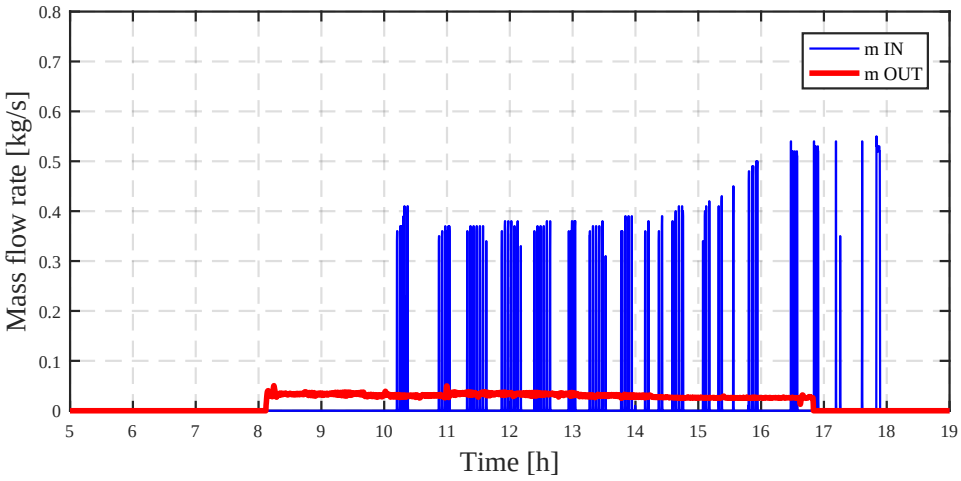

Figure 6.20: Level drum variation of the 2016/07/03

The third of the four observations show a strong impact on level variation of an inaccurate feed-in mass flow rate control. Especially in winter (see figure 6.17), due to a low pressure in the solar system and comparatively lower solar steam generation, it is important to feed a smaller quantity of mass flow rate, see figure 6.19. Because of a too high feed water flow rate, the evaporation starting point in the absorber pipes moved strongly in the solar field whenever the feed water pump was turned on or switched off, leading to non-intuitive large level variations in the drum (ie. initial level decrease when feed water pump is activated). In fact, water is fed to the system to increase the drum level and balance the steam delivered but a too

high mass flow rate would firstly reduce the drum level. This issue is negligible in summer as the solar system pressure is higher which leads to lower mass flow rates in the biphasic piping sections, and as the solar gain is higher, the evaporation start point in the solar field is much less affected. This issue could technically be solved by either improving the control of feed water mass flow rate to match the solar steam generation and system pressure or by integrating a mixing vessel to smooth the temperature variation of inlet water into the solar field.

And lastly the fourth observation was a level increase, when the first steam of the day is delivered at the steam exit valve to the user's steam grid. This non-intuitive effect was expected as the fast pressure decrease leads to flashing inside the solar field, which drives liquid water from the solar field to the drum and hence increases the liquid level inside the drum.

6.4.5 Daily flow pattern analysis

The flow pattern analysis is crucial in DSG plant where possible harmful conditions could appear such as stratified or dry-out flow patterns. In fact, they can cause thermal stress on the absorber tube, see section 2.4.1 for more detailed. This analysis would be supported by a numerical model as no flow pattern sensor has been installed on the real plant.

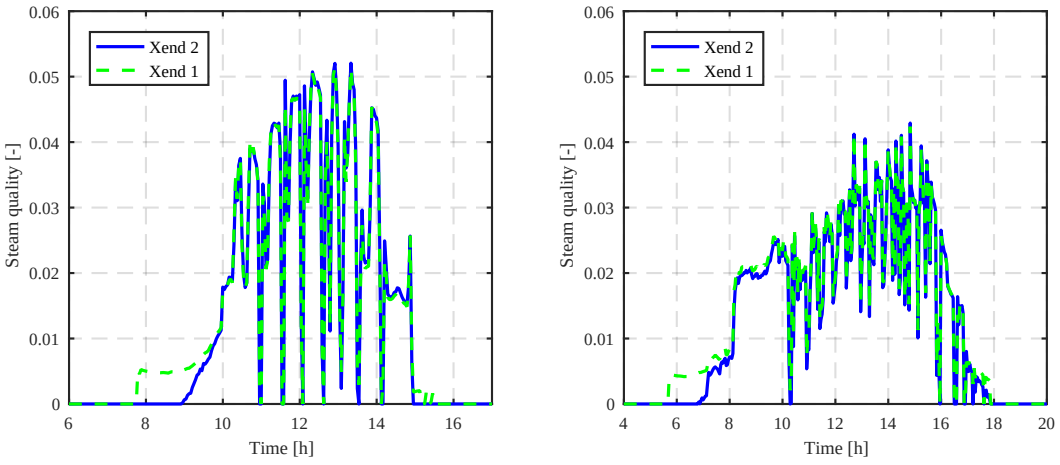

Figure 6.21: Final steam quality on 2015/12/25 (left) and on 2016/07/03 (right).

To determine the flow pattern within the absorber, the correct steam quality should be figured out. The expected monitored steam quality, x_2, is calculated

based on measured pressure P5, which is the pressure sensor between the two solar fields, and on the simulated specific enthalpy calculated with the numerical Model 1. This modified steam quality is analyzed at the absorber outlet, called Xend2, and compared to the simulated steam quality, Xend1. Figure 6.21 shows that the steam quality based on measured pressure is positive for a shorter period, due to pressure distribution error during start-up and shut-down periods, described in the previous section 6.4.3. This fact is coherent with the level variation analysis, which predicted steam in the solar fields during start-up L_{Sim}, whereas monitoring data indicate liquid water L_{Meas}.

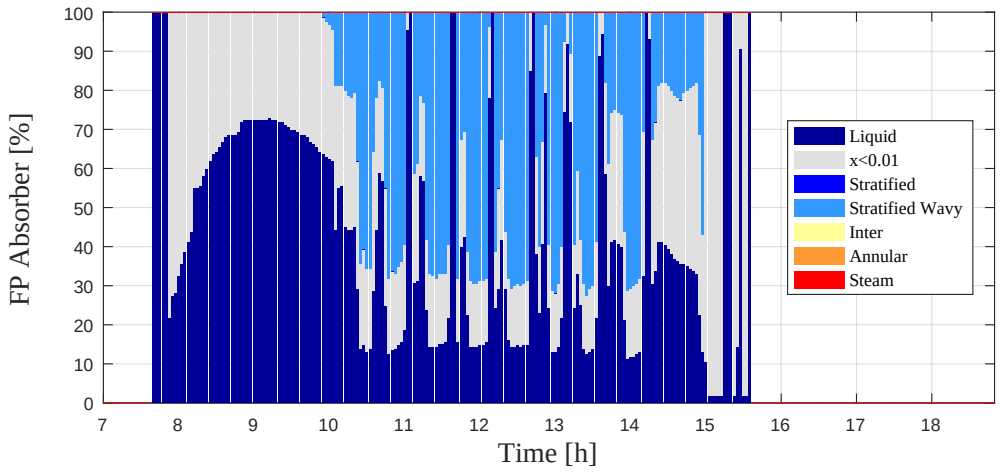

Figure 6.22: Flow pattern distribution along the receiver on 2015/12/25 based on simulation

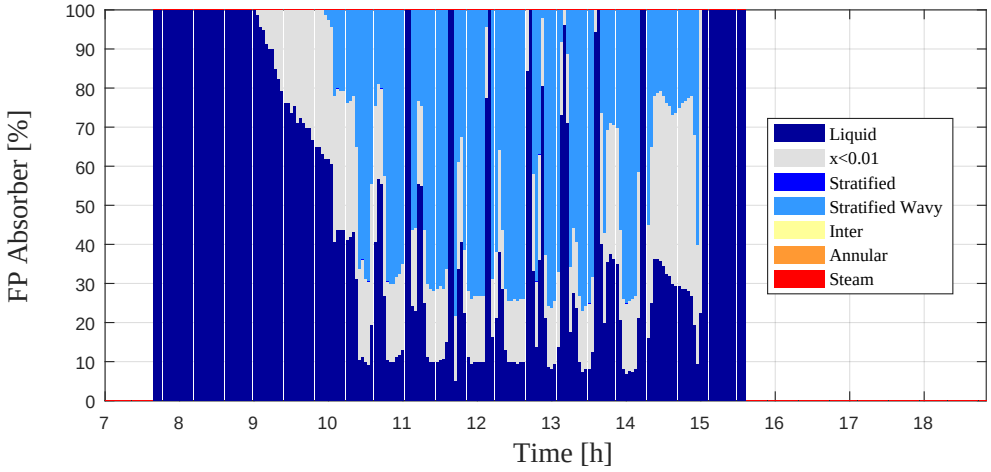

Figure 6.23: Flow pattern distribution along the receiver on 2015/12/25 based on monitoring data

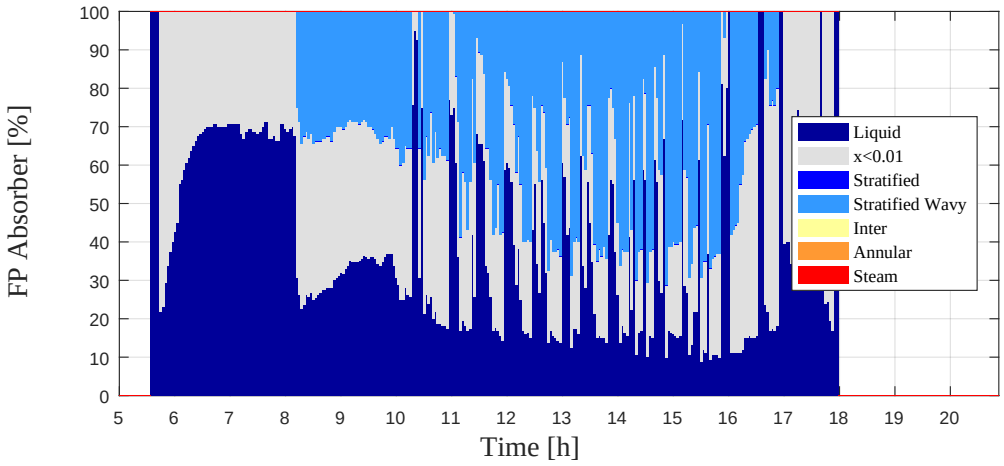

Figure 6.24: Flow pattern distribution along the receiver on 2016/07/03 based on simulation

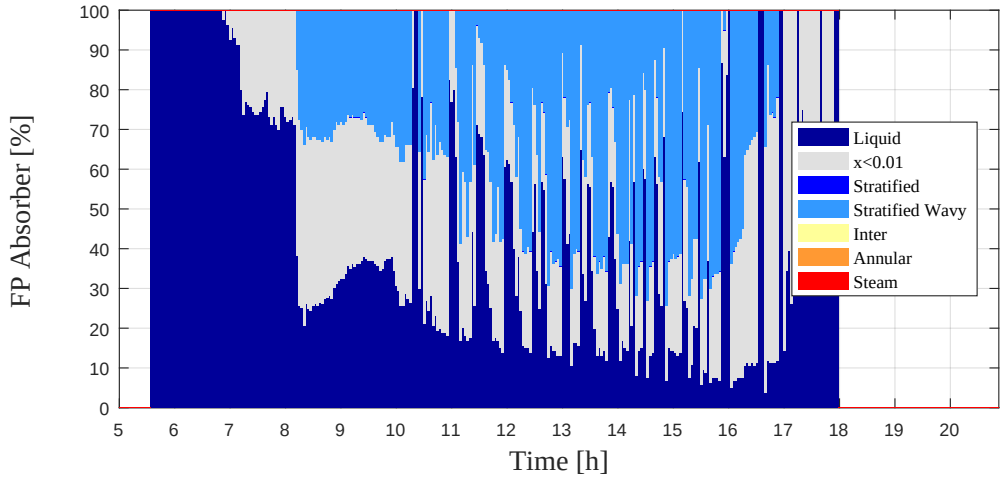

Figure 6.25: Flow pattern distribution along the receiver on 2016/07/03 based on monitoring data

The flow pattern distribution defined in section 4.5.1.3 has been applied for each time step of the simulation using the absorber outlet temperature as input of the *modified KTF* correlations [79], [89]. Two *modified KTF* correlations are defined. The first one used simulation output whereas the other one used the measured data of the outlet solar field temperature sensor, T6. Then, based on the specific mass flow rate and steam quality, simulated x_1 for the first case and x_2 for the second case, the flow pattern of each node is obtained.

In figures 6.22, 6.23, 6.24 and 6.25 the flow pattern conditions along the absorber pipes during the whole active mode is shown. As expected, start-up and shut-down

present strong deviations, whereas in the time between, during steam production, the results are consistent. For the first opening of the steam exit valve to the user's steam grid, at 10:10 am of 25^{th} and at 08:05 am of the 3^{rd}, a flashing appears inside the absorber as described in the fourth point in the level analysis. They show that the first 10% of the solar field is always liquid whereas the rest experiences mainly stratified wavy flow pattern. The main result of this flow pattern analysis is that the harmful flow patterns, as stratified and dry out, described in [71], are successfully avoided during the whole days which could result in a longer lifetime of the solar fields. They also show the impact of feed water mass flow, where the evaporation start point moves, and the absorber on 25^{th} of December is completely filled up by liquid water, everytime when the feed water pump is switched on, and the expected weaker effect on 3^{rd} of July, when the solar collector power is higher in summer and hence the movement of the evaporation start point is reduced. Rapid movement of the evaporation start point downstream could destabilize the DSG operation, as the outlet mass flow rate is significantly lower than at the inlet. In fact, the last section of the absorber would have a low mass flow rate with high linear irradiation thus some harmful flow pattern as stratified pattern or dry-out could appear. For the size of a system as the one under consideration, this is not an issue, because the biphasic region can be filled very quickly by the recirculation pump, less than 2.5 min in the worst case. Based on the dynamic Model 2, a more detailed analysis is done in the section 7.3. The impact of fast moving of evaporation start point is quantified for larger system.

6.4.6 Pressure analysis

The daily pressure analysis shows a strong pressure decrease during start-up, when the cold water from the solar fields is mixed with the thermal equilibrium water of the drum. The steam condenses until reaching a new equilibrium. The measured pressure drop has been 2.0 bar in 14 min on 25^{th} of December, and with 1.7 bar in 13 min slightly smaller on 3^{rd} of July. The expected pressure drop is calculated using perfect mixing assumption, as shown in section 2.3.3. The ratio $\frac{V_{drum}}{V_{abs}}$ equals to 5.3 in the specific case of RAM plant and the initial conditions are summarized in table 6.7. By using, stand-by model to calculate the average

Table 6.7: Plant condition before start-up

Initial Condition	***Unit***	***2015/12/25***	***2016/07/03***
$T_{av,rec}$	°C	63.2	66.5
L_{drum}	m^3	1.3	1.45
P_{drum}	bar-a	4.4	3.7

temperature of the recirculation loop, pressure drops of 1.9 bar on the 25^{th} and of 1.2 bar on the 3^{rd} are obtained. As expected the pressure drops is slightly smaller in summer and this methodology slightly underestimate the pressure reduction as metal inertia of the recirculation loop is neglected. Two solutions to avoid this strong pressure drop are thinkable. One solution would be to by-pass the steam drum during this warm-up period. The second solution would be a re-design of the steam drum, so that the incoming colder liquid water from the solar field during start-up does not mix, but rather stratify on the bottom of the drum instead.

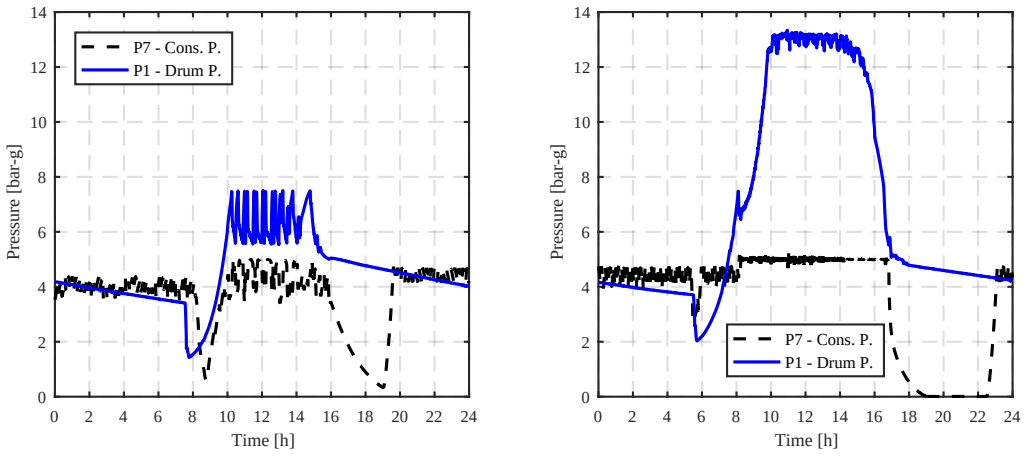

Figure 6.26: Pressure variation, left: 2015/12/25 and right: 2016/03/07

For both of the days, which have been analyzed in detail, the steam boiler is shut down during the day time and the steam is provided only by the solar system. Also in both cases, the user's steam grid pressure stays in the pressure requirement range, despite variations of the solar system pressure due to the gliding pressure design of the steam drum as 15-min steam accumulator. In summer, the user's grid pressure variations are reduced, when the solar system is used, compared to operation by the conventional steam boiler. Whereas in winter, the observed drum pressure variation would not allow the same accuracy. This pressure variation in

winter was caused by strong temperature variations at the inlet of the solar field, due to control of feed water mass flow rate, as described in section 6.4.4. The mixing tank at the inlet of the pump or a precise control of feed water mass flow, as described in section 6.4.4, would smooth the pressure variations in winter to reach the same stability as in summer. But it must be stated, that the pressure fluctuations in winter have never been problematic, since the pressure fluctuations during operation of the conventional steam boiler are even higher.

Chapter 7

System Optimization

7.1 Objectives

The overall objective of this chapter is to apply the three numerical models, developed in chapter 4, to improve the solar DSG design and control strategy for the specific application of industrial process heat. The discussion consists of different levels of optimization:

- The first one focuses on the methodology to design the solar field layout (parallel vs series, ideal mass flow rate) applied to a MW plant based on Model 1.

- The second and third optimizations are used for design purposes and control strategy optimization and they focus on unexpected behaviors highlighted in the case study presented in chapter 6:

  - the second one analyzes the effect of fast moving evaporation start point impact with the numerical Model 2. It highlights possible harmful situations in some specific conditions at the absorber outlet when the inlet absorber temperature decreases suddenly; Two simple indicators are defined as benchmarks for these phenomena.

  - and third one analyzes how night heat loss can be reduced with an improved control strategy. It consists in injecting cold water in the evening in the recirculation loop to push the hot water in the well insulated steam drum. The improvement quantification is done with Model 3.

7.2 Solar field optimization: Example of MW plant

The optimization process of a MW solar DSG plant is presented hereafter, based on numerical Model 1, where the inputs of active model are arbitrary fixed. This section gets inspiration from Odeh's analysis, a thermal-hydraulic study of solar DSG for CSP power plant [[67], [35], [68], [69]], with relevant change in the boundary conditions: industrial process heat application and use the *modified KTF* correlation. Results have been published in 2016 [71]. The plant at issue is a second case study: the generated steam is integrated in the existing saturated steam line at 20 bar-g of a tire manufacturing facility in Brazil. The solar field is made of 16 Linear Fresnel Reflectors with vacuum absorber, with an overall collector surface of 2400 m^2. The technical characteristics of the solar plant, which are the starting point of the optimization process, are reported in table 7.1.

Table 7.1: Solar DSG parameters - 1 MW case study

Name	***Z*** *[m]*	***L*** *[m]*	***D*** *[mm]*	ζ *[-]*	$\boldsymbol{U}_1$ *[kW/K.m]*	$\boldsymbol{U}_4$ *[kW/K⁴.m]*
Liq1	-6.0	10.0	70.3	55.0	1.2E-03	0
Liq2	-6.0	50.0	70.3	20.0	1.2E-03	0
Liq3	0.0	10.0	70.3	10.0	1.2E-03	0
CS1	0.0	190.0	66.0	0.0	1.8E-04	8.2E-12
Int1	0.0	7.5	56.3	5.0	1.6E-04	0
CS2	0.0	190.0	66.0	0.0	1.8E-04	8.2E-12
Bi1	0.0	10.0	107.7	10.0	1.5E-03	0
Bi2	0.0	50.0	107.7	30.0	1.5E-03	0

The optimization process of a MW solar DSG plant has the objective to define:

- the optimal recirculation mass flow rate;
- the best solar field layout (series vs parallel);

The approach used in this section is the following. First, characteristic scenarios are defined to apply the optimization. Then, the criteria to define an optimal mass flow rate are discussed. And finally, the optimization analysis is applied for two solar plant layouts: series and parallel rows.

7.2.1 Scenario selection

A methodology to select the operating conditions to be analyzed is proposed hereafter. The ambient temperature and the feed-in water temperature are set constant, respectively 25 °C and 105 °C. The other three inputs, linear heat flux, feed-in mass flow rate and pressure are defined according to four scenarios defined in table 7.2. In the first extreme scenario, hereafter called Scenario A, the highest steam quality is achieved. This occurs under high irradiation when the specific enthalpy at the absorber inlet is close to saturation condition, ie. the recirculate water from the steam drum is not mixed with cold water. This phenomena could happen during start-up operation at noon. Indeed, during the start-up no feed-in water is supplied to the loop, thus the fluid at the inlet of the absorber tubes is the saturated liquid from the drum.

Then the next three scenarios (B, C & D) are obtained using different irradiations when saturated steam is supplied to the process line, and an equivalent mass flow rate of water is fed into the recirculation loop. This equivalent mass flow rate is approximated based on eq. 7.1. Scenario B represents the full load scenario and Scenarios C and D represent part load conditions at 80% and 50% of the full load.

$$\dot{m}_{in} = \frac{\dot{Q}_{in}}{h_{sat,g}(p) - h_{in}} \tag{7.1}$$

where $\dot{m}_{in}$ is feed-in mass flow rate [kg/s], $\dot{Q}_{in}$ is the solar gross heat gain [kW], $h_{sat,g}$ the specific enthalpy of the saturated steam [kJ/kg], h_{in} is the specific enthalpy of the feed-in water[kJ/kg].

The pressure of the DSG plant fluctuates during the day due to the difference between the steam generation and the real load. Three different running pressures are defined: maximum (26 bar-a), nominal (21 bar-a) and minimum (15 bar-a). The saturated steam density is reduced with low pressure and it leads to higher pressure drops. In order to characterize the maximum pressure drops the scenario A is performed at the minimum pressure. The other three scenarios are defined to characterize the nominal condition thus the nominal pressure is used for these scenarios. The maximum pressure condition is less restrictive for pressure drops calculation and is not used to define the four scenarios.

Table 7.2: Operating conditions (Inputs of Model 1) for the four scenarios

Scenario	***A***	***B***	***C***	***D***
Pressure	Min. pressure	Nom. pressure		
Linear heat flux	100%	100%	80%	50%
Feed-in mass flow rate	0	$\sim \dot{m}_{out}$, see eq 7.1		
Ambient temperature	25 °C	25 °C		
Feed-in water temperature	105 °C	105 °C		

7.2.2 Optimal mass flow rate definition

For a given boundary condition, the choice of the recirculation mass flow rate has an impact on the overall pressure drops and on the flow pattern in the boiling zone. The optimal mass flow rate is set to achieve the following objectives:

- Pressure drops has to be minimized. The pressure drops has to be minimized mainly in order to maximize the stability of the plant for a chosen pressure rating.

  First, the pressure rating of the hydraulic components has to be chosen. The first requirement is to be at least higher than steam line process pressure. Then, the cost/benefit optimization consists in determining how much should be the differences between the steam line process pressure and the condition of full load. In fact, on the one hand an upgrade of the pressure rating is very costly but one the other hand a high maximum pressure of the steam drum allows a better stability of the system.

  Once the pressure rating is selected, the pressure range of the steam drum (ie. difference between the minimum and maximum running pressure) should be maximized. The minimum drum pressure is defined as the minimum required pressure to be able to feed steam into the process steam line. Whereas the maximum drum pressure is defined based on the pressure rating and on the pressure drops from the pump to the drum. In fact, the outlet pressure of the pump (the highest pressure of the recirculation loop) is the most restrictive condition for pressure rating. This value is defined backwards starting from maximum drum pressure plus the expected pressure drops from the pump to the drum. Thus, for lower pressure drops an higher maximum drum pressure

could be used to respect the pressure rating at pump outlet. This is the main reason why the pressure drops should be minimized.

- Harmful flow pattern has to be avoided. The originality of this methodology is to complete the optimization process with a flow pattern analysis. In fact, some of the flow patterns, such as stratified, dry-out and in some extent wavy stratified, generate a thermal stress on the absorber, see section 2.4.1.

  The intermittent flow pattern avoids this thermal stress but it could generate some mechanical stress due to vibration and water-hammer-like phenomena. Based on the literature review of mechanical instability of two-phase flow, Miwa shows that slug and churn flow regimes have the strongest fluctuation compared to other flow regimes [55]. Therefore, he recommends to minimize slug flow pattern, when operating under two-phase flow condition. In order to diminish the collision effect, sharp-tuning elbow section should be avoided. Thus, a suitable anti-vibration procedure should be elaborated to diminish the vibrations on the weakness point of the solar field.

  The flow pattern optimization should maximize the annular flow pattern as it cools down the absorber and avoid any water-harmer effect. This optimization is applied based on flow pattern description for the whole absorber at different mass flow rates, eg. figure 7.2. This figure represents the local flow pattern for each discretized volume of the absorber.

7.2.3 Solar field layout - series configuration

Once the number of Linear Fresnel Reflectors (LFR) has been defined, the solar field layout has to be optimized: as mentioned above, the pressure drop and electrical consumption has to be minimized and harmful flow pattern avoided. For a MW solar plant, there are two alternatives for the solar field layout: the series configuration (all absorber connect in a unique loop), or the two parallel rows, defined in the next section 7.2.4.

Mass flow rate is a critical parameter and needs a specific optimization, particularly in a solar system where operating conditions are variable. In the present analysis, a lower steam quality is targeted than the value suggested by Eck et al.

(0.7-0.8) [108]. Low steam quality means a high flow rate, so the risk of harmful flow patterns - stratified and dry-out - can be avoided. On the other hand, an excessive mass flow rate leads to large electricity consumptions and to large liquid pipe diameter. At high flow rate the intermittent and wavy-stratified are the main flow patterns.

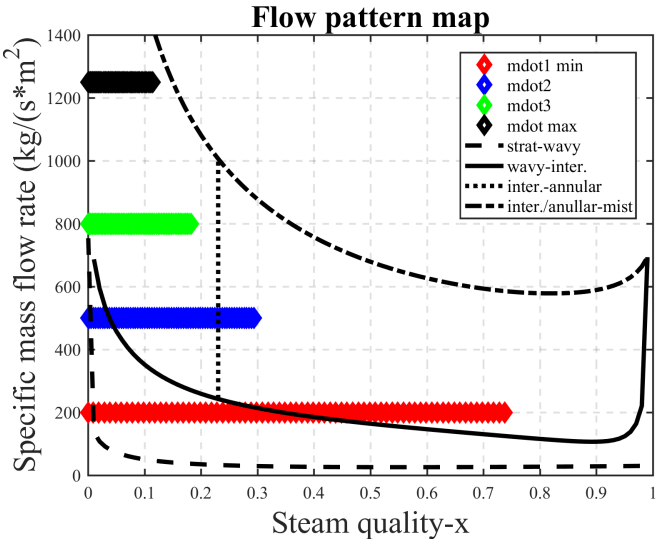

Figure 7.1: Average fluid conditions for each finite volume of the absorber (diamond) for Scenario A on *modified KTF* flow pattern map

The optimization process to find the suitable mass flow rate of the second case study has been done for specific mass flow rate in the range 200 kg/s.m^2 - 1250 kg/s.m^2, ie. 0.68 kg/s - 4.28 kg/s, under constant boundary conditions (irradiation, pressure and diameter) in the four scenarios defined above.

The *modified KTF* map can effectively show the flow pattern according to the specific mass flow rate and the steam quality. An example, related to Scenario A, is presented in figure 7.1. Each diamond represents a section of the absorber and four specific mass flow rates are analyzed. In steady state condition, the specific mass flow rate is constant over the whole absorber and the steam quality increases from 0 at the inlet to the final steam quality at the outlet of the absorber (eg. 0.75 for a specific mass flow rate of 200 kg/s.m^2 in scenario A). Under constant boundary conditions, the final steam quality is function only of the mass flow rate. It increases with low specific mass flow rate.

Nevertheless, to find the suitable mass flow rate another representation is used. The vertical axis represents the absorber length in percent, where water inlet is at

0% and absorber outlet at 100%. Each vertical bar is done for a fixed specific mass flow rate (represented on the horizontal axis), figure 7.2.

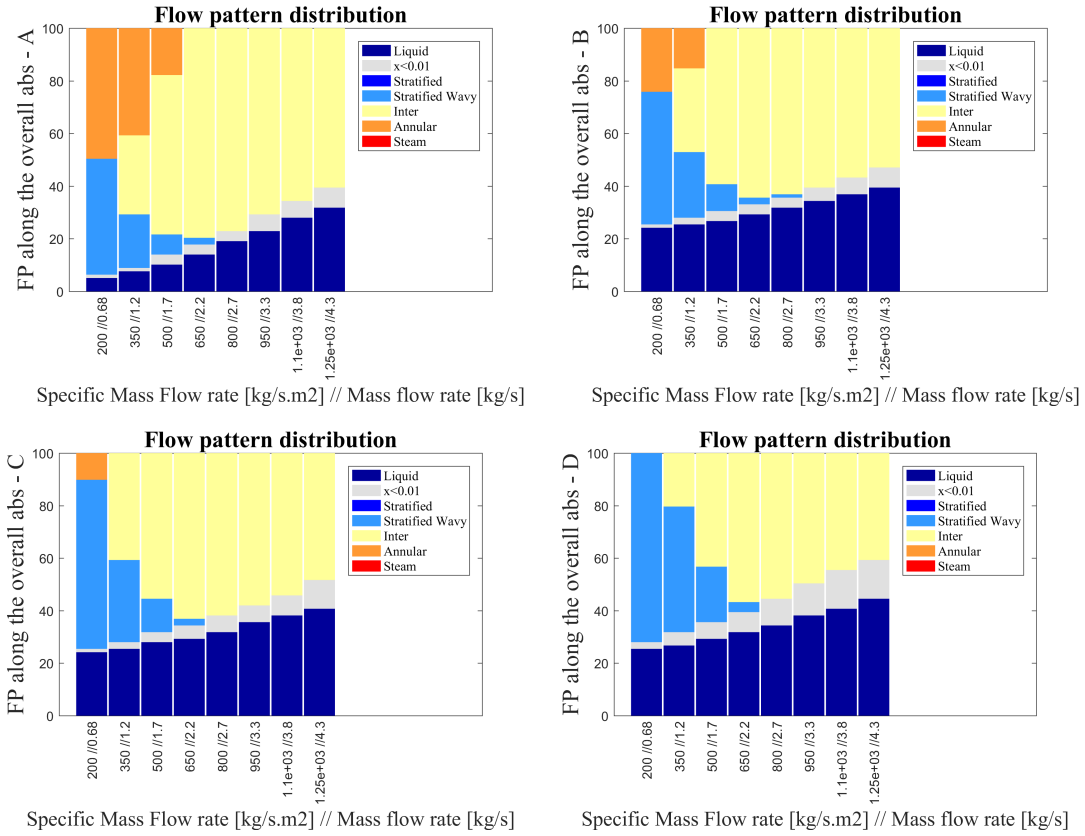

Figure 7.2: Flow pattern distribution in the four scenarios for the series configuration

Based on the analysis of flow pattern, an optimal range for the mass flow rate rather than an optimal value has been defined. In scenario A, annular flow pattern is obtained at the absorber outlet for a specific mass flow rate from, 200 to 500 kg/s.m^2. However, in this range, the wavy stratified flow pattern is large. Thus, to maximize the annular flow pattern, the wavy stratified flow pattern region has to be increased. In scenarios B and C, the annular flow pattern region appears for a lower mass flow rate range. However, the wavy stratified region at 200 kg/s.m^2 is more than 50% of the overall absorber, thus 350 kg/s.m^2 would be preferred. In scenario D, the annular region could not be reached and the optimal specific mass flow rate is in the range 350-650 kg/s.m^2. Thus, the common optimal specific mass flow rate for each scenario is in the range 350-500 kg/s.m^2, ie. 1.2-1.7 kg/s. In this range, the superheated steam and stratified flow pattern are avoided. In order to minimize the pressure drops and electrical consumption, the lowest mass flow rate should be used thus 1.2 kg/s would be preferred. Moreover, the liquid region increases with the

mass flow rate increase. This is due to higher absorber inlet pressure thus higher liquid saturated specific enthalpy. Scenarios B, C and D have a high liquid region, since "colder" water is fed to the system to balance the steam generation.

7.2.4 Solar field layout - two parallel rows

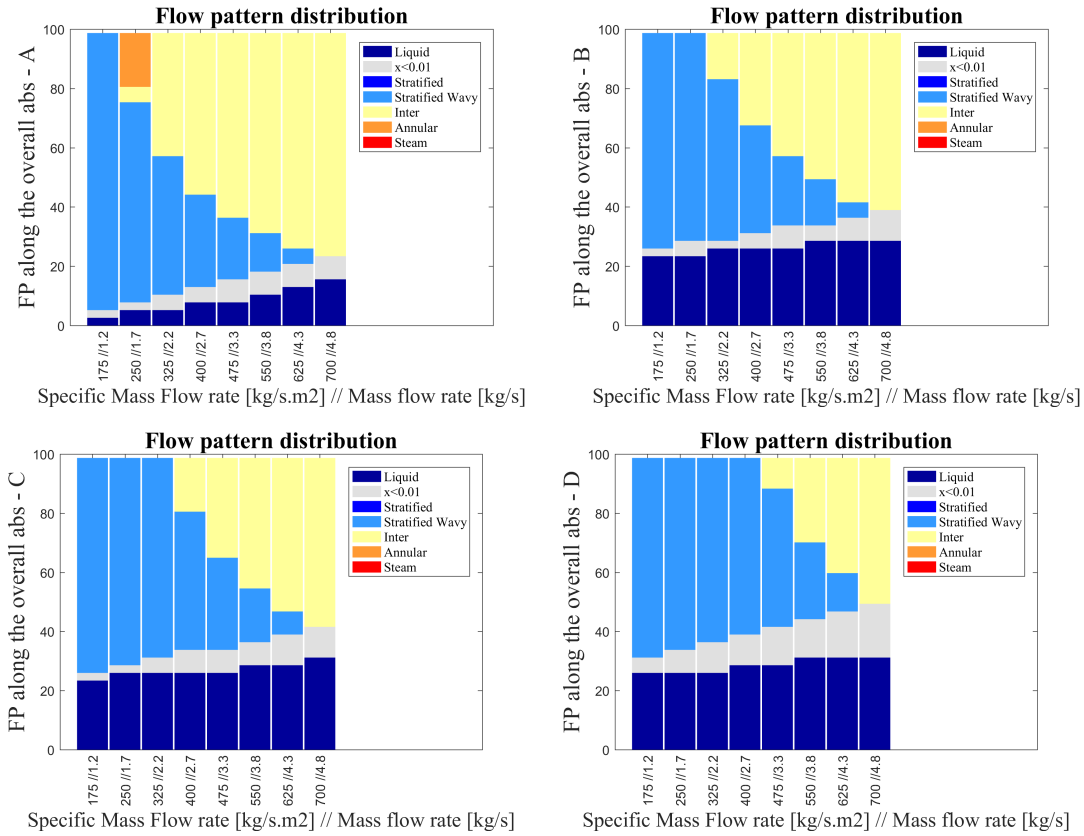

Figure 7.3: Flow pattern distribution in the four scenarios for parallel rows configuration

As presented in previous section 7.2.3, for a MW solar plant two alternatives solar field layout exist: the series configuration (presented above) and two parallel rows. The latter one has the objective to minimize the pressure drops inside the absorber at equivalent pump mass flow rate. However, the instability of transient flows of evaporating fluid in parallel pipes must be considered [41]. Since for asymmetric heating the mass flow rate is larger in the absorber with smaller heating [43], the steam quality unbalance is emphasized between the two lines. As a consequence more complex control systems can be required.

Hereafter, a similar methodology to the one for series configuration is used to find the optimal range analysis, in which the four scenarios presented above are

analyzed. The steady state analysis is assuming that the pump mass flow rate is divided fairly between the two rows and an uniform heat flux is used for the two strings. Figure 7.3 shows the flow pattern distribution analysis for the four scenarios in parallel configuration

In the present case study, the mass flow rate has to be drastically increased to avoid a large share of stratified wavy pattern. Moreover the annular flow pattern cannot be obtained. The optimal mass flow rate is in the range of 475-625 kg/s.m^2, ie. a mass flow rate of 3.3-4.3 kg/s at pump outlet. In order to minimize the pressure drops and electrical consumption, the lowest mass flow rate should be used thus 3.3 kg/s would be preferred. Thus, to maintain a satisfactory flow pattern distribution, the optimal mass flow rate in parallel configuration (3.3 kg/s) is higher than the one in series configuration (1.2 kg/s). So the expected pressure drop decrease due to the split of the mass flow rate is partially balanced by an higher mass flow rate at the pump outlet. Figure 7.4 shows how the overall pressure drops is calculated in the specific case of scenario A and table 7.3 summarizes the overall pressure drops for the two optimal mass flow rates.

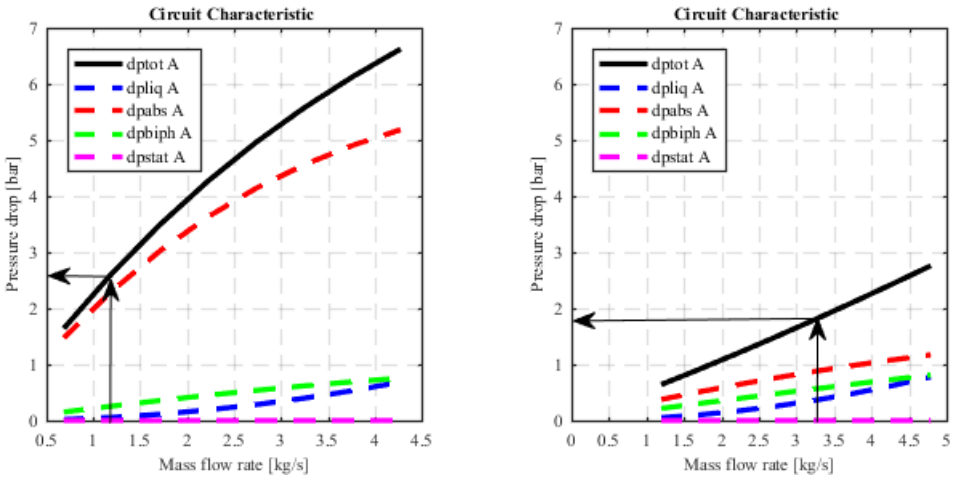

(a) (b)

Figure 7.4: (a) Characteristic curve of the series configuration. (b) Characteristic curve of the parallel configuration.

The overall pressure drop is composed by four sections: the liquid pipe (liq) from the Drum to the absorber inlet, the absorber (abs) from the inlet to the outlet of the absorber, the biphasic pipe (biph) from the absorber outlet to the drum inlet and finally the static pressure drops which is null for this second case study

Table 7.3: Overall pressure drops for the two solar field configurations under optimal mass flow rate.

Scenario	***A***	***B***	***C***	***D***
Serie at 1.2 kg/s	2.6 bar-a	1.4 bar-a	1.2 bar-a	0.86 bar-a
Parallel at 3.3 kg/s	1.8 bar-a	1.1 bar-a	1.0 bar-a	0.84 bar-a

since the absorber is at the same level than the steam drum. Figure 7.4 shows the contributions of each section for the example of scenario A for the series and parallel configuration. This analysis highlights that the contribution of liquid piping pressure drop is lower for the series configuration at optimal mass flow rate condition ($< 3\%$) than the one of parallel configuration which represents 20%. Thus pipe diameter could be downsized to reduce the investment cost in the series configuration.

To summarize this solar field layout analysis, three points are highlighted and justified the use of series configuration for a 1 MW plant :

- higher mass flow rate is required in the parallel configuration in order to maintain a satisfactory flow pattern distribution;
- overall pressure drop is reduced in the parallel configuration but less than expected due to higher optimal mass flow rate;
- higher investment costs for parallel configuration are expected due to higher piping cost and complex control systems.

7.2.5 Additional results of optimization work

7.2.5.1 Numerical model simplification.

In the numerical model here presented, the heat transfer rate is calculated for each node and based on specific correlations according to the fluid condition. Given the solar radiation, the heat transfer rate determines the temperature difference between the wall and the fluid. A higher wall temperature means higher thermal losses. Anyway, thanks to the effective insulation of absorber tubes, the impact of the increase of wall temperature on overall losses is limited except for dry-out region. Thus, for design purposes, the Model 1 could be simplified by using a simplified heat transfer rate for the whole absorber.

In the specific case of this plant configuration with a mass flow rate of 1.2 kg/s in the scenario B, the internal heat transfer rate is around 4 kW/K m^2 for sub-cooled water at the absorber inlet and increases along the absorber up to 12 kW/K m^2 at the absorber outlet. The simplification to use the heat transfer rate correlation of liquid flow in the whole recirculation loop has been investigated. By using a lower mass flow rate (approx 4 kW/K m^2) for the whole absorber, the average wall temperature and heat losses increase. Nevertheless, this heat loss increase is negligible, since the overall net solar gain is underestimated just by 0.05%. Thus, to use a simplify form of the heat transfer for the whole absorber strongly reduce the computational effort and at the same time does not affect strongly the system performance.

A similar simplification has been applied for the Model 2, where it has been chosen a constant value for the heat transfer rate of 10 kW/K m^2 in the range of [4 kW/K m^2; 12 kW/K m^2].

7.2.5.2 Variable absorber tube diameter to minimize the harmful flow pattern.

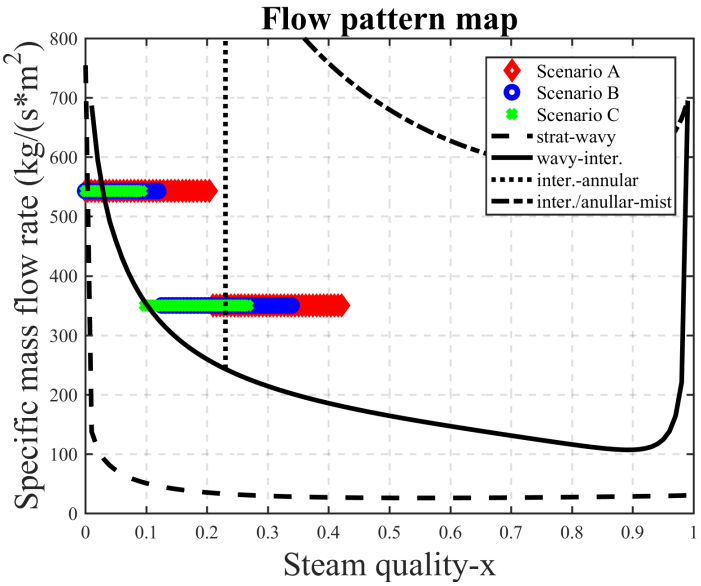

Figure 7.5: *modified KTF* map with variable diameters

As shown in Figure 7.2, the tube length where wavy stratified flow pattern occurs cannot be reduced by varying the flow rate without decreasing also the length of annular flow pattern. A way to overcome this problem can be the use of different absorber tube diameters, in order to increase the specific mass flow rate just in the

first section of the solar field. For example, with a mass flow rate of 1.2 kg/s, if the diameter of the first 200 m of absorber tubes is reduced by 20%, from 53 mm to 66 mm, the tube length affected by wavy stratified pattern is strongly reduced in the four scenarios, see table 7.4. For instance, in scenario A the wavy stratified flow pattern region decrease from 20% to 1% with variable pipe diameter. Nevertheless, this diameter reduction increases the pressure drops between 26% to 46% which reduces pressure range of the steam drum thus reduce slightly the stability of the system, see table 7.4.

Moreover, this concept is a theoretical consideration and the technical application of this concept has not been considered.

Table 7.4: Effect of smaller diameter (53 mm) for the first 200m of the solar field.

Scenario	***A***	***B***	***C***	***D***
WS [%]: D. const. at 1.2 kg/s	20%	25%	31%	48%
WS [%]: D. var at 1.2 kg/s	1%	3%	8%	31%
dp rec variation	+46%	+26%	+33%	+28%

7.3 Moving Evaporation start point impact

A transient simulation, based on Model 2, is presented in this section. The objective is to analyze fast movement of the evaporation start point inside the absorber. More precisely the purpose is to study the movement generated when the two-phase region into the absorber is reduced due to fast temperature decrease at the inlet of the absorber tube. This phenomena is of crucial importance for solar DSG as a fine control of the feed-in water pump is an issue due to very large operation condition. For instance it could happen condition with low mass flow rate and high hydraulic head or vice versa (ie. high mass flow and low hydraulic head). Thus, an non accurate feed-in control of the mass flow rate could generate a fast temperature decrease at the absorber inlet. This fast movement of evaporation start point leads to low mass flow rate in the two-phase flow region thus high specific enthalpy could be reached and could generate harmful conditions at the absorber outlet.

This non-intuitive effect has been discussed by Eck et al. in the case of superheating generation with a local solar irradiation decrease [[16], [59]]. In fact, by

shading a mirror in the evaporator region the expected result is to see a temperature decrease at the superheating region exit whereas it has been observed an increase of temperature during transient conditions.

In this work an approach in three steps to tackle the problem through simulation is presented:

- First, a qualitative analysis is performed to define two simple correlations in order to indicate if harmful conditions could appear.

- Then, the monitoring data of RAM plant is used as boundary condition. The outlet specific enthalpy and mass flow rate are calculated for the two selected days: the 25^{th} of December and the 3^{rd} of July.

- Finally, the analysis is extended to a 1 MW solar system. The transient responses for a 40 °C decrease of the inlet temperature is analyzed and potential harmful conditions are highlighted. An optimization scenario is proposed by using a mixed tank at the inlet of feed-in water to smooth the temperature variation and protect the absorber to high specific enthalpy condition.

7.3.1 Qualitative analysis

Within the absorber, rapid movement of the evaporation start point downstream could destabilize the DSG operation, as the outlet mass flow rate is significantly lower than the inlet one, as illustrated in figure 7.6. This phenomenon could be generated by a linear irradiation decrease (first case) or inlet temperature decrease (second case) :

- This first case has been analyzed by Eck et.al for superheating steam [[16], [59]]. In the case of industrial application, this phenomena is not relevant as no harmful condition is expected. In fact, for industrial sector, the solar fields are smaller than for CSP. Thus, moving cloud (which generates sudden irradiation decrease) covers a large part of the solar field thus we could expect that the last section of the absorber has a low mass flow rate with low linear irradiation. The latter condition does not generate any harmful condition.

- Whereas for the second one, the risk of having harmful condition is higher as low mass flow rate and high heat flux could generate high specific enthalpy at the absorber outlet. Low mass flow rate and high specific enthalpy characterized harmful condition such as stratified or dry-out flow patterns. This phenomena is not intuitive as we could expect that a decrease of the inlet temperature leads to a decrease of the specific enthalpy at the absorber outlet. However, during transient condition, this temperature decrease at the absorber inlet could generate a specific enthalpy increase.

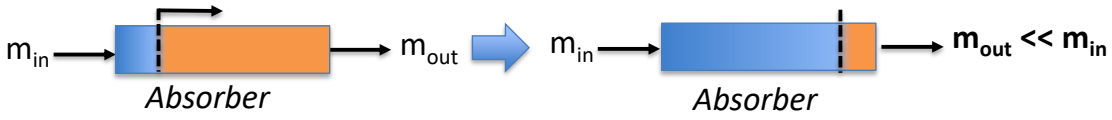

Figure 7.6: Moving evaporation start point *(blue liquid and orange two-phase mixture)*

The objective of this section is to understand if and when a large temperature variation could generate harmful conditions. In order to understand when this phenomena could appear, three novel indicators have been defined: ΔL, τ_w and τ_m. The evaporation start point moves toward the pipe outlet when the inlet temperature decreases. The displacement length of evaporation start point before and after the step change is defined as ΔL, see eq. 7.2. In the volume generated by movement of evaporation start point ($\Delta L \cdot A$), the two-phase mixture is replaced by liquid water. Thus, the mass of the finite volume increases, and the inlet mass flow rate is higher than the outlet mass flow rate. τ_w defines the minimum required time lapse to fill this volume, ie. when the outlet mass flow rate is null, see eq. 7.3. The internal energy of metal absorber decreases in the sub-cooled region during this transition period. This energy variation causes the increase of the heat flux transmitted to the fluid. Thus, the transition boundary does not move instantaneously to the steady state condition and the outlet mass flow rate is not null but only reduced. Nevertheless, the metal inertial is low. To quantify this phenomena, the metal temperature is calculated. If thermal loss is neglected then the energy balance equation of metal absorber can be solved as a differential equation of first order, and we obtain the eq. 7.4. The decay characteristic time, τ_m, is defined as eq. 7.5. Thermal equilibrium is

reached after $5\tau_m$ as the metal temperature equals 99.3% of the final value.

$$\Delta L = \frac{\dot{m}_{rec} \cdot C_{p,w} \cdot \Delta T_w}{\dot{Q}_{in,lin}} \tag{7.2}$$

$$\tau_w = \frac{A \cdot C_{p,w} \cdot \Delta T_w \cdot \rho_{w,l}}{\dot{Q}_{in,lin}} \tag{7.3}$$

$$\theta_m(t,x) = \left[T_{w,sat} - T_w(x) + \frac{\dot{Q}_{in,lin}}{\pi D h_{conv}} \right] \cdot e^{\frac{-t}{\tau_m}} + T_w(x) \tag{7.4}$$

$$\text{with } \tau_m = \frac{C_{p,m} \cdot \rho_m \cdot A_m}{\pi D \cdot h_{conv}} \tag{7.5}$$

ΔT_w is the water inlet temperature decrease [°C], T_w is the water temperature [°C], θ_m is metal temperature [°C], $\dot{m}_{rec}$ is the mass flow rate at the absorber inlet [kg/s], $C_{p,w}$ is the specific capacity of the liquid water [kJ/kg.K], $C_{p,m}$ is the specific capacity of the metal absorber [kJ/kg.K], $\dot{Q}_{in,lin}$ is the linear heat flux [kW/m], $\rho_{w,l}$ is density of liquid water [kg/m^3], ρ_m is density of metal absorber [kg/m^3], h_{conv} is convective heat transfer rate [kW/K.m^2].

Hereafter, some comments on the previous equations. For a given linear Fresnel reflector and a given solar irradiation, the linear heat flux is fixed and defined as a parameter of the test condition. Thus, τ_w is a function of only one variable, ΔT_w. A higher temperature decrease at the absorber inlet would increase the time required to fill this volume. Moreover, this characteristic time is independent of the mass flow rate. τ_m is proportional to metal inertia, defined as absorber parameter, and to the convective heat transfer rate. The convective heat transfer rate calculation is complex, see section 4.4.1, but is proportional to the mass flow rate and fluid state. And finally, ΔL is function of mass flow rate and inlet water temperature variation.

High specific enthalpy at the absorber outlet is reached if a long section of the absorber has a low mass flow rate for a long period. In other words, if the two-phase region after the evaporation start point region is long and is heated for a sufficient duration significant to increase strongly the metal pipe temperature. This condition is true if $\frac{\Delta L}{L_{tot}} \ll 1$ and $\frac{5\tau_m}{\tau_w} \ll 1$. Thus, harmful condition appears for low $\dot{m}_{rec}$,

large plant size (L_{tot}) and large ΔT_w, see eq. 7.6 and eq. 7.7.

$$\frac{\Delta L}{L_{tot}} = \frac{\dot{m}_{rec} \cdot C_{p,w} \cdot \Delta T_w}{\dot{Q}_{in,lin} \cdot L_{tot}} \ll 1 \tag{7.6}$$

$$\frac{5\tau_m}{\tau_w} = \frac{5C_{p,m} \cdot \rho_m \cdot A_m}{A \cdot C_{p,w} \cdot \Delta T_w \cdot \rho_{w,l}} \frac{\dot{Q}_{in,lin}}{\pi D \cdot h_{conv}} \ll 1 \tag{7.7}$$

The indicators are calculated for the three case studies defined in this PhD work:

- DSG bench used in chapter 2,
- RAM plant defined in chapter 6
- Theoretical 1 MW plant described in section 7.2

Table 7.5: Qualitative analysis of fast temperature decrease at the absorber inlet:- 40 °C

Scenario	***DSG lab.***	***RAM plant***	***MW plant***
$\dot{Q}_{in}$ (kg/s)	2.5	3.2	3.2
$\dot{m}_{rec}$ (kg/s)	0.088	1.2	1.2
L_{abs}(m)	5.9	72	313
$5^*\tau_m$ (s)	7.5	4	4
τ_w (s)	11.3	169	169
$\frac{\Delta L}{L_{tot}}$ (-)	1.0	0.9	0.2
$\frac{5\tau_m}{\tau_w}$ (-)	0.66	0.02	0.02

No harmful condition is expected for the first two real case studies as the two conditions defined above are not reached (see table 7.5). For the DSG bench, experimental activity confirms that this transient condition is not observed. For the RAM plant, the Model 2 confirms that no harmful behavior is expected, see following section 7.3.2. Whereas for the theoretical MW plant we could expect some harmful conditions. This specific case study is analyzed more in details in the next section 7.3.3.

7.3.2 RAM case study analysis

An accurate control of the feed-in water is a strong issue for solar DSG, as shown in section 6.4. The qualitative analysis of previous section shows that no harmful

condition is expected for the case study of RAM. In this section, Model 2 is used to quantify the impact of this inaccuracy on the outlet specific enthalpy for the two selected days.

7.3.2.1 Input

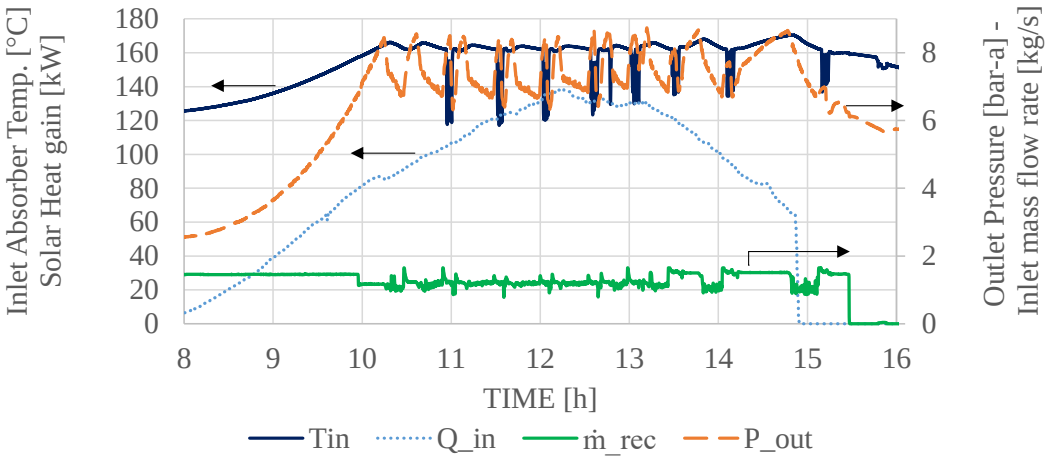

Figure 7.7: INPUT Model 2 for RAM case study on 2015/12/25

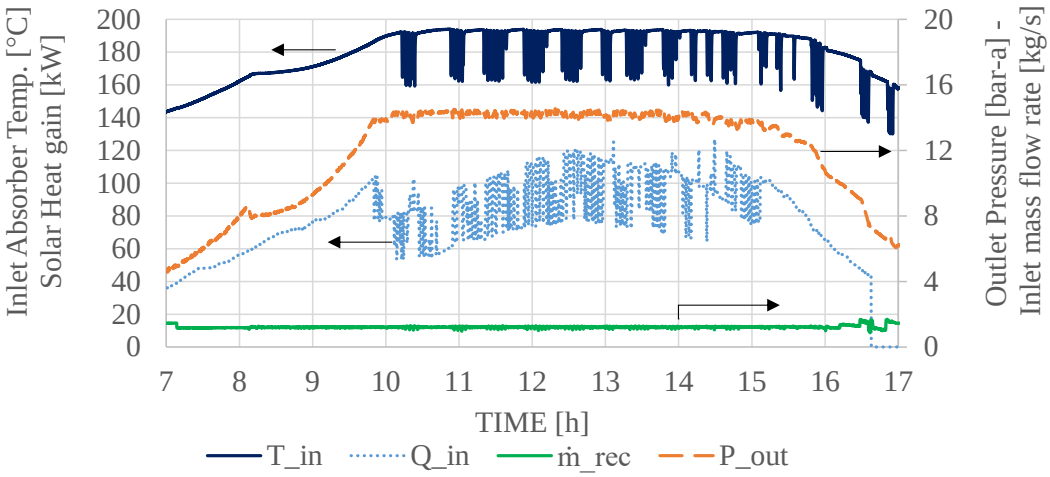

Figure 7.8: INPUT Model 2 for RAM case study on 2016/07/03

Figure 7.7 and figure 7.8 show the four input variables based on monitoring data. Inlet temperature (sensor T4), inlet mass flow rate (sensor $\dot{m}_{rec}$) and outlet pressure (sensor P6) use directly the measured values whereas solar heat gain is a result of Model 1 (DNI sensor by LFR efficiency). The inlet temperature decrease is approximatively 40 °C on the 25^{th} of December and is 30 °C on the 3^{rd} of July.

7.3.2.2 Partial validation

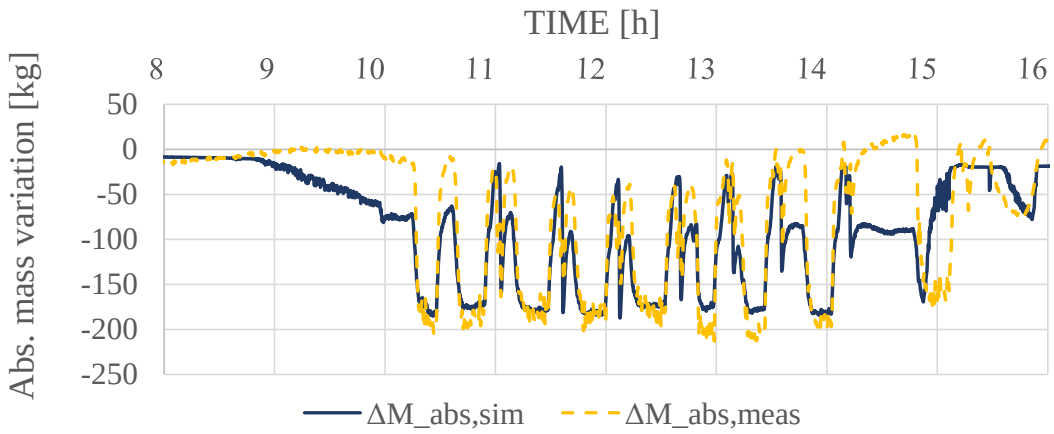

Figure 7.9: Comparison of absorber mass on the 2015/12/25

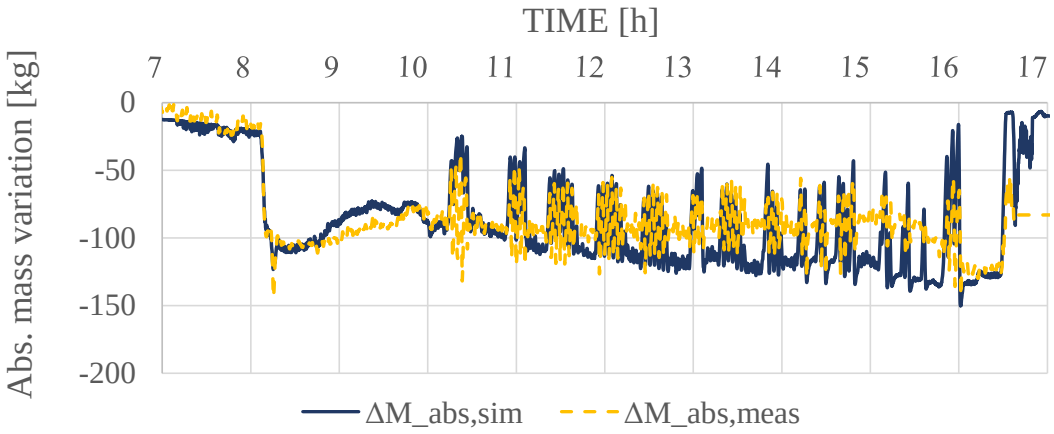

Figure 7.10: Comparison of absorber mass on the 2016/07/03

Only a partial validation is possible as numerous outputs of the model (steam quality, outlet mass flow rate, specific enthalpy at the absorber outlet) are not monitored in the real case study. Nevertheless, thanks to the post processing model of Model 1, a rough estimation of the absorber mass variation could be obtained at each time step. In fact, the water mass variation contained in the absorber (M_{abs}) is indirectly measured as a function of water mass in the steam drum (M_D), inlet feed-in water ($\dot{m}_{in}$) and outlet steam mass flow rate ($\dot{m}_{out}$), see eq. 7.8. Where the water mass in the steam drum is a function of the measured liquid level, temperature and pressure of the steam drum.

$$M_{abs}(t) - M_{abs}(0) = \left[M_D(t) - M_D(0) - \int_0^t \dot{m}_{in}(t) + \int_0^t \dot{m}_{out}(t) \right] \tag{7.8}$$

Figure 7.9 and figure 7.10 show the comparison of the "measured" and expected (Model 2) mass variation in the absorber for the two selected days. A relatively good agreement is observed in the peak variation. The initial and final mismatch between the simulated and measured absorber mass variation are mainly due to solar heat gain uncertainty. In fact, solar heat gain uncertainty has a strong impact on the mass variation close to saturation condition. Indeed, a lower heat flow in the real case study than in the simulation one leads to steam in the simulated absorber whereas the fluid remains liquid for the real absorber. Nevertheless, the model focuses on inlet temperature variation during nominal condition, which corresponds to the peak variations. Thus, Model 2 can be considered validated to highlight the physical phenomena of moving evaporation start point.

7.3.2.3 Results

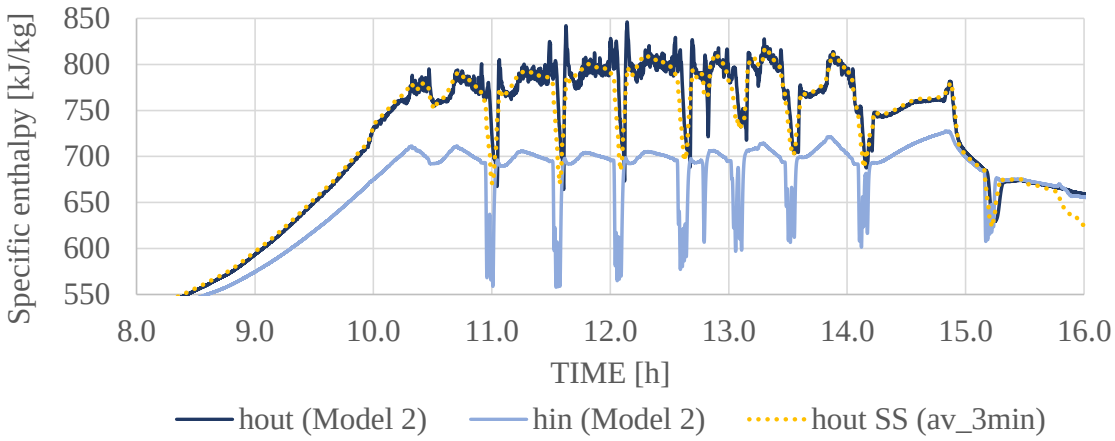

Figure 7.11: Inlet and outlet specific enthalpy of the absorber on the 2015/12/25

At the first step of result analysis, the outlet specific enthalpy is calculated under steady state condition where input data are the average of measured data (every 1s) for 3 min. Then the outlet specific enthalpy calculated based on the Model 2 and based on the steady state approach are compared to quantify the effect of transient

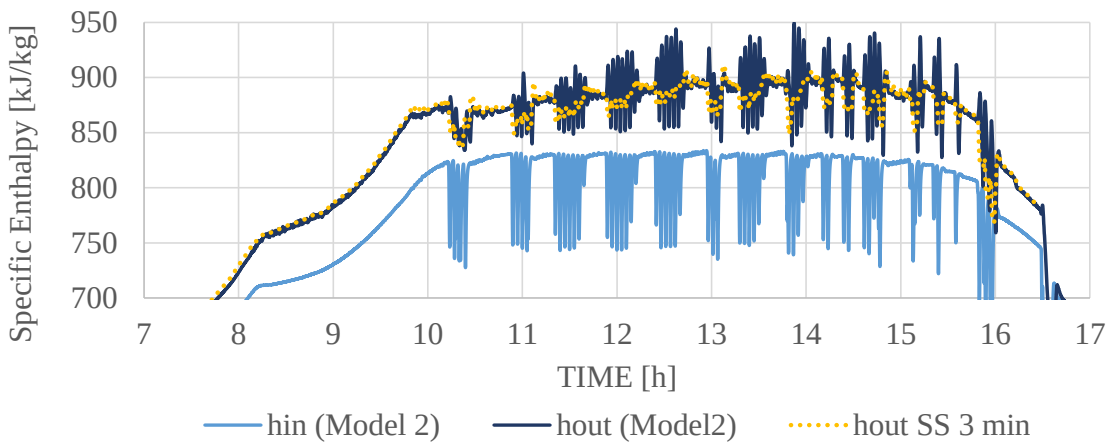

Figure 7.12: Inlet and outlet specific enthalpy of the absorber on the 2016/07/03

condition. Figure 7.11 and figure 7.12 show very small deviation between these two variables and this behavior agreement confirms the use of steady state approach in chapter 6. Thus, the inlet temperature variation (between 30 °C -40 °C) does not generate any harmful conditions in RAM plant, ie. high specific enthalpy and high steam quality are not observed.

7.3.3 MW plant case study

The case study in issue is the MW plant defined in section 7.2. A deeper analysis is performed since the qualitative analysis showed possible harmful behavior due to fast temperature decrease at absorber inlet, see table 7.5.

7.3.3.1 Boundary Condition

This "fast" temperature decrease at absorber inlet is illustrated with an inlet temperature decrease of 40 °C, from 160 °C to 120 °C, in 40 seconds as the one observed on the 25^{th} of December in the RAM plant. The step change is applied after 4 min. The solar heat gain is set constant for the whole simulation and equal to 1 MW. The same linear heat flux as the one of the RAM plant at peak power is used. In fact, the heat flux is proportional to the LFR type and solar irradiation and thus it is independent of plant size. Thus, the absorber length is calculated as the ratio between the peak power capacity and the linear heat flux. The absorber is discretized in 60 finite-difference nodes. The inlet mass flow rate and outlet pressure

are kept constant and equal to 1.2 kg/s and to 7 bar − a.

7.3.3.2 Result

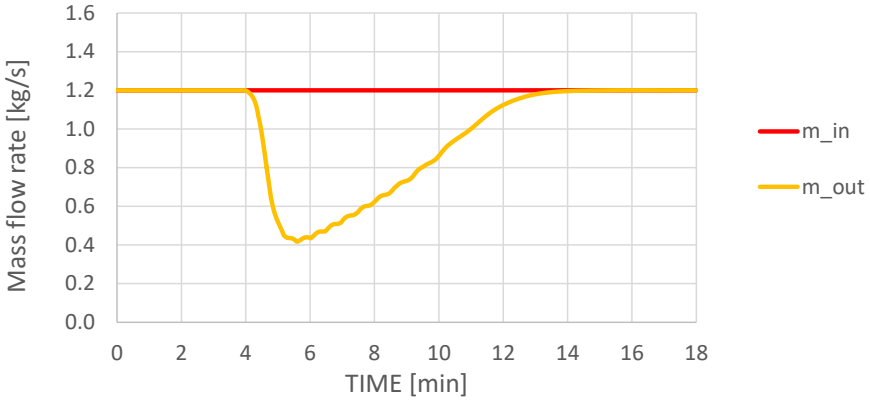

Figure 7.13: Transient response of mass flow rate variation due to "fast" inlet temperature decrease with a mass flow rate of 1.2 kg/s

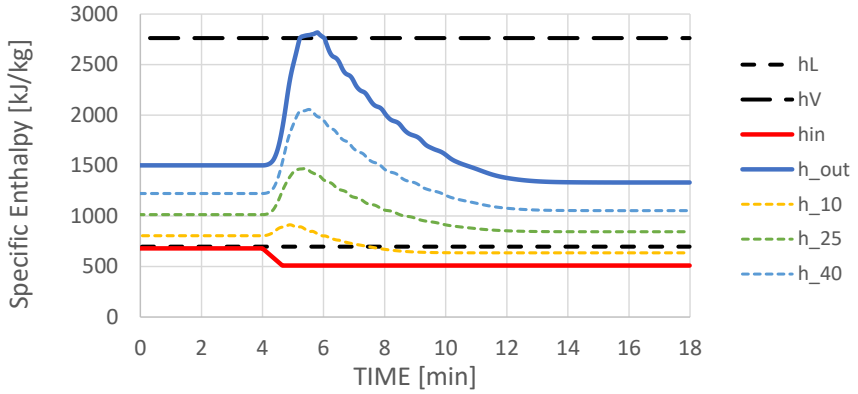

Figure 7.14: Transient response of specific enthalpy due to "fast" inlet temperature decrease with a mass flow rate of 1.2 kg/s

Steady-state is seen to be re-established approximately 9 min after the step-change, i.e. 3 times longer than the minimum characteristic time, τ_w, calculate in table 7.5 with an instantaneous step change. Transient response in fluid specific enthalpies (in 5 different nodes) and mass flow-rate are given in figures 7.13 and 7.14. It can be seen from the transient response that the mass flow rate peaks reach 0.4 kg/s before returning to a steady-state condition of 1.2 kg/s. This mass flow rate variation leads to a maximum outlet specific enthalpy equals to the saturated steam. Moreover, the steam quality is higher than 0.8 for duration longer than 2 min. This condition can be harmful due to stratified or dry-out flow pattern conditions, characterized with high steam quality and low mass flow rate.

- For stratified flow pattern, a strong temperature difference is expected in absorber cross section.

- For dry-out flow pattern, the heat transfer rate decreases strongly thus metal temperature is expected to reach high temperature.

Nevertheless, Model 2 is not able to quantify this thermal stress. In fact, the one dimensional approach would not show the temperature difference into the cross section. Moreover, the simplification that consists into using constant heat transfer rate does not allow to characterize dry-out condition.

7.3.3.3 Optimization

The extreme flow condition during transient has to be minimized in order to have the system working properly. Two alternatives exist: improve the system response or minimize this temperature step change:

1. First, to improve the system response the two ratios defined above ($\frac{\Delta L}{L_{tot}}$ and $\frac{5\tau_m}{\tau_w}$) should be maximized. This can be achieved by increasing the recirculation mass flow rate. With a mass flow rate of 2.5 kg/s, $\frac{\Delta L}{L_{tot}}$ increases to 0.4 (instead of 0.2 in table 7.5) but $\frac{5\tau_m}{\tau_w}$ remains very low. As expected, the transient duration is independent of the mass flow rate and equals to 9 min with 1.2 kg/s and 2.5 kg/s, see figure 7.15. This high mass flow rate condition is not sufficient to avoid specific enthalpy peak, see figure 7.16. Nevertheless, the minimum mass flow rate and maximum specific enthalpy remains within the design range, see figure 7.15 and figure 7.16. However, the optimal mass flow rate, defined in the section 7.2 based on pressure drops and flow pattern analysis, leads to lower mass flow rate.

2. Thus, the second option is developed to maintain the "optimal" mass flow rate or if maximizing the ratios is not sufficient then the step change should be minimized. It could be done technically by either improving the control of feed water mass flow rate to match the solar steam generation and system pressure (not easily applicable) or by integrating a mixing vessel to smooth the temperature variation of inlet water into the solar field, see figure 7.17.

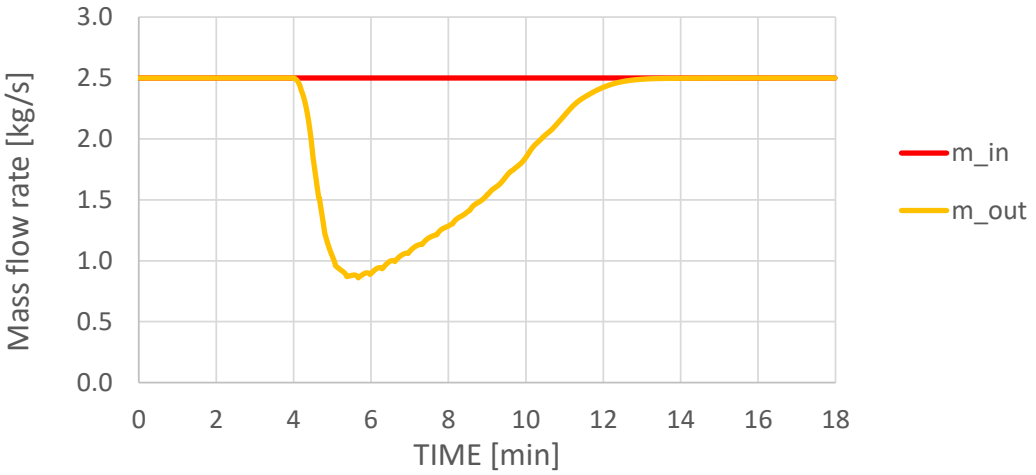

Figure 7.15: Transient response of mass flow rate variation to "fast" inlet temperature decrease with higher mass flow rate (2.5 kg/s)

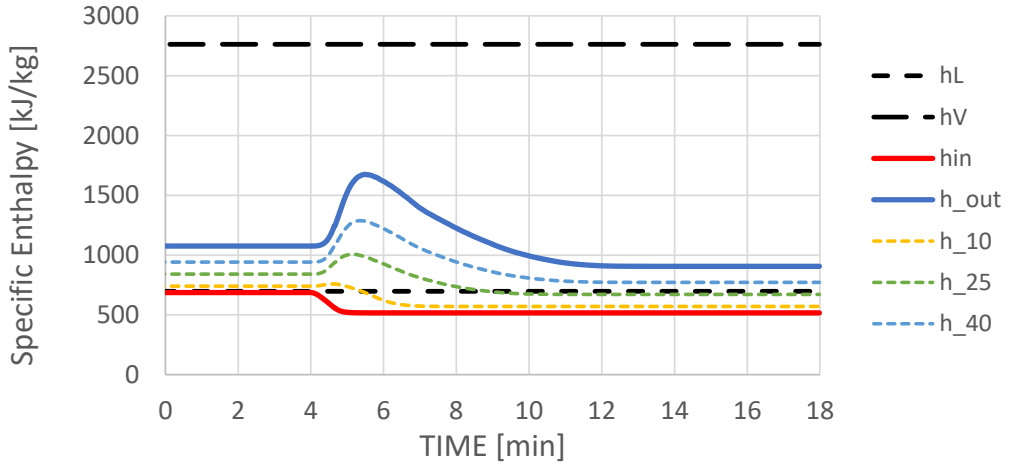

Figure 7.16: Transient response of specific enthalpy to "fast" inlet temperature decrease with higher mass flow rate (2.5 kg/s)

With a mixing vessel of 100 L, the temperature decrease from 160 °C to 120 °C is done in 5 min instead of 40 s without any mixing vessel. The improvement of an ideal mixing vessel of 100 L is quantified thanks to Model 2. Figure 7.18 shows that outlet mass flow rate variation is smooth (minimum mass flow rate is 0.8 kg/s) but it lasts 12 min, ie. more than the scenario without any mixing tank. Thus, the outlet specific enthalpy reaches lower value and the temperature decrease does not generate harmful conditions during transient, see figure 7.19. Moreover, the design optimization presented in section 7.2 is still applicable.

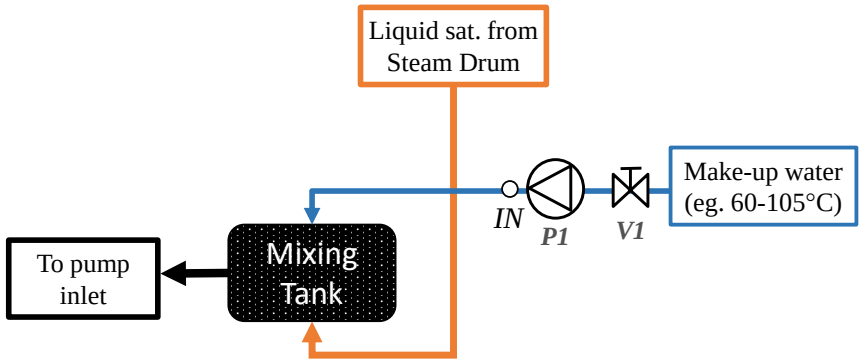

Figure 7.17: Mixing vessel configuration

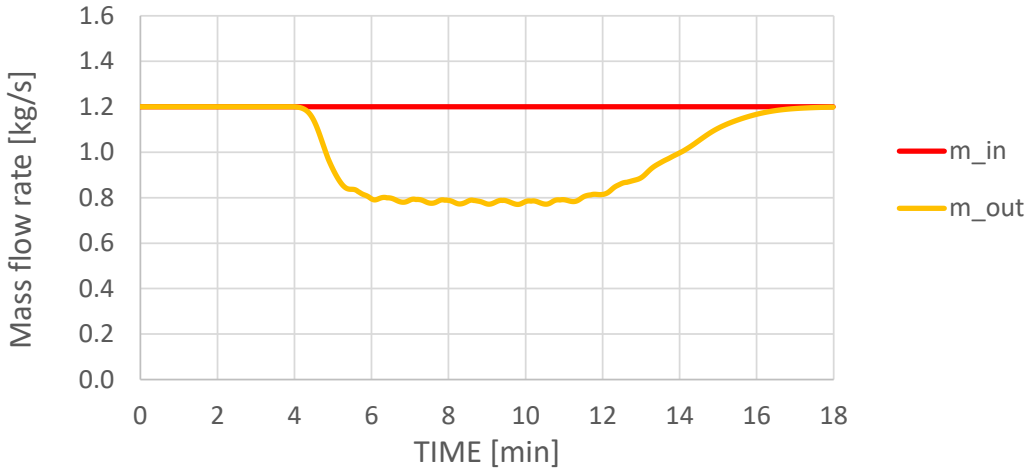

Figure 7.18: Transient response of mass flow rate variation to "fast" inlet temperature decrease with mixed tank with a mass flow rate of 1.2 kg/s

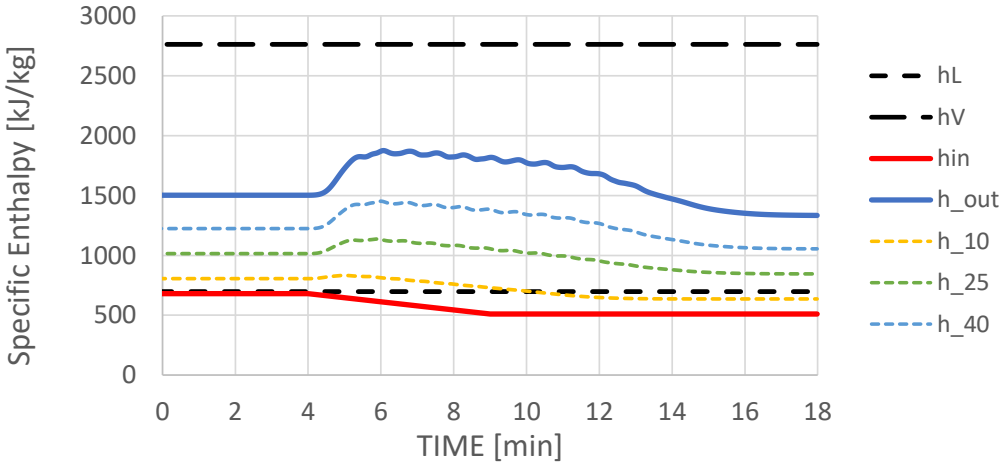

Figure 7.19: Transient response of specific enthalpy to "fast" inlet temperature decrease with mixed tank with a mass flow rate of 1.2 kg/s

7.4 Control Strategy: Night cooling impact

The objective of this section is to analyze, quantify and then optimize the night heat loss. The plant in issue is the solar plant installed at RAM by the manufacturer Industrial Solar, described in details in chapter 6. First, a four steps tuning and validation procedure has been performed for Model 3. Then, an optimized control strategy has been proposed and implemented into the real plant in April 2016 to minimize the start-up losses of RAM installation. The saved energy of this optimized control strategy is quantified with Model 3 on the night between the 3^{rd} and the 4^{th} of July. And finally, the expected theoretical energy saving of an ideal control strategy during winter is analyzed based on a representative day, 25^{th} of December 2015.

7.4.1 Model validation

Model 3, presented in section 4.6.2, has the purpose to describe the real plant performance. Thus, a model tuning and a validation in three steps have been performed. First, tuning coefficients are used to match the theoretical heat loss calculation with the real one (section 7.4.1.1). The temperature cooling curve of a standard winter night is used to tune the heat loss coefficients. The validation of the heat loss of each section is an issue. Thus, the validation is performed in two different conditions, in active (section 7.4.1.2) and in stand-by (section 7.4.1.3) modes, and the expected pressure variation is compared with the measured one. The two modes are described in section 4.6.2. If both conditions lead to a good agreement between the model and the measurement then the heat loss coefficients of each section are considered valid to perform the optimization of the control strategy. And finally, the night heat loss is compared to the other two methodologies (section 7.4.1.4) based on Model 1 and the temperature profile approach, see section 6.3.1.

7.4.1.1 Tuning coefficient:

The heat loss, calculated as eq. 4.62, underestimates the expected heat loss since no thermal bridges and an ideal installation (ie. dry insulation, all hydraulic components insulated, average wind load ...) are assumed. The tuning coefficients

have been applied to all the piping sections where local installation was performed and could generate extra pressure drops. For instance, the vacuum of evacuated tube has been generated during the production process in the factory and heat loss coefficients are not affected by the local installation. Thus, the heat loss coefficients of the evacuated tubes are not adjusted. Then, correction factors are tuned thanks to the temperature sensors installed along the recirculation loop. Each node of the lumped model represents a section of the recirculation loop, described in chapter 6 (see figure 6.2). The liquid section is characterized with the pump inlet temperature (sensor T2); the sensor installed between the two collector strings is used (sensor T5) for the interconnection I1 and drum temperature sensor is used for the steam drum. The tuned coefficients have been obtained in order to match the measured and simulated temperatures in the morning of the 26^{th} December. The following correction factors have been chosen:

- Coefficients of the liquid sections, ie. liq1, liq2 and liq3, equal to **2.5**.
- Interconnection coefficient equals to **1.3**.
- Steam drum correction factor equals to **2**
- Remaining nodes, CS1, CS2, Bi1 and Bi2 equal to **1** (no correction).

Figure 7.20 shows the result of the tuning phase with the four temperature sensors. A good agreement is observed between the different cooling curves. Nevertheless, this approach is not sufficient to validate the model as the temperature sensor selected could be an non-representative temperature of the specific section. The overall heat loss of each node, including the correction factors, are summarized in table 4.2.

7.4.1.2 Active mode validation: cooling curve test

To validate the correction factors, the first step consists in evaluating the overall heat loss in active mode. Active mode is defined when the recirculation pump is activated and water of the solar system is uniform along the recirculation loop and its temperature equals to the saturated temperature. A cooling curve test has been performed by Industrial Solar during the night of 2016/10/18.

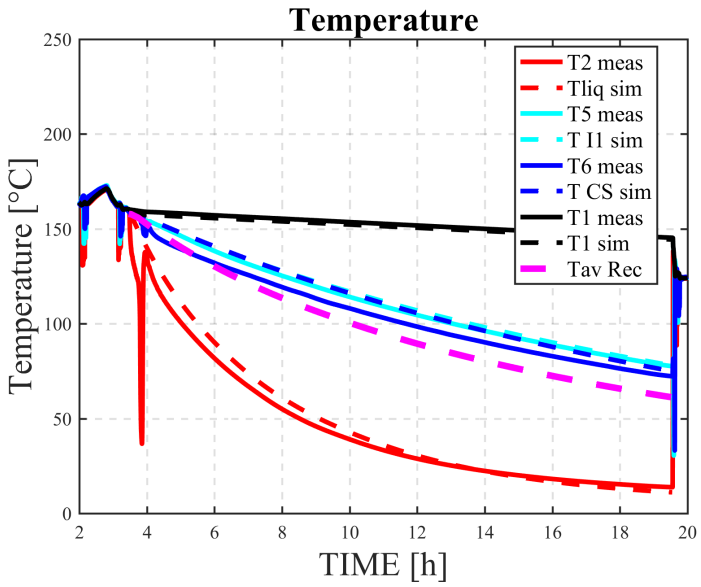

Figure 7.20: Cooling curve during stand-by mode - 2015/12/25

Cooling curve procedure: The solar system is warmed-up to the maximum temperature condition to validate the heat loss for a large temperature range. Then, the reflectors are unfocused and the system is closed (no feed water and steam generation) for the whole cooling curve test.

In the 2016/10/18 the saturated temperature decreased from 195 °C at the beginning of the cooling curve test to 120 °C after 17 hours. The monitored pressure is compared to expected pressure decrease. The initial condition of dynamic model is based on monitored sensors when the recirculation loop is fully liquid. To be sure to have liquid in the recirculation loop, the recirculation mass flow rate is increased to 1.8 kg/s before being set a 1.0 kg/s during the test.

Cooling curve result: Figure 7.21 shows the test performance result. On the left, the mass analysis confirms that the system is closed during the test as the monitored mass in the steam drum remains almost constant (calculated based on level and temperature sensors in the drum). The right figure shows the decrease of monitored pressure at Drum level (black curve) and the expected pressure (dashed blue curve). A good agreement is observed between the two curves.

And finally, figure 7.22 confirms the assumption of Model 3 which assumes that the two phases of the whole system are at thermal equilibrium, ie. the temperature of the system is uniform and equals to saturated condition.

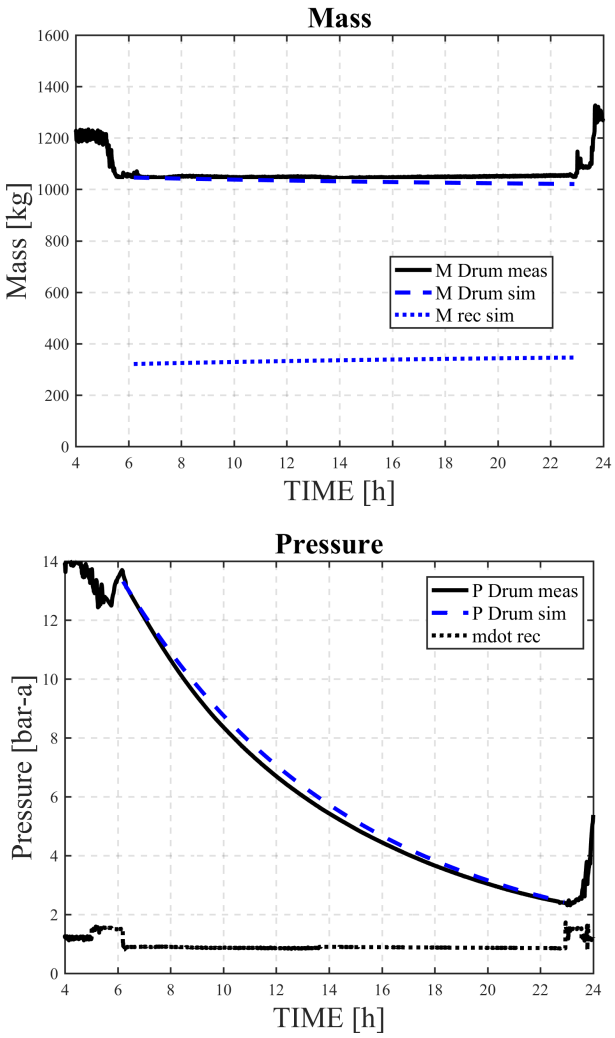

Figure 7.21: Cooling curve test result on the 2016/10/18. *Left: Mass variation; Right: Pressure variation*

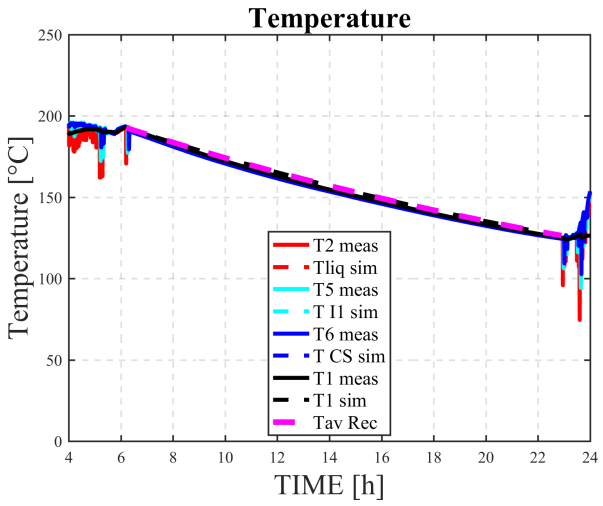

Figure 7.22: Cooling curve test result on the 2016/10/18: Temperature variation

7.4.1.3 Stand-by mode validation

During stand-by mode, the mass flow rate is zero and corresponds to standard night control. In this condition the temperature of the recirculation loop decreases faster than the one of the steam drum. Unlike the active mode where temperature is uniform, this dis-uniform temperature distribution leads to a another validation scenario. Figure 7.23 shows the good agreement of pressure decrease on 2015/12/25 and 2016/07/03, which are the two days selected in chapter 6 to apply a detailed analysis.

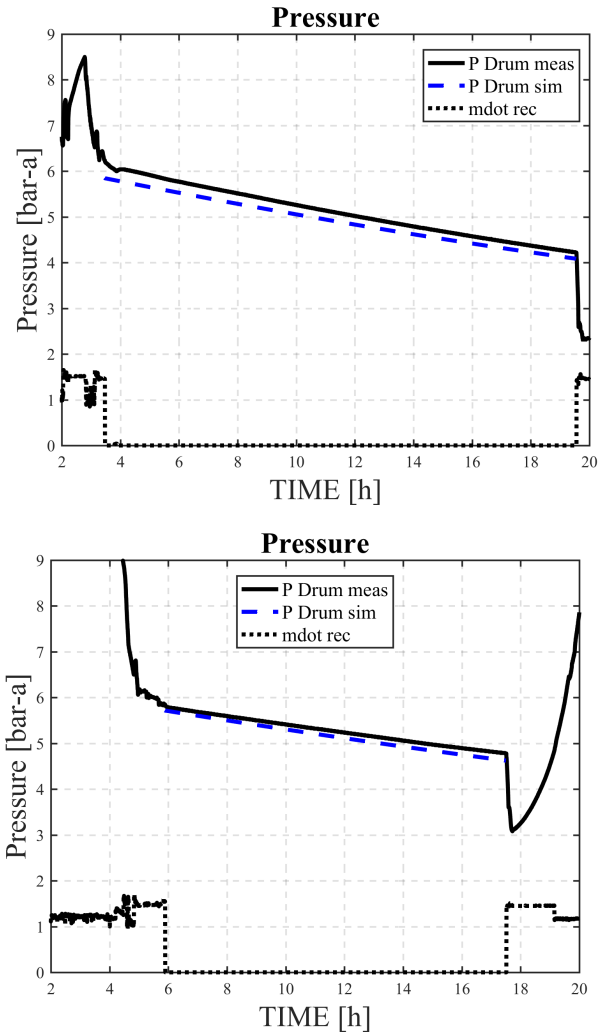

Figure 7.23: Pressure decrease during stand-by mode. *Left: the night of 2015/12/25; Right: the night of 2016/07/03*

In the description of Model 3, in section 4.6.2, the mass variation due to thermal expansion is assumed to be low compared to the overall system mass. For the two selected days, the mass increase of the recirculation loop is approximatively 25 kg

in a winter night of 16.5 h and approximatively 15 kg in a summer night of 11.5 h. Since the overall water mass is approximatively 1500 kg, the model assumption seems correct (mass variation is two orders of magnitude higher than the overall mass). In fact in Model 3, the mass increase of each node is directly balanced with saturated liquid without respecting the piping configuration but it will not affect strongly the overall result.

Furthermore, this cooling curve test highlights how crucial is to stop the pump during the night in order to keep the system pressurized. In fact once the solar system is closed (ie. no water inlet and steam outlet) the smooth pressure decrease due to night cooling is higher on the 2016/10/18 where the pump is active all the night, see figure 7.21, than when the pump is stopped, eg. 2015/12/25 and 2016/07/03, see figure 7.23.

7.4.1.4 Model comparisons

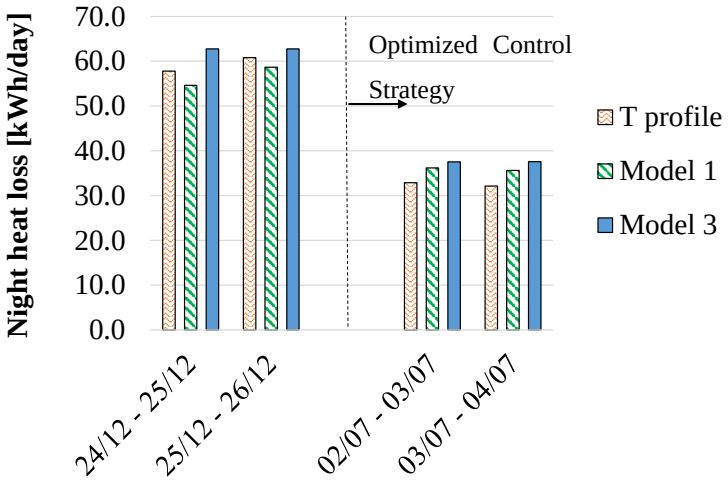

Figure 7.24: Model comparison of night heat loss

The last part of the model validation is the comparison of the night heat loss results with two other approaches. In section 6.3.1, the temperature profile approach is described. It analyzes the temperature variation during start-up and shut-down. The second approach is the one developed with Model 1 in stand-by mode. As presented in section 6.3.1.5, the Model 1 result has to be slightly adjusted to be compared with the other approaches. Due to different integration time, the night duration is shorter for the stand-by approach and the missed heat loss of the recir-

culation loop is approximatively 3 kWh. Thus, in order to have comparable Model 1 results, this extra energy is added to the Model 1 results. Figure 7.24 shows the comparison of the three different approaches presented in this work during four nights. Model 3 has a relatively good accuracy but it slightly overestimates the night heat loss compared to the other two approaches. However, Model 3 is sufficiently accurate to quantify the effect of optimized control strategy and can be considered validated.

7.4.2 Optimization Start-up heat loss

7.4.2.1 Control strategy description

An optimized control strategy has been proposed and implemented in April 2016 to minimize the start-up loss of RAM installation. With the new control strategy, just before to shut down the plant for the night, some feed water, which is much colder compared to the recirculated condensate, is fed into the system to replace the hot water from the recirculation loop. As an advantage, the hot water and steam is now stored in the well-insulated steam drum overnight, and heat losses over night are reduced.

7.4.2.2 Quantification summer improvement

To quantify the effect of the new control strategy, Model 3 is used. The night heat loss of two scenarios, with and without the new control strategy, are compared. The first one uses the real monitoring sensors to initialize Model 3. The second one is initialized with the monitoring data before feed water is added to the system and removing this extra mass to the overall initial mass. Figure 7.25 shows the temperature variation of the recirculation loop with the new control strategy. It shows that recirculation loop is filled with water at 120 °C instead of 160 °C. The new control strategy of injecting some cold water in the evening saved approximatively 8.3 kWh/day in the 3^{rd} of July. The saving represents approximatively 20% of start-up losses and 1.5 % of steam generated in 3^{rd} of July.

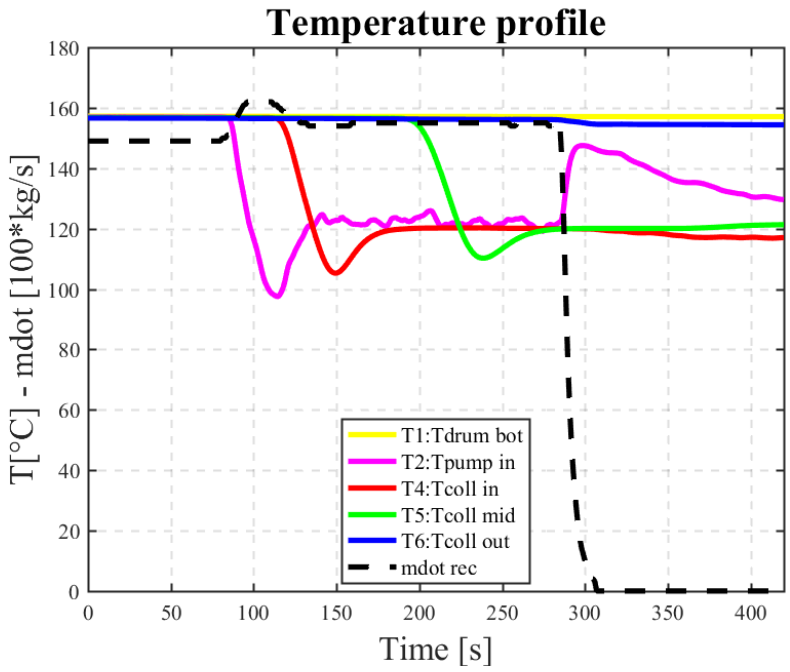

Figure 7.25: Shut down temperature sensor variation on the 2016/07/03

7.4.2.3 Quantification of optimized winter night

In winter, an ideal control strategy is defined. It is assumed that the hot recirculation water is replaced with 100% of feed-in water at 60 °C (average feed-in water temperature at RAM plant). The hot water is pushed to the well insulated steam drum. It would have a strong benefit as start-up loss reaches 19% of net energy gain. In fact, on the 25^{th} of December 2015 such control strategy would decrease the start-up losses by 25 kWh/day, which is 43% of start-up losses and 11% of the steam generated. But in the same time, it should be done carefully in order to avoid large level increase or condensation of steam in the drum.

Conclusions

In the last decades, numerous research projects (DISS, INDITEP) demonstrated the feasibility of the Direct Steam Generation (DSG) in horizontal parabolic trough collectors. Its advantages such as thermal performance, economic improvements and environment constraint reduction have been highlighted for power generation. However, the available know-how focuses mainly on power applications. The latter implies different levels of temperature and steam quality compared to other applications, such as industrial process heat. In literature, published performance results from existing "real" operating solar DSG installations are yet scarce.

The peculiarity of the use in the industrial sector respect to the conventional CSP application are: the use of saturated steam at lower pressure [3; 30 bar-g] instead of [55-110 bar-g]; smaller solar plant installed close to the end user; lower steam stability required; and finally a colder sub-cooled water at the absorber inlet. The industrial sector has been identified as a high-potential and still largely unexplored application for solar thermal.

- *High-potential*, since the industrial sector represents a large share of the overall energy consumption. Moreover, a large share of this energy is heat at low and medium level temperature which is suitable for the solar application.

- *Unexplored*, since only few Solar Heating for Industrial Processes (SHIP) plants have been installed all over the world. In January 2017, of the 195 ship plants listed in the IEA SHIP plants database [48], only 25 plants are larger than 1000 m^2. This difficult development is due to several technologies barriers [6] from which unstable oil prices does not enable forecast investment for ship plants, concentrated technology needs Direct Normal Irradiation which is not everywhere available in abundance and the lack of technology reliability.

Mathematical modeling and numerical implementation

In order to study the physical phenomena which take place in solar DSG plants and affect the generation and their performance, a specific class of mathematical models has been developed and implemented in this PhD. Based on the literature review presented in the section 4.3 and 4.4, three numerical models have been developed.

- A first model (steady state Model 1), see section 4.5, is developed to study performance and behavior (pressure drops, steam drum level, flow pattern) of existing solar DSG plants. It is applied to the test laboratory (chapter 5) and to a specific case study (chapter 6).

- A second model (dynamic Model 2) is developed to analyze the potential harmful conditions at the absorber outlet due to fast moving evaporation start point within the absorber, see section 4.6.1.

- A third model (dynamic Model 3) is developed to characterize and quantify the night heat loss of the solar DSG plant and the potential energy saving due to an optimized control strategy, see section 4.6.2.

Experimental activities

A DSG bench was developed at the Energy department of Politecnico di Milano (POLIMI), with the objective to validate Model 1 and some of its assumptions:

- pressure distribution over the recirculation loop;

- head loss correlations implemented in the numerical model;

- validation of the extension of the flow pattern map outside its validation range.

The latter is the most original point as the flow pattern maps used in Model 1 are an extrapolation of *modified KTF* correlations [[88], [89]] which have been developed and tuned for refrigerant in small diameter pipes at low pressure. The *modified KTF* correlations have been used outside their boundary conditions for water flow in larger diameter pipes (70 mm compared to 8-20 mm) and higher pressure (3-30 bar

compared to 1.1-8.9 bar). An experimental campaign validates the use of water instead of refrigerant for the transition curves encounter with solar DSG for industrial heating processes (ie. intermittent, stratified wavy and annular flow patterns).

Real case study

Once Model 1 is validated on a lab-scale, it has been applied to a real case study: the plant in Amman-Sahab / Jordan at RAM Pharmaceuticals Company. The so-called RAM plant has been installed by Industrial solar in 2015 and it is composed of 18 linear Fresnel modules, connected in serial, for a total aperture area of 394 m^2 [[28], [27]]. A generation performance analysis is carried out for two distinct periods one in winter (two weeks) and one in summer (two weeks). It consists in the comparison of expected and measured results. It shows that most of the measured energy balance is within the uncertainty range of the model. Moreover, the impact of bad cleaning conditions is highlighted with an increase of 45% in the measured daily energy balance (ε_Q) after cleaning, in one occasion after a long period of non-cleaning. Nevertheless, due to a low accuracy of the irradiation sensor, the uncertainty range is large and does not allow a deeper analysis.

Then a detailed analysis is applied to one sunny day in winter (2015/12/25) and one in summer (2016/07/03), where the mass and energy balance are within the uncertainty range.

Head loss analysis shows a good agreement between simulation and measurement during active steam production. Whereas, during the start-up and shut-down period the simulated overall pressure drop is underestimated compared to the measurement. This discrepancy is due to the presence of steam in the downward vertical pipes whereas it was expected liquid phase. Small design improvement has been proposed to limit this effect (siphon, larger pipe diameter)

Within the given accuracy of the measurement data, several interesting aspects have been observed thanks to the analysis of the steam drum level. For instance, that flashing appears in the solar field when the recirculation pump stops or when the steam valve opens for the first time. The strong level variation due to the water temperature decrease at the absorber inlet is observed (due to the difficulty to control the feed-in water pump). A more detailed analysis is performed with a

transient model.

The flow pattern analysis shows that harmful flow patterns as stratified and dry out are successfully avoided by the existing control strategy, and the main flow pattern in the steam region is expected to be stratified wavy, as a result of the simulation.

Optimization processes

An optimization process has been applied to improve the solar DSG design and control strategy for the specific application of industrial process heat. The approach consists of different levels of optimization.

- The first one focuses on the methodology to design the solar field layout (parallel vs series, ideal mass flow rate) for a MW plant based on Model 1.

- The second and third optimizations focus on unexpected behavior highlighted in the case study, with two transient models:

  - Effect of fast moving evaporation start point: it highlights possible harmful situations in some specific conditions at the absorber outlet when the inlet absorber temperature decreases suddenly; Two simple indicators are defined as benchmarks for these phenomena.

  - Night heat losses: a new control strategy devoted to energy savings is presented. It consists in injecting cold water in the evening in the recirculation loop to push the hot water in the well insulated steam drum. It has been implemented in April 2016 at RAM plant by Industrial Solar. The saving represents approximatively 20% of start-up losses and 1.5% of steam generated in summer. In winter, an ideal control strategy would decrease the start-up losses by 25 kWh/day, which is 43% of start-up losses and 11% of the steam generated. This new control strategy has the advantage to push the hot water and steam in the well-insulated steam drum overnight and to avoid possible flashing in the recirculation when the recirculation stops.

It is concluded that solar Direct Steam Generation has been successfully modeled, experimentally evaluated (in a laboratory scale and in a real case study) and system optimizations have been proposed for the design and control scheme. The analysis shows that solar DSG is a feasible alternative to introduce renewable energy into industrial processes in the region with high DNI, when the design is done properly.

Further developments:

In order to pursue the analysis of the solar DSG integration into industrial heating processes the following ideas can be developed:

- The validation range of the *modified KTF* correlations could be extended to reduce the gap between laboratory condition and real case study:
  - For instance, the validation procedure could be applied for larger diameters at higher pressure and for higher steam quality than the one used in this PhD work.
  - The impact to use uniform heat flux instead of real dis-uniform solar heat flux could be analyzed.
  - The use of more advanced flow pattern sensor (eg. wire mesh) on a large case study would be a very innovative approach to analyze the real flow pattern. In this specific application, the steam quality at the absorber outlet has to be measured with a different approach than the one proposed in this PhD.
- The case study analysis could be extended to a larger solar plant (1 MW) for a longer period. It is recommended to use accurate DNI sensor and to monitor the cleaning day frequency. This analysis would demonstrate furthermore the feasibility of the Direct Steam Generation (DSG) process in medium temperature concentrating collectors.

Acknowledgments

I would like to acknowledge my colleagues, friends and family, whose help and support allowed me to complete this research.

Firstly I must thank my supervisor Professor Mario Motta and my tutor Professor Livio Mazzarella, for their guide and advice during the course of this work.

I would also like to thank Lorenzo for his support and his precious advices which guide me during these last years.

Thanks to all my colleagues, in particular to the *Gruppo Solare*: thanks to Marco, Alice and Matteo for their good moods and for making these years fun such as the *petard time* during the thesis write-up.

Many thanks to the Michael Berger for his precious support and to Christian Zahler and all the members of Industrial Solar who hosted me very kindly and made my stay in Freiburg im Breisgau very pleasant.

Thanks to my family and friends for the good time spent together, which gave me the energy to complete this work.

Finally, I would like to thank Anna, for always supporting, advising and encouraging me. I was able to measure your effort when I realized that you became an expert of the solar DSG.

Nomenclature

SYMBOLS

p	pressure (bar)
h	specific enthalpy (kJ/kg)
$\dot{m}$	mass flow rate (kg/s)
$\dot{v}$	volume flow rate (kg/s)
G	specific mass flow rate (kg/(s.m^2))
Q	thermal energy (kWh)
$\dot{Q}$	thermal power (kW)
t	time coordinate (h)
T	temperature (°C)
V	volume (m^3)
A	surface area (m^2)
D	diameter (m)
L	liquid level in volume (L)
y	length along recirculation loop (m)
z	Height (m)
U_1	convective heat loss coefficient (kW/(K.m))
U_4	radiative heat loss coefficient (kW/(K^4.m))
M_{on}	Number of active mirrors (-)
M_{all}	Number of mirrors (-)
u	relative uncertainty (-)
g	gravity acceleration, 9.8 (m/s^2)
c_p	Specific isobaric heat capacity ($kJ/kg.K$)
h_{conv}	Convective heat transfer rate (kW/K.m^2)

h_{cont}	Thermal contact conductance (kW/K.m^2)
k	Thermal conductivity (kW/K.m)
dp_{fri}	friction pressure drop (bar)
dp_{comp}	component pressure drop (bar)
dp_{stat}	static pressure drop (bar)
dp_{pump}	hydraulic pump head (bar)
f	friction factor (-)
IAM_L	Longitudinal Incidence Angle Modifier [-]
IAM_T	Transversal Incidence Angle Modifier [-]

GREEK SYMBOLS

η	efficiency (-)
ε_M	mass balance indicator [-]
ε_Q	energy balance indicator [-]
η_0	optical efficiency (-)
ρ	mass density (kg/m^3)
μ	Dynamic viscosity [Pa/s]
σ	surface tension for water[N/m]
Δ	difference (-)
θ	wall temperature (-)
Θ_{inc}	incidence angle (°)
Θ_{tra}	transversal angle (°)
ε	roughness [μm]
ζ	singular pressure drop coefficient [-]

SUBSCRIPT

A..H	point along the recirculation loop
f	feed-in water
D	Steam drum

rec	recirculation loop
ins	thermal insulation
ab,i	Intern absorber pipe
ab,o	Outer absorber pipe
res	electrical heater
meas	measurement result
sim	simulation result
m	metal
t	thermal (eg. efficiency)
e	electrical (eg. efficiency)
a	ambient
in	inlet
out	outlet
lat	latent
sat	saturation condition
sens	sensible
lo	liquid only
nbd	nuclear boiling dominant
cbd	convective boiling dominant
L	loss
SF=Steam	solar field is assumed full of saturated steam
SF=Liq	solar field is assumed full of saturated liquid

SUPERSCRIPT

w	water fluid medium
l	liquid phase
g	steam phase
bi	biphasic phase

ACRONYMS

KTF	Kattan Thome and Favrat
CSP	Concentrate Solar Power
LFR	Linear Fresnel Reflectors
PTC	Parabolic Trough Collector
DSG	Direct Steam Generation
BoP	Balance of Plant
SHIP	Solar Heating for Industrial Processes
SS	Steady State approach
FP	Flow Pattern
S	stratified flow pattern
WS	wavy stratified flow pattern
Int	Intermittent flow pattern
An	annular flow pattern
Dry	Dry-out flow pattern
Mist	Mist flow pattern
SF	Solar Field
CS	Collector String
Liq	Liquid pipe
Bi	Biphasic pipe
R	electrical heater
Co	Convective number
Bo	Boiling number
Fr	Froude number
We	Weber number
Re	Reynolds number
Nu	Nusselt number
Pr	Prandlt number
NPSH	Net Pressure Suction Head

List of Figures

List of Tables

Bibliography

[1] Framework Convention on Climate Change (FCCC). Report of the Conference of the Parties on its twenty-first session, held in Paris from 30 November to 13 December 2015 Part two: Action taken by the Conference of the Parties at its twenty-first session. Technical report, United Nations, Paris, 2016.

[2] EU-Commission. An Energy policy for Europe - COM(2007). Technical report, EU-Commission, Brussel, 2007.

[3] IEA - International Energy Agency. OECD's final energy consumption in 2014, 2017.

[4] Tobias Naegler, Sonja Simon, Martin Klein, and Hans Christian Gils. Quantification of the European industrial heat demand by branch and temperature level. *Internation journal of energy research*, 39:2019–2030, 2015.

[5] EUROSTAT. Consumption of energy : http://ec.europa.eu/eurostat/data/database, 2014.

[6] Cédric Philibert. Barriers to technology diffusion: The case of solar thermal technologies. Technical report, International Energy Agency (IEA), 2006.

[7] Guangdong Zhu, Tim Wendelin, Michael J. Wagner, and Chuck Kutscher. History, current state, and future of linear Fresnel concentrating solar collectors. *Solar Energy*, 103:639–652, 2014.

[8] John G. Collier and John R. Thome. *Convective boiling and condensation*. Clarendon Press Oxford, UK, third edit edition, 1994.

[9] A. Fernández-García, E. Zarza, L. Valenzuela, and M. Pérez. Parabolic-trough solar collectors and their applications, 2010.

[10] John D Pye. *System Modelling of the Compact Linear Fresnel Reflector*. PhD thesis, University of New South Wales - Sydney - Australia, 2008.

[11] L.G. Radosevich. Final report on the power production phase of the 10 MWe solar thermal centrale receiver pilot plant. Technical report, Sandia National Laboratories livermore, 1988.

[12] J. Ajona, Ulf Herrmann, F. Sperduto, and J. Farinha-Mendes. Main achievements within ARDISS Advanced Receiver for Direct Solar Steam Production in Parabolic Trough Solar Power Plant Project. Technical report, 1996.

[13] E Zarza, A Morales, E Rojas, K Hennecke, O Goebel, P Geskes, S Zunft, F Lippke, U Hermann, and J Langenkamp. DISS-phase I PROJECT Publishable Final Report. 1996.

[14] Eduardo Zarza, Loreto Valenzuela, Javier Leó, H.-Dieter Weyers, Martin Eickhoff, Markus Eck, and Klaus Hennecke. The DISS Project: Direct Steam Generation in Parabolic Trough Systems. Operation and Maintenance Experience and Update on Project Status. *Journal of Solar Energy Engineering*, 124:126–133, 2002.

[15] Rafael Almanza, Alvaro Lentz, and Gustavo Jiménez. Receiver behavior in direct steam generation with parabolic troughs. *Solar Energy*, 61(4):275–278, 1997.

[16] M. Eck and W.-D. Steinmann. Direct Steam Generation in Parabolic Troughs: First Results of the DISS Project. *Journal of Solar Energy Engineering*, 124(2):134, 2002.

[17] Rafael Almanza, Gustavo Jimé, Alvaro Lentz, Alberto Valdé, and Alberto Soria. DSG Under Two-Phase and Stratified Flow in a Steel Receiver of a Parabolic Trough Collector. *Journal of Solar Energy Engineering*, 124:140–144, 2002.

[18] Eduardo Zarza, Loreto Valenzuela, Javier Leon, Klaus Hennecke, Markus Eck, H.-Dieter Weyers, and Martin Eickhoff. Direct steam generation in parabolic troughs: Final results and conclusions of the DISS project. *Energy*, 29:635–644, 2004.

[19] Loreto Valenzuela, Eduardo Zarza, Manuel Berenguel, and Eduardo F. Camacho. Control concepts for direct steam generation in parabolic troughs. *Solar Energy*, 78(2):301–311, 2005.

[20] L. Valenzuela, E. Zarza, M. Berenguel, and E. F. Camacho. Control scheme for direct steam generation in parabolic troughs under recirculation operation mode. *Solar Energy*, 80(1):1–17, 2006.

[21] Eduardo Zarza, Ma Esther Rojas, Lourdes González, José Ma Caballero, and Fernando Rueda. INDITEP: The first pre-commercial DSG solar power plant. *Solar Energy*, 80(10):1270–1276, 2006.

[22] Andreas Haeberle, Christian Zahler, Hansjoerg Lerchenmueller, Max Mertins, Christof Wittwer, Franz Trieb, and Juergen Dersch. The Solarmundo line focussing Fresnel collector. Optical and thermal performance and cost calculations. *Proceedings of SolarPACES*, (March 2014):1–11, 2002.

[23] Novatec Solar. PE-2 Plant : http://www.novatecsolar.com/56-1-PE-2.html, 2012.

[24] K Hennecke and T Hirsch. Pilot plant for solar process steam supply. In *Eurosun*, number February, 2008.

[25] Dirk Krüger, Niels Lichtenthäler, Jürgen Dersch, Heiko Schenk, Klaus Hennecke, Anette Anthrakidis, Markus Rusack, Ahmet Lokurlu, Karim Saidi, Marcus Walder, Stephan Fischer, and Hans Peter Wirth. Solar Steam Supply : Initial Operation of a Plant. In *ISES Solar World Congress*, number SEPTEMBER, page 7, 2011.

[26] Alice Vittoriosi, Roberto Fedrizzi, Radko Brock, Francesco Orioli, Vittorio Orioli, and Dirk Pietruschka. Monitoring of a MW class solar field set up in a brick manufacturing process. *Energy Procedia*, 48:1217–1225, 2014.

[27] Martin Haagen, Christian Zahler, Elke Zimmermann, and Mahmoud M. R. Al-Najami. Solar process steam for pharmaceutical industry in Jordan. *Energy Procedia*, 70:621–625, 2015.

[28] Michael Berger, Mirko Meyer-Grünefeldt, Dirk Krüger, Klaus Hennecke, Marwan Mokhtar, and Christian Zahler. First Year of Operational Experience with a Solar Process Steam system for a Pharmaceutical Company in Jordan. *Energy Procedia*, 91:591–600, 2016.

[29] D Krüger, M Berger, M Mokhtar, Lisa Willwerth, C Zahler, M M R Al-Najami, and Klaus Hennecke. Experiences with industrial solar process steam generation in Jordan. In *SolarPACES 2016*, 2016.

[30] Bettina Muster, Ilyes Ben Hassine, Annabell Helmke, Stefan Heß, Pierre Krummenacher, Bastian Schmitt, and Hans Schnitzer. Solar process heat for production and advanced applications. In *IEA SHC TASK 49 : Solar Process Heat for production and advanced applications*, number December 2014, chapter Integratio, pages 1–5. 2012.

[31] Wolf Dieter Steinmann and Markus Eck. Buffer storage for direct steam generation. *Solar Energy*, 80(10):1277–1282, 2006.

[32] Jan Fabian Feldhoff, Kai Schmitz, Markus Eck, Lars Schnatbaum-Laumann, Doerte Laing, Francisco Ortiz-Vives, and Jan Schulte-Fischedick. Comparative system analysis of direct steam generation and synthetic oil parabolic trough power plants with integrated thermal storage. *Solar Energy*, 86(1):520–530, 2012.

[33] M. Eck, E. Zarza, M. Eickhoff, J. Rheinländer, and L. Valenzuela. Applied research concerning the direct steam generation in parabolic troughs. *Solar Energy*, 74(4):341–351, 2003.

[34] John D Pye, Graham L Morrison, and Masud Behnia. Unsteady effects in direct steam generation in the CLFR. In *Australia and New Zealand Solar Energy Society (ANZSES) Conference*, 2007.

[35] S.D. Odeh, M. Behnia, and G. L. Morrison. Hydrodynamic Model for Horizontal and Inclined Solar Absorber Tubes for Direct Steam Generation Collectors. In *13th Australasian Fluid Mechanics Conference*, pages 969–972, 1998.

[36] M Eck and W D Steinmann. Modelling and design of direct solar steam generating collector fields. *Journal of Solar Energy Engineering-Transactions of the Asme*, 127(3):371–380, 2005.

[37] Vicente Flores and Rafael Almanza. Direct steam generation in parabolic trough concentrators with bimetallic receivers. *Energy*, 29(5):645–651, 2004.

[38] Vicente Flores and Rafael Almanza. Behavior of Bimetallic Absorber in Parabolic Collectors During DSG to Low Powers. *Journal of Solar Energy Engineering*, 129(2):249, 2007.

[39] M. Baikin, Y. Taitel, and D. Barnea. Flow rate distribution in parallel heated pipes. *International Journal of Heat and Mass Transfer*, 54(19-20):4448–4457, 2011.

[40] U. Minzer, D. Barnea, and Y. Taitel. Flow rate distribution in evaporating parallel pipes-modeling and experimental. *Chemical Engineering Science*, 61(22):7249–7259, 2006.

[41] Yehuda Taitel and Dvora Barnea. Transient solution for flow of evaporating fluid in parallel pipes using analysis based on flow patterns. *International Journal of Multiphase Flow*, 37(5):469–474, 2011.

[42] S. Natan, D. Barnea, and Y. Taitel. Direct steam generation in parallel pipes. *International Journal of Multiphase Flow*, 29(11):1669–1683, 2003.

[43] F. Aguilar-Gastelum, S. L. Moya, O. Cazarez-Candia, and L. Valenzuela. Theoretical study of direct steam generation in two parallel pipes. *Energy Procedia*, 57:2265–2274, 2014.

[44] Energy Information Administration (EIA). Annual Energy Outlook 2014. Technical report, U.S. Department of Energy, 2014.

[45] U.S. Department of Energy. Improving Steam System Performance : A Sourcebook for Industry Second Edition, 2012.

[46] Spirax - Sarco. Module 1.1 : Steam-The Energy fluid. In *The steam and condensate loop*, page 3.6.5. 2014.

[47] Franz Mauthner and Werner Weiss. Solar Heat Worldwide:Markets and Contribution to the Energy Supply. *Iea Shc*, 1, 2013.

[48] IEA Task 49. SHIP plant database : http://ship-plants.info/.

[49] A. Frein, M. Calderoni, and M. Motta. Solar thermal plant integration into an industrial process. *Energy Procedia*, 48:1152–1163, 2014.

[50] Markus Eck, Holger Schmidt, Martin Eickhoff, and Tobias Hirsch. Field Test of Water-Steam Separators for Direct Steam Generation in Parabolic Troughs. In *SolarPaces 2006*, volume 130. American Society of Mechanical Engineers, 2008.

[51] Geroge E. Alves. Cocurrent liquid-gas flow in a pipe-line contactor. *Chemical Engineering Progress*, 50(9):449–456, 1954.

[52] A. E. Dukler and Y. Taitel. *Multiphase Science and Technology Chapter 1 : Flow Pattern Transitions in Gas-liquid Systems: Measurement and Modeling*, volume 2. Springer Berlin Heidelberg, Berlin, Heidelberg, 1986.

[53] D Barnea. A Unified Model for Predicting Flow-Pattern Trasitions for the Whole Range of Pipe Inclinations. *Int. J. Multiphase Flow*, 13(1):1–12, 1987.

[54] F. Lippke. Direct Steam Generation in Parabolic Trough Solar Power Plants: Numerical Investigation of the Transients and the Control of a Once-Through System. *Journal of Solar Energy Engineering*, 118(1):9, 1996.

[55] Shuichiro Miwa, Michitsugu Mori, and Takashi Hibiki. Two-phase flow induced vibration in piping systems. *Progress in Nuclear Energy*, 78:270–284, 2015.

[56] J. Adams, D. R. Clark, J. R. Louis, and J. P. Spanbauer. Mathematical Modeling of Once-Through Boiler Dynamics. *IEEE Transactions on Power Apparatus and Systems*, 84(2):146–156, 1965.

[57] Asok Ray. Nonlinear dynamic model of a solar steam generator. *Solar Energy*, 26(4):297–306, 1981.

[58] T Hirsch, W Steinmann, M Eck, Gerhard Schmitz, Bernhard Bachmann, Katrin Prölß, Wilson Casas, Henning Knigge, Jens Vasel, Stefan Wischhusen, Tobias Hirsch, Markus Eck, and Wolf-Dieter Steinmann. Simulation of transient two-phase flow in parabolic trough collectors using Simulation of transient two-phase flow in parabolic trough collectors using Modelica. In *4th International Modelica Conference*, pages 403–412, 2005.

[59] Markus Eck and Tobias Hirsch. Dynamics and control of parabolic trough collector loops with direct steam generation. *Solar Energy*, 81(2):268–279, 2007.

[60] Jürgen Birnbaum, Jan Fabian Feldhoff, Markus Fichtner, Tobias Hirsch, Markus Jöcker, Robert Pitz-Paal, and Gerhard Zimmermann. Steam temperature stability in a direct steam generation solar power plant. *Solar Energy*, 85(4):660–668, 2011.

[61] F. Casella. Object-Oriented modelling of two-phase fluid flows by the finite volume method. In *5th Symposium on Mathematical Modelling*, number 30, 2006.

[62] F. Casella. ThermoPower library home page : http://thermopower.sourceforge.net/.

[63] K.J. Åström and R.D. Bell. Drum-boiler dynamics. *Automatica*, 36(3):363–378, 2000.

[64] Vladimir D. Stevanovic, Blazenka Maslovaric, and Sanja Prica. Dynamics of steam accumulation. *Applied Thermal Engineering*, 37:73–79, 2012.

[65] David H. Lobón, Emilio Baglietto, Loreto Valenzuela, and Eduardo Zarza. Modeling direct steam generation in solar collectors with multiphase CFD. *Applied Energy*, 113:1338–1348, 2014.

[66] David H. Lobón, Loreto Valenzuela, and Emilio Baglietto. Modeling the dynamics of the multiphase fluid in the parabolic-trough solar steam generating systems. *Energy Conversion and Management*, 78:393–404, 2014.

[67] S.D. Odeh, G.L. Morrison, and M. Behnia. Modelling of parabolic trough direct steam generation solar collectors. *Solar Energy*, 62(6):395–406, 1998.

[68] S. D. Odeh, M. Behnia, and G. L. Morrison. Hydrodynamic Analysis of Direct Steam Generation Solar Collectors. *Solar Energy Engineering*, 122(1):14, 2000.

[69] S. D. Odeh, M. Behnia, and G. L. Morrison. Performance evaluation of solar thermal electric generation systems. *Energy Conversion and Management*, 44(15):2425–2443, 2003.

[70] Jie Sun, Qibin Liu, and Hui Hong. Numerical study of parabolic-trough direct steam generation loop in recirculation mode: Characteristics, performance and general operation strategy. *Energy Conversion and Management*, 96:287–302, 2015.

[71] Antoine Frein, Lorenzo Pistocchini, Victor Tatay, and Mario Motta. Modeling and Sizing of a MW Solar DSG plant. *Energy Procedia*, 91:620–629, 2016.

[72] B.S. Petukhov. Heat Transfer and Friction in Turbulent Pipe Flow with Variable Physical Properties. *Advances in Heat Transfer*, 6:503–564, 1970.

[73] V. Gnielinski. On heat transfer in tubes. *International Journal of Heat and Mass Transfer*, 63:134–140, 2013.

[74] John C. Chen. Correlation for boiling heat transfer to saturated fluids in convective flow. *IEC Process Design and Development*, 5(3):322–329, 1966.

[75] M.M. Shah. Chart Correlation for saturated boiling heat transfer : equations and further study. *ASHRAE Trans.*, 88(1):185–196, 1982.

[76] K.E. Gungor and R.H.S. Winterton. A general correlation for flow boiling in tubes and annuli. *International Journal of Heat and Mass Transfer*, 29(3):351–358, 1986.

[77] S G Kandlikar. A General Correlation for Saturated Two-Phase Flow Boiling Heat Transfer Inside Horizontal and Vertical Tubes. *Journal of Heat Transfer*, 112:219–228, 1990.

[78] J. R. Thome. *Engineering Data Book III Chapter 12 Two-Phase Flow Patterns*. 2006.

[79] N. Kattan, J. R. Thome, and D. Favrat. Flow Boiling in Horizontal Tubes: Part 3-Development of a New Heat Transfer Model Based on Flow Pattern. *Journal of Heat Transfer*, 120(1):156, 1998.

[80] John H. Lienhard IV and John H. Lienhard V. *A heat transfer textbook*. Phlogiston Press, third edit edition, 2003.

[81] S. E. Haaland. Simple and Explicit Formulas for the Friction Factor in Turbulent Pipe Flow. *Journal of Fluids Engineering*, 105(1):89, 1983.

[82] P.B. Whalley. See Hewitt, G. F. (1983). Multiphase flow and pressure drop. *Heat Exchanger Design Handbook*, 2, 1980.

[83] L. Friedel. Improved Friction Pressure Drop Correlations for Horizontal and Vertical Two-Phase Pipe Flow. *European two-phase flow group Meeting*, 2, 1979.

[84] D. Chisholm. Pressure gradients due to friction during the flow of evaporating two-phase mixtures in smooth tubes and channels. *International Journal of Heat and Mass Transfer*, 16(2):347–358, 1973.

[85] R. W. Lockhart and R. C. Martinelli. Proposed correlation of data for isothermal two-phase two-component flow in pipes. *Chemical Engineering Progress*, 45(1):39–48, 1949.

[86] Ovid Baker. Design of pipelines for the simultaneous flow of Oil and Gas. *Oil and Gas Journal*, 1954.

[87] Dieter Steiner and Matthias Kind. *VDI Heat Atlas. H3.1 Flow Patterns in Evaporator Tubes.* VDI-Gesellshaft Verfahrenstechnik und Chemieingerieurwesen, second edi edition, 2010.

[88] N. Kattan, J. R. Thome, and D. Favrat. Flow Boiling in Horizontal Tubes: Part 1-Development of a diabatic two-phase flow pattern map. *Journal of Heat Transfer*, 120(140-147), 1998.

[89] O. Zurcher, J. R. Thome, and D. Favrat. Evaporation of Ammonia in a Smooth Horizontal Tube: Heat Transfer Measurements and Predictions. *Journal of Heat Transfer*, 121(1):89, 1999.

[90] J R Cooper and R. B. Dooley. Revised Release on the IAPWS Industrial Formulation 1997 for the Thermodynamic Properties of Water and Steam. Technical Report August 2007, International Association for the Properties of Water and Steam, Lucerne, Switzerland, 2007.

[91] Johannes Pernpeintner. Test- and Qualification Center for Concentrating Solar Power Technologies Measurement of Parabolic Trough Receiver Thermal Loss Power and Relative Optical Efficiency under Solar Simulator Light Test Report. Technical report, DLR, 2012.

[92] Michael Berger, Andreas Häberle, Johannes Louw, Tobias Schwind, and Christian Zahler. Mirroxx Fresnel process heat collectors for industrial applications and solar cooling. *SolarPaces Conference*, pages 1–8, 2009.

[93] E.W. Jassim, T.A. Newell, and J C Chato. *Probabilistic Flow Regime Map Modeling of Two-Phase Flow.* PhD thesis, University of Illinois at Urbana-Champaign Air, 2006.

[94] E. W. Jassim, T. A. Newell, and J. C. Chato. Prediction of two-phase condensation in horizontal tubes using probabilistic flow regime maps. *International Journal of Heat and Mass Transfer*, 51(3-4):485–496, 2008.

[95] H. G. Hubbard and A. E. Dukler. The Characterization of Flow Regimes for Horizontal Two-Phase Flow. *Proceedings of the 1966 Heat Transfer and Fluid Mechanics Institute*, pages 101–121, 1966.

[96] H. M. Prasser, A. Böttger, and J. Zschau. A new electrode-mesh tomograph for gas-liquid flows. *Flow Measurement and Instrumentation*, 9(2):111–119, 1998.

[97] Horst-michael Prasser. Short Courses : Modelling and Computation of Multiphase Flows - Chapter IX : Advanced two-phase flow instrumentation. Technical report, Swiss Federal Institute of Technology (ETHZ), Zurich, Switzerland, 2015.

[98] F Danel and JM Delhaye. Optical probe for measuring the local voidage in two-phase flow systems. *Mes., Regul., Automat.*, 36(8-9):99–101, 1971.

[99] V.T. Morgan. *The Overall Convective Heat Transfer from Smooth Circular Cylinders*. In Fundamental of Heat and Mass Transfer of Bergman Et.al, 1975.

[100] Leonardo Carlos Ruspini, Christian Pablo Marcel, and Alejandro Clausse. Two-phase flow instabilities: A review. *International Journal of Heat and Mass Transfer*, 71:521–548, 2014.

[101] M. Ledinegg. Instability of flow during natural and forced circulation. *DieWärme*, 61(8):891–898., 1938.

[102] J.R. Thome. *Engineering Data Book III Chapter 13 Two-Phase Pressure Drops*. Wolverine Tube, Inc., 2006.

[103] D. Chisholm. A theoretical basis for the Lockhart-Martinelli correlation for two-phase flow. *International Journal of Heat and Mass Transfer*, 10(12):1767–1778, 1967.

[104] John A. Duffie and William A. Beckman. *Solar engineering of thermal processes*. John Wiley & Sons Inc, 1980.

[105] William R. McIntire. Factored Approximations for biaxial incident angle modifiers. *Solar Energy*, 29(4):315–322, 1982.

[106] Mats Rönnelid, Bengt Perers, and Björn Karlsson. On the factorisation of incidence angle modifiers for CPC collectors. *Solar Energy*, 59(4-6):281–286, 1997.

[107] Max Mertins. *Technische und wirtschaftliche Analyse von horizontalen Fresnel-Kollektoren*. PhD thesis, Universität Karlsruhe (TH), 2009.

[108] Markus Eck, Holger Schmidt, Martin Eickhoff, and Tobias Hirsch. Field Test of Water-Steam Separators for the DSG Process. *SolarPaces Conference*, pages 1–9, 2006.

Appendix

A System of equation

The two-phases flow numerical models used for this work is based on a control volume approach. The system of equations on the integral form applied to the control volume is composed of 6 conservation equations, ie. three conservation equations for each phase. The equation of continuity eq. A.1, the equation of change of momentum eq. A.2 and the equation of conservation of energy eq. A.3 are written for steam phase and the equations are similar for the liquid phase by changing the index $g \leftrightarrow l$ and $\epsilon \rightarrow (1-\epsilon)$

$$\frac{d\left(V \cdot \langle \rho_g \cdot \epsilon \rangle_{cell}\right)}{dt} = \sum_{all faces} A \cdot \langle w_g \cdot \rho_g \cdot \epsilon \rangle_{face} + \dot{m}_{l\rightarrow g} - \dot{m}_{g\rightarrow l} \tag{A.1}$$

$$\begin{aligned}\frac{d\left(V \cdot \langle \rho_g \cdot w_g \cdot \epsilon \rangle_{cell}\right)}{dt} &= \sum_{all faces} A \cdot \langle w_g \cdot w_g \cdot \rho_g \cdot \epsilon \rangle_{face} + \sum_{all faces} A \cdot cos(\gamma) \cdot \langle \epsilon \cdot p \rangle_{face} \\ &- V \langle \rho_g \epsilon \rangle_{cell} g \cdot cos(\theta) + F_{g,ext} + w_l \cdot \dot{m}_{l\rightarrow g} - w_g \cdot \dot{m}_{g\rightarrow l} \\ &+ F_{wall\rightarrow g} + F_{l\rightarrow g}\end{aligned} \tag{A.2}$$

$$\begin{aligned}\frac{d\left(V \cdot \langle \rho_g \cdot e_g \cdot \epsilon \rangle_{cell}\right)}{dt} &= \sum_{all faces} A \cdot \langle e_g \cdot w_g \cdot \rho_g \cdot \epsilon \rangle_{face} + \sum_{all faces} A \cdot \langle w_g \cdot \epsilon \cdot p \rangle_{face} \\ &- p \cdot \frac{d\langle V \cdot \epsilon \rangle_{cell}}{dt} + \langle u_g \cdot (\dot{m}_{l\rightarrow g} - \dot{m}_{g\rightarrow l}) \rangle_{cell} \\ &+ \langle p \cdot v_g \cdot (\dot{m}_{l\rightarrow g} - \dot{m}_{g\rightarrow l}) \rangle_{cell} + \dot{Q}_{wall\rightarrow g} + \dot{Q}_{int\rightarrow g} + \dot{Q}_{dissipation}\end{aligned} \tag{A.3}$$

where :

V	is the control volume [m^3]
A	is the cell faces [m^2]
w	is the fluid velocity [m/s]
ρ	is the density [kg/m3]
$\dot{m}_{l\rightarrow g}$	is the evaporation mass flow rate [kg/s]
$\dot{m}_{g\rightarrow l}$	is the condensation mass flow rate [kg/s]

p	is the pressure [Pa]
ϵ	is the void fraction
γ	is the angle between the normal vector of the cell face and the main flow direction [rad]
g	is gravity acceleration [kg/s^2]
$F_{g,ext}$	is external force [N]
$F_{wall \to g}$	is friction force [N]
$F_{l \to g}$	is interfacial friction force [N]
$\langle u_g \cdot (\dot{m}_{l \to g} - \dot{m}_{g \to l}) \rangle_{cell}$	is internal energy submitted by phase transition [W]
$\langle p \cdot v_g \cdot (\dot{m}_{l \to g} - \dot{m}_{g \to l}) \rangle_{cell}$	is displacement work by phase transition [W]
$\dot{Q}_{wall \to g}$	is wall heat transfer [W]
$\dot{Q}_{int \to g}$	is interfacial heat transfer (heat from gas-liq interface) [W]
$\dot{Q}_{dissipation}$	is thermal ernergy produced by dissipation (friction) [W]

B Kattan Thome Favrat's flow pattern map

A two-phase flow pattern map for flow boiling in horizontal tubes has been published by N.Kattan, J.R.Thome and D.Favrat in 1998 [88]. This section summarizes the transition boundary curves use in this PhD work, ie. the boundaries for the following flow patterns : stratified, stratified wavy, intermittent and annular.

- The transition boundary curve between annular and intermittent flows to stratified-wavy flow is defined in eq. B.1.

$$\dot{m}_{SW\leftrightarrow A-I} = [C_1 \cdot C_2]^{0.5} + 50 \tag{B.1}$$

$$C_1 = \frac{16 A_{Gd}^3 \cdot g \cdot d_i \cdot \rho_l \cdot \rho_g}{x^2 \pi \left(1 - (2h_{Ld} - 1)^2\right)^{0.5}} \tag{B.2}$$

$$C_2 = \frac{\pi^2}{25 \cdot h_{Ld}^2} \cdot (1-x)^{-F_1(\dot{q})} \cdot \left(\frac{We}{Fr}\right)_l^{-F_2(\dot{q})} + 1 \tag{B.3}$$

with: A_{Gd} defined as the non-dimensional cross section [-], h_{Ld} defined as the non-dimensional the reference liquid level[-],$\dot{q}$: the heat flux over the cross section [kW/m^2], d_i: internal tube diameter [m], ρ_l: liquid density [kg/m^3], ρ_g: steam density [kg/m^3], x: steam quality [-].

where the ratio between the Weber and Froude number is defined as eq. B.4

$$\left(\frac{We}{Fr}\right)_l = \frac{g \cdot d_i^2 \cdot \rho_l}{\sigma} \tag{B.4}$$

with g: the gravity acceleration [m/s^2], σ: surface tension for water [N/m]

The two non-dimensional functions are defined in eq. B.5 and eq. B.6.

$$F_1(\dot{q}) = 646.0 \left(\frac{\dot{q}}{\dot{q}_{DNB}}\right)^2 + 64.8 \cdot \left(\frac{\dot{q}}{\dot{q}_{DNB}}\right) \tag{B.5}$$

$$F_2(\dot{q}) = 18.8 \cdot \left(\frac{\dot{q}}{\dot{q}_{DNB}}\right) + 1.023 \tag{B.6}$$

with the nucleate boiling $\dot{q}_{DNB}$ [kW/m^2] defined as eq. B.7

$$\dot{q}_{DNB} = 0.131 \rho_g^{0.5} \cdot h_{lat} \cdot (g \cdot (\rho_l - \rho_g) \cdot \sigma)^{0.25} \tag{B.7}$$

- The transition boundary curve between stratified-wavy flow and fully stratified flow is defined in eq. B.8

$$\dot{m}_{S\leftrightarrow SW} = \left[\frac{226.3^2 \cdot A_{Ld} \cdot A_{Gd} \cdot \rho_g \cdot (\rho_l - \rho_g) \cdot \mu_l \cdot g}{x^2 (1-x) \pi^3}\right]^{1/3} \tag{B.8}$$

with μ_l: the dynamic viscosity of liquid phase [Pa/s]

- The vertical transition boundary curve between intermittent flow and annular flow is defined for a fixed value of Martinelli coefficient equal to 0.34. Solving the equation boundary steam quality is defined in eq. B.9.

$$x_{I\leftrightarrow A} = \left[\left(0.2914 \cdot \left(\frac{\rho_g}{\rho_l}\right)^{-1/1.75} \left(\frac{\mu_l}{\mu_g}\right)^{-1/7}\right) + 1\right]^{-1} \tag{B.9}$$

with μ_g: the dynamic viscosity of steam phase [Pa/s]

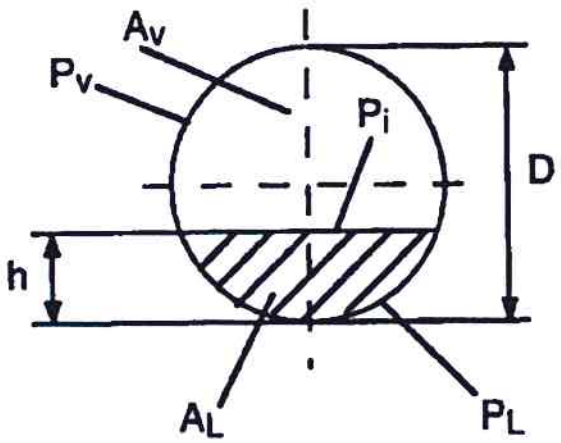

Figure B.1: Cross-sectional and peripheral fractions in a circular tube [88].

The non-dimensional cross section A_{Gd} and the non-dimensional reference liquid level h_{Ld} are defined below by solving the following system of equations. The six unknown are defined below in eq. B.10

$$\begin{aligned} h_{Ld} &= \frac{h}{d_i}, \quad P_{Ld} = \frac{P_L}{d_i}, \quad P_{Gd} = \frac{P_G}{d_i}, \quad P_{id} = \frac{P_i}{d_i}, \\ A_{Ld} &= \frac{A_L}{d_i^2}, \quad A_{Gd} = \frac{A_G}{d_i^2} \end{aligned} \tag{B.10}$$

Then, the system of 6 equation is defined below. The form of the first four equations depend to the variable h_{Ld} whereas the eq. B.19 and eq. B.20 are used for each value of h_{Ld}.

If $h_{Ld} \leq 0.5$:

$$P_{Ld} = \frac{8\left(h_{Ld}\right)^{0.5} - 2\left(h_{Ld} \cdot (1 - h_{Ld})\right)^{0.5}}{3} \tag{B.11}$$

$$P_{Gd} = \pi - P_{Ld} \tag{B.12}$$

$$A_{Ld} = \frac{\left(12\left(h_{Ld} \cdot (1 - h_{Ld})\right)^{0.5} + 8\left(h_{Ld}\right)^{0.5}\right) \cdot h_{Ld}}{15} \tag{B.13}$$

$$A_{Gd} = \frac{\pi}{4} - A_{Ld} \tag{B.14}$$

If $h_{Ld} > 0.5$:

$$P_{Ld} = \pi - P_{Gd} \tag{B.15}$$

$$P_{Gd} = \frac{8\left(1 - h_{Ld}\right)^{0.5} - 2\left(h_{Ld} \cdot (1 - h_{Ld})\right)^{0.5}}{3} \tag{B.16}$$

$$A_{Ld} = \frac{\pi}{4} - A_{Gd} \tag{B.17}$$

$$A_{Gd} = \frac{\left(12\left(h_{Ld} \cdot (1 - h_{Ld})\right)^{0.5} + 8\left(1 - h_{Ld}\right)^{0.5}\right) \cdot (1 - h_{Ld})}{15} \tag{B.18}$$

$$P_{id} = 2 \cdot (h_{Ld} \cdot (1 - h_{Ld}))^{0.5} \tag{B.19}$$

$$X_{tt}^2 = \left[\left(\frac{P_{Gd} + P_{id}}{\pi} \right)^{0.25} \cdot \left(\frac{\pi^2}{64 \cdot A_{Gd}^2} \right) \cdot \left(\frac{P_{Gd} + P_{id}}{A_{Gd}} + \frac{P_{id}}{A_{Ld}} \right) \right] \cdot \left(\frac{\pi}{P_{Ld}} \right)^{0.25} \cdot \left(\frac{64 \cdot A_{Ld}^3}{\pi^2 \cdot P_{Ld}} \right) \tag{B.20}$$

with the Martinelli parameter defined as eq.B.21

$$X_{tt} = \left(\frac{1 - x}{x} \right)^{0.875} \cdot \left(\frac{\rho_g}{\rho_l} \right)^{0.5} \cdot \left(\frac{\mu_l}{\mu_g} \right)^{0.125} \tag{B.21}$$

In 1999, Zurcher, Thome and Favrat study [89] extended the range of validity of the KTF flow pattern map proposed by Kattan, Thome and Favrat [88], called *modified KTF* in this document. They show that the boundary curve between stratified / wavy statified was too low at high steam quality, see eq. B.22, whereas the stratified wavy to annular flow was too high at high steam quality, see eq. B.23.

$$\dot{m}_{S \leftrightarrow SW,modified} = \dot{m}_{S \leftrightarrow SW,KTF} + 20 \cdot x \tag{B.22}$$

$$\dot{m}_{SW \leftrightarrow A-I,modified} = \dot{m}_{SW \leftrightarrow A-I,KTF} - 75 \cdot e^{\frac{\left(x^2 - 0.97\right))^2}{x \cdot (1-x)}} \tag{B.23}$$

$$\tag{B.24}$$